MANY-BODY QUANTUM TUNNELING OF ULTRACOLD BOSONIC GASES: QUANTUM PHASE TRANSITIONS, BOSONIC JOSEPHSON JUNCTIONS, AND MOTT SWITCH ATOMTRONICS

by

Marie Anne Patton McLain

A thesis submitted to the Faculty and the Board of Trustees of the Colorado School of Mines in partial fulfillment of the requirements for the degree of Doctor of Philosophy (Applied Physics).

Golden, Colorado

Date _____

Signed: _____
Marie Anne Patton McLain

Signed: _____
Dr. Lincoln D. Carr
Thesis Advisor

Golden, Colorado

Date _____

Signed: _____
Dr. Uwe Greife
Professor and Department Head
Department of Physics

ABSTRACT

Ultracold Bose gases as precise quantum simulators have emerged amongst the leaders in the current race – a second quantum revolution – toward the promise of unfathomable sensitivity, scope, and speed of a new era of technology. The only path leading to these advancements is through many-body descriptions, especially in regimes where interatomic interactions render many approximations incompatible with the physics. The research in this dissertation unlocks a piece of this mystery through investigations of many-body quantum tunneling of ultracold bosons in optical lattices. A key mechanism to characterizing the dynamics, matrix product state simulations equip the many-body toolbox with efficient optimization of large Hilbert spaces together with correlation and entropy measures that help clarify when semiclassical or mean-field approximations fail. In this thesis we obtain the following results.

Macroscopic quantum tunneling escape of a Bose-Einstein condensate – comprised of tens of thousands of ^{87}Rb atoms – from a single well, as portrayed through both experiment and theory, highlights non-exponential decay in the number of atoms trapped behind the barrier. Additionally, explicit symmetry breaking of a biperiodic optical lattice ring trap to a uniform one illustrates a critical symmetry-breaking strength at which the system transitions from a state of remembering to a state of forgetting its initial symmetry state; this symmetry memory indicates a new form of quantum dynamics that requires the quantum advantage for scaling up particle number and lattice sites.

Extensive characterization of dynamical regimes in a bosonic Josephson junction – underlaid by an optical lattice as described by the Bose-Hubbard model – reveal substantial deviation of many body dynamics from the mean field or semiclassical predictions underlying the usual operating regime of Josephson junctions. Initial state population and phase yield insight into dynamic tunneling regimes of a quasi one-dimensional double well po-

tential, through the $\mathbb{Z}_2$ spontaneous symmetry-breaking phase transition from Josephson oscillations to macroscopic self-trapping. We demonstrate that with increasing repulsive interaction strength, the $U(1)$ superfluid-Mott insulator phase transition induces localized dynamics in the number density, such as particle-hole and soliton formation. Moreover, $g^{(2)}$ correlations unveil a new dynamic regime – the Fock flashlight.

The new field of atomtronics – or atomic circuits – has emerged with many studies of weakly-interacting condensates. In contrast, and building on our work on many-body effects in the double wells underlying Josephson junctions, we present a proof-of-principle of a Mott-insulating atomtronic switch that requires strongly-interacting bosons. Through transient analysis, we reveal that hole conductance can be modulated via tuning interaction strength through a critical value, thus propelling the state to the next "wedding cake" layer of the Mott insulating structure. This critical interaction strength is a result of the confining potential and corresponds with critical phenomena in transport properties as measured via transmission and fidelity. $g^{(2)}$ two-point correlators provide an experimentally viable means of identifying superfluid fragments as a means of identifying switching state.

Finally, the research presented in this dissertation provides a foundation for many-body quantum tunneling that can be further expanded to the emerging field of quantum atomtronics. The highly precise architectures needed for such technologies are conducive to understanding many-body phenomena for the creation of quantum-engineered devices, from atomic clocks and simulation techniques to biomedical magnetic sensors and secure communications.

TABLE OF CONTENTS

LIST OF FIGURES AND TABLES

LIST OF ABBREVIATIONS

Bose-Einstein Condensate or Condensation . . . . . BEC

Bose-Hubbard Hamiltonian . . . . . BHH

Bosonic Josephson Junction . . . . . BJJ

Josephson Junction . . . . . JJ

Macroscopic Quantum Tunneling . . . . . MQT

Matrix Product State . . . . . MPS

Quantum Phase Transition . . . . . QPT

Superconducting Quantum Interference Device . . . . . SQUID

Time Evolving Block Decimation . . . . . TEBD

ACKNOWLEDGMENTS

First and foremost, I must thank my advisor, Dr. Lincoln Carr, for his continued support and investment in me throughout my tenure at the Colorado School of Mines. Without his careful constructive criticisms, I would have never been able to reflect upon my own work – and life – with a critical eye. As I slowly and methodically drove myself into the deep, dark spaces comprising the nighttime of the soul, as one must in order to make it out of a PhD thesis alive, Lincoln patiently waited and offered guidance so I could learn from my mistakes and make it to the other side. Thank you, Lincoln, for believing in me when I didn't believe in myself, and thank you for everything.

I am especially grateful for all of the students, friends, and post-docs with whom I suffered throughout graduate school. There is no replacement for the type of friendship that develops in commiseration, especially as the wounds begin to heal and smiles begin to regrow. A huge thank you to Diego Alcala, for voicing those difficult inner thoughts that are so often avoided – and for providing non-stop inspiration and practical wisdom – I will always cherish our conversations. Many thanks to Daniel Jaschke for countless simulation help-sessions, for setting a great example through an admirable work ethic, for snow-shoeing treks, hikes in the mountains, and wonderful conversations. Much gratitude goes to Xinxin Zhao, for inspiring me with her bravery and poise in a new culture, and for always maintaining that positive attitude, no matter how difficult or frustrating the calculations were; thanks also for the adventures, I will never forget the summer sledding and snowball fights. Thanks goes to Gavriil Shchedrin for ample calculation help, especially in Quantum II, and for boundless energy and laughs, especially when nothing was going right. Gavriil, thanks for the coffee conversations, great stories, and dare I say the occasional alcoholic beverage or two. Thanks to Marc Valdez, for showing me that the best way to face your fears is head-on; and thanks also to Kirsten Blagg for showing me that the other best way to face your fears is with

laughter. Thanks to Kirsten, David Hensle, Matt Jones, Kevin Merenda and Alex Wilhelm, for putting a positive spin on enduring you-know-what class with me (no offense, Lincoln). Thanks to Warren Coulomb and Andrew Proudian for busting the rust off of undergaduate physics with me, especially that mentally-tough first year. Special thanks to Logan Hillberry for a contagious, insatiable curiosity, and passing on Python-scripting wisdom. Additionally, I wish to acknowledge my wonderful colleagues at Northrop Grumman, who have gone out of their way to support me in the final year and a half of my PhD. Particularly, thanks to Jonar Cochran, Dr. Ryan Epstein, Dr. Eli Galan, Lewis Graninger, Dr. Annemarie Hoyer, Dr. Aaron Lee, Dave McGuire, Nate Mungo, Dr. Mark Nowakowski, Dr. Ollie Oberg, Dr. Tony Przybysz, and Bob Zimmerman.

Many heartfelt thanks to LeeAnna Grauel and Barbara Shellenberger for all of their eager support – without which I never would have been able to graduate – and for always being open to talking about cheerful things other than the daily grind, and reminding me where puppies belong on my priority list. Thanks to Dr. Jeff Squier and Dr. Uwe Griefe for going above and beyond the call of department head duties to help me on the path to graduation. Thanks to my committee members, Dr. Geoff Brennecka, Dr. Susanta Sarkar, Dr. Meenakshi Singh, and Dr. Craig Taylor, along with the support of Dr. John Scales, for believing in me and providing the gentle encouragement I needed to make it to the finish line. Thanks to all the people in the graduate office, especially Jahi Simbai, Suzanne Beach, Roxane Aungst, Dr. Tina Voelker, and to everyone else who works hard behind the scenes at Mines to ensure students like me are able to graduate in a reasonable time.

Without the support group of wonderful, caring friends and family, I would no doubt be lying dead, face-down in a drain pool somewhere. First and foremost, a humble thank-you to Kory Riskey, who goes out of her way to attend my presentations (even when I beg her not to), who has taught me the value of dropping everything to hang out with a very dear friend, and who kept me moving forward when all I wanted to do was fall back. Thanks to Mark Husted, for random late-night study sessions, setting a wonderful example of where

running should be on one's priority list, and for having a helluva lot of grit. Thanks to Dave Patton and Jamie Miller for unwavering support and endless advice. A huge thank-you to Cam, Margaret, and Kate, for taking me under your wing and reminding me of God's subtle nature. Thank you to Mike, for being a role model and mentor as I went through the darkest days of my life; thank you to Keith for being the control variable; thank you to Shelly for nearly driving me insane – just kidding. Thanks Mom for driving Shelly insane – just kidding – thanks for always carrying all the bags and thanks Dad for not being insane. In all seriousness, Shelly – you know what you did, and I'll let everyone else reading this wonder forever in what ways you have influenced this work. Keith, you taught me how to be tough and how to compete with myself, and most importantly, how to giggle (instead of cry) at one in the morning even if there were a million things to do. Mike, you know what you want and you go for it, you have always been an individual and that driving force you carry everywhere is something I have been striving to achieve my whole life. Mom, thanks for taking care of me and making endless sacrifices when I wasn't taking care of myself. Dad, Physics, thank you for inspiring me to study physics in the first place and thanks for showing me what selflessness truly is. And thanks to everyone else not mentioned here who has inspired me in other ways.

Last but not least, Mack, you get your own paragraph, as a token of my appreciation. At this very moment, I am only able to type right now because you massaged my crippled-from-carpal-tunnel right arm. I am only able to go to work tomorrow because you have done everything to help me get ready. Thanks for all the little things that I forget to thank you for every day. Thanks for tirelessly helping me back to my feet, no matter how many times I tripped or how far I fell.

For Shelly. You are braver than whipped cream.

For Mack. Let it be known there is a fountain that was not made by the hands of men.

–Grateful Dead

For Physics. Little by little, one travels far. –J.R.R. Tolkien

CHAPTER 1

OVERTURE AND SYNOPSIS: MOTIVATIONS, BACKGROUND, AND RESULTS

Initially, the driving questions for the research in this dissertation were foundational in nature: What happens when we take tunneling – a fundamentally quantum feature – and extend it into macroscopic regimes? How do ultracold bosons tunnel in the double well? What influence does the dynamic tunneling regime have on boson behavior? In what ways does the parameter space affect the superfluid-Mott insulator phase transition, and vice versa? As the research progressed, the driving questions began shifting toward potential applications of this work to quantum devices. What are some real world uses for quantum tunneling beyond, for example, tunneling diodes?

As we move forward in the world of the second quantum revolution, the invasion of quantum mechanics into our everyday lives is inevitable, and in fact, has already begun. If you are one of the 5 billion mobile phone users in the world, for instance, its GPS relies on the precise timing of atomic clocks, which are fundamentally quantum in that they rely on atomic transition frequencies. As the field of quantum physics matures, the focus is slowly shifting from research on fundamental principles to quantum applications. It is very possible that quantum engineering may soon emerge as the newest academic department at universities. This shift of the quantum research field is correlated with the research shift in this dissertation – from a fundamental focus to an applied one.

The goal of this introductory chapter is to provide an accessible background on key topics and highlight principal methods and research findings for the general scientific readership, as well as outline the rest of the dissertation.

1.1 Understanding quantum mechanics

At very small length scales, on the order of nanometers or smaller, particles such as electrons, atoms, and molecules exhibit wave-like properties that are rooted in statistics:

there is some probability of measuring a particle in a certain location, but the outcome has a range of possibilites. Just as in statistics, there is a distribution about the average value of these measurements. This does not mean we are "uncertain" about the properties of quantum mechanics, rather that quantum uncertainty is a highly-specific property that gives us insight into the pixel size of a quantum measurement, much like digital cameras have finite resolution. The total probability of these measurement outcomes is conserved – which leads to unitary time evolution – where dynamics are determined based on an initial quantum state. Finally, these tiny particles are divided into two large groups: bosons, which tend to stay together like photons in a laser, all one color; and fermions, which tend to repel like the neutrons in a neutron star, stable against collapse due to Fermi pressure. All the research discussed in this thesis pertains to bosons, and is particularly focused on their dynamic behavior.

1.1.1 Macroscopic quantum tunneling

The distribution of quantum measurements provides the basic idea underlying quantum tunneling: particles whose distributions – or wavefunctions – overlap a potential barrier have a finite probability of going through the barrier. If we think about a barrier as a container, say we trap an atom in the container whose wavefunction penetrates the surrounding walls, there is some possibility the atom will pop out. In contrast, if you put a marble, a macroscopic object, in a closed container, it remains stuck inside. Macroscopic quantum tunneling means that many particles can be represented by a single probability distribution, or macroscopic wavefunction, that overlaps the barrier, and the particles tunnel collectively. Does that mean your marble, composed of 10^{23} atoms, can tunnel through the container? Or that a tennis ball can really go *through* a net? This seemingly silly question in fact addresses a fundamental question of quantum mechanics: how does microscopic behavior of atoms, for example, become macroscopic?

Furthermore, quantum state transfer is akin to the movement of particles via quantum tunneling, though the presence of a barrier is not required. In fact, it may be more correct

to refer to the particles as matter-waves, or simply bosons. The quantum state transfer in this dissertation specifically concerns the movement, or tunneling, of bosons in an optical lattice.

1.1.2 Ultracold atoms in optical lattices

Ultracold atoms are experimentally isolated in ultra high vacuums and cooled down to temperatures in the tens to hundreds of nanoKelvin range. This extreme isolation from the environment allows for very fine levels of control. Optical lattices of ultracold atoms provide a tunable crystal structure, where, in principle, the atoms can be trapped on a grid of any geometry, and they offer an ideal setting for probing the limits of quantum physics. These grid structures can be thought of as egg cartons, where the atoms sit in the wells of the carton. Ultracold atoms in optical lattices provide a system tunable over seven orders of magnitude in strength and sign of interaction that can mimic other physical architectures, such as solid state materials, and provide precise quantum simulation of e.g. lattice structures, transport dynamics, and defect formation.

Bose-Einstein condensates (BECs) are an area of continuing and still growing research interest in ultracold atoms since they were first created in 1995 (Nobel prize, 2001) [1]. A macroscopic number of neutral atoms (often on the order of a million) Bose condense when their temperature is cooled below a critical point, and a large fraction occupy the same quantum state: they have the same energy and momentum. This means we can represent nearly all of the atoms with a single wavefunction [2]. Besides their ability to bridge the gap from the quantum realm into the macroscopic realm, their applications include high-precision quantum simulators, interferometers, and atom lasers.

1.1.3 Quantum phase transitions and symmetry

Quantum phase transitions are similar to thermodynamic phase transitions in that tuning of a parameter through a critical point will cause a change in a state of matter. In thermodynamic transitions, this parameter is the temperature, pressure, etc. and the state

of matter or phase change is driven by thermal fluctuations. The effects of quantum phase transitions are typically observed at low temperatures, where thermal effects become small or negligible, and tuning a separate parameter, usually controlling one term or another in the quantum Hamiltonian describing different contributions to the energy of the system, will cause the phase change. The transition is driven instead by quantum fluctuations [3].

Between two states of matter, one of the phases has a certain symmetry associated with it, and moving through the critical point to the other phase breaks this symmetry. If we return to our notion of an optical lattice as an egg carton with atoms in each well, when the wells are shallow, the atoms will tunnel freely between wells in the carton; the phase-locking between atoms in the optical lattice leads to a global symmetry, and the result is a superfluid. As the wells of the carton are raised, the probability of atoms tunneling decreases and they are more likely to be trapped within a well. When they are fully trapped, the result is a Mott insulator, the ultracold gas has undergone a quantum phase transition, and the symmetry of the phase has been broken, leading to a sort of quantum solid, where matter is "frozen out" in a crystal of light.

1.2 Methods: a many-body bosonic Josephson junction

The paper in chapter 4 comprises a large proportion of the research performed as part of this dissertation, focusing on full characterization of the parameter space for a long bosonic Josephson junction – or a square double well with spatial extent. How do we investigate the many-body dynamics?

In order to understand the tunneling behavior of an ultracold Bose gas Josephson junction, we use open source time-evolving block decimation (openTEBD) [4, 5] to run numerical simulations. This method is adapted to producing many-body quantum mechanics with a variety of measures that can be directly compared to experiment. We impose an optical lattice on the double well potential to establish a grid for many-body dynamics. The Bose-Hubbard Hamiltonian describes the two length scales of the double well or Josephson junction via two rivaling energy terms: the on-site interaction and the Josephson tunneling strength. Exper-

imentalists tune the on-site interaction in the optical lattice by Feshbach resonances or by modulating lattice depth. Similarly, Josephson energy is adjusted by modifying the barrier height or width, which depends on the specific type of barrier chosen. One length scale is the distance between the two minima in the double well. The second, much smaller length scale, is the wavelength of the optical lattice underlying the double well, which can also be considered a discretization scheme for numerical simulation toward a continuum. However, in this thesis we focus on the explicitly enforced lattice available in BEC experiments.

This leads us to investigate the impact of the $U(1)$ superfluid – Mott insulator quantum phase transition, the first type of phase transition, on this multi-scale tunneling behavior. $U(1)$ is the symmetry associated with phase, a circle running 0 to 2π. The second type of phase transition is a discrete $\mathbb{Z}_2$ transition from a Josephson oscillation phase to a macroscopic self-trapping phase. $\mathbb{Z}_2$ is the symmetry associated with the sign, plus or minus, or in our case, left or right. The interplay of the two quantum phase transitions, $\mathbb{Z}_2$ and $U(1)$, reduces to tuning of the barrier height for the spontaneous symmetry breaking transition and tuning of the laser intensity, thus changing the ratio of tunneling to interaction, for the superfluid-Mott transition. The ultimate goal then is to characterize the dynamic tunneling regimes that result, from Josephson oscillations to self-trapping. Some of the regimes have previously been identified in literature for weakly-interacting systems, while we explore the dynamics through the $U(1)$ quantum phase transition into the Mott insulating regime.

1.3 Dissertation Organization

The introductory chapter 1 features easily-digestible descriptions of three foundational sub-fields underlying much of the research in this dissertation: many-body and macroscopic quantum tunneling, ultracold atoms in optical lattices, and quantum phase transitions and symmetry. Chapter 2 expands on these introductory concepts with detailed technical background for these domains, together with the derivations and the comparisons of theoretical models for bosonic Josephson junction descriptions, and the outlining of numerical and analytical techniques.

My research contributions are presented in the two first-author papers in this dissertation as chapters 4 and 6, as well as the results shown in the follow-up chapter 5, together with my contributions as co-author on two separate projects in chapter 3 [6, 7]. The paper shown in chapter 4 outlines the many-body physics of a bosonic Josephson junction and its dynamic regimes [8]. In chapter 5, I summarize research performed as part of this dissertation that is either not published elsewhere or contains substantial open questions. Chapter 6 demonstrates a proof-of-principle of a Mott insulating switch for applications in atomic circuits, or atomtronics [9]. Finally, in chapter 7, I summarize with a brief overview of the four research papers presented in this dissertation and suggest logical future research directions.

CHAPTER 2
PRINCIPLES OF MANY-BODY QUANTUM TUNNELING WITH ULTRACOLD ATOMS

This chapter provides technical background and motivation for this research and provides a context of recent and relevant literature. Particularly, we get an of overview many-body quantum tunneling of ultracold quantum gases and how to describe them theoretically in a double well or Josephson junction. We also outline most of the methods used to perform the research for this dissertation.

2.1 Quantum tunneling and the macroscopic limit

Tunneling is a hallmark feature of quantum mechanics, typically associated with microscopic phenomena. Quantum tunneling describes the mobility of a particle or particles through a barrier in a manner that is forbidden classically – meaning the total energy of the system is less than that of the potential energy of the barrier. Tunneling plays a central role in diverse disciplines in contexts such as double beta decay in nuclear physics [10–12], photosynthesis in biology [13], transitions between chiral isomers in chemical molecular spectra [14, 15], nuclear fusion in stars and quantum cosmology [16, 17], chromodynamics [18], and enzyme reactions [19]. Even electronics and modern devices require quantum descriptions, such as tunneling diodes [20] and scanning tunneling microscopes [21, 22]. And quantum tunneling continues to be a highly active area of research, for example, in 2016 tunneling of water was discovered [23].

Friederich Hund is credited with the first description of the tunneling effect. In 1927, while calculating double well ground states, an interesting coincidental overlap with the work presented in this thesis, Hund discovered quantum mechanical barrier penetration for the first time [24]. While tunneling was first applied to nuclear physics [10, 11], it was soon

expanded and applied in the creation of transistors and diodes [25] prior to acceptance in mainstream quantum theory.

Take, for example, a finite rectangular barrier of height V_0, and a particle of constant energy E moving toward the barrier. The barrier could be an electromagnetic field, an insulator, a vacuum, or other region with a larger potential energy than its surroundings. If $E > V_0$, then the particle has enough energy to classically spill over the barrier, analogous to a ball (particle) having enough energy to roll over a hill (barrier). This is the classical regime. Conversely, if $E < V_0$, then the particle cannot possibly surmount the barrier in a classical sense. Rather, it has a nonzero probability of quantum mechanical barrier penetration. This probability is based on the parameters of the system. In addition to E and V_0, the barrier width, w, also dictates the probability of particle transmission and reflection. Transmission probability declines in proportion with the increased scaling of the barrier volume, $T \simeq e^{-2\gamma/\hbar}$ where $\gamma = w\sqrt{2m(V-E)}$. While typical tunneling processes are assumed to undergo exponential decay, a number of effects, including atomic interactions, can lead to non-exponential behavior [6].

We now consider tunneling in the framework of macroscopicity. The macroscopic limit can be explored through a variety of avenues. This includes, but is not limited to, larger length scales, larger numbers of particles and/or active degrees of freedom, classical or Newtonian gravitational effects, and complexity.

There is no agreed upon no critical point deeming a length scale as macroscopic; however, we may begin to understand a macroscopic length scale by a separation in phase space. Instinctively, the macroscopic limit approaches large numbers, on the order of $\sim 10^{23}$ particles; but, these large numbers are not exclusive to macroscopic physics. For example, Nobel prize-winning work on Bose-Einstein condensation (BEC) [26–28] demonstrated macroscopic mode occupation on the length scale of hundreds of microns, with atom numbers ranging from 10^3 to 10^9. For weakly-interacting, dilute Bose gases in an optical lattice, phase coherence is typically large, meaning the macroscopic phase $e^{i\phi(x_j)}$ is well-defined in each potential well j

on the lattice located at position x_j. The number of particles on the lattice site therefore has a high uncertainty due to the number-phase uncertainty relationship $\Delta n_j \Delta \phi_j \geq 1$ where n_j and ϕ_j are the particle number and phase on the lattice site. In this regime, dynamics are governed by superfluid flow – a macroscopic phenomenon. The discussion on superfluidity will continue in section 2.4.

Another prime example of macroscopic quantum physics is the Josephson effect. The Josephson effect has been demonstrated in multiple architectures, but is most often associated with superconducting Josephson junctions (JJs), which are composed of two superconductors separated by a weak link. Nobel laureate Brian Josephson is credited with the prediction of the macroscopic quantum tunneling of Cooper pairs, or pairs of electrons, across the insulating barrier of a JJ [29, 30]; P.W. Anderson and John Rowell quickly confirmed this prediction and published the first paper on its discovery [31]. Superconducting circuits comprised of these junctions are the epitome of macroscopic quantum tunneling devices and are used in a practical sense as the voltage standard by the National Institute of Standards and Technology: arrays of JJs are exceptionally accurate frequency-to-voltage converters [32]. The macroscopic tunneling effect is also seen in cold atom architectures, for example in Bose-Einstein condensate tunneling in a bosonic Josephson junction [33, 34]. And, even more recently, the first observation of macroscopic quantum escape of a BEC, comprised of more than 100,000 atoms, was made in Toronto, including work found in this thesis [35, 36].

Philosophically, one interpretation of the macroscopic limit is the classical limit - where and why does quantum mechanics break down? As an introduction to the classical limit, we begin with a familiar time-dependent wave equation and follow an argument in [37],

$$i\hbar \frac{\partial}{\partial t}\psi(\vec{r},t) = -\frac{\hbar^2}{2M}\nabla^2\psi(\vec{r},t) + V(\vec{r})\psi(\vec{r},t), \tag{2.1}$$

where $\psi(\vec{r},t)$ is a quantum state depending on time t and written in the position $\vec{r}$ basis, and M is the mass. We assume a constant Hamiltonian operator of the form $H = \frac{\vec{p}^2}{2M} + V(\vec{r})$,

where $\vec{p}$ is momentum and $V(\vec{r})$ is a time-independent potential. As a gentle reminder, the time-independent Schrödinger equation is more specific than its time-dependent cousin, as the time-independent wave equation in one dimension is satisfied by energy eigenfunctions $\psi_E(\vec{x})$ with energy eigenvalues E. The fascinating equivalence of matrix mechanics and wave mechanics via partial differential equations, as demonstrated by Erwin Schrödinger, was surprisingly made via the influence of an analogy from W.R. Hamilton between optics and mechanics, rather than from the more contemporary work of Heisenberg, Born, or Hilbert [37, 38]. This connection is critical for understanding the quantum nature of energy levels. In order to reach the classical limit in this discussion, we must first establish what makes quantum quantum.

In order to solve a time-independent wave equation, we must first establish boundary conditions. Suppose we take $E < V(\vec{x})$ in the limit as $|\vec{x}| \to \infty$. The boundary conditions would thus be $\psi_E(\vec{x}) \to 0$ as $|\vec{x}| \to \infty$. With the energy eigenfunction decaying to zero with physical distance, this means the particle occupies a finite, less-than-infinite volume. The the time-independent Schrödinger equation, in conjunction with these boundary conditions, yields a nontrivial solution only for discrete eigenvalues E. If this boundary condition is not satisfied, however, the energy levels will be continuous – this is one perspective of the classical limit. A second perspective relates the values of the conserved energy E to the value of the potential $V(\vec{x})$. If $E > V(\vec{x})$, the system is in the classical regime and the energy eigenfunctions $\psi_E(\vec{x})$ in one dimension are sinusoidal. On the other hand, if $E < V(\vec{x})$, then the system is in the quantum regime and the energy eigenfunctions are damped. This is particularly important with regards to quantum tunneling, which occurs when $E < V(\vec{x})$. The Jeffreys, Wentzel, Kramers, and Brillouin (JWKB or WKB) approximation, often used as a semiclassical analytical technique for solving tunneling problems, relies on the description of the particle's semiclassical momentum, $p(\vec{x}) = \sqrt{2M(E - V(\vec{x}))}$, which is real in the classical region and imaginary in the quantum region.

One interpretation of a general position $\vec{r}$ measurement might begin with the continuous matter-wave occupation of a finite volume and end with the collapse of this volume to a single point with no spatial extension. Leaning instead on the statistical interpretation of the wave function, where $\rho(\vec{r},t) = |\psi(\vec{r},t)|^2$ is a probability density, we write a general complex wave function,

$$\psi(\vec{r},t) = \sqrt{\rho(\vec{r},t)}\, \exp[\frac{iS(\vec{r},t)}{\hbar}], \tag{2.2}$$

so the value of the probability density is always positive, $\rho > 0$, and $S(\vec{r},t)$ is real and its identity will become apparent momentarily. To investigate the classical limit through the wave equation, we take Equation (2.2) and insert ψ into Equation (2.1). Now if we take $\hbar$ to be small we recover

$$\frac{1}{2M}|\nabla S(\vec{r},t)|^2 + V(\vec{r}) + \frac{\partial}{\partial t}S(\vec{r},t) = 0, \tag{2.3}$$

an equation you may recognize as the Hamilton-Jacobi equation from classical mechanics, where $S(\vec{r},t) = W(\vec{r}) - Et$ is Hamilton's principle function and $W(\vec{r})$ is Hamilton's characteristic function. The conclusion here is that in a classical limit, as $\hbar \to 0$, classical mechanics is contained in the Schrödinger equation. It is also important to note that the semiclassical limit of the single-particle Schrödinger equation is a particle. However, the semiclassical limit of the many-body Schrödinger equation is the nonlinear Schrödinger equation, a nonlinear wave equation. So a wave limits to a particle in the single particle case, but a many-body quantum state limits to a wave in the many particle case. While this is one of many viewpoints for probing macroscopic quantum physics, understanding the classical correspondence provides a foundation for more targeted exploration.

2.2 Bose-Einstein condensation in optical lattices

Einstein predicted BEC in 1925 [39] based on quantum statistical properties of photons calculated by Bose the previous year [40]. Below a critical temperature, the wavefunctions of a macroscopic number of bosons begin to overlap and a BEC is created. The result

is a collective occupation of the lowest energy state at ultracold temperatures [41]. In this manner, a group of bosons can behave as a single boson on the scale of microns or millimeters in a way that classical physics fails to describe – true macroscopic quantum physics [2]. Bose-Einstein condensation is the underlying principle describing the puzzling nature of superfluidity in ^{4}He [42], a surprising result due to the strong interactions of Helium atoms.

In 1995, the first realization of a BEC in dilute gases was achieved due to advances in laser and evaporative cooling [43], with a series of BECs created in dilute alkali gases of rubidium [26], sodium [27], and lithium [44]. One advantage of BEC in alkali gases stems from weak two-body interactions, allowing the atoms to be described by a single macroscopic wavefunction with small quantum fluctuations that to lowest order can be neglected [45]. In the weakly-interacting regime, a dilute Bose gas may be approximated by a mean-field description, however atomic interactions are then treated perturbatively.

Studying macroscopic quantum tunneling (MQT) in the context of BECs offers many advantages. First, BECs offer a high degree of controllability: interactions can be tuned over seven orders of magnitude and sign using Feshbach resonances [46, 47]. Second, experimental advances in radio-frequency (RF) magnetic traps [48] as well as optical trapping [49], allow for greater access to controllable experiments and defect-free systems needed to study MQT. Third, BECs enable manipulation of many-body states [50–52] that are inaccessible in other experimental settings. Many-body simulations in this proposal elucidate the importance of this point. For example, bosonic and fermionic Hubbard models in optical lattices [53–58] can provide tight levels of control in condensed matter [59, 60] and solid-state models [61] for the purposes of quantum simulation beyond what a classical computer can achieve.

In order to achieve a BEC, experimentalists must cool the bosons below the critical temperature: this arises during cooling when the de Broglie wavelength, which scales as temperature $T^{-\frac{1}{2}}$, becomes sufficiently large to approach the particle-particle mean separation. The dimensionless phase space density of the atomic Bose gas must increase above

$n\lambda_{\mathrm{dB}}^3$, where n is the atomic number density and λ_{dB} is the de Broglie wavelength, in conjunction with cooling below the condensate critical temperature [62, 63]. Typically this is performed using a combination of Doppler laser cooling and evaporative cooling to reach temperatures in the regime of tens to hundreds of nanoKelvin, although temperatures as low as picoKelvins have also been achieved [3, 64, 65]. The most common atomic species for BEC implementation is ^{87}Rb, since it provides convenient parameter values for magnetic and optical trapping, as well as laser cooling [66].

Interactions of atoms with an electro-magnetic field comprise the heart of trapping atoms in a light field [67]. The a.c. Stark effect is responsible for optical trapping, determined by the detuning of the laser from the atomic transition frequency together with the laser intensity [49, 67]. While there are many methods for neutral atom trapping in ultracold quantum gases, magneto-optical techniques are also common, relying on the Zeeman hyperfine magnetic splittings of the atom [48].

To create an optical trap, lasers are red (blue) detuned from the atomic transition frequency. The resulting dipole moment thereby traps the atoms at the intensity maxima (minima) of the beam [68]. This optical trapping can be accomplished in one, two, or three dimensions. To cool off the atoms, they are Doppler-laser cooled, which repels the atoms from the intensity maxima (minima), thereby decreasing the molecular motion, and thus, the temperature [69]. Doppler laser cooling, often called optical molasses [70], can be implemented to cool atoms to temperatures in the tens of micro-Kelvin range [71]. In order to achieve BEC, further cooling is needed to decrease the particle-particle mean separation. The final cooling step, evaporative cooling, can be implemented when atoms are confined in a trap with variable depth [72]. By decreasing the depth of the trap, higher-energy atoms escape out of the trap, thereby decreasing the average kinetic energy of the atoms in confinement, with average temperatures in the range of tens to hundreds of nanoKelvin.

What does it mean for an ultracold quantum gas to be Bose condensed? First, we note that above the critical temperature, a Bose gas behaves like a classical gas, shown

in Figure 2.1(**a**). To represent the collective Bose gas as a tensor product of n atomic wavefunctions with N atoms, where n is the number of possible modes for each atom, we first write the wavefunction of a single boson as

$$|\phi\rangle = |\phi_0\phi_1\phi_2....\phi_n\rangle. \tag{2.4}$$

Then, an ideal Bose gas at zero temperature can be represented by a single macroscopic wavefunction,

$$|\psi\rangle = |\phi_0\rangle^{\otimes N}, \tag{2.5}$$

such that all bosons occupy the single particle ground mode $|\phi_0\rangle$. This is depicted heuristically in Figure 2.1(**c**). Since we live in a non-ideal world, experiments operate at temperatures above absolute zero. So, assuming T $>$ 0, as temperatures drop below the condensate critical temperature, the macroscopic wavefunction $|\psi\rangle$ has nonzero occupation of the lowest single particle mode $|\phi_0\rangle$ and a BEC is born, portrayed in Figure 2.1(**b**) In the BEC regime, the higher-order single particle modes that do survive tend to be the low-lying excited states, as thermal fluctuations are minimal; depletion in typical BECs is on the order of 0.01% [73]. We calculate depletion as $D = 1 - \lambda_1/\sum_j \lambda_j$ where λ_1 is the largest eigenvalue of the single particle density matrix (SPDM) and the sum is over all eigenvalues of the SPDM. The SPDM is constructed from the correlations of $\hat{b}_i^\dagger$ and $\hat{b}_i$, the bosonic creation and destruction operators, respectively, so the elements are $\langle \hat{b}_i^\dagger \hat{b}_j \rangle$, where i, j run over modes n. The closer the depletion is to 0, the more condensed the BEC is, and the more superfluid behavior we see. As the gas becomes less condensed, the depletion increases and should be close to 1 for a Mott insulator.

2.3 Bose-Hubbard Hamiltonian

In the weakly-interacting regime, a dilute Bose gas may be approximated by a mean-field description based on the Gross-Pitaevskii equation (GPE) [74, 75]. However, the GPE provides an estimation that neglects quantum fluctuations, such that all atoms must be in the condensed state; in other words, the GPE wavefunction is also the dominant eigenmode

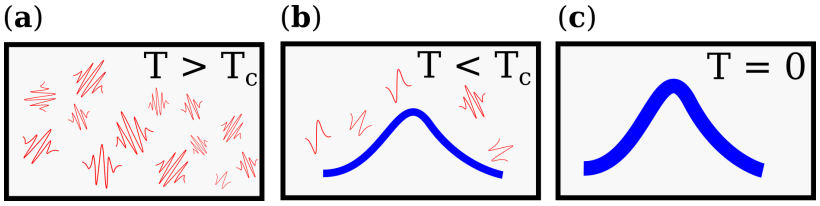

Figure 2.1: *Schematic representation of a Bose-Einstein condensate.* The first panel (**a**) displays the classical behavior of a Bose gas above its critical temperature. (**b**) Below the condensate critical temperature, a BEC has some non-zero fraction of higher order single-particle modes due to thermal fluctuations. Finally, (**c**) an ideal Bose gas at zero temperature is depicted as a macroscopic wavefunction, where all bosons occupy the same single-particle ground state, here of a harmonic trap, leading to a Gaussian profile.

of the single-particle density matrix [2]. Second-order fluctuations may be added to the GPE mean-field using Bogoliubov perturbations [76], though these descriptions fall short of approaching a complete many-body picture with fourth-order fluctuations [6, 77].

While there are many available many-body models for studying a double well in the context of ultracold quantum gases, we have chosen the Bose-Hubbard model for this work for its simplicity and flexibility dealing with many-body bosonic interactions. We write the Bose-Hubbard Hamiltonian (BHH)

$$\hat{H}_{\mathrm{BHH}} = -J \sum_{\langle i,j \rangle} (\hat{b}_i^\dagger \hat{b}_j + \hat{b}_i \hat{b}_j^\dagger) + \frac{1}{2} U \sum_i \hat{n}_i (\hat{n}_i - 1) + \sum_i V_i \hat{n}_i \,, \tag{2.6}$$

where J is the bosonic tunneling strength, U is the bosonic interaction strength, V_i is the external double well potential, $\hat{b}_i^\dagger$ and $\hat{b}_i$ are bosonic creation and destruction operators, respectively, satisfying bosonic commutation relations, $\hat{n}_i$ is the bosonic number operator, and $\langle i, j \rangle$ indicates nearest neighbors. The time scale of the problem is determined from Planck's energy-frequency relation, with tunneling parameter J in units of energy and $\hbar$ in units of energy times time, yielding $\hbar/J$ as the hopping time, which we take to be the fundamental unit of time in our analysis throughout this thesis. One length scale of the problem is determined by the spacing of the optical lattice, which experimentally is on the order of about 500 μm [78]. The other length scale is determined based on the double well potential width, resulting in hierarchies of scale due to the superposition of the two lengths.

To describe the many-body double well we express the potential V_i from Equation (2.6) as

$$V_i = \begin{cases} 0, & i < i_{\text{barrier}}, i > i_{\text{barrier}} \\ V_0, & i = i_{\text{barrier}}, \end{cases} \tag{2.7}$$

where V_0 is the height of the potential energy barrier, i is the lattice site index, and i_{barrier} is the site of the central barrier, and the height and width can be contracted into a single parameter, V_0, for easier navigation of the parameter space.

First, the BHH describes an underlying optical lattice, with parameters J/U, where J is the bosonic tunneling or hopping strength between lattice sites and U is the bosonic interaction strength between atoms on the same lattice site. Next, E_J or the Josephson energy is the tunneling between wells in the double well potential, and $\tilde{E}_C$ describes the interaction between atoms in the same well, a modified charging energy. The $E_J/\tilde{E}_C$ parameters together represent the ratio of tunneling between the two wells and interaction within each well. $E_J/\tilde{E}_C$ reduces to a function of V_0, the barrier height between the two wells, when the width of the barrier is held constant. We will refer to limiting cases of the optical lattice BHH as strong (weak) interaction when J/U is small (large). The nature of these two scales of the problem, in addition to system size, leads to multiscale behavior.

Importantly, the BHH yields a good representation of a BEC in an optical lattice [65], providing an excellent landscape for macroscopic tunneling dynamics. It is not without its limitations, however, as we have already made some approximations. First, we assume tight-binding and lowest band approximations, so our model is true only for $J/U, U, k_B T \ll E_{\text{bg}}$ where E_{bg} is the band gap energy for exciting to the next band, T is the temperature and k_B is the Boltzmann constant. Adding higher bands for example, or more terms in the Hamiltonian, called extended Bose-Hubbard models, adds difficulty to the problem but allows for more detailed physics [79, 80]. We also assume that the interaction or scattering length is much smaller than the extent of the Wannier functions of the optical lattice as well as smaller than the transverse confinement creating the 1D system. Our construction allows

for Wannier creation and annihilation operators in the BHH, although other approaches to ladder operators in the BHH have been successful [79]. Furthermore, we assume only short-range interactions; we assume a closed system and no external fields; we assume that the entanglement is small enough that we can describe the system using TEBD or MPS, among other standard and physically reasonable assumptions borne out in our calculations, and discussed in more detail contextually in each chapter.

Limitations of the Bose-Hubbard model stem from the approximations made in this derivation. First, in the kinetic energy (tunneling) term, the next-to-nearest neighbor tunneling is approximately two orders of magnitude smaller than the nearest-neighbor tunneling [65], so in the cases studied in this research, the approximation is valid. Second, because we consider repulsive interactions, the interaction term is always positive. In this instance, we make the single band approximation, meaning the optical lattice is deep enough that mean field interactions fail to modify the shape of the lowest band. In reality, interactions can cause occupation of higher bands distorting the basis function. For N mean number of atoms, the lowest-band approximation for the optical lattice means $Un_j < E_{\text{bg}}$ [65].

To derive the BHH from first principles, we start with the second quantized Hamiltonian in three dimensions describing interacting bosonic atoms in an external trapping potential

$$\begin{aligned}\hat{H} = &\int d\vec{x}\hat{\psi}^\dagger(\vec{x})\left(-\frac{\hbar^2}{2M}\vec{\nabla}^2 + V_{\text{latt}}(\vec{x})\right)\hat{\psi}(\vec{x}) \\ &+ \frac{1}{2}\int d\vec{x}d\vec{x}'\hat{\psi}^\dagger(\vec{x}')\hat{\psi}^\dagger(\vec{x})V_{\text{int}}(\vec{x}-\vec{x}')\hat{\psi}(\vec{x})\hat{\psi}(\vec{x}') \\ &+ \int d\vec{x}V(\vec{x})\hat{\psi}^\dagger(\vec{x})\hat{\psi}(\vec{x}),\end{aligned} \tag{2.8}$$

where $\hat{\psi}^\dagger(\vec{x})$, $\hat{\psi}(\vec{x})$ are bosonic field operators that create, annihilate atoms at position $\vec{x}$, $V_{\text{latt}}(\vec{x})$ is the periodic lattice potential, and $V_{\text{int}}(\vec{x})$ is the interaction potential. Assuming s-wave scattering reduces the potential to [81]

$$V_{\text{int}}(\vec{x}) \approx \frac{4\pi a_s \hbar^2 \delta(\vec{x})}{M} \tag{2.9}$$

where a_s is the inter-particle scattering length and M is the mass. When a_s is positive, the interactions between bosons are repulsive. For this work, we focus on repulsive interactions due to the presence of the Mott phase and to align more closely with current experiments [82]. Since our system is number-conserving, the chemical potential is approximated with a finite-difference of the energy levels for lattice filling factor N, $\mu \approx E(N+1) - E(N)$. If μ is less than the single particle excitation energy to the second band, then we can assume a lowest-band approximation is valid.

In order to expand field operators in the basis of the lattice, we revisit the Bloch theorem for periodic potentials, which states that wave functions in such a potential can only change under translation by a phase factor. The discretized version of Equation (2.8) will treat the total Hamiltonian based on individual wave functions located at each lattice location. These wave functions overlap neighboring wave functions, and the result is a Hamiltonian that requires some correction for this overlap. However, in solid state theory this overlap is minimized in a crystal when the electrons are tightly bound to atoms of the crystal – the tight binding approximation. In our case we do not have electrons bound to atoms, but rather bosonic atoms centered on an optical lattice site. In this manner, we can write the Bloch periodic wave functions as a Fourier series and take the real values, yielding the Wannier functions, as demonstrated in [54, 83]. Wannier functions centered on lattice locations represent atomic occupation at these locations. In order to discretize our system and write Equation (2.8) in terms of the optical lattice, we expand the field operators in the Wannier basis,

$$\hat{\psi}(x) = \sum_i \hat{b}_i w_0(x - x_i), \tag{2.10}$$

where $w_0(\vec{x})$ are Wannier functions of the lowest vibrational band. Inserting $\hat{\psi}(x)$ into a reduced quasi-1D version of Equation (2.8) and making the nearest-neighbor tunneling

approximation,

$$\begin{aligned}\hat{H} = &\sum_{\langle i,j\rangle}\int dx\hat{b}_i^\dagger w_0^*(x-x_i)\left(-\frac{\hbar^2}{2M}\frac{\partial^2}{\partial x^2}+V_{\text{latt}}(x)\right)\hat{b}_j w_0(x-x_j)\\ &+\frac{1}{2}\frac{4\pi a_s\hbar^2}{M}\sum_{jklm}\int dx\hat{b}_j^\dagger\hat{b}_k^\dagger\hat{b}_l\hat{b}_m w_0^*(x-x_j)w_0^*(x-x_k)w_0(x-x_{l+1})w_0(x-x_{m+1})\\ &+V(x)\sum_i\int dx\hat{b}_i^\dagger\hat{b}_i w_0^*(x-x_i)w_0(x-x_i),\end{aligned} \tag{2.11}$$

we find the definitions of the tunneling, interaction, and trapping potential parameters emerging in each term, respectively. Assuming we are looking at a quasi-one dimensional potential, we rearrange the field operators in Equation (2.11) noting that $\hat{b}_i^\dagger\hat{b}_i = \hat{n}_i$ is the number operator, and the integral in the external potential term normalizes to 1 such that

$$\begin{aligned}\hat{H} = &-\int dx w_0^*(x-x_i)\left(-\frac{\hbar^2}{2M}\frac{\partial^2}{\partial x^2}+V_{\text{latt}}(x)\right)w_0(x-x_{i+1})(\sum_{\langle i,j\rangle}\hat{b}_j^\dagger\hat{b}_i+\hat{b}_i\hat{b}_j^\dagger)\\ &+\frac{4\pi a_s\hbar^2}{2M}\int d\vec{x}|w_0(x)|^4\sum_i\hat{b}_i^\dagger\hat{b}_i^\dagger\hat{b}_i\hat{b}_i\\ &+\sum_i V(x_i)\hat{b}_i^\dagger\hat{b}_i.\end{aligned} \tag{2.12}$$

The resulting discretized Hamiltonian is Equation (2.6), where Equation (2.6) follows from substituting the definitions of J, U, and $V_i \equiv V(x_i)$. The definition of the hopping and interaction terms, J and U, respectively, are

$$\begin{aligned}J = &-\int dx w_0^*(x-x_i)\left(-\frac{\hbar^2}{2M}\frac{\partial^2}{\partial x^2}+V_{\text{latt}}(x)\right)w_0(x-x_{i+1})\\ U = &\frac{g_{1\text{D}}}{2}\int dx|w_0(x)|^4,\end{aligned} \tag{2.13}$$

where the tight binding approximation means the tunneling integral between sites other than nearest neighbors is negligible, the Wannier function densities exhibit minimal overlap between sites, and g is the effective 1D interaction parameter. These quasi-1D systems are really arrays of tubes due to freezing out transverse degrees of freedom with a very high lattice in y, z. This leads to a local effective transverse harmonic potential. These

approximations begin to break down as the optical lattice height V^0_{latt} approaches the recoil energy $E_{\text{R}} = \hbar^2 k^2/2m$. For $V^0_{\text{latt}} > 2E_{\text{R}}$, the approximation is already quite good, and for $V^0_{\text{latt}} > 5E_{\text{R}}$ the approximation is excellent [65]. Of course, next-nearest neighbor and longer range Hubbard models would include another term in the tunneling integral; a study of the decreasing strengths of longer range tunneling is demonstrated in reference [84].

2.4 Quantum phase transitions

The research presented in this thesis concerns two different types of quantum phase transitions (QPTs) in a square double well potential. The first phase transition is a discrete, $\mathbb{Z}_2$ phase transition from a Josephson oscillation phase to a self-trapping phase, breaking $\mathbb{Z}_2$ symmetry by localizing the condensate on the left or the right [85]. Note that quantum phase transitions obey the same universality class as their classical counterparts [86]. By universality, we mean that the spectral density of fluctuations will vanish as the interaction parameter approaches a critical value, and that systems with the same symmetries will exhibit the same critical exponents regardless of the microscopic nature of the Hamiltonian [87]. The second phase transition is the result of imposing an optical lattice underneath the double well potential. This second type of phase transition is the continuous $U(1)$ transition from a Mott insulator to a superfluid [88, 89]. Continuous phase transitions occur where there is a discontinuity not in the energy, but in its first derivative, second derivative, or higher order, yielding a second order, third order, etc. phase transition [90]. The Bose-Hubbard parameters J/U of the optical lattice are responsible for driving the $U(1)$ or Berezinskii-Kosterlitz-Thoulles (BKT) transition while double well parameters $E_J/\tilde{E}_C$ drive the $\mathbb{Z}_2$ transition.

We note that while all simulations performed are number conserving, due to the confinement of the trapping potential, the phase transition influence on dynamics is not strictly limited to a pure canonical ensemble as we might expect for a bare optical lattice. For example, atoms move through the barrier, and from the perspective of the left well the number of atoms is not fixed. Thus we can actually observe both BKT transitions – along the tip of

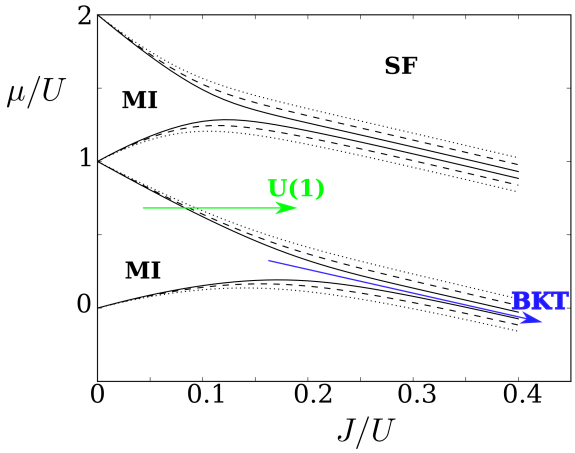

Figure 2.2: *Mott lobes – phase boundaries for a square well.* Mott lobes in the limit as the barrier goes to zero demonstrate typical superfluid-Mott insulator (SF-MI) phase transition behavior. The BKT transition occurs through the point of the lobes, which would be represented by truncating the phase boundaries at this critical value of J/U. The simulations were performed on an open-boundary lattice consisting of 21 sites. The solid lines depict filling factors of ± 1, the dashed lines are for ± 2, and the dotted lines are for ± 3.

the Mott lobes in the phase diagram – and $U(1)$ transitions – along the body of the lobes [3]. The BHH phase diagram in Figure 2.2 shows the BKT and $U(1)$ Mott insulator – superfluid transitions for an unconfined lattice.

To the best of our knowledge, the connection of quantum phase transitions and dynamics in this context remains an open question. In studying the dynamic regimes, we hope to answer fundamental questions about tunneling in BECs: In what ways does the tunneling regime affect the superfluid-Mott insulator (SF-MI) phase transition? Is MQT affected by the presence of the Mott gap? How much do ground and low-lying excited states influence the dynamics? Are entanglement or correlations important in MQT dynamics? Do they depend on the ground state phase diagram? While we don't necessarily expect ground state properties to govern dynamics, much of the dynamics can in fact be predicted by the quantum phase diagram or initial states, as we will show in chapter 4.

To answer these questions, we first discuss quantum phase transitions in general. In the low temperature range where Bose-Einstein condensates live, the thermodynamic fluc-

tuations that drive many classical phase transitions become increasingly negligible as the temperature decreases. Rather, quantum fluctuations dominate the particle behavior and compose the driving force behind quantum phase transitions (QPTs) [3, 53, 86]. QPTs occur at low temperature between two or more states of matter, generally described by different symmetries and by a discontinuity in the energy or derivative thereof, with the BKT transition presenting a special "infinite-order" or maximally smooth case that nevertheless displays long-range order [90, 91]. Specifically, the symmetry in the superfluid regimes stems from the continuous overlap of phases, while the Mott regime breaks this continuous symmetry [92]. The phase transition from a superfluid (SF) to a Mott insulator (MI) in the Bose-Hubbard model is achieved by varying the ratio of tunneling to interaction parameters, two competing energy terms [53], across the critical value [63, 73, 93, 94]. The superfluid regime is distinguished by all particles occupying one single-particle mode, where each atom is unfurled over the entire system with long range phase coherence [2, 95, 96]. A Mott insulator, on the other hand, is often described by unit filling or integer numbers of particles localized in each well of an optical lattice, and there is no corresponding phase coherence [65, 94]. The characteristic signature of the insulating phase is a gap in the excitation spectrum above the ground state, [53, 88]. The Mott insulator is of particular interest for quantum information applications, as the interaction is very strong and tunneling is suppressed, allowing for highly-controllable, long-lived quantum memory through the number of bosons [65, 97, 98]. The system typically is considered to approach the phase transition in the thermodynamic limit, as the number of lattice sites and number of particles becomes large [90]. Technically in one dimension there are no phase transitions in the thermodynamic limit. However, phase coherence can be quite long in extent, so that for finite-size BECs for all practical purposes we can indeed observe QPTs in 1D [3].

We will return to the idea of thermodynamic limits in one moment, while we consider more deeply the idea of a quantum phase transition. The basic premise stems from the non-analytic evolution of the energy levels $E_i(\psi)$ as a function of a non-thermal order parameter,

ψ. First order ground state quantum phase transitions demonstrate a non-analyticity in $E_i(\psi)$, second order ground state QPTs exhibit a non-analyticity in $\partial E_i(\psi)/\partial\psi$, and so on [86]. Excited state QPTs, while similarly dependent on a non-thermal control parameter, instead rely on the non-analytic behavior of energy level density as a function of energy [3, 99]. While nonanalytic features of QPTs only strictly appear as the system size approaches an infinite limit, many precursors to these transitions are measurable in finite systems with few degrees of freedom [100]. For example, the QPT is truly first order as a system is taken to the thermodynamic limit if two energy levels cross, the $\partial E_i(\psi)/\partial\psi$ jumps, and the two wavefunctions switch. However, in mesoscopic systems, the signature may instead manifest as a cusp in the energy as a function of the order parameter. Second order and higher, also called continuous phase transitions, are instead characterized by avoided level-crossings with large numbers of interacting local energy levels [101]. Typically a phase transition requires the thermodynamic limit $N \to \infty$ and $N \to \infty$, with N/L held constant. However, some QPT signatures arise in systems with few degrees of freedom or limited dimensionality; these signatures can be purely quantum and have significant impact on dynamics [3, 102]. For example, avoided level crossings are an indicator of degeneracy [100]. The less-intuitive, lower-dimensional phase transitions in 1D, quasi-1D, and 2D models that exhibit quantum phase transitions, such as Lipkin-Meshkov-Glick models, Hubbard models, and Heisenberg spin models, often have 2-or-more-level systems with some sort of two-body pairing interaction, whether via an external field, a capacitance, or tunnel coupling [103].

2.4.1 Mott insulator – superfluid transition in the Bose-Hubbard model

Here we examine the superfluid to Mott insulator quantum phase transition from the perspective of the single-particle density matrix. First, we define the particle: a bosonic atom. A common choice is ^{87}Rb [26]. We then recall that the SPDM elements are $\langle \hat{b}_i^\dagger \hat{b}_j \rangle$, and that the phase transition requires the breaking of some symmetry. In the case of the SF-MI, the symmetry that is broken is the relative phase [86]. To determine the phase, we diagonalize the SPDM, taking the $\vec{v}^{(1)}$ eigenvector linked to the largest λ_1 eigenvalue;

here the vector specifies distribution over optical lattice sites $v_j^{(1)}$, $j \in \{1, \ldots, L\}$. This eigenvector is the nearest approximation to the Landau mean field theory definition of the superfluid order parameter $v_j^{(1)} = \psi_j = \sqrt{n_j} \exp i\phi_j$. Thus the dominant eigenmode of the single-particle density matrix yields one method of calculating phase that in turn provides information about the phase transition. What is more, the SPDM signals the QPT in other ways; for example, off-diagonal long-range order indicates Bose superfluidity. Depletion of the condensate, also calculated from the SPDM as introduced in section 2.2, indicates the level of macroscopic occupation of the BEC mode. Thus a Bose gas Mott insulator will have maximal depletion, while a superfluid indicates higher occupation of the BEC mode and minimal depletion; depletion can therefore pinpoint the J/U_{critical} as the value for J/U at which the derivative of the depletion is maximum.

The SF-MI crossover in the BHH occurs at a $J/U_{\text{critical}} \approx 0.305$ in one dimension [104]. These ratios are tuned using Feshbach resonances [46, 47] or by increasing the lattice depth, which suppresses tunneling, for example. The MI regime requires $J/U < J/U_{\text{critical}}$. When the lattice is infinitely deep, or $J = 0$, the result is a perfect MI; in Fock space notation this state is written $|111...1\rangle$ for unit filling, i.e. the number of particles exactly equals the number of sites $N \approx L$. For small, nonzero J, the quantum state exhibits correlated paired sites that are particle-hole pair excitations, which are $|...02...\rangle$ or $|...20...\rangle$ on a $|...11...\rangle$ Mott background. This fundamental Mott behavior provides the basis for key results exhibited in chapters 4 and 6.

Furthermore, since we are in the canonical ensemble, our system is number conserving, and thus we do not have an exact formulation of a chemical potential. Instead, we write the chemical potential as a finite difference, $\mu \approx E(N+1) - E(N)$, which is discretized as a function of the number of atoms N. Then we can create a phase diagram of μ/U versus J/U, as depicted in the many-body version in Figure 2.2. The mean-field phase diagram shown in Figure 2.3, calculated analytically, provides approximations of phase boundaries that are parabolic, though we note there are no quantum phase transitions in mean field theory

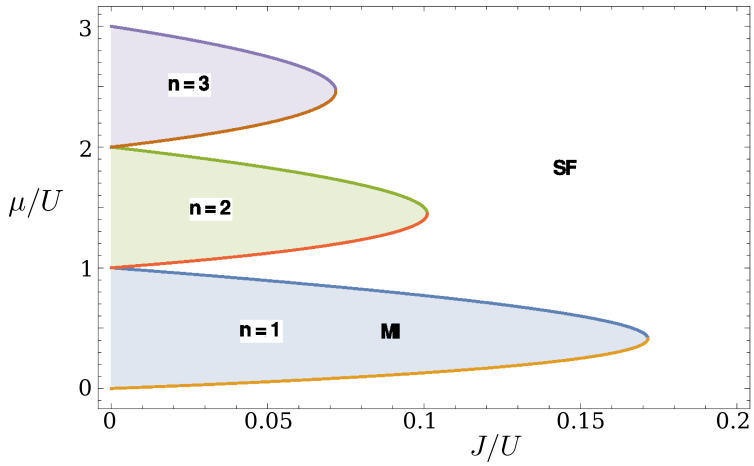

Figure 2.3: *Mean field Mott insulator – superfluid phase boundaries for a square well.* This mean field phase diagram yields an approximation of the phase boundaries for a lattice in a square well.

by definition. While the phase transition is typically approached from the thermodynamic limit, research throughout this thesis often involves mesoscopic systems. One method we use to address this concern is through examination of finite size effects by studying many lattice lengths and particle numbers to confirm signatures of quantum phase transitions, for example, which appear even in 1D optical lattices as small as about 10 sites [105].

2.4.2 Symmetry breaking phase transition in a double well

The spontaneous symmetry breaking inherent in the double well is a $\mathbb{Z}_2$ phase transition from a Josephson oscillation phase to a self-trapping phase [85, 106]. A Josephson junction from a theoretical perspective is a system of two superfluids (or superconductors) separated by a weak link, which will be discussed in more detail in section 2.6. To understand the $\mathbb{Z}_2$ phase transition, we first examine the two-mode model of the double well, discussed in more detail in section 2.6. The blue ground state satisfies the symmetry of the one-dimensional potential, and the orthogonal state in red is antisymmetric, seen in Figure 2.4(**a**). Spontaneous symmetry breaking in the double well means there are two concurrent ground state wavefunctions that no longer conform to the symmetry of the potential: each ground state is asymmetric. Now, the yellow and green wavefunctions in Figure 2.4(**b**) are clearly

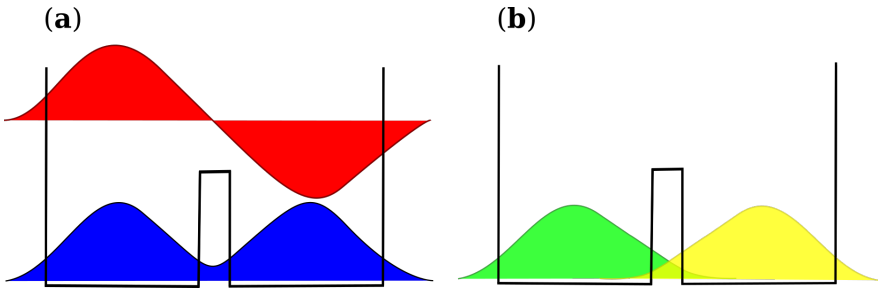

Figure 2.4: *Schematic of the two mode model.* (**a**) The ground state (blue) is symmetric about the barrier (black square double well potential), and the excited state (red) is antisymmetric about the barrier. (**b**) The left (green) and right (yellow) states are Wannier superpositions of the ground state and excited state. Spontaneous symmetry breaking occurs when the blue, symmetric ground state is broken up into either green or yellow asymmetric states.

not ground states of the double well on its own, rather the atoms have been forced to choose one well or the other, and the yellow and green states depict the ground states of right and left wells, respectively. The $\mathbb{Z}_2$ quantum phase transition arises due to the tuning of the barrier height beyond a critical value such that tunneling between the two wells is suppressed, leading to macroscopic quantum self-trapping of the atoms in one well or the other.

2.5 Experimental considerations

Experimental realization of the Josephson effect in a BEC was first demonstrated in 2005 [33]. More recently, microscopes of quantum gases have been able to image individual atoms in optical lattices [84, 107], allowing direct observation of localized many-body dynamics with high resolution [108]. Even further, experimental advancements have led to the ability to create arbitrary optical potentials with the resolution of a single lattice site [109–112]. With this experimental progress – the parameters discussed in this dissertation are feasible for creation and measurement in current quantum simulator platforms – thus, it is a good time to probe one such optical potential: a double well with a superimposed optical lattice, otherwise known as a long bosonic Josephson junction.

Josephson effects due to macroscopic tunneling of ultracold quantum gases are analogous to that of coherent Cooper pair tunneling in superconductors. For example, the d.c. Joseph-

son effect occurs when there is zero voltage applied across the junction, and yet a d.c. current can be measured. The key is that most cold atom experiments are not connected to external biasing circuits, and thus a source and sink scheme must be devised in order to measure the current [34]. The a.c. Josephson effect arises when a constant voltage is applied across the junction, which is akin to an energy difference or tilt between the two sides of a double well; the result is an alternating current measurable across the junction [113]. Additional Josephson effects occur in isolated systems, such as macroscopic oscillations of a condensate between two wells in a double well [33], or even internal Josephson tunneling such as that between orbital degrees of freedom [114].

While there are many possible implementations of cold atoms in a double well, one particular implementation relies on advancements in micromirror device technology [110–112]. Microelectromechanical system (MEMS) can be used to control an array of mirrors, which are placed at a point in the beam path where the laser is not focused. MEMS mirrors are tuned using applied voltages on electrodes surrounding the mirrors, which selectively turn off regions of light at the mirror locations. When the laser is focused on the atoms, the optics essentially perform a Fourier transform of the beam with site resolution down to about 700nm [108]. This allows for the creation of arbitrary optical potentials, including a double well with a superimposed periodic lattice.

Other techniques that contribute to the high number resolution of such ultracold atom experiments rely on controllability of the repulsive interactions between atoms, such as splitting condensates into multiple wells [115], loading atoms into deep optical lattices [109], electron microscopy, especially for imaging [116], absorption imaging [109], or lattices of magnetic traps [117]. One experimental scheme uses a trapped ion as a binary-tunable barrier in a double well, where tunneling is suppressed if the ion is spin-down and the BEC is self-trapped, and Josephson oscillations ensue if the ion is spin-up [118, 119].

2.6 Theoretical models: Double well Hamiltonians

In the double well, we have the convenience of a finite number of bound states on both sides of a potential barrier. Distinct dynamical regimes of ultracold bosons in a double well trap, also called a bosonic Josephson junction, have been identified in literature [33, 34, 120]. The first regime manifests in low-barrier cases, though not low enough as to allow classical spilling over the barrier. In this instance, Josephson oscillations mean the particles tunnel or slosh back and forth between wells in a macroscopic manner. These are Rabi oscillations in the single particle limit, when $NE_J/\tilde{E}_C >> 1$ [85, 121]. Beneath this limit, for $NE_J/\tilde{E}_C > 1$, Josephson effects emerge [34, 122]. The critical point $NE_J/\tilde{E}_C = 1$ marks the $\mathbb{Z}_2$ phase transition. The other regime, the high-barrier limit, or $NE_J/\tilde{E}_C < 1$, leads to macroscopic self-trapping of the condensate on one side of the well [123, 124].

The additional derivations in this chapter are meant to provide a context of the long or extended bosonic Josephson junction, as well as to give a relation of this work to relevant Josephson junction Hamiltonians in literature.

2.6.1 Relative number, relative phase formulation of the double well

While it is convenient for our research to observe bosons in number space, often it is more appropriate to work in a relative number and relative phase formulation between the two wells. For example, in superconducting Josephson junctions, the number of Cooper pairs is not a direct observable, rather phases are measured using Bardeen-Cooper-Shrifer (BCS) theory. BCS theory is a mean field description of a superconducting Josephson junction. In the general double well problem, mean field theory provides an excellent description of the relative dynamics under certain assumptions: the coherence length must be large compared to the lattice spacing and relative phase well-defined.

General phase and number field operators obey a canonical commutation relation, as they are conjugate variables, such that $[\hat{\phi}, \hat{N}] = -i$, noting that $\hat{\phi}$ is not the dominant mode in the single particle density matrix. Now we can define the raising and lowering operators

in terms of $\hat{N}$ and $\hat{\phi}$,

$$\begin{aligned} \hat{b}^\dagger &= \sqrt{\hat{N}} e^{-i\hat{\phi}}, \\ \hat{b} &= e^{i\hat{\phi}} \sqrt{\hat{N}}. \end{aligned} \tag{2.14}$$

We take the sine and cosine of the phase operator and obtain new commutation relations for each, $[\sin\hat{\phi}, \hat{N}] = -i\cos\hat{\phi}$ and $[\cos\hat{\phi}, \hat{N}] = i\sin\hat{\phi}$. Using the trigonometric identity

$$\langle \cos\hat{\phi}^2 \rangle + \langle \sin\hat{\phi}^2 \rangle = 1, \tag{2.15}$$

to normalize by $\sqrt{N(N+2) - 4\langle \hat{n}^2 \rangle}$, the sine and cosine relative phase operators between two general fields 1 and 2 in terms of raising and lowering operators are

$$\begin{aligned} \hat{\cos}\,\phi &= \frac{\hat{b}_1^\dagger \hat{b}_2 + \hat{b}_2^\dagger \hat{b}_1}{\sqrt{N(N+2) - 4\langle \hat{b}^2 \rangle}}, \\ \hat{\sin}\,\phi &= \frac{\hat{b}_1^\dagger \hat{b}_2 - \hat{b}_2^\dagger \hat{b}_1}{i\sqrt{N(N+2) - 4\langle \hat{n}^2 \rangle}}, \end{aligned} \tag{2.16}$$

where $\hat{n}$ is the relative number of atoms between the two fields, $\hat{n} = (\hat{n}_1 - \hat{n}_2)/2$. While we wrote these relative phase operators from the perspective of field operators $\hat{b}_i^\dagger$ and $\hat{b}_i$, the same reasoning holds for the relative phase operators in a double well, where the two fields are replaced by the two wells, left and right symbolized by L and R. Multiplying the normalization factor by both sides of $\cos\hat{\phi}$ in Equation (2.16), we now have the tunneling term of the Bose-Hubbard model for the double well,

$$\hat{b}_L^\dagger \hat{b}_R + \hat{b}_R^\dagger \hat{b}_L = \cos\hat{\phi} \sqrt{N(N+2) - 4\langle \hat{n}^2 \rangle} \tag{2.17}$$

where the 1 and 2 field operators were translated to left L and right R tunneling operators of the double well, and $\hat{n} = (\hat{n}_L - \hat{n}_R)/2$ is the population imbalance between the two wells. Thus, we can substitute this into Equation (2.6) without the external potential, because the two wells have already been taken into account, and the resulting relative number, relative phase Hamiltonian for the double well is

$$\hat{H} = -J\cos\hat{\phi} \sqrt{N(N+2) - 4\langle \hat{n}^2 \rangle} + \frac{1}{2} U \hat{n}(\hat{n} - 1). \tag{2.18}$$

In the thermodynamic limit, as the number of bosons become large, the expectation values of $\sin\hat{\phi}$ and $\cos\hat{\phi}$ operators obey semiclassical evolution equations. The definitions of sine and cosine operators from Equation (2.16) can then be approximated

$$\begin{aligned} \cos\hat{\phi} &\approx \frac{\hat{b}_L^\dagger \hat{b}_R + \hat{b}_R^\dagger \hat{b}_L}{N}, \\ \sin\hat{\phi} &\approx \frac{\hat{b}_L^\dagger \hat{b}_R - \hat{b}_R^\dagger \hat{b}_L}{iN}. \end{aligned} \tag{2.19}$$

In order to devise a Hamiltonian of the same form as typical superconducting Josephson junction Hamiltonians, we take the average population imbalance of the two wells to zero $\langle\hat{n}\rangle = 0$ – which is accounted for when the junction is connected to a biasing circuit – and as the number of particles becomes large in the interaction term, $\hat{n}(\hat{n}-1) \approx \hat{n}^2$. Then, solving Equation (2.19) for the tunneling operators,

$$\hat{b}_L^\dagger \hat{b}_R + \hat{b}_R^\dagger \hat{b}_L = N\cos\hat{\phi}, \tag{2.20}$$

and substituting the tunneling term into Equation (2.6) without the external potential, the semiclassical version of Equation (2.18), with the distinct difference of zero net population imbalance, becomes

$$\hat{H} = -JN\cos\hat{\phi} + \frac{1}{2}U\hat{n}^2. \tag{2.21}$$

2.6.2 Josephson formulation of the double well

The usual description of superconducting Josephson junctions follows the same principles as the semiclassical relative number/relative phase formulation of the double well presented in Equation (2.21). We include the description here as a demonstration of the equivalence of the many different architectures of the double well. A typical Josephson junction consists of two superconductors separated by a thin barrier, which is often an insulating material with a thickness on the order of 1 nm [125]. The two superconductors can be considered as the two wells in a double well system, and the thin insulator as the barrier between them. If the barrier is thin enough, typically on the order of 3 nm or less, single electrons will tunnel through the barrier, and the barrier will act as a resistance. As the barrier

increases in thickness beyond about 3 nm, the barrier becomes too thick for tunneling to take place [125]. If the barrier thickness is decreased to about 1 nm or less, the macroscopic wave functions of the two superconductors begin to overlap. This weak overlap is the basis for macroscopic quantum tunneling of Cooper pairs between the two superconductors [106, 126], a phenomenon called the Josephson effect. Cooper pairs are pairs of electrons that collectively act as a single boson; for more background on superconductivity and Josephson junctions, see [127–129].

Following Feynman's method for deriving the Josephson equations [113], we note that the following only holds true for specific barrier widths where the overlap between the wavefunctions is weak. Beginning with the macroscopic wavefunctions for each superconductor, ψ_L and ψ_R, we represent the weak link with a constant, C, so the coupled Schrödinger equations for each read

$$\begin{aligned} i\hbar\frac{\partial}{\partial t}\psi_L &= E_L\psi_L + C\psi_R, \\ i\hbar\frac{\partial}{\partial t}\psi_R &= E_R\psi_R + C\psi_L. \end{aligned} \tag{2.22}$$

Taking the ansatz for the wavefunctions, analogous to the semiclassical version of Equations (2.14), we have

$$\begin{aligned} \psi_L &= \sqrt{\rho_L}e^{i\phi_L}, \\ \psi_R &= \sqrt{\rho_R}e^{i\phi_R}, \end{aligned} \tag{2.23}$$

where ρ_L and ρ_R represent Cooper pair densities, and ϕ_L and ϕ_R represent the phases of each macroscopic wavefunction. The understanding of these phases becomes more intuitive when linked with Equation (2.14), and semiclassically represented in Equation (2.19). We have also made one more semiclassical assumption for the ansatz Equation (2.23) to be true: the phases are assumed constant throughout each superconductor. Then, exchanging (2.23) into (2.22), we separate the equations into real and imaginary parts and invoke continuity

in the exchange of Cooper pairs, $\partial_t \rho_R = -\partial_t \rho_L$,

$$\begin{aligned} \partial_t \rho_L = -\partial_t \rho_R &= \frac{2C}{\hbar}\sqrt{\rho_L \rho_R}\sin(\phi_R - \phi_L), \\ \partial_t(\phi_R - \phi_L) &= \frac{E_R - E_L}{\hbar} + C(\sqrt{\frac{\rho_L}{\rho_R}} - \sqrt{\frac{\rho_R}{\rho_L}})\cos(\phi_R - \phi_L). \end{aligned} \tag{2.24}$$

We assume the superconductors are identical, so $\rho_L = \rho_R = \rho$, $\sqrt{\frac{\rho_L}{\rho_R}} = \sqrt{\frac{\rho_R}{\rho_L}}$, and the cosine term goes to zero; and we define the relative phase between the two wavefunctions $\phi = \phi_R - \phi_L$. Equations (2.24) then simplify to

$$\begin{aligned} \partial_t \rho &= \frac{2C}{\hbar}\rho \sin\phi, \\ \partial_t \phi &= \frac{E_R - E_L}{\hbar}, \end{aligned} \tag{2.25}$$

where $\partial_t \rho$ is nonzero, despite our assumption that the Cooper pair densities are assumed constant across each superconductor, due to the application of an external current source across the junction. In order to translate parameters from Equation (2.25) to superconducting Josephson junction parameters, we note the charge of a single Cooper pair as $2e$, where e is single electron charge. The voltage across the junction is equivalent to the energy difference between the two superconductors $V = (E_R - E_L)/2e$. Then, we can write the semiclassical Josephson equations in terms of the voltage and the current density J rather than the Cooper pair density $\partial_t \rho$,

$$\begin{aligned} J &= J_c \sin\phi \\ \partial_t \phi &= \frac{2eV}{\hbar}, \end{aligned} \tag{2.26}$$

where $J_c = 4eC\rho/\hbar$ is the critical current density, delineating the maximum Cooper pair tunneling current density. Note that Equations (2.26) only hold for ideal junction behavior. In reality, the nonlinear Josephson junction circuit elements exhibit measurable capacitance, resistance, and inductance. The resistively and capacitively shunted junction (RCSJ) model addresses this by modeling an equivalent circuit of a junction with a capacitor and resistor in parallel [130]. This well-known model also has its limitations [127]. Studying bosonic

Josephson junctions from the perspective of BEC provides a unique, highly-controllable, insight of the many-body effects that may prove crucial to improving superconducting junction performance.

2.6.3 Superconducting phase qubit

Josephson junctions provide a prime architecture for quantum bit (qubit) implementation [131–133]. First, JJs supply the nonlinearity necessary for qubit creation, since linear circuit elements, such as resistors and inductors, are degenerate in their low-lying energy levels and are thus unsuitable for qubits. The large nonlinearity of JJs breaks this degeneracy, bifurcating the energy into two accessible levels. Second, superconductors inherently exhibit negligible resistance, meaning energy dissipation is essentially negligible, providing a means for increasing qubit coherence times. Third, fabrication of superconducting circuits can be accomplished using many processing techniques already refined by the semiconductor integrated circuit industry, allowing for future scalability.

A phase qubit is generated from Josephson inductance and capacitance in the JJ; it is implemented as a single well qubit within a cubic potential, with the ground state and first excited states comprising the two-level system [134]. Nonlinearity of the JJ produces the multiple energy levels, but successful qubit implementation requires that the transition rate of the first and second excited states ω_{12} must be different than that of two lowest states, $\omega_{01} \neq \omega_{12}$. In order to write the Hamiltonian for a phase qubit, we start from the classical Josephson Equations (2.26), and we define a single flux quantum as $\Phi_0 = h/2e$. Dividing by the area of the junction, such that I_J is the current, not current density, through the junction, we rewrite Josephson's equations with typical superconducting notation [127]

$$I_J = I_c \sin\phi \tag{2.27}$$

$$V = \frac{\Phi_0}{2\pi}\frac{d\phi}{dt}, \tag{2.28}$$

and I_c is the critical current of the JJ. To calculate the nonlinear inductance of the junction, we recall the definition of inductance $V = LdI/dt$ and then differentiate Equation (2.27) with respect to time. Solving Equation (2.28) for $d\phi/dt$ and substituting yields the differential equation

$$\frac{dI_J}{dt} = I_c \frac{2\pi}{\Phi_0} V \cos\phi. \tag{2.29}$$

The inductance of the JJ is the voltage across the junction divided by Equation (2.29)

$$L_J = \frac{\Phi_0}{2\pi I_c} \frac{1}{\cos\phi}, \tag{2.30}$$

which demonstrates nonlinearity of the inductance through the $1/\cos\phi$ term. The inductance is energy conserving, thus we calculate the energy stored in a junction by integrating $I_J V$

$$\begin{aligned} U_J &= \int dt I_J V \\ &= \int dt \frac{\Phi_0}{2\pi} I_c \sin\phi \frac{d\phi}{dt} \\ &= \int d\phi \frac{I_c \Phi_0}{2\pi} \sin\phi \\ &= -\frac{I_c \Phi_0}{2\pi} \cos\phi \end{aligned} \tag{2.31}$$

where the constant factor $E_J = I_c\Phi_0/2\pi$ is the Josephson energy. The Hamiltonian term associated with the Josephson energy for the phase qubit is the same term that dictates tunneling in the Bose-Hubbard model, making the $I_c\Phi_0/2\pi = NJ$ from Equation (2.21), where N is the number of particles and J is the tunneling energy. The same process as (2.31) gives us the energy from adding a biasing current across the junction, $U_{\text{bias}} = -I_{\text{bias}}\Phi_0\hat{\phi}/2\pi$, which is directly proportional to the phase $\hat{\phi}$, and follows the same commutation relation as was used in the relative number, relative phase formulation of the double well for Equation (2.14). Replacing the number operator in this commutation relation with a charge operator, with $\hat{N} = -2e\hat{Q}$, where $-2e$ is the charge of a Cooper pair of electrons, the commutation relation becomes $[\hat{\phi}, \hat{Q}] = 2ei$. We substitute $\hat{Q}$ into the interaction term of the mean field relative number, relative phase Hamiltonian in Equation (2.21), and we substitute the interaction energy constant $U = 1/4e^2C$ to include the Josephson capacitance C, such that the charging

energy is defined $E_c = e^2/2C$. Adding these three terms: the capacitance term is analogous to the particle-particle interactions, the Josephson energy is analogous to the tunneling or kinetic energy, and an extra phase term is added for a biasing current, we can write the Hamiltonian for the phase qubit

$$H = \frac{1}{2C}\hat{Q}^2 - \frac{I_c\Phi_0}{2\pi}\cos\hat{\phi} - \frac{I_{\text{bias}}\Phi_0}{2\pi}\hat{\phi}. \tag{2.32}$$

The energy terms in this Hamiltonian compete for dominance of the wavefunction width in a fundamental manner, based on the canonically-conjugate operators, $\hat{\phi}$ and $\hat{Q}$. This fundamental understanding is applicable to all double well models described thus far. For example, we find dynamical regimes, one of which occurs when the Josephson energy dominates over the charging energy, $E_J >> E_c$, and $\hat{\phi}$ can be described semiclassically; the phase fluctuations are small and the charge fluctuations are large. For phase qubits, this is often the optimal operating regime, and the bias current is tuned to increase the separation of the ω_{01} and ω_{12} by as much as possible, typically on the order of 5 to 10% [127]. Other dynamical regimes, $E_J \approx E_c$ and $E_c >> E_J$, are avoided for phase qubits since they do not provide the optimal transition frequencies necessary to isolate two energy levels.

2.7 Numerical techniques

A standard approach to understanding many-body systems begins with a simplified model, such as Hubbard models or those discussed in section 2.6. Often these models are not exactly solvable, with some exceptions for small systems or limiting cases. Thus, one needs reliable numerical methods to simulate such systems. Tensor network methods are one family of methods that have gained popularity for simulating many-body quantum physics [135–137]. The commonality among different tensor network methods is the decomposition of a quantum state into constituent tensors the size of which is controlled via a cut-off on the entanglement.

Regardless of choice of numerical technique, one must start by understanding limitations and assumptions. Exact diagonalization is restrained to small system sizes due to com-

putational demand. Mean field techniques fail to incorporate quantum correlations [138]. Quantum Monte Carlo methods suffer from the sign problem, such as that encountered with strongly interacting fermions whose highly-oscillatory wavefunctions are difficult to integrate, and are constrained to statics, so not suitable for our dynamical studies [139]. Series expansion techniques are confined to the approximations of perturbation theory [140]. The main restriction on tensor network methods differs considerably: the extent and arrangement of entanglement determines the best method. One advantage of tensor networks is they provide information about the correlations and entanglement of many-body states inherently. In fact, without a tensor network, one may be tempted to determine coefficients of a many-body state in a given basis without understanding the its internal entanglement properties. The multi-configurational time-dependent Hartree method for bosons (MCTDHB), an example of a many-body method, relies on calculating coefficients of constituents of many-body states without regard to the structure of their connection [141]. Furthermore, the entanglement structure will naturally change depending on the spatial dimension of the system; the area law posits that entanglement scales with the boundary between a subsystem and its environment [142]. Matrix product state (MPS) methods are a subset of tensor network methods that work particularly well for one dimensional or quasi-one dimensional lattices. In this case, the boundary is small, i.e. always one site and thus entanglement is limited. Projected entangled pair states, on the other hand, are designed to simulate lattices in two dimensions. Though, the boundary for a single site in a 2D square lattice, for example, is 8 sites – making entanglement much worse – which is one reason 2D systems are difficult to simulate [143]. So, the entanglement of the many-body state motivates geometry. Interestingly, this idea has been extended to curvature in spacetime and has been proposed as a link between quantum entanglement and gravity [3, 144, 145].

Matrix product state methods such as TEBD provide numerical solutions of many-body dynamics that depend on the level of Hilbert space truncation. For example, a study on the BHH for a superfluid decay uses TEBD methods similar to our own many-body simulations

and has confirmed numerical limits on instanton computations [146, 147]. Another many-body method, MCTDHB, has also been used to study the quantum escape problem [148, 149]; though this work examined depletion, it missed some key measures such as number fluctuations and von Neumann entropy. Such measures help illustrate when semiclassical or mean-field approximations fail.

2.7.1 Matrix Product States and Time Evolving Block Decimation

Matrix product states, a 1D subset of tensor network methods, are a family of algorithms well-suited to solve certain types of numerical problems. They are based on the fundamental principle of decomposing a tensor into a sum of series of other tensors and then truncating the Hilbert space in a way that is numerically optimized and minimizes information loss. For the Bose-Hubbard model in the number-conserving canonical ensemble, the total dimension of the Hilbert space is

$$\Omega_{\mathrm{BH}} = \frac{(L+N-1)!}{L!(N-1)!} \tag{2.33}$$

where L is the number of lattice sites and N is the total number of bosons. For typical experimental parameters in the tens or hundreds of lattice sites with similar numbers of particles, exact diagonalization is intractable. Much effort in the past decade [143] has been made to increase the numerical efficiency of simulating many-body systems applicable to a variety of architectures.

Interacting ultracold quantum gases in optical lattices are one example of a type of system where matrix product state methods may be the most efficient choice for numerical simulation [41]. The specific choice of algorithm will depend on system geometry, parameters, boundary conditions, statistical ensemble, and experiment design, among other considerations. MPS algorithms are specifically efficient at simulating 1D and quasi-1D systems.

Next, we will describe a TEBD algorithm from a top-level perspective as an example of the power of matrix product state methods. OpenTEBD is an open source matrix product state (MPS) method maintained by the Carr theoretical research group at the Colorado

School of Mines [4]. There are clear indications that MPS methods such as TEBD provide a rich and more encompassing view of physics beyond that of semiclassical or instanton methods [77, 143, 150]. OpenTEBD is based on the general mathematical principal of singular value decomposition (SVD), which is like matrix diagonalization except it works for non-square and non-diagonalizable matrices as well [151]. SVD in TEBD is performed via Schmidt decomposition, which gives a physical representation of SVD in tensor product space. Because of correlations in the matrix, as opposed to a random matrix with no discernable correlations, we see a rapid decay in the magnitude of the singular values. We can visualize this as projections into the energy eigenstates where the weight of each projector decays rapidly with increasing eigenenergy. Figure 2.5(d) demonstrates the computational advantage of keeping only the most important singular values for a correlated matrix in blue, compared with the slow decay of random matrix singular values in red.

With this in mind, we can now represent the TEBD algorithm mathematically. Suppose we have a lattice of size L with indices i_L and a general many-body quantum state in a Fock basis on the lattice that can be written

$$|\psi\rangle = \sum_{i_1 \ldots i_L} c_{i_1 \ldots i_L} |i_1, i_2, \ldots i_L\rangle, \tag{2.34}$$

where $c_{i_1 \ldots i_L}$ is an L-index tensor which can be decomposed such that $|\psi\rangle$ is represented with tensors of smaller rank. The number of total parameters is $D = d^L$, where d is the local Hilbert space dimension at a single lattice site.

We can then write the same many-body wavefunction as a matrix product state,

$$|\psi_{\mathrm{MPS}}\rangle = \sum_{i_1 \ldots i_L = 1}^{d} \sum_{\alpha_1 \ldots \alpha_{L-1} = 1}^{D} \Gamma^{[1] i_1}_{\alpha_1} \lambda^{[2]}_{\alpha_1} \Gamma^{[2] i_2}_{\alpha_1 \alpha_2} \lambda^{[3]}_{\alpha_2} \Gamma^{[3] i_3}_{\alpha_2 \alpha_3} \ldots \lambda^{[L]}_{\alpha_{L-1}} \Gamma^{[L] i_L}_{\alpha_{L-1}} |i_1, i_2, \ldots i_L\rangle, \tag{2.35}$$

where the first sum is over all the lattice indices up to the local dimension and the second sum is over singular values. Each tensor is given a numeric label $^{[j]}$ for the j^{th} lattice site to emphasize that each one is distinct in general. The Γs are rank-3 tensors save for the ones on the boundaries, which are rank-2 tensors for open boundary conditions; the λs are

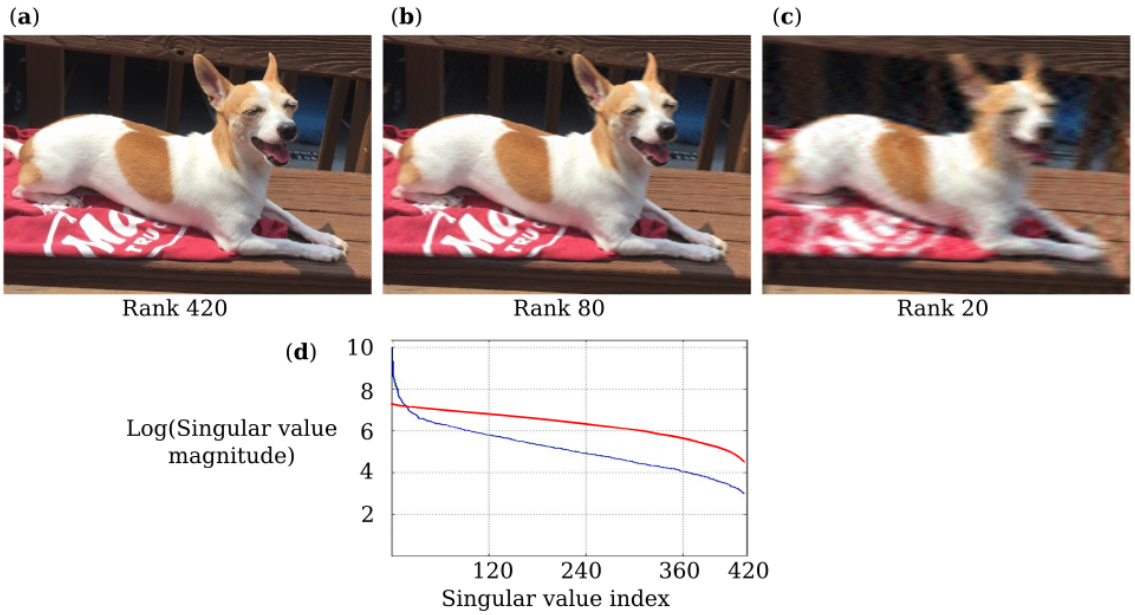

Figure 2.5: *Singular value decomposition image compression.* The rank of the matrix denotes the number of singular values kept; (**a**) the maximal number of singular values is 420, which is the full photograph of my dog Scarlet. (**b**) From a visual perspective, the rank 80 Scarlet image may be within error, while (**c**) the rank 20 Scarlet may or may not be a dog, a cat, or even some other loveable creature, which is most likely not within error. (**d**) Plot of singular value magnitudes demonstrates the rapid decay of the singular values (blue) compared with a random matrix (red).

also rank-2. The neighboring $\Gamma^{[j]}$ and $\lambda^{[j]}$ tensors could be contracted into a single rank-3 tensor for each lattice site for a more general matrix product state, however, it is convenient for TEBD to keep them separate. At this point we have not gained any computational advantage, and the number of parameters is at minimum d^L.

The decomposition ansatz, in this case a Vidal Decomposition [4, 152, 153], is the particular way of splitting the system consecutively into two parts and repeatedly performing SVD, where a single decomposition into parts A and B looks like $\Gamma_{\mathrm{A}}\lambda\Gamma_{\mathrm{B}}^{T}$. Γ_{A} and Γ_{B}^{T} are not necessarily the same dimension, but are square matrices of rank proportional to the bipartite splitting and λ is a diagonal matrix. The wavefunction representation of the bipartite

splitting between sites l and $l+1$ is

$$|\psi\rangle = \sum_{\alpha_l=1}^{\chi} \lambda_{\alpha_l}^{[l+1]} |\phi_{\alpha_l}^{[1\ldots l]}\rangle |\phi_{\alpha_l}^{[l+1\ldots L]}\rangle, \tag{2.36}$$

where $1 \leq \chi \leq \min(d^l, d^{L-l})$ and χ is the total number of singular values that are kept after truncation and is often called the bond dimension. TEBD deciphers optimal truncation based on the state at each time step; thus, it is time-adaptive. Also note the singular values for correlated systems decrease such that $\lambda_1 \geq \lambda_2 \geq ... \geq \lambda_\chi > 0$.

The truncation algorithm based on Vidal decomposition is designed to keep the most important singular values depending on the convergence criteria or user-specified bond dimension and discard the rest, ideally yielding a system that is not only numerically feasible to simulate, but can be drastically smaller than the initial system [143]. Often the ideal bond dimension for the system is determined via convergence analysis, discussed in more detail in chapter 5. The bond dimension is also invariant under local unitary transformations, which is important when applying unitary propagators. In order to perform state initialization or ground state calculations and time propagation, TEBD uses the Suzuki-Trotter approximation for exponentiation of matrices. This assumes that the Hamiltonian can be broken into non-overlapping "odd" and "even" pieces like $\hat{b}_1^\dagger \hat{b}_2 + \hat{b}_3^\dagger \hat{b}_4$ separate from $\hat{b}_2^\dagger \hat{b}_3$. The time evolution operator $\hat{U} = \exp(-i\hat{H}\delta t/\hbar)$ then becomes

$$\hat{U}(\delta t) = \exp(-\frac{i\delta t}{\hbar}(\sum_{\text{odd } l} \hat{H}_l + \sum_{\text{even } l} \hat{H}_l)). \tag{2.37}$$

2.8 Analytical techniques

A number of analytical methods were used in addition to numerical simulations. Two analytical techniques outlined here are the sudden approximation and perturbation theory. The sudden approximation supports results from the bosonic Josephson junction paper in chapter 4 such that a rapid quench of the potential can lead to excited mode formation, both in the optical lattice and macroscopically in the double well. Degenerate perturbation theory corroborates findings in the partial symmetry breaking paper in section 3.2, as well

as the analytical calculations in chapter 4.

2.8.1 The sudden approximation

The sudden approximation allows one to examine time-dependent Hamiltonians in a time-independent manner, assuming the Hamiltonian is either changing very suddenly with respect to the natural time scale of the problem, or the initial state remains the same at time t_1 and t_2 when the Hamiltonian changes from $\hat{H}_1$ to $\hat{H}_2$, respectively. The time frame of interest is $\Delta t = t_2 - t_1$, where the overall Hamiltonian is

$$\hat{H} = \begin{cases} \hat{H}_1, & t < t_1, \\ \hat{H}(t), & t_1 < t < t_2, \\ \hat{H}_2, & t > t_2, \end{cases} \tag{2.38}$$

so for the sudden approximation to be valid, Δt must be small. The initial state for the dynamics is an eigenfunction of $\hat{H}_1$,

$$\hat{H}_1|j_1\rangle = E_{j_1}|j_1\rangle, \tag{2.39}$$

such that $|j_1\rangle$ is the ground state of $\hat{H}_1$ in this case and E_{j_1} is the corresponding eigenenergy. So the initial state is

$$|\psi(t_1)\rangle = |j_1\rangle. \tag{2.40}$$

Then, for $t > t_2$, the dynamics are determined by $\hat{H}_2$,

$$|\psi(t)\rangle = e^{-i\hat{H}_2(t-t_2)/\hbar}|j_1\rangle, \tag{2.41}$$

and the initial state $|j_1\rangle$ is projected onto a new basis,

$$|\psi(t)\rangle = \sum_k e^{-iE_k(t-t_2)/\hbar}|k_2\rangle\langle k_2|j_1\rangle, \tag{2.42}$$

where $H_2|k_2\rangle = E_{k_2}|k_2\rangle$, with k_2 a complete basis of H_2. The motivation for using this technique stems from strongly-interacting systems in the Josephson regime, where we found particle-hole pairs form immediately across the lattice, seen as bright and dark bands in number density plots. Because they form too quickly for matter to propagate across the lattice, we allege they are due to the diabatic quench of the potential from a single to

a double well. A Mathematica notebook of these results for toy models is given in the Appendix A.1.

2.8.2 Perturbation theory

A second analytical technique we highlight here is perturbation theory. This discussion particularly refers to degenerate perturbation theory and follows an argument in [154], though the goal of perturbation theory in general is to obtain the eigenvalues, E_n, and eigenstates, $|n\rangle$, of the total Hamiltonian

$$\hat{H} = \hat{H}_0 + \hat{V}, \tag{2.43}$$

where $\hat{H}_0$ is the unperturbed Hamiltonian and $\hat{V}$ is the perturbing Hamiltonian. We obtain the zeroth order solution for eigenenergies $E_n^{(0)}$ and eigenstates $|n^{(0)}\rangle$ for free from the diagonalization of $\hat{H}_0$,

$$\hat{H}_0|n^{(0)}\rangle = E_n^{(0)}|n^{(0)}\rangle, \tag{2.44}$$

however, we need a new basis that takes into account the degeneracy, and one way of implementing this basis is with an extra index, $m = 1, 2, ..., d_n$, where d_n is the degree of degeneracy of the n^{th} energy level. For the sake of this derivation we assume the perturbation lifts the degeneracy; so we re-write Equation (2.43) with a small perturbation parameter λ,

$$\hat{H} = \hat{H}_0 + \lambda\hat{V}, \tag{2.45}$$

then the unperturbed basis is unique if

$$|nm^{(0)}\rangle = \lim_{\lambda\to 0} |nm\rangle. \tag{2.46}$$

Note that there are multiple ways of obtaining the expressions for degenerate perturbation theory, but ultimately we are looking for the energy expansion to second order $E_{nm} = E_n^{(0)} + \lambda E_{nm}^{(1)} + \lambda^2 E_{nm}^{(2)} + \mathscr{O}(\lambda^3)$ and the states to first order $|nm\rangle = |nm^{(0)}\rangle + \lambda|nm^{(1)}\rangle + \mathscr{O}(\lambda^2)$. For first order energies, we can write $V_n|nm^{(0)}\rangle = v_{nm}|nm^{(0)}\rangle$ where $V_n = I_n V I_n$ and I_n is a projector into the degenerate subspace; then, the first order energies are the eigenvalues

of this equation $E^{(1)}_{nm} = v_{nm}$. To obtain the second order terms, one method [154] allows us to map the zeroth and first order terms onto the non-degenerate case, such that $E^{(0)}_{nm} = E^{(0)}_n + \lambda v_{nm}$. Then, $V_{n'm'nm} = \langle n'm'^{(0)}|V|nm^{(0)}\rangle$, d_n is the degree of degeneracy of n, and we can write the total energy up to second order,

$$E_{nm} = E^{(0)}_n + \lambda v_{nm} - \lambda^2 \sum_{n' \neq n} \sum_{m'=1}^{d_n} \frac{|V_{n'm'nm}|^2}{E^{(0)}_{n'} - E^{(0)}_n} + \mathscr{O}(\lambda^3). \tag{2.47}$$

Translating the indices of the states from the non-degenerate case to the degenerate case follows the same principle, and rendering the state to the same order as the the energy expansion yields the state expansion up to first order in λ [154],

$$\begin{aligned} |nm\rangle = |nm^{(0)}\rangle(1 + \mathscr{O}(\lambda^2)) \\ + \sum n' \neq n \sum_{m'=1}^{d_{n'}} |n'm'^{(0)}\rangle \left(-\frac{\lambda V_{n'm'nm}}{E^{(0)}_{n'} - E^{(0)}_n} + \mathscr{O}(\lambda^2) \right) \\ + \sum_{\substack{m'=1 \\ m' \neq m}} |nm'^{(0)}\rangle \left(\lambda \sum_{n'' \neq n} \sum_{m''=1}^{d_{n''}} \frac{V_{nm'n''m''} V_{n''m''nm}}{(v_{nm'} - v_{nm})(E^{(0)}_{n''} - E^{(0)}_n)} + \mathscr{O}(\lambda^3) \right). \end{aligned} \tag{2.48}$$

CHAPTER 3

PARTIAL SYMMETRY BREAKING AND MACROSCOPIC QUANTUM ESCAPE

This chapter highlights key points of two papers on which I was co-author and details my part in each. The MQT escape paper was published in *Physical Review A* [6] as an Editor's Suggestion. The partial symmetry breaking paper is submitted to Physical Review Letters (PRL) [7] and is under review. I provide a brief summary of the projects and then clarify my contributions.

3.1 Macroscopic quantum tunneling escape of Bose-Einstein condensates

This project is a combined theoretical and experimental effort performed at CSM and at the University of Toronto, respectively. The *Physical Review A* paper is a follow-up to a *Physical Review Letters* publication [35]. I acknowledge Xinxin Zhao as first author as well as Diego Alcala for his contributions; in Toronto, co-authors Shreyas Potnis, Ramon Ramos, and Aephraim M. Steinberg carried out the experiments. I also acknowledge co-authors Kenji Maeda and Lincoln D. Carr for their role in the work.

In the experiment, a BEC, composed of tens of thousands of ^{87}Rb atoms is trapped in a single three-dimensional well with two escape pathways through a pair of saddle points, as shown in Figure 3.1. Modeling the dynamics reveals two regimes: the first is a classical spilling regime, where atoms escape over the saddle point barriers. The classical spilling is modeled with a variational dynamical Lagrangian method. The second quantum tunneling regime exhibits non-exponential decay and is described using modified Jeffreys-Wentzel-Kramers-Brillouin (JWKB or WKB) [35]. Both regimes are shown in Figure 3.2 with curves of theoretical models fit to the experimental data points. Our modified JWKB method adds an offset interaction term to the mean field factor and provides a more accurate description of dynamics than previous mean field descriptions. Three-dimensional Gross-Pitaevskii (GPE) simulations support a mean field result when compared with the experiment. Both the

experiment and theory demonstrate that interactions between atoms modify the potential in time and contribute to a non-exponential decay in the number of trapped atoms. Also, while the experiment is three-dimensional, the effective escape path of the atoms at the weakest part of the potential, the saddle points, may be mapped onto one dimension. Effective one-dimensional simulations in TEBD reveal many body dynamics beyond that of mean field, though we caution that these simulations may overlook effects such as chaos present in the full 3D trapping well. Also in this paper, we recommend experiments in MQT that are yet to be explored, delineating the many manifestations of MQT and the factors that affect the tunneling process.

A large interest of the paper was a review of recent literature, especially on macroscopic quantum tunneling, which highlighted key literature and suggested in detail future research direction in MQT. A majority of my contributions were in the literature review of macroscopic quantum tunneling and its many regimes, which I highlight here. Among the properties I will focus on in this section are (i) the governing statistics of the species in question, (ii) the interatomic interaction strength, (iii) the geometry and the symmetry of the potential, and (iv) the system dimensionality, both local and global [6].

In order to address statistical properties, we briefly revisit the nuanced idea of macroscopicity discussed in section 2.1, where the macroscopic limit in general refers to a large separation of entities in phase space. While the term often ellicits semiclassical descriptions, macroscopic phenomena are not universally describable semiclassically, or an extension of a semiclassical limit may be the most appropriate. This is the case in a driven bosonic Josephson junction described by a two-mode model, which can be mapped to an analogous phase space of a macroscopic superposition of two pendulum rotor states [155]. The macroscopic tunneling then applies when the wavefunctions of the two macroscopic states overlap. Macroscopic can also refer to large numbers of particles, many active degrees of freedom, or exhibition of aspects of quantum complexity, such as mutual information complex networks [156].

Additionally, the statisical properties of the tunneling species must be considered when examining macroscopicity in the context of quantum tunneling, whether bosonic obeying Bose-Einstein statistics, fermionic obeying Fermi-Dirac statistics, a mixture thereof, quasiparticles, or anyonic particles depending on dimension. In fact, the species does not strictly need to consist of particles, as various quasiparticles such as vortices, skyrmions, or solitons, magnetization, such as in spin-1 BECs, and molecular states such as in ammonia and similar pyramid-shaped molecules all exhibit quantum tunneling [157, 158]. Most if not all of these are attainable in ultracold quantum gas experiments, which can provide immense insights into the nature of tunneling phenomena across a variety of platforms. Preliminary studies in mesoscopic systems have already begun uncovering deviations from single-particle tunneling: Tonks-Girardeau gases deviate from exponential decay at short time scales due to disparities in ground state energy [159], and fermion pairing deviates from boson statistics such as two interacting fermionic superfluids coupled by a weak link to create a Fermi-gas Josephson junction [160, 161]. It is also conceivable that quasiparticle tunneling prompts new phenomena. For example, nonequilibrium single electrons in Josephson junctions instigate decoherence and energy decay in qubits and resonators [162, 163].

Interactions play a major role in governing tunneling dynamics, and the behavior of larger systems can be predicted with precursors and signatures from few-body systems [6]. The well-known Josephson effects relying on coherent macroscopic tunneling of condensates are typically considered in weakly interacting systems. However, tunneling times can be reduced by multiple orders of magnitude by instead biasing a more strongly-repulsive interacting system [164, 165], whereas attractive interactions decrease tunneling rates [77]. This interaction, ranging from strongly repulsive to strongly attractive, not only affects the tunneling rate, it also helps to indicate the appropriate theoretical method for describing the tunneling [166, 167]. For instance, weakly interacting bosons are often well-described by mean field theory, and the semiclassical wavefunction is then dominated by a complex scalar field [168, 169]. However, even weakly interacting particles can induce a time-dependent

effective potential that requires modifications to mean-field theory [6]. What is more, an increase in interaction strength incites stronger quantum fluctuations, correlations, and entanglement, all of which can minimize the effectiveness of mean-field theory. For example, fragmentation – or a macroscopic occupation of multiple modes of the SPDM – of a coherent state arises for strong interactions above a threshold [77]. Depletion is less stringent, where the occupation of the dominant mode diminishes due to nonmacroscopic mode occupation. Because phase coherence is tied to a single macroscopic mode occupation, fragmented and depleted states are not phase-coherent. Additionally, quantum fluctuations alter the MQT process. The fluctuation-induced Josephson-Leggett mode in a superconducting JJ, for instance, amplifies MQT, whereas quantum dissipation attenuates it [170].

Finally, the trapping potential and its dimension govern tunneling behavior. A 3D potential can be mapped to a 1D or quasi-1D potential, as the true tunneling path will follow the weakest point(s) of the potential, such as the experimental potential in Figure 3.1, where the MQT out of a single well is facilitated by repulsive interactions [6]. This case exhibits tunneling escape from a bound or quasi-bound state to an unbound one; in contrast, the double well with two bound states, or even tailored lattice potentials, exhibit their own contrasting effects, such as those discussed in chapter 2. One common potential, the harmonic trap, imbues a power law behavior of a BEC during macroscopic quantum tunneling as it approaches its critical point of collapse: this power law decay vanishes for anharmonic traps [171]. 2D and 3D potentials also have the possibility of chaotic dynamics which can lead to intermittent tunneling fluctuations or even chaos-assisted oscillations [172, 173].

3.2 Partial symmetry breaking

The focus of this second project is on nonequilibrium dynamics of ultracold bosons in an optical lattice ring trap. Xinxin Zhao is given first-author credit for the work on this paper; I also acknowledge co-authors J. Vijande, A. Ferrando, Lincoln D. Carr, and M.A. Garcia-March.

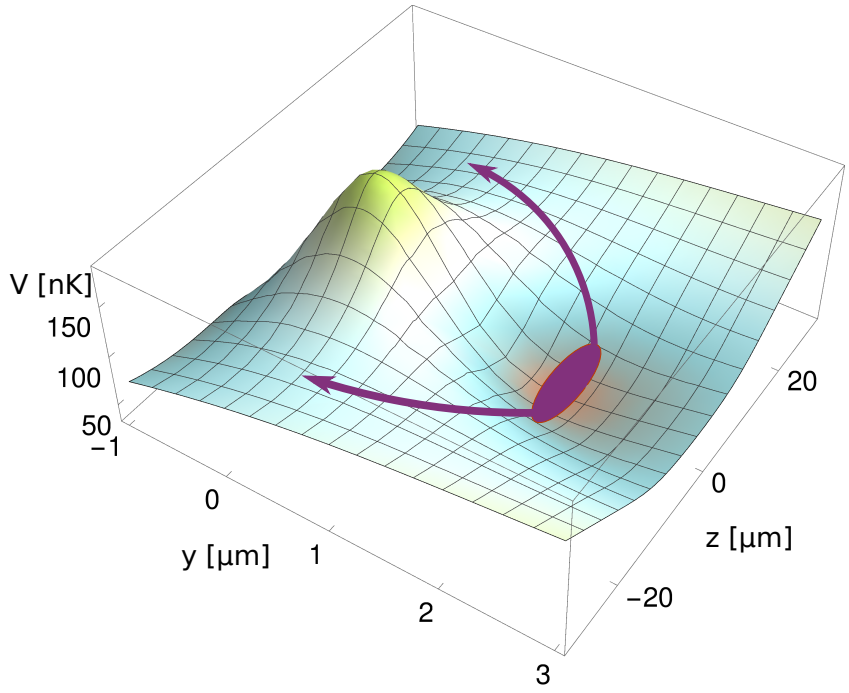

Figure 3.1: *Macroscopic quantum tunneling escape trapping potential.* Three dimensional experimental potential with a barrier or peak height of 190 nK. The purple ellipse represents a trapped BEC in the local minimum of the potential as it escapes, displayed as purple arrows, at the weakest points, or saddle points. The experimental distance from a saddle point to the trap minimum is $x_0 = 18(1)\,\mu$m. Reproduced with permission from [6].

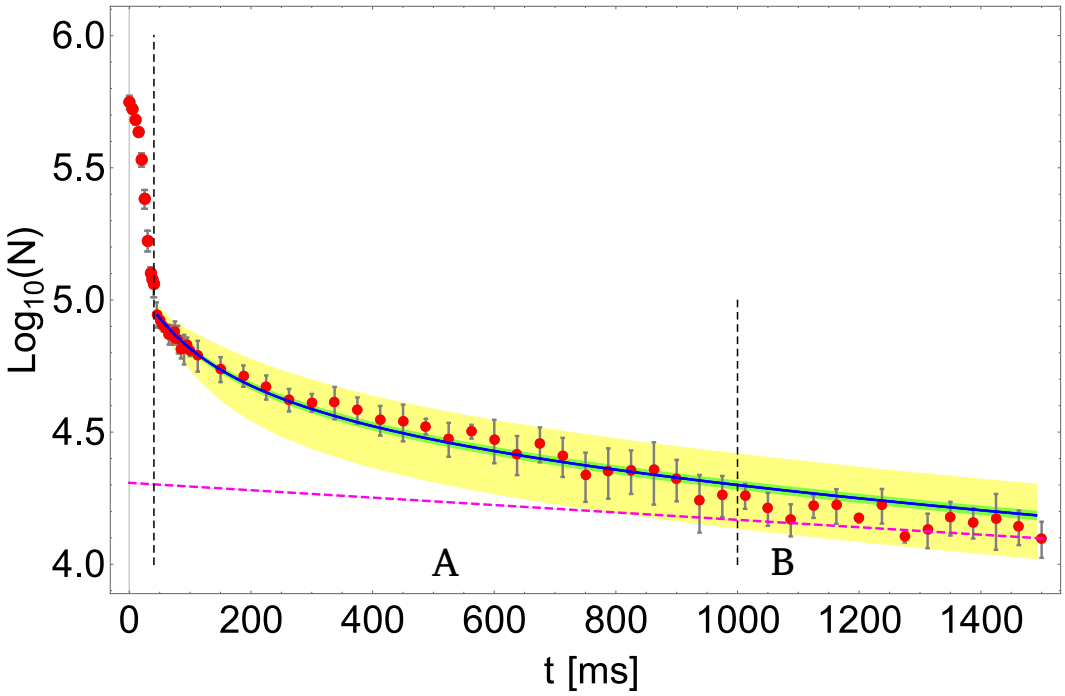

Figure 3.2: *Regions of macroscopic quantum tunneling escape.* The red circles depict the mean number of trapped bosons in time with 1σ error bars. The theoretical model is the solid blue curve, an exponential fit through the tunneling dominated regime is the dash dot black line, and experimental background loss is the dashed pink line. The tunneling decay curve is sub-divided into three regions: the initial transient classical spilling from $t = 0$ to the first vertical dashed line, (A) "the mean field assisted quantum tunneling with non-exponential decay", and (B) "the background loss dominated region". The green envelope indicates uncertainty in fitting parameters from modified JWKB. The yellow envelope indicates combined uncertainty due to experimental noise and fit parameters error. Reproduced with permission from [6].

Rather than spontaneous symmetry breaking, such as that present in the Kibble-Zurek mechanism, we explicitly break the symmetry of the system. Recent experiments exploring Anderson localization, for example, have taken a biperiodic optical lattice and quenched to a uniform lattice, resulting in the "first experimental demonstration of many-body localization [174, 175]" [7]. Our simulations perform the opposite, we begin with a uniform optical lattice ring trap and quench to a biperiodic one, "thereby partially breaking the discrete rotational symmetry" [7].

The partial-symmetry breaking Hamiltonian posits this additional symmetry onto the usual Bose-Hubbard model,

$$\frac{\hat{H}_\varepsilon}{\bar{J}} = \frac{U}{2\bar{J}} \sum_{i=1}^{L} \hat{n}_i(\hat{n}_i - 1) - \sum_{\langle i,j \rangle} (1 + \varepsilon_{ij})(\hat{b}_i^\dagger \hat{b}_j + \hat{b}_j^\dagger \hat{b}_i) \tag{3.1}$$

"where U determines the on-site two-particle interaction; $\langle i, j \rangle$ denotes summation over the nearest neighbors; $\hat{b}_i^\dagger$ ($\hat{b}_i$) is the creation (annihilation) operator for bosons at site i satisfying $[\hat{b}_i, \hat{b}_j^\dagger] = \delta_{ij}$; $\hat{n}_i \equiv \hat{b}_i^\dagger \hat{b}_i$ is the number operator; and $\varepsilon_{ij} \equiv \mathrm{Sign(i,j)}(J_\mathrm{e} - J_\mathrm{o})/(J_\mathrm{e} + J_\mathrm{o})$, with $|\varepsilon_{ij}| \in [0, 1]$. The function $\mathrm{Sign(i,j)} \equiv \pm 1$ where the plus (minus) sign is taken for site i even (odd). The hopping energy J_e (J_o) encapsulates the biperiodic lattice through the usual overlap integral [59]. We scale our study to the average hopping energy $\bar{J} \equiv (J_e + J_o)/2$ so that energies are in units of $\bar{J}$ and times in units of $\hbar/\bar{J}$. Finally, we further define *symmetry breaking strength* $\varepsilon = |\varepsilon_{ij}|$. As we will show, there exists a critical ε_c determining the vortex dynamics on the ring" [7].

Then, examination of the excitation spectrum yields an energy gap in low-lying excited states; this is the symmetry gap, and we demonstrate its manifestation in a multitude of system sizes, though for simplicity we focus on even L. We demonstrate that there is a critical value of the symmetry breaking strength at which the system transitions away from remembering its initial quantum state. This *symmetry gap* trends with the *symmetry memory*; and thus we demonstrate a novel form of symmetry-based critical dynamics that opens the door for further exploration in quantum simulators.

Rotational eigenstates of the periodic lattice obey the eigenvalue equation $\hat{C}|m_n\rangle = e^{i2\pi m_n/n}|m_n\rangle$, where m_n is the rotational quantum number, or winding number, associated with the n-fold symmetry of the ring. The partial symmetry breaking Hamiltonian is symmetric under time reversal, so the $|m_n\rangle$ corresponding to $\pm m_n$ are degenerate, which is shown in Figure 3.6. The energy thus relies only on $|m_n|$ [7].

For the dynamics of the $L = 6$ case, the initial state $t < 0$ has $n = 6$, $\varepsilon = 0$ and $m_6 = +1$, which corresponds to a vortex winding number $+1$. The quench for $t \geq 0$ then proceeds with $n = 3$ and $\varepsilon \neq 0$.

We define the symmetry gap by

$$\Delta_s = |E_{(m_3=+1,m_6=-2)} - E_{(m_3=+1,m_6=+1)}|, \tag{3.2}$$

"which is the energy difference between the nearest compatible pair of m_6 states" [7], a definition that is independent of particle number or interaction strength. $m_6 = +1$ in the symmetry gap, for example, would be the lower of the excited energy states.

Furthermore, we define a *symmetry memory* [7]

$$M_{\mathrm{s}} \equiv \tfrac{1}{\tau}\textstyle\int_0^\tau dt\, m_6(t) \tag{3.3}$$

that captures time-dependent critical or cusp-like behavior where microscopic and macroscopic measures fidelity and current, respectively, fail to do so. The result is shown in Figure 3.3.

I now clarify my contribution to this project. First, I present exact-diagonalization for N bosons and L lattice sites to solve the partial symmetry breaking Hamiltonian for periodic boundary conditions. The Python script is included in Appendix A.2. These calculations diagonalize the Hamiltonian for a number-conserving Bose-Hubbard model for systems from 2 to 6 particles and 2 to 6 sites for both even and odd system sizes. Figure 3.4 demonstrates the eigen-energies for a system of 3 bosons on 3 sites and $U = 0.001, 3, 30$, where the symmetry has not yet been broken such that $J_{\mathrm{e}} = J_{\mathrm{o}} = 1$. The eigenstates manifest as clusters where several states are nearly degenerate and correspond to a gapped excitation

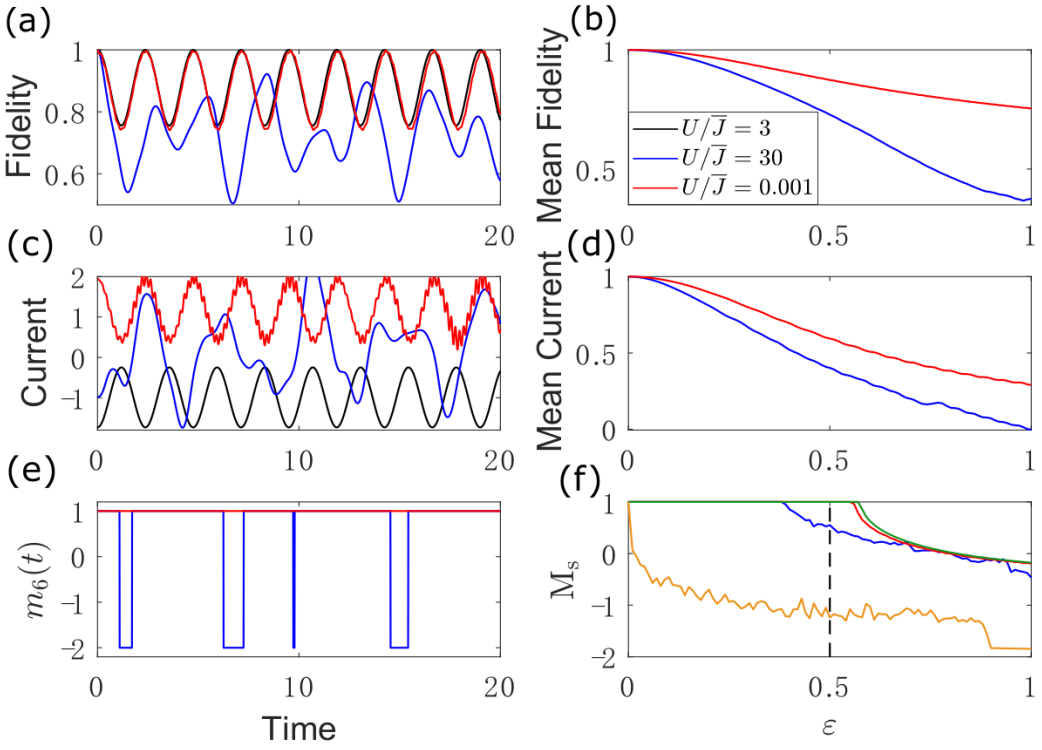

Figure 3.3: *Microscopic, macroscopic, and symmetry-based dynamical quantum measures.* The (a & b) fidelity and (c & d) current are void of critical phenomena. For interaction strengths $U/\bar{J} = 0.001, 3, 30$ for black, blue, and red curves, respectively, the left column depicts dynamics. The right column portrays a time average of 100 circuits around the ring as a function of symmetry breaking strength. (e) The rotational quantum number $m_6(t)$ provides a symmetry-based measurement, and (f) the symmetry memory evidently portrays critical behavior via a cusp in the time-average of the rotational symmetry operator $\hat{C}_6$, see Equation (3.3). Reproduced with permission from [7].

spectrum; the first gap of which, from the ground state to the lowest energy cluster, is the Mott gap [86].

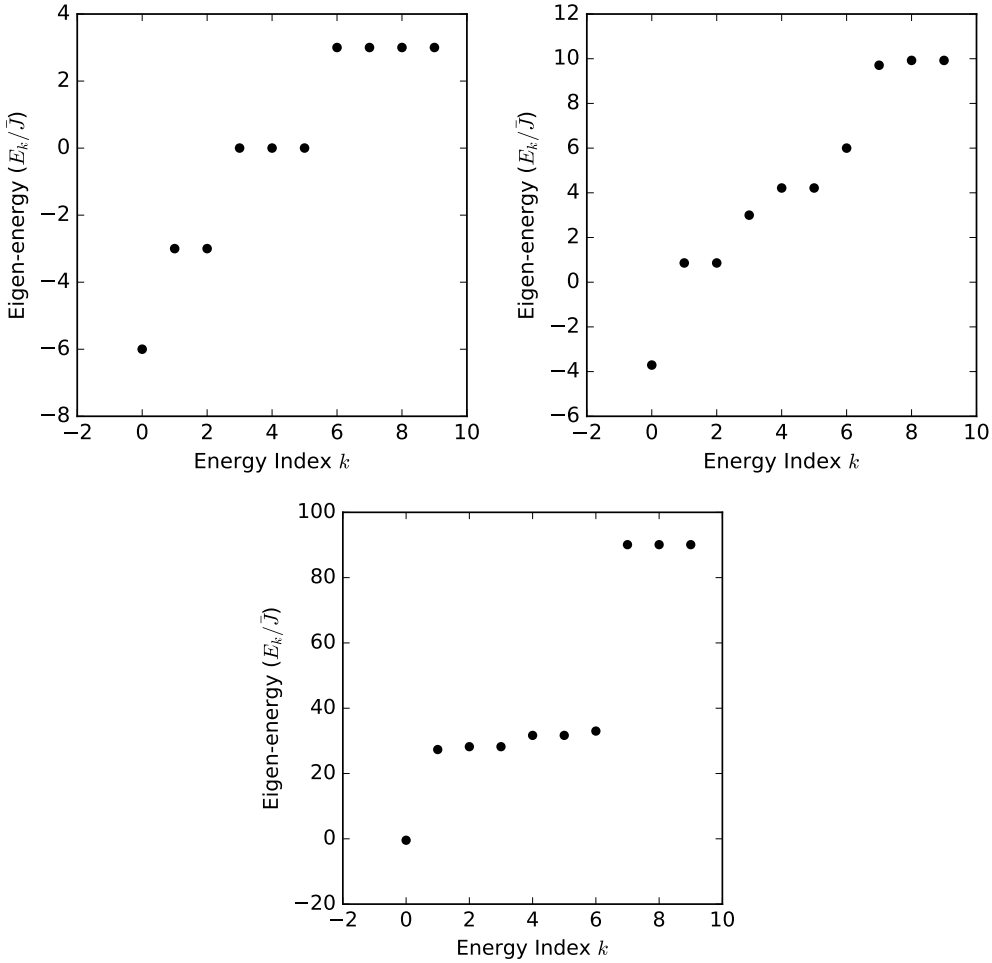

Figure 3.4: *Eigen-energies show gapping in spectra.* With 3 bosons in a 3-site ring trap, $U = 0.001, 3, 30$ from left to right and the stronger interactions induce stronger energy clustering and a larger Mott gap.

We choose exact diagonalization for this paper because the entanglement grows quickly with the quench dynamics, making it ill-suited for matrix product states, for example. While computational tricks are not needed for such small systems like $N = 3$, $L = 3$, scaling up to larger Hilbert spaces requires analyzing the structure of the Hamiltonian and establishing the best method for information storage. For example, those shown in Figure 3.5 are stored as sparse arrays, or arrays where it is computationally cheaper to store only nonzero values and

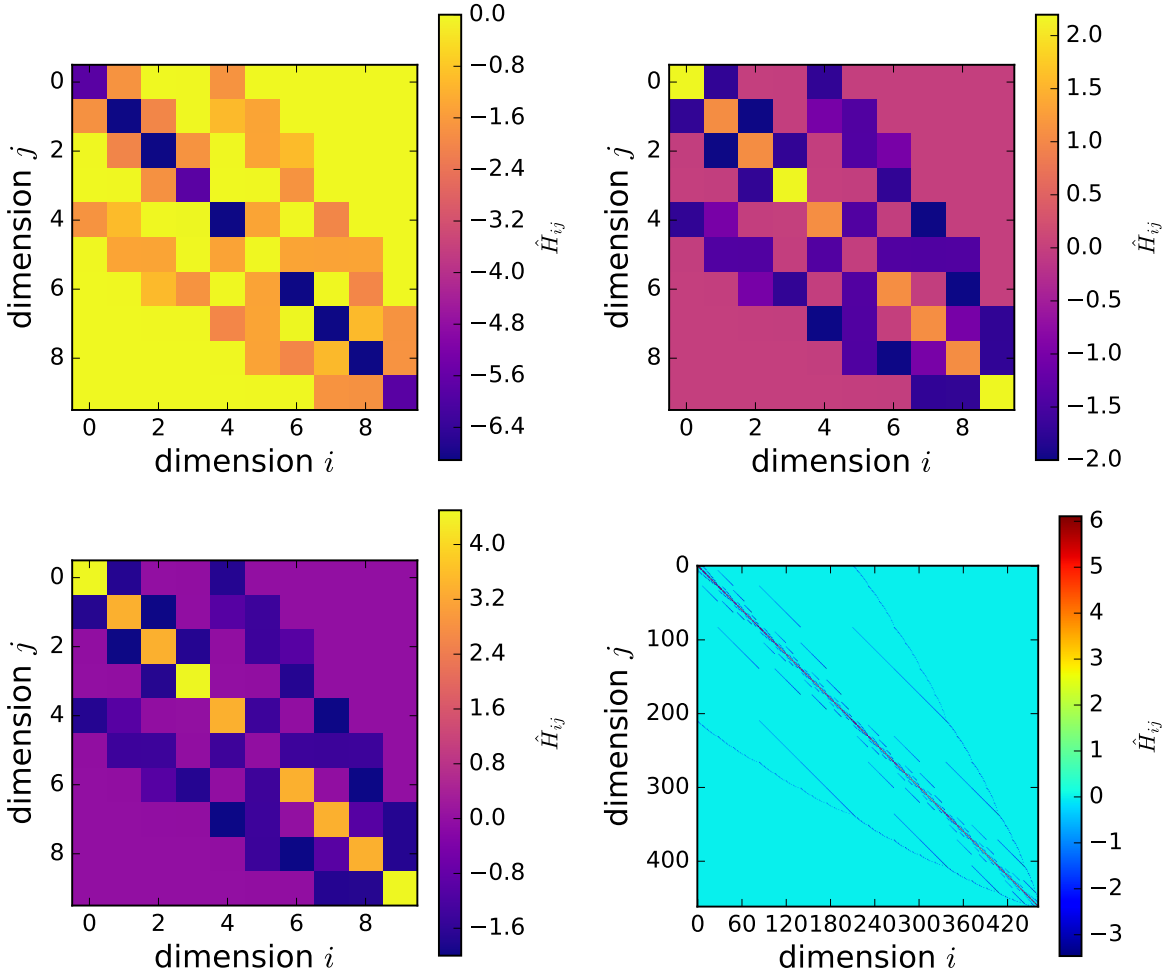

Figure 3.5: *Sparse Hamiltonians for $N = 3$ and $N = 6$.* For a smaller system size with 3 bosons on 3 sites and (**a**-**c**)$U = 0.001, 3, 30$, the Hilbert space has a dimension of 10, which is easily feasible using exact diagonalization. For all three panels, $J_\mathrm{e} = J_\mathrm{o} = 1$. Determining the structure of the Hamiltonian is an important consideration in deciding how best to store the information – in this case, the matrices are 95.5% sparse. (**d**) For 6 bosons on 6 sites and $U = 30$, the Hamiltonian is 92.5% sparse.

their locations than to store all the information together. This computational advantage can change drastically depending on how the information needs to be accessed or post-processed together with the dimension, which depends on system size.

The honeycomb case with a 6-site ring trap is of particular interest, e.g. because of its correspondence "to breaking the A-B sublattice geometry in graphene, creating a gap at the Dirac point" [7]. We consider the the $L = 6$ case for $N = 6, 5, 4, 3$; larger system sizes scale exponentially in computation time and for simplicity are not discussed here. The $L = 6$ and $N = 6$ energy spectrum shown in Figure 3.6 corresponds to the first figure in the paper, produced by both Xinxin and myself, and it showcases the formation of the symmetry gap in the eigenenergy splitting of the first energy cluster for a strongly-interacting ring trap [7].

As another significant contribution to the project, I perform second order degenerate perturbation theory together with Xinxin's calculation to corroborate the results from the paper shown in Figure 3.7 in the strong interaction limit. The results convey that the symmetry gap, $\Delta_s/\bar{J}$, trends with the critical symmetry memory ε_c, and the perturbation theory confirms this. Considering the degeneracy of the eigenstates, the calculations extend to second order in the energy as depicted in Equation (2.47). We calculate the symmetry gap and rescale to $\bar{J}$, so to second order in $\bar{J}/U$,

$$\Delta_s/\bar{J} \simeq a(N)U/\bar{J} + b(N) + c(N)\bar{J}/U. \tag{3.4}$$

For the zeroth order term, we find that $a(N) = 0$ in all cases, because the two states of Δ_s are in the same energy cluster, translating to the same degenerate sub-space. The first order term breaks this degeneracy for odd N such that $b(N) = 0, 1, 0, 2$ for $N = 2$ through 5. The second order term dominates the symmetry gap for even N such that $c(N) = 8/3, -2, 8/3, 0$ for $N = 2$ through 5.

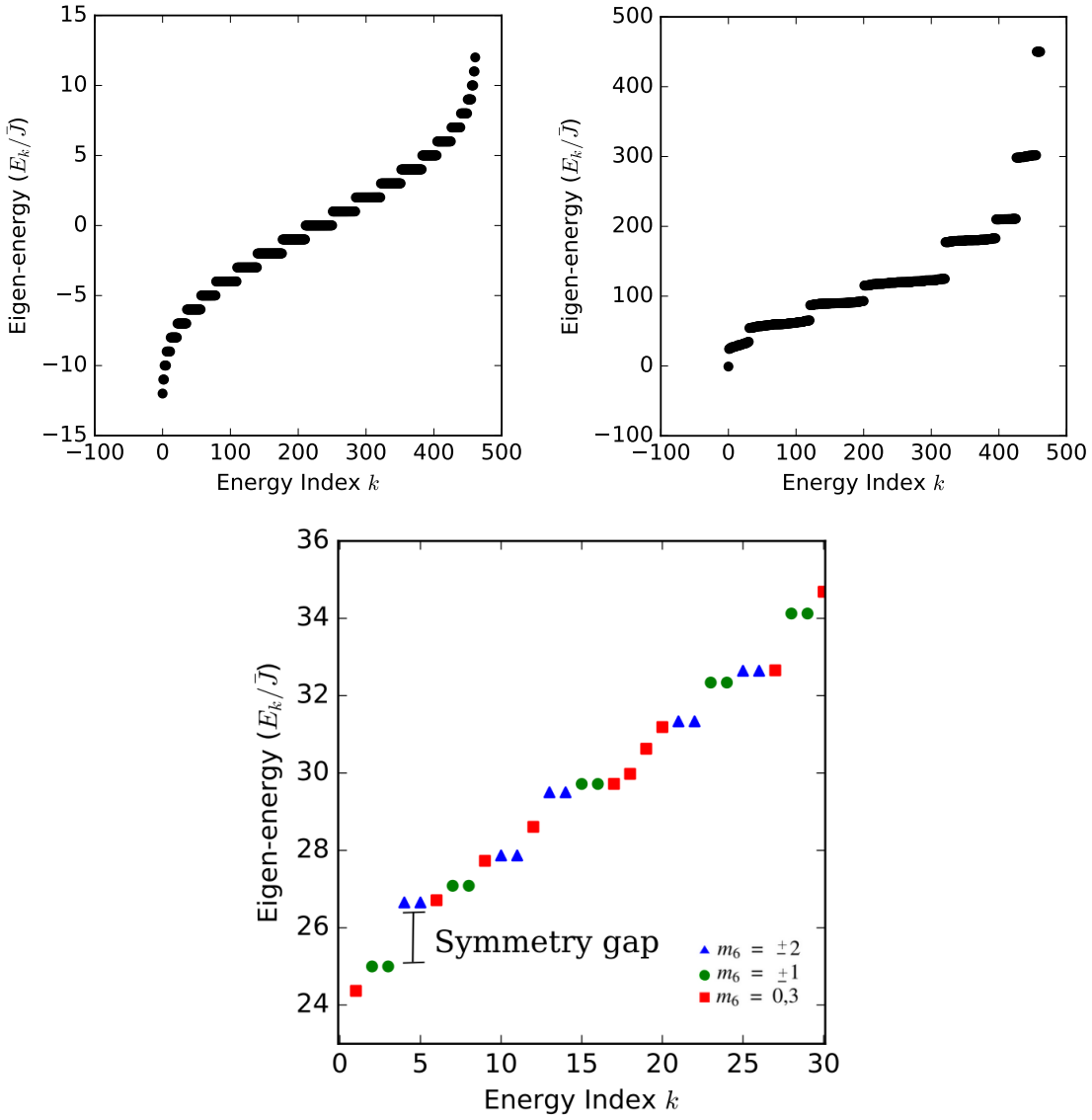

Figure 3.6: *The symmetry gap emerges in the first energy cluster.* In a 6-site ring trap with 6 bosons and $J_e = J_o = 1$, (**a**) $U = 0.001$ the interactions are weak and the clustering is due to the single-particle gap. Panel (**b**) with $U = 30$ strong interactions and (**c**) a zoomed-in panel on the first energy cluster of (**b**) unveil the symmetry gap in the low-lying energy spectrum.

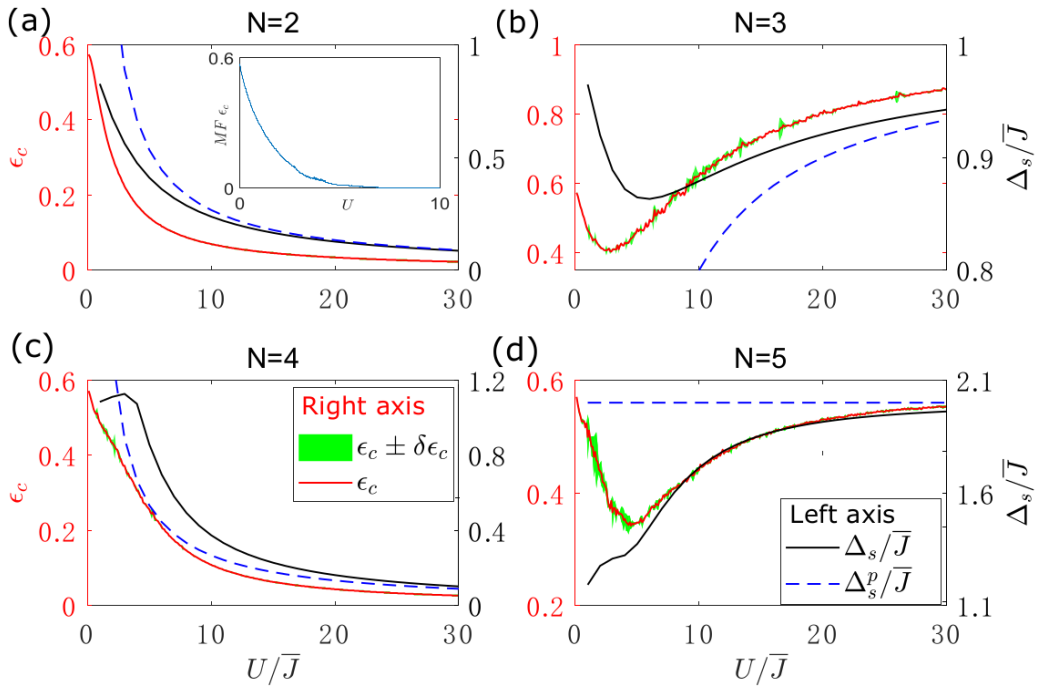

Figure 3.7: *Interaction strength influence on critical behavior.* The critical symmetry breaking strength ε_c – on the left axis and red curves – calculated from the symmetry memory, follows the trend with the symmetry gap $\Delta_s/\bar{J}$ – on the right axis and black curves – calculated from the spectrum $U/\bar{J}$ when interaction strength is large. Displayed are (a) $N = 2$, (b) $N = 3$, (c) $N = 4$, and (d) $N = 5$ particles on 6 lattice sites. Perturbation theory is shown with blue dashed curves and corroborates the two types of asymptotic behavior for either even or odd N. Convergence error is shown in green and was calculated by quadrupling the simulation time and increasing the resolution of ε_c. Reproduced with permission from [7].

CHAPTER 4
FOR HIGH-PRECISION BOSONIC JOSEPHSON JUNCTIONS, MANY-BODY EFFECTS MATTER

A paper submitted to *Quantum Science and Technology*

Marie A. McLain, Diego A. Alcala, and Lincoln D. Carr

4.1 Abstract

Typical treatments of superconducting or superfluid Josephson junctions rely on mean-field or two-mode models; we explore many-body dynamics of an isolated, ultracold, Bose-gas long Josephson junction using time-evolving block decimation simulations. We demonstrate that with increasing repulsive interaction strength, localized dynamics emerge that influence macroscopic condensate behavior and can lead to formation of solitons that directly oppose the symmetry of the junction. Initial state population and phase yield insight into dynamic tunneling regimes of a quasi one-dimensional double well potential, from Josephson oscillations to macroscopic self-trapping. Population imbalance simulations reveal substantial deviation of many-body dynamics from mean-field Gross-Pitaevskii predictions, particularly as the barrier height and interaction strength increase. In addition, the sudden approximation supports localized particle-hole formation after a diabatic quench, and correlation measures unveil a new dynamic regime: the Fock flashlight.

4.2 Introduction

Ground states of linear systems comply with the symmetry of their underlying confining potential. For example, in a one-dimensional double well, the ground state is symmetric about the barrier and the orthogonal state is antisymmetric. Spontaneous symmetry breaking in such a potential means that tuning a control parameter beyond a critical value leaves the system with two concurrent ground states that no longer conform to the symmetry of the

double well: each ground state is asymmetric. In an isolated Josephson junction such as that realized in Bose-Einstein condensates (BECs), spontaneous symmetry breaking can be observed as a $\mathbb{Z}_2$ quantum phase transition (QPT) from Josephson oscillations to a macroscopic self-trapping phase [33, 176]. The effect is observed in many physical systems, particularly nonlinear optics [177, 178] and BECs [122, 176] where recent experimental progress has accelerated [179–181]. For example, this symmetry breaking offers coexistent states that can be used in quantum memory applications such as quantum flip-flops [178, 182]. In superconducting systems, the Coulomb blockade effect occurs when the critical parameter exceeds that of the external current bias and holds exciting prospects for use as a noise filter [183–186]. Superconducting Josephson junctions can be compared for example to driven bosonic Josephson junctions, where the population imbalance between the left and right wells differs as a result of this external bias [187]; in this paper we investigate instead an isolated bosonic Josephson junction. In order for full characterization of such devices, the many-body influences in dynamic regimes must first be understood, and BECs provide a promising architecture to do so as precise quantum simulators.

BECs pose a highly-controllable mechanism for probing the many-body effects that become crucial in high-precision applications: interactions can be swept over seven orders of magnitude with Feshbach resonance manipulation of scattering length [46, 47]. The advancement of experimental technique in radio frequency magnetic traps [48] together with improvements in optical traps [49] enable enhanced control of experiments and provide systems devoid of defects, which is critical for highly precise characterization of dynamics. In addition, Bose-Einstein condensates in optical lattices facilitate the measuring and manipulating of many body quantum states [50–52] that remain intractable in many other experimental platforms. Therefore, BECs such as those formed by ^{87}Rb are an ideal backdrop for investigating the dynamics of a long bosonic Josephson junction, or a double well with spatial extent. The spatial extent of the double well is experimentally imposed in a 1D waveguide with an optical lattice, where the transverse degrees of freedom have been suppressed [188].

This underlying lattice enables precise study of the many-body interactions. We represent the discrete nature of the lattice by the Bose-Hubbard Hamiltonian (BHH),

$$\hat{H}_{\mathrm{BH}} = -J\sum_{\langle i,j\rangle}(\hat{b}_i^\dagger\hat{b}_j + \hat{b}_i\hat{b}_j^\dagger) + \frac{1}{2}U\sum_i \hat{n}_i(\hat{n}_i - 1) + \sum_i V_i\hat{n}_i\,, \tag{4.1}$$

where J is the bosonic tunneling strength, U is the interaction strength, $\hat{b}_i^\dagger$ and $\hat{b}_i$ are bosonic creation and destruction operators, respectively, satisfying bosonic commutation relations, $\hat{n}_i$ is the bosonic number operator, $\langle i,j\rangle$ indicates nearest neighbors, and the indices $i,j\epsilon\{1,...,L\}$ run over the 1D lattice of length L. V_i is the height of the external double well potential. While experimental double wells may be implemented with smoother potentials, by describing the barrier with a single parameter, the barrier height, we minimize the size of the parameter space and thus increase numerical efficiency. It is important to note that the shape of the potential may influence the dynamics [187], and in our case the barrier is square and thin compared to the length of the junction, which relates to e.g. the weak link in superconducting Josephson junctions [32]. This BHH model is applicable when the lattice sites are sufficiently deep to allow for tight binding and single band approximations [54].

For unit filling with fixed particle number, the optical lattice introduces a second quantum phase transition (QPT) to the Josephson junction in addition to the well-known $\mathbb{Z}_2$ transition, a continuous $U(1)$ transition from a Mott insulator to a superfluid [88, 89]. In the BHH for $V_i = 0$, $L \to \infty$, $N \to \infty$, $N/L = 1$, where N is the number of atoms, the crossover from the superfluid phase to the Mott insulating phase occurs at a $J/U_{\mathrm{critical}} \approx 0.305$ in one dimension [104], while the mean-field approximation underestimates this at $J/U_{\mathrm{critical}} \approx 0.086$ [189]. Superfluid behavior manifests for weakly-interacting systems such that $J/U > J/U_{\mathrm{critical}}$; in contrast, the Mott-insulating regime requires strongly-interacting bosons such that $J/U < J/U_{\mathrm{critical}}$. When the lattice is infinitely deep, or $J = 0$, the result is a perfect Fock state; in Fock space notation this state is written $\mid 111...1\rangle$ for unit filling, i.e., the number of particles is approximately commensurate with the number of lattice sites. In this paper we focus on 1D optical lattices, which translates to experiment e.g. via

"cigar"-shaped waveguides, where the atoms are contained in one-dimensional potentials by transverse optical confinement [188].

While it is convenient for our research to observe bosons in a Fock or number basis, often it is more appropriate to use a different framework or basis, for example in cases of macroscopic phase coherence and Josephson-like dynamics, the phase basis is often represented as a phase difference between the two wells of a double well potential. The dictionary in Table 4.1 gives a flavor of common models of Josephson junctions and their relation to one another. The first Hamiltonian is the Bose-Hubbard model; it differs from the other Hamiltonians in that it is presented as a discretization scheme, where tunneling strength J and atomic interaction strength U are local and are defined by integrals over lowest-band Wannier functions centered on periodic lattice sites, $w_0(\vec{x})$; alternately, as in our present study, we may take the lattice as an explicitly imposed potential. The second Hamiltonian, the two-mode model presented in Table 4.1(2) is the same as the Bose-Hubbard Hamiltonian, but with only two lattice sites, one for each well. The general phase and number field operators are conjugate variables, such that $[\hat{\phi}, \hat{N}] = -i$, and the raising and lowering operators to obtain Table 4.1(3) and (4) are $e^{i\hat{\phi}}$ and $e^{-i\hat{\phi}}$, respectively. In the general double well problem, mean-field theory provides a description of the relative dynamics under certain assumptions: the coherence must be large and relative phase well-defined. This mean-field approximation is generally very good in regimes where interactions are weak, such as the superfluid or superconducting regimes [34, 127, 183, 186].

The tunneling dynamics are underlaid by the interplay of the two QPTs, $\mathbb{Z}_2$ and U(1). This reduces to tuning of the barrier height for the spontaneous symmetry breaking transition and tuning of the interaction strength for the superfluid-Mott transition. The ultimate goal then is to characterize the dynamic tunneling regimes that result, from Josephson oscillations to self-trapping. Some of these regimes have previously been identified in literature for weakly-interacting systems [33, 34, 120, 122, 176]. In a single-particle limit, the Rabi frequency is dependent on E_{DWT}, the Josephson tunneling energy, $\omega_R \propto 2E_{\mathrm{DWT}}/L\hbar$, where the

Table 4.1: *Translation dictionary of Josephson junction naming conventions.* (1) The Bose-Hubbard Hamiltonian used to describe Fock space number operators on an optical lattice used as a discretization scheme. (2) The Lipkin-Meshkov-Glick model is a two-mode model, which as a distinction from the BHH does not capture many-body effects in a long BJJ; it refers to two macroscopic Wannier functions in a Fock basis, where the tunneling parameter is the Josephson or double well tunneling energy E_{DWT}, and the the inter-atomic charging energy, $\tilde{E}_C$, is between particles in the same well. (3) The many-body relative number, relative phase formulation in a phase basis allows for number fluctuations. (4) The mean-field limit of (3), when the number of particles becomes large, is a semiclassical description void of number fluctuations. (5) The Hamiltonian for an unbiased Josephson junction in a superconducting circuit or an atomic gas with an applied current takes an analogous form as (4), where the change in representation here is the charging energy, $1/[2C]$, which is the capacitance between Cooper pairs on opposing sides of the junction. Finally, (6) a phase qubit Hamiltonian includes the same tunneling and interaction terms as the mean-field Josephson junction, with the benefit of an added current bias term that tunes the tilt of the potential in the phase basis.

Double Well Convention	**Hamiltonian**	**Tunneling Parameter**	**Interaction Parameter**
(1) Bose Hubbard as Discretization	$\hat{H}_{\mathrm{BH}} = -J\sum_i(\hat{b}_i^\dagger\hat{b}_{i+1} + \text{h.c.}) + \frac{1}{2}U\sum_i \hat{n}_i(\hat{n}_i - 1) + \sum_i V_i\hat{n}_i$	$J = -\int d\vec{x} w_0^*(\vec{x} - \vec{x}_i)(-\frac{\hbar^2}{2m}\vec{\nabla}^2 + V_{\mathrm{latt}}(\vec{x}))w_0(\vec{x} - \vec{x}_{i+1})$	$U = g\int d\vec{x} \mid w_0(\vec{x}_i) \mid^4$
(2) Lipkin-Meshkov-Glick	$\hat{H}_{\mathrm{LMG}} = -E_{\mathrm{DWT}}(\hat{b}_L^\dagger\hat{b}_R + \hat{b}_L\hat{b}_R^\dagger) + \frac{1}{2}\tilde{E}_C(\hat{n}_L(\hat{n}_L - 1) + \hat{n}_R(\hat{n}_R - 1))$	NE_{DWT}	$\tilde{E}_C$
(3) Relative Number/Phase	$\hat{H}_{\hat{n}\hat{\phi}} = -E_{\mathrm{DWT}}\sqrt{N(N+2) - 4\langle\hat{n}^2\rangle}\cos\hat{\phi} + \frac{1}{2}\tilde{E}_C\hat{n}(\hat{n} - 1)$	E_{DWT}	$\tilde{E}_C$
(4) Semiclassical Rel. Number/Phase	$H_{\mathrm{iso}} = -E_{\mathrm{DWT}}\sqrt{1 - n^2}\cos\phi + \frac{\tilde{E}_C}{2}n^2$	E_{DWT}	$\tilde{E}_C$
(5) Unbiased Superconducting JJ	$\hat{H}_{\mathrm{JJ}} = -\frac{I_c\Phi_0}{2\pi}\cos\hat{\phi} + \frac{1}{2C}\hat{Q}^2$	$I_c\Phi_0/2\pi$	$\frac{1}{4e^2C}$
(6) Superconducting Phase Qubit	$\hat{H}_{\mathrm{PQ}} = -\frac{I_c\Phi_0}{2\pi}\cos\hat{\phi} + \frac{1}{2C}\hat{Q}^2 - \frac{I_{\mathrm{bias}}\Phi_0}{2\pi}\hat{\phi}$	$I_c\Phi_0/2\pi$	$\frac{1}{4e^2C}$

frequency decreases with increasing system size and L is the number of lattice sites [85, 121].

The mean-field equations of motion, from [123], are similar to Josephson's equations; the major difference stems from the assumption in Josephson's equations that the time derivative of population density is identically the same in the two wells [123, 124]. Relinquishing this restriction elicits the equations of motion:

$$\begin{aligned} n'(t) &= -\sqrt{(1-n(t)^2)}\sin\phi(t) \\ \phi'(t) &= \Delta E + E_C n(t) + \frac{n(t)}{\sqrt{1-n(t)^2}}\cos\phi(t). \end{aligned} \tag{4.2}$$

The true Rabi or sinusoidal regime occurs when the charging energy is zero, $\tilde{E}_C = 0$, since the charging energy term in the mean-field Hamiltonian (unbiased JJ (4 and 5) in the Table 4.1) provides a nonlinear effect that takes us out of the Rabi and into the Josephson regime [33, 123]. Josephson oscillations have a frequency proportional to $\omega_J = \sqrt{\tilde{E}_C E_{\mathrm{DWT}}}/\hbar$, where $\tilde{E}_C$ is an inter-atomic charging energy between bosonic atoms. A mean-field measure often used to characterize Josephson dynamics is the relative particle number between the two wells, or the population imbalance, $(n_L(t) - n_R(t))/N_{\mathrm{tot}}$, a variable that is close to zero in superconducting circuits due to a dominating external current [113]. The initial population imbalance, n_0, and relative overall phase between the two wells, ϕ_0, provide information to predict the dynamic tunneling regime. When n_0 exceeds a critical threshold, the particles will be self-trapped on one side of the junction, thus breaking the ground state symmetry in a $\mathbb{Z}_2$ transition. This out-of-equilibrium phenomenon renormalizes the energy to a metastable tunneling-suppressed Fock regime [85].

To characterize these dynamic regimes in relation to the superfluid-Mott phase transition, we annotate the relevant parameter space. First, we have the BHH describing the underlying optical lattice, with parameters J/U, where J is the local bosonic tunneling or hopping strength between lattice sites and U is the local bosonic interaction strength between atoms on the same lattice site. Next, we have a two-mode model with E_{DWT} the tunneling between wells, or Josephson energy, and $\tilde{E}_C$ the interaction between atoms in the same well, a modified charging energy. $E_{\mathrm{DWT}}/\tilde{E}_C$ parameters together represent the ratio of tunneling between the

two wells and interaction within each well. $E_{\mathrm{DWT}}/\tilde{E}_C$ reduces to a function of ζ, the effective energy ratio for the two wells (see Equations (4.3), (4.4), (4.5) below), when the width of the barrier is held constant. The nature of the two scales of the problem, in addition to system size, leads to multiscale behavior.

To initialize a state for the dynamics, we run imaginary time propagation to obtain a ground state of a single well potential as shown in Figure 4.1(**a**). The finite potential on the right in this instance is at the same height as the double well barrier. Then, we diabatically quench to a symmetric bosonic Josephson junction by lowering the right side potential before propagating in real time, as portrayed in Figure 4.1(**b**). This protocol is performed both in time-evolving block decimation (TEBD) and in solving the Gross-Pitaevskii equation (GPE) as a mean-field approximation for symmetric double wells with a single lattice site as the barrier and with open boundary conditions. The system sizes range from four sites for analytical sudden approximation calculations to 55 sites for $g^{(2)}$ number fluctuations calculated with TEBD.

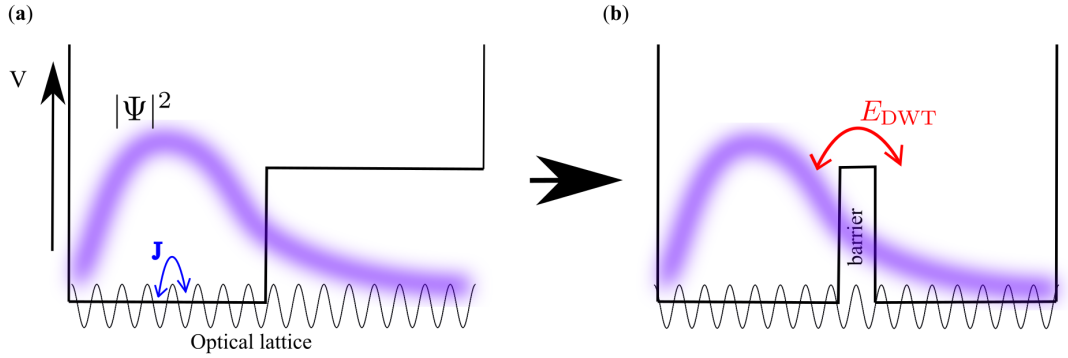

Figure 4.1: *Initial bound state and time propagation.* (**a**) We run imaginary time propagation in the potential (solid black curve) to obtain a ground state wavefunction (blurred purple curve) of the left well, (**b**) then lower the right well and propagate in real time. The optical lattice is superimposed on the Josephson junction as a discretization scheme.

This paper is outlined as follows. Results are presented first in terms of static initial states in section 4.3.1. We propose a method for characterizing the dynamic regimes based

on the initial state number and phase from both a mean-field and a many-body perspective, and we demonstrate that the mean-field representation fails to recognize the self-trapping transition above a weak-interaction threshold. For strongly-interacting bosons, the diabatic quench instigates particle-hole creation and low-lying junction modes; the result is corroborated by sudden approximation calculations. In section 4.3.2, we find the particle-hole pairs, which are number-squeezed, are exceptionally stable over long time scales and are particularly pronounced in the Josephson regime. When the filling factor is slightly above or below one, we observe what appear to be emergent solitons or solitary waves – they form as pairs on either side of the barrier and propagate in parallel without dispersing and with a speed less than the sound speed – a striking contrast to the symmetry of the underlying potential. Furthermore, we compare the dynamical similarities of TEBD and the GPE for weakly-interacting particles, along with the failure of the GPE to capture the $\mathbb{Z}_2$ transition for strongly-interacting bosons. Section 4.3.3 focuses on correlation measures, which are easily calculated from matrix product states and illuminate the many-body physics especially as interaction strengths increase. For example, the depletion of the condensate as a function of barrier height becomes quantized in the Mott regime due to the Mott gap, whereas in the superfluid regime the BEC is universally strong except near the symmetry-breaking critical point. We also present the time-dependence of the $g^{(2)}$ measure, or number fluctuations, through snapshots that can be directly compared with experimental results. Then, in the materials and methods of section 4.4, we present more detail on our open-source time-evolving block decimation simulations and segue to open-source matrix product state (OSMPS) software. We also describe our protocol for numerically solving the GPE and our analytical sudden approximation calculations, as well as how to access our open data repository. In the final section 4.8, we conclude with a brief summary of our results, apply our findings in a broader context, and suggest future research direction.

4.3 Results and Discussion

4.3.1 Initial state influence on dynamics

While typical treatments of the dynamics of quantum phase transitions focus on a quench of the parameter space using ground states, the goal of this work is to characterize the dynamical parameter space associated with macroscopic quantum tunneling. Using the initial states, we can make many predictions about the dynamics, though behavior such as soliton creation or number fluctuation propagation do not follow from from initial states alone.

We devise a method that maps out dynamical regimes, both from a many-body and a mean-field perspective, based on initial state number and phase information. To quantify the competing energy terms, we define a mean-field and many-body version of a critical parameter, which is a ratio of tunneling and interaction energies, to distinguish between Josephson and self-trapping or Fock regimes. When the energy ratio exceeds one, $\zeta > 1$, the system exhibits spontaneous symmetry breaking and the particles remain confined on one side of the potential. The mean-field version is based on an energy ratio suggested in [124]. For initial population imbalance n_0 and initial relative phase ϕ_0, we define the mean-field (MF) energy ratio from Hamiltonian (4) of Table 4.1,

$$\zeta_{\mathrm{MF}} = \frac{n_0^2}{2(1+\sqrt{1-n_0^2}\cos\phi_0)} \tag{4.3}$$

where the initial state has a well-defined relative number and phase.

From Hamiltonian (1) in Table 4.1, we calculate a many-body (MB) version of Equation (4.3), where we have not yet subtracted to obtain the relative phase and number information,

$$\begin{aligned}\zeta_{\mathrm{tot}} &= \frac{\frac{1}{2}\sum_j n_j^{(0)}(n_j^{(0)}-1)}{\sum_{\langle j,k\rangle} A_{jk}(\exp[i\phi_{jk}^{(0)}]+\exp[-i\phi_{jk}^{(0)}])} \\ &= \frac{\frac{1}{2}\sum_j n_j^{(0)}(n_j^{(0)}-1)}{\sum_{\langle j,k\rangle} 2A_{jk}\cos\phi_{jk}^{(0)}}\end{aligned} \tag{4.4}$$

where $n_j^{(0)} \equiv \langle \hat{n}_j(t=0) \rangle$ is the initial number on site j and $\phi_{jk}^{(0)}$ is the initial phase between nearest neighbor sites j and k. The superscript $^{(0)}$ is a label indicating an initial value. The denominator of Equation (4.4) is calculated from the single particle density matrix (SPDM), $\rho_{jk} = \langle \hat{b}_j^\dagger \hat{b}_k \rangle = A_{jk} \exp(i\phi_{jk})$ between nearest neighbor sites j and k, which comprises the tunneling term of the BHH (see Table 4.1) without the tunneling constant J. The phase is calculated as follows. We take the eigenvector $\vec{v}^{(1)}$ associated with the largest eigenvalue λ_1 of the SPDM, where the vector indicates distribution over lattices sites of the form $v_j^{(1)}$, $j \in \{1, \ldots, L\}$. This eigenvector is the closest approximation to the mean-field in the Landau definition of the superfluid order parameter, discretized on the lattice as $v_j^{(1)} = \psi_j = \sqrt{n_j} \exp i\phi_j$. The phase is thus taken as the phase of the dominant eigenmode of the SPDM, and the relative phase is calculated as the difference between the average phase in the left and right wells, $\Delta\phi = L_{\text{leftwell}}^{-1} \sum_{j \in \text{leftwell}} \phi_j - L_{\text{rightwell}}^{-1} \sum_{j \in \text{rightwell}} \phi_j$ with L_{leftwell} the number of sites in the left well, and likewise for the right well. Alternately one can calculate a particular phase difference, e.g. between the sites in the left and right wells closest to the barrier, respectively. The cosine representation of the tunneling term is a reminder of the analogies presented in Table 4.1. Then, the numerator of Equation (4.4) comprises the interaction term of the BHH without the constant U. Next, we define the initial SPDM as $\rho_{jk}^{(0)} \equiv \langle \hat{b}_j^\dagger(0) \hat{b}_k(0) \rangle$. This leads to a many-body ratio analogous to the mean-field ratio of Equation (4.3), where we calculate the difference of the interaction terms (tunneling terms) of the BHH between the two wells in the numerator (denominator) of Equation (4.5). We express ζ_{MB} as these many-body differences between the two wells,

$$\zeta_{\text{MB}} = \frac{\sum_{j=1}^{\lfloor L/2 \rfloor} n_j^{(0)}(n_j^{(0)} - 1) - \sum_{j=\lfloor L/2 \rfloor}^{L} n_j^{(0)}(n_j^{(0)} - 1)}{4\left(\sum_{\langle j,k \rangle = 1}^{\lfloor L/2 \rfloor} (\rho_{jk}^{(0)} + \rho_{jk}^{(0)*}) - \sum_{\langle j,k \rangle = \lfloor L/2 \rfloor}^{L} (\rho_{jk}^{(0)} + \rho_{jk}^{(0)*}) \right)} \tag{4.5}$$

where $\rho_{jk}^{(0)}$ is a complex element of the single particle density matrix for lattice sites j and k at time $t = 0$ and L is the total number of lattice sites. The sums $\sum_{j=1}^{\lfloor L/2 \rfloor}$ and $\sum_{\langle j,k \rangle = 1}^{\lfloor L/2 \rfloor}$ are sums over the left well, and $\sum_{j=\lfloor L/2 \rfloor}^{L}$ and $\sum_{\langle j,k \rangle = \lfloor L/2 \rfloor}^{L}$ are sums over the right well.

The energy ratio ζ is one way of characterizing distinct dynamical regimes. The Josephson regime manifests in low-barrier cases, meaning the particles tunnel or oscillate back and forth between wells in a macroscopic manner. These are Rabi oscillations when ζ approaches 0 . Above the single particle limit, for $\zeta < 1$, Josephson or plasma oscillations emerge. The critical point $\zeta = 1$ marks the phase transition; the high-barrier limit, or $\zeta > 1$, leads to macroscopic self-trapping of the condensate on one side of the well. The isolation of the junction, unlike that of superconducting circuits with external biases, allows for a more tenable parameter space to observe self-trapping [176]. The ratio as a function of interaction strength or lattice depth U/J and barrier height V_0 is represented in Figure 4.2 for a double well with 15 total sites and 7 total particles. The resolution in U/J is 1, with $J = 1$ and U from 0 to 15. The resolution in V_0 is 0.5. For small U/J, both ζ_{MB} and ζ_{MF} experience the $\mathbb{Z}_2$ critical region about $V_0 = 1$. For large interactions U/J, ζ_{MF} in Figure 4.2(**b**) does not reach the critical point and the mean-field measure thus fails to recognize the spontaneous symmetry breaking.

In Figure 4.3, the initial states immediately post-quench display a larger population imbalance n_0 toward the left well as the barrier height V_0 is increased. For weak interactions in Figure 4.3(**a**), the functions are smooth in portrayal of their condensed and superfluid nature. On the other hand, strong interactions instigate particle-hole pair formation as low-lying excited states of a Mott insulator, such as for $V_0 = 0.1, 1$ in Figure 4.3(**b**), an effect which is not seen in mean-field simulations. The interaction of the particle-hole pairs with the condensate are a probable source of damping of the plasma oscillations in a closed system, as [34] suggests, the interaction of the condensate with a non-condensed fragment is a source of phase decoherence – an influence which may need consideration for high-precision applications such as superconducting quantum interference devices or BEC quantum simulators. For higher barriers such as $V_0 = 3$ in Figure 4.3(**b**), we find lowly-excited modes of the junction, with increasing excitations for higher barriers. In the dynamics, these modes are largely masked by stronger energy scales, but they are especially visible on the cusp of

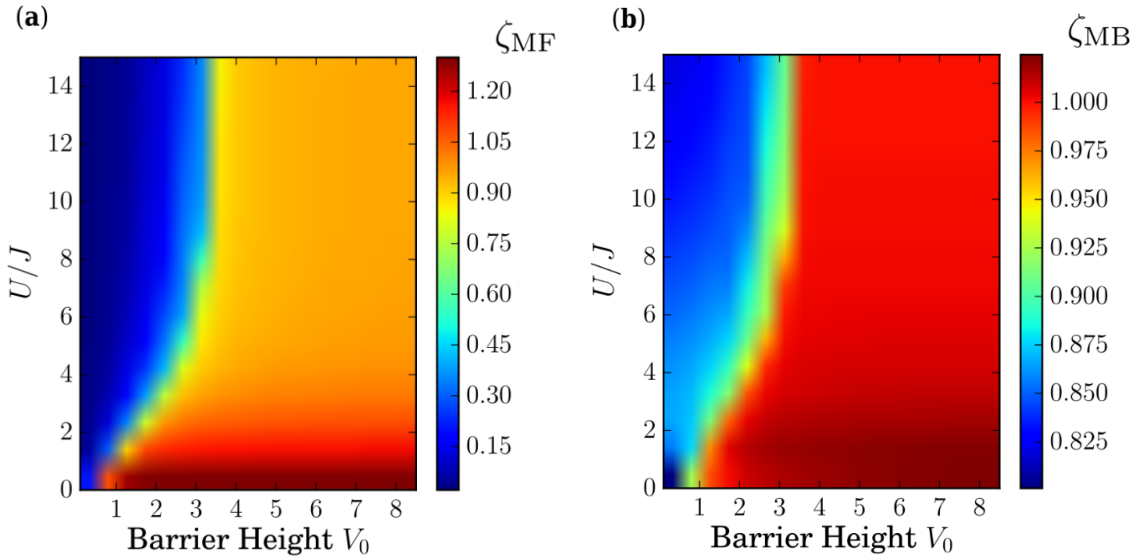

Figure 4.2: *Dynamic regimes predicted by initial states.* Using the ratio of the interaction to the tunneling energy, we can predict dynamics using information from static initial states. For a system of 15 lattice sites and 7 total particles, (**a**) the mean-field energy ratio depicts the Josephson regime in blue, the Fock regime in red for weak interactions, and the orange region does not reach the critical point $\zeta = 1$: the mean-field ratio fails to predict the symmetry-breaking phase transition for stronger interactions. In contrast, the many-body energy ratio (**b**) demonstrates a decisive Fock region in red where $\zeta_{\mathrm{MB}} = 1$ for all interaction strengths.

the transition to self-trapping, where the barrier is not yet high enough to completely trap the bosons in the left well, but the nonlinear disturbances from macroscopic tunneling are suppressed. The strongly-interacting Fock regime is reached for larger barrier heights than for the weakly-interacting regime due to repulsive interactions between atoms in the left well.

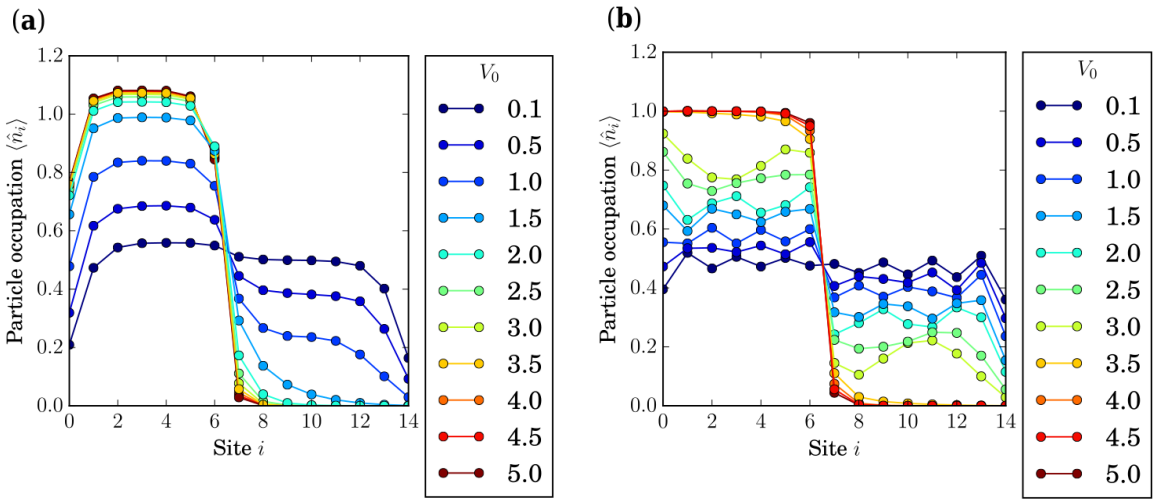

Figure 4.3: *Initial bound states through the Mott-superfluid critical point.* State initialization traps the bosons largely in the left well for an optical lattice with 15 sites and 7 total particles. (**a**) Beyond the Mott-superfluid critical point, interactions are weak, $U = 2$, $J = 1$, and smooth superfluid behavior aligns more closely with mean-field theory. (**b**) In the Mott regime, interactions are strong, $U = 15$, $J = 1$, and low-lying excited modes inject deviations from mean-field theory that provide significant influence even with fluctuations as small as ± 0.05 particles.

4.3.2 Dynamic regimes and Fock measures

The three dynamic regimes previously identified in isolated bosonic Josephson junctions are Rabi, Josephson, and Fock regimes [33]. For weakly-interacting systems, where U is small, these regimes are well-characterized with mean-field theory. In order to see the effects of a Mott insulator on the dynamics, we must have a number of particles that is approximately commensurate with the number of sites, though the presence of the barrier influences the Mott behavior [190]. Due to the nature of our state initialization, choosing a number of particles that is about half the number of sites gives a filling factor close to one for the single-

well initial potential. This unit filling becomes more important as we increase interaction strength. For example, in Figure 4.3, there are a total of 15 sites with a 1-site barrier, and 7 bosons in one well enables close to unit filling for larger barriers.

Fock states or local particle numbers are one type of convenient measure of ultracold atom experiments. For realistic comparison with experiment, we characterize local particle densities as a function of time. Figure 4.4 epitomizes the real time dynamics of a system with 55 lattice sites, 27 sites in each well, and 27 total particles, through the $\mathbb{Z}_2$ phase transition from Josephson in Figure 4.4(**a**) to Fock in Figure 4.4(**d**). The units are scaled by the tunneling parameter, where $J = 1$, the units of time are $\hbar/J$, and typical lattice separation in experiments is $\simeq 1/2$ micron, with the units chosen such that the lattice constant $\Delta x = 1$ [104, 110]. In this case, the interaction parameter $U = 0.3$ is small and the barrier height is increasing from (**a**) $V_0 = 0.2$, (**b**) $V_0 = 0.4$, (**c**) $V_0 = 0.6$, (**d**) $V_0 = 2$, where the critical initial population imbalance is exceeded in (**c**) and (**d**) and the condensate is self-trapped as determined by ζ – both mean-field and many-body versions.

Next, we look at the transition from Josephson to Fock regimes when interactions are strong. In Figure 4.5(**a**), Mott behavior is dominant, and particle-hole pairs form in response to the rapid quench of the potential. These quasiparticles form faster than matter could possibly propagate from the left to the right well, indicating the sudden approximation may explain the phenomenon, as excited modes of the Mott insulator are visible in the Josephson regime.

Furthermore, the Josephson oscillations, likely a superfluid fragment or skin [190], slosh over the top of the insulating quasiparticles and the interaction of the two fragments leads to a damping of the Josephson tunneling in Figure 4.5. As demonstrated with the energy ratio ζ, the Josephson regime extends farther into the barrier height parameter space when interactions are strong, $U/J > 3$. This extension of the parameter space is a mean-field effect, seen in both ζ_{MB} and ζ_{MF} diagrams of Figure 4.2.

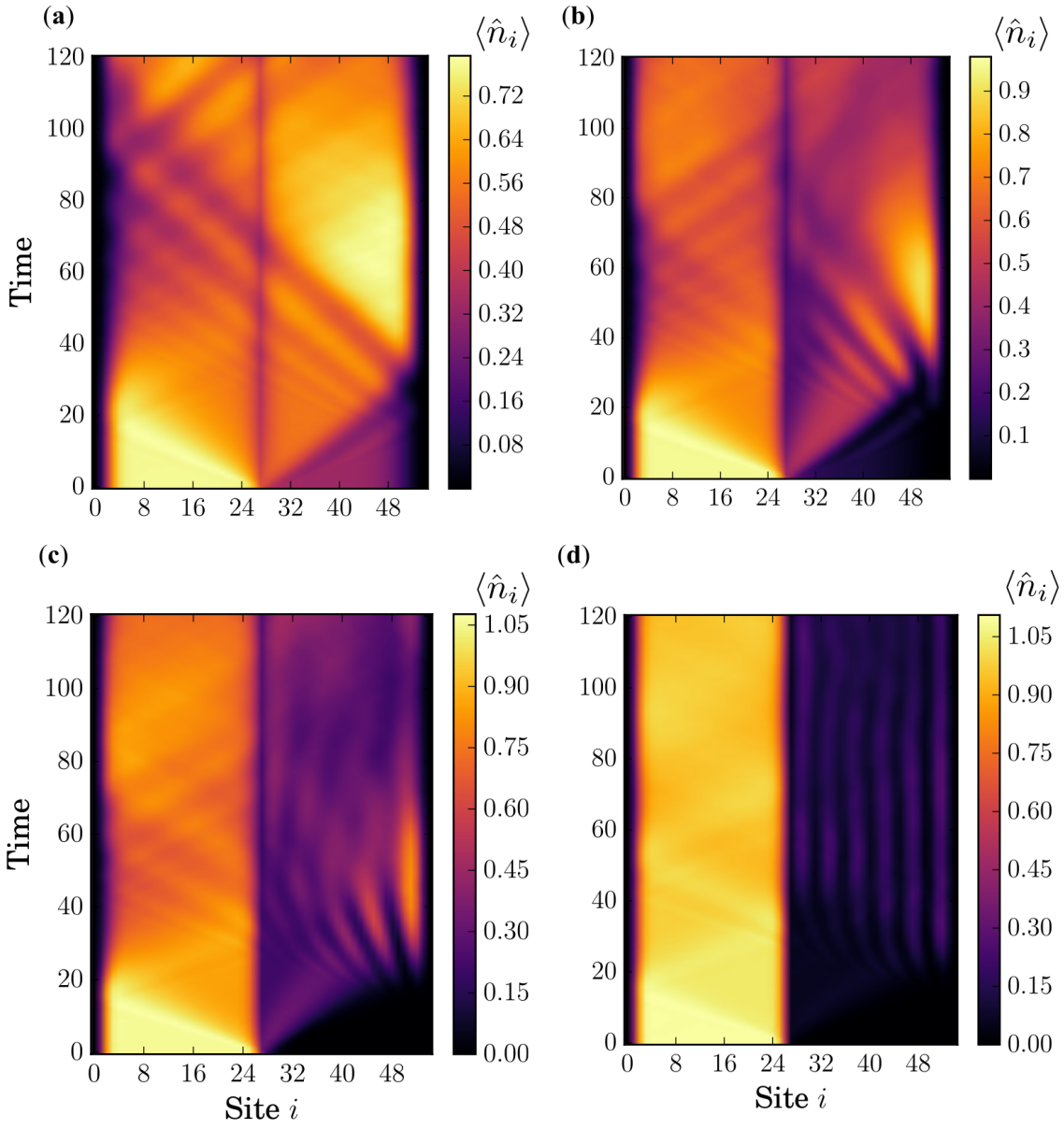

Figure 4.4: *Weakly-interacting spontaneous symmetry breaking transition.* Tunneling dynamics range from (**a**) the Josephson regime to (**d**) the Fock self-trapping regime for a system of 55 sites and 27 atoms, $U = 0.3$ and $J = 1$. The barrier height increases from (**a**) $V_0 = 0.2$ to (**d**) $V_0 = 2$. In the critical regions, (**b**) $V_0 = 0.4$ the dynamics are Josephson-like with interference patterns due to the interferometer nature of the double well. The diffraction fringes become more pronounced in the right well as the barrier height increases to (**c**) $V_0 = 0.6$ and becomes self-trapped in (**d**).

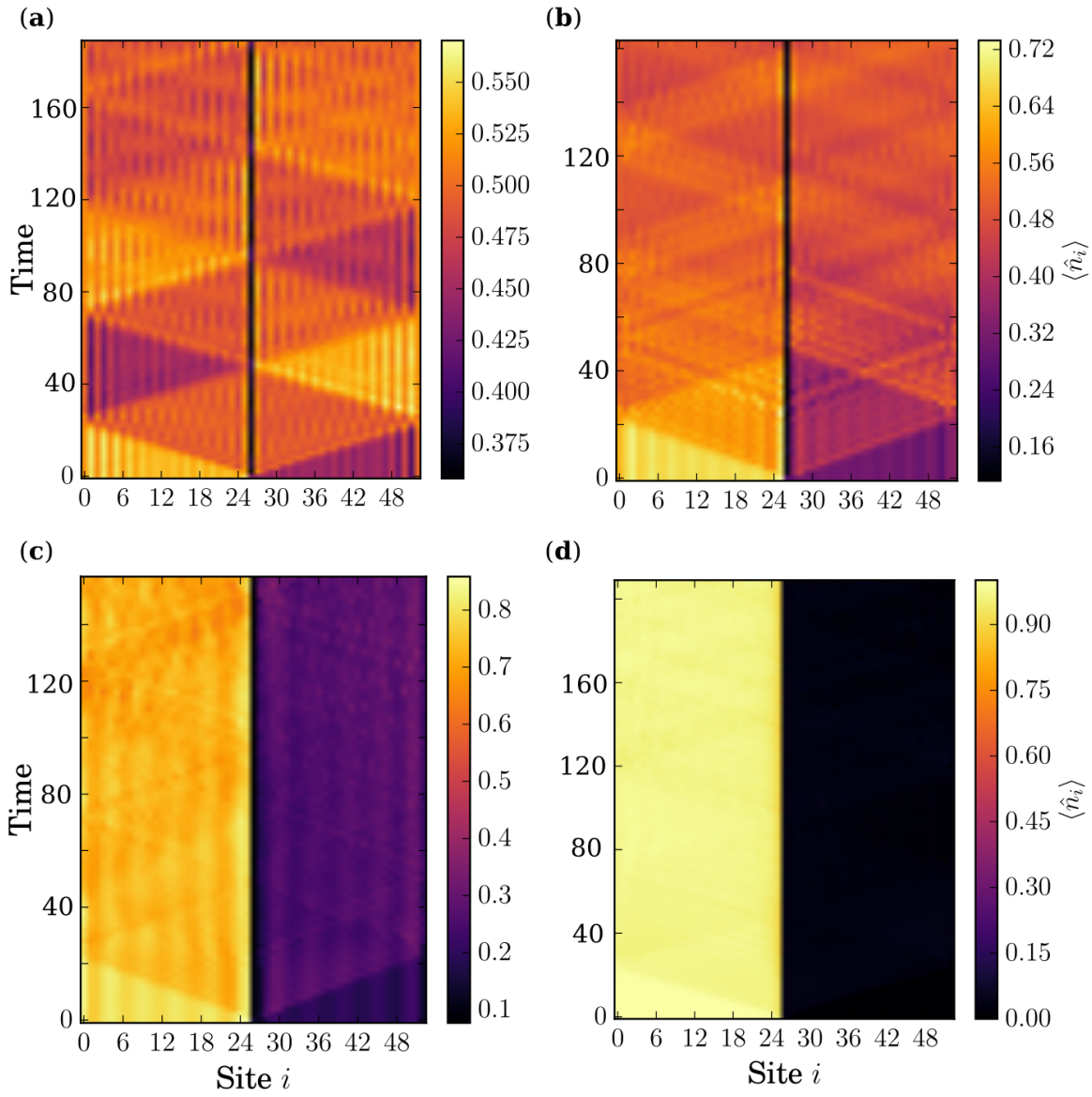

Figure 4.5: *Strongly-interacting spontaneous symmetry breaking transition.* For low barriers such as (**a**) $V_0 = 0.5$, particle-holes emerge across the entire lattice. Through the critical region of (**b**) $V_0 = 1$, the damping is large and phase coherence rapidly decays – likely due to interaction of the quasiparticles with the condensate. Just beyond the critical point into the Fock regime for $V_0 = 3$ (**c**), the nonlinear waves that would otherwise dominate the dynamics are suppressed, making way for more timid modes of the double well, a result of the diabatic quench: these modes are sustained for unexpectedly long time scales. Finally, the bosons are self-trapped (**d**) for a larger barrier, $V_0 = 5$.

To further characterize the dynamics regimes, we consult the energy ratios suggested in Equations (4.3) and (4.5), which call for initial phase and number conditions. For simplicity, the initial relative phase is zero, leaving the initial relative number to determine the dynamic regime with this method. First we replicate research in [33, 124] supporting Josephson and Fock regimes for weakly-interacting ^{87}Rb bosons from a mean-field perspective. Figure 4.6(**a**) reveals the qualitative agreement of mean-field GPE simulations and many-body TEBD for dynamics of the population imbalance or relative number for $J = 1$ and $U = 0.3$. The system consists of 27 total lattice sites, 13 sites in each well, and 14 particles, which enables approximate commensurate filling for one of the wells plus the barrier. For $V_0 = 0.2$, both mean-field and many-body simulations are in the Josephson regime as determined by ζ_{MB} and ζ_{MF}. A quick method for diagnosing the dynamical regime is to plug the critical ratio $\zeta = 1$, and relative phase, $\phi_0 \approx 0$, into Equations (4.5) and (4.3) and solve for the critical population imbalance n_0. In this instance, the initial population imbalance $n_0 \approx 0.5$ is less than the critical value and thus it is in the Josephson regime. This conclusion supports the dynamical results: Josephson oscillations occur about the x-axis, so the average value of the function should be close to zero. This is akin to an average d.c. component of zero, meaning the particles are tunneling and moving freely across the barrier region.

Additionally, for $V_0 = 1, 2$, and 5, the initial population imbalance $n_0 = 1$ is greater than the critical value, in this case, for both many-body and mean-field simulations, suggesting that these systems are in the Fock regime. The next clue that particles are self-trapping behind the barrier, no longer able to freely tunnel, is the d.c. component of the relative number, as well as the smaller magnitude of the a.c. component. As pointed out in [124], there are sub-regimes within the macroscopic-self trapping region. The farther into the symmetry-breaking regime, the smaller the amplitude of the oscillations within the left well. Closer to the $\mathbb{Z}_2$ phase transition, the oscillations will resemble critical damping; the curves for $V_0 = 1$ (solid) demonstrate under-damping close to the critical damping region. Not coincidentally, $V_0 \approx 1$ is where we find the $\mathbb{Z}_2$ critical region for small U/J in the energy

ratio ζ diagrams of Figure 4.2.

We apply the same approach to Figure 4.6(**b**) using energy ratios. Both ζ_{MB} and ζ_{MF} predict Josephson dynamics for $V_0 = 0.2, 1$, and 5, as evidenced by the small initial population imbalances for TEBD (solid) and GPE (dashed) simulations. The TEBD solid red curve depicts macroscopic self-trapping for $V_0 = 5$, which agrees with ζ_{MB} in Figure 4.2(**b**) for strong interactions. However, the GPE dashed red curve at the same barrier height falsely depicts Josephson oscillations with larger magnitudes – a result that corroborates $\zeta_{\mathrm{MF}} < 1$ for all barrier heights in Figure 4.2(**a**), meaning there is no symmetry breaking transition. The disparity of MF from MB theory is not surprising, as often MF theories break down for strongly-interacting systems.

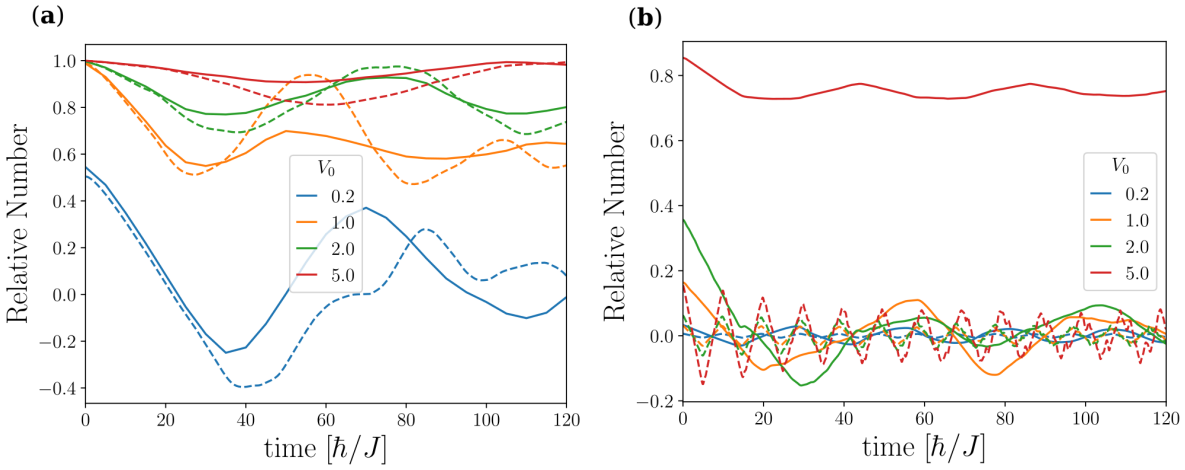

Figure 4.6: *Weak interaction similarities and strong interaction disparities: Time-evolving block decimation and the Gross-Pitaevskii equation.* For a system of 27 lattice sites and 14 particles, GPE (dashed curves) and TEBD (solid curves) simulations show (**a**) agreement of dynamical regimes for weak interactions and (**b**) a GPE failure to predict self-trapping for strong interactions. (**a**) Larger barrier heights $V_0 = 1, 2$, and 5 are self-trapped for $J = 1$ and $U = 0.3$, and the low barrier $V_0 = 0.2$ is in the Josephson regime. (**b**) For $J = 1$ and $U = 30$, TEBD results (solid) predict self-trapping for a barrier height of $V_0 = 5$ whereas GPE results (dashed) predict Josephson oscillations for all barrier heights.

The final figure of our Fock space focuses on what appears to be soliton formation. Specifically, in the Josephson regime with strong repulsive interactions, particle-hole pairs form as excitations of a Mott insulator, seen as the bright and dark vertical bands in Figure 4.7.

The very dark band in the center is a density minimum due to the barrier. For $V_0 = 0.2$, with $J = 1$, $U = 30$, the double well has 27 sites, and the number of particles for each plot is (**a**) 12, (**b**) 13, (**c**) 14, and (**d**) 15. The magnitude of the quasiparticles, or the number separation between bright and dark bands, is larger closer to the edge walls compared with the quasiparticle magnitude in the center of the wells; we attribute this outcome to the counteraction of the double well boundaries, which asserts an effect akin to compressing an accordion. The smaller particle numbers, such as (**b**) and (**c**), display greater repulsion from the edge boundaries on sites 0 and 54. The larger particle numbers show the opposite effect and collide more directly with the walls due to the larger superfluid fragment sloshing between the wells. The solitons form for particle numbers immediately above or below commensurate filling. In this case, (**a**) has 12 particles and (**d**) has 15 particles, and the 13 and 14 particle cases are both relatively commensurate because of the thin barrier. The commensurate-filling plots do not demonstrate any soliton behavior, though the 14-particle case, perhaps closest to unit filling, illustrates the superposition of the superfluid fragment and the particle-holes when the quasiparticles disappear for brief regions in between macroscopic sloshing. The solitons in (**a**), beginning from site 12 in the left well and 21 in the right well, are 180 degrees out of phase from the solitons in (**d**) beginning from sites 5 and 14. Both plots show the same soliton oscillation magnitude of about 9 sites, indicating there may be number symmetry about commensurate filling. The antisymmetric nature of the solitons on opposing sides of the barrier, as they propagate in parallel, provides a striking contrast to the double well symmetry.

We identify these excitations as solitons because (i) they move at a velocity of about half the sound speed, (ii) they survive multiple collisions with the barrier as well as motion in the effective potential created by the accordion-like compression of the particle-hole background, and (iii) they occur only for particle numbers incommensurate with the number of lattice sites in the well. The point of (iii) is that the extra particles above the Mott insulating background create a superfluid film or skin in the "wedding cake" structure well-known from

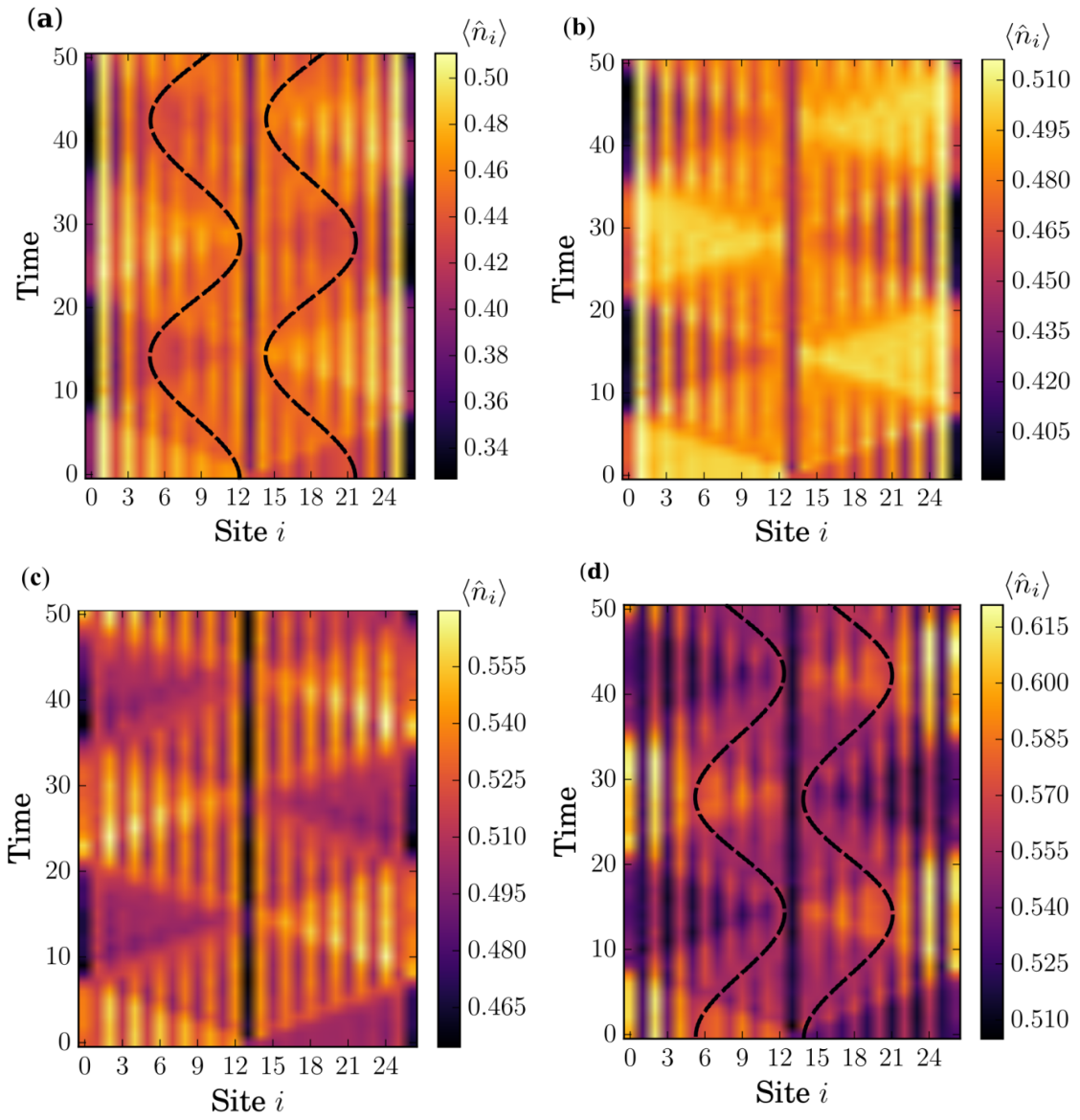

Figure 4.7: *Emergent solitons counter the double well symmetry.* In the Josephson regime, (**a**) and (**d**) show pairs of propagating solitons – one in each well – potentially manifesting with a dressing of particle-hole pairs. In the plots, they appear as blurred sinusoids with a color halfway between the bright particles and the dark holes. The 27-site system has $V_0 = 0.2$, with $J = 1$, $U = 30$. The filling factor is not precise due to the presence of the barrier, so (**b**) 13 and (**c**) 14 particles are close to unit filling and do not exhibit soliton formation. Slightly (**d**) $N = 15$ above or (**a**) $N = 12$ below commensurate particle numbers seem to provide a ripe environment for these solitons, which oscillate in unison and against the mirror symmetry of the junction.

other studies of the Bose-Hubbard model [190]. There is also some precedent for solitons in the particle-hole limit in a related context to the one here [191]. Finally we point out that in simulations doubling the number of particles and the number of sites we saw the same kind of solitons form, showing that this effect depends on the density, not the number of particles.

4.3.3 Dynamic regimes and correlation measures

Beyond local particle numbers, we also examine correlation measures that highlight some advantages of matrix product state methods. For example, one method of identifying the superfluid-Mott phase transition is by tracking the depletion of the condensate, $D = 1 - \lambda_1/(\sum_i \lambda_i)$, where the sum is over the L eigenvalues of the SPDM, $\lambda_1 > \lambda_2 > \ldots > \lambda_L$, and taking the maximum $|\delta D|$ over a J/U parameter quench as the critical point. The depletion gauges the amount of quantum gas living outside the BEC ground mode: λ_1 is this BEC mode, or the dominant eigenvalue of the SPDM, and the sum is over all eigenvalues of the single particle density matrix. The less depleted the condensate, the more superfluid the behavior will be. We emphasize that mean-field calculations cannot account for this many-body effect, with $D = 0$ always.

We now consider the depletion of the left well for the same system size as in Figure 4.2, 15 sites and 7 particles. In Figure 4.8(**a**), we first address a system of non-interacting atoms, $U = 0$, and the oscillations approach the Rabi limit for small barriers. The energy ratio ζ confirms that $V_0 = 2, 3, 4$, and 5 are all self-trapped. The curve for $V_0 = 1$ displays a dynamic empirical signature of the symmetry-breaking transition: the dynamics exhibit critical growth as the condensate depletes over time without returning to its initial condition. This divergence of the depletion from its initial condition is also seen in Figure 4.8(**b**) near the critical point $V_0 = 1$, and this divergence diminishes the farther the barrier height is from its critical value.

In addition, Figure 4.8(**a**) and (**b**) are uniformly initialized in the superfluid regime, but as the dynamics progress, higher barriers induce either oscillations or decays into more

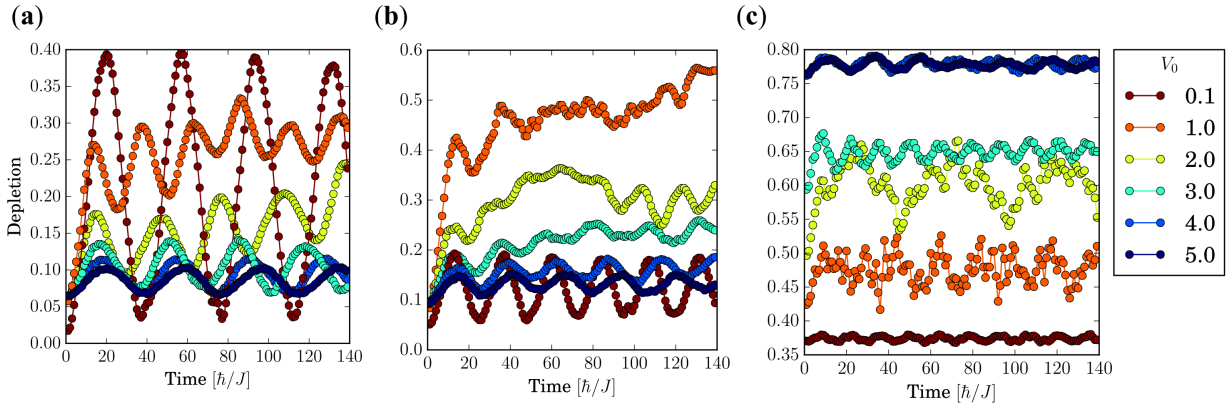

Figure 4.8: *Condensate depletion dynamics.* We consider a double well of 15 lattice sites and 7 atoms, and (**a**) the non-interacting case $J = 1$ and $U = 0$ most closely resembles Rabi oscillations, (**b**) the weakly-interacting case $U = 2$ passes from Josephson to self-trapping at $V_0 = 1$, and (**c**) the strongly-interacting case $U = 15$ is self-trapped for $V_0 \geq 4$. While the dynamics do not necessarily maintain the Mott or superfluid integrity they start with, (**c**) the Mott gap appears to influence the nearly fixed amount of the depletion when interactions are strong, as compared to the superfluid case.

depleted states. In such cases, the systems are no longer strictly superfluid, nor are they in a Mott state. However, this initial state does influence the dynamics. For example, the initial depletion for superfluid states is continuous, while for the initial Mott states of Figure 4.8(**c**), the initial depletion is quantized, which is a signature of strong interatomic interactions. The energy ratio ζ_{MB} confirms the highly-depleted states of $V_0 = 4$ and 5 are self-trapped, and even the Josephson $V_0 = 0.1$ dynamics are substantially depleted due to the Mott influence.

The remaining figures demonstrate second order correlations via the $g^{(2)}$ measure, which we choose due to its accessibility in experiments [192]. The $g^{(2)}$ correlators quantify the fluctuation of particles for lattice sites i and j such that $g^{(2)}_{ij} = \langle \hat{n}_i \hat{n}_j \rangle - \langle \hat{n}_i \rangle \langle \hat{n}_j \rangle$. A positive $g^{(2)}$ means that the expectation value of measuring two particles simultaneously at sites i and j is larger than that of measuring the individual particles sequentially and vice versa. All $g^{(2)}$ plots have a minimum resolution of a single lattice site. These fluctuations are an important measure for determining limits of mean-field theory and provide insight into the overlapping nature of the two phase transitions. We use the standard normalization for optical lattices as opposed to quantum optics. In lattices because only a small number of on-site number

states are allowed, and the average occupation $\langle \hat{n}_j \rangle$ can be very small in places, one can get near-divergences in the usual normalized quantum optics $g^{(2)}$.A detailed discussion of this choice can be found in [152].

Figure 4.9 delineates half of a period of Josephson oscillation in the weakly-interacting regime for a larger system size with 55 lattice sites, 27 particles, $V_0 = 0.2$, $J = 1$ and $U = 0.3$; in the first panel (**a**) at time $t = 1$, fluctuations are, unsurprisingly, strongest in the left well where the condensate is initialized and decrease smoothly into the right well prior to collision with the far right wall. After this reflection, (**b**) a diffraction pattern emerges at $t = 5$ for fluctuations $g^{(2)} \approx 4 - 9$. The reflected fluctuations (**c**) at $t = 10$ create interference patterns both for the more highly-entangled regions within the two wells when $g^{(2)} > 0$, and the non-entangled correlations between the two wells when $g^{(2)} < 0$. (**d**) As the BEC begins to macroscopically tunnel to the right well at $t = 20$, the negative fluctuations of the off-diagonals deepen, while the off-diagonals near the far left and right walls approach zero. (**e**) This trend continues for $t = 40$ as the BEC collides with the right wall: the contrast of the off-diagonal pattern deepens from $g^{(2)} = -10$ to 6. These positive fluctuations for correlations between sites $\sim 42 - 54$ and $\sim 0 - 18$ are likely due to momentary accumulation along the outer walls. Finally, (**f**) for $t = 60$, the BEC largely occupies the right well, completing a half-period of the Josephson oscillation.

Figure 4.9: *Superfluid number fluctuation snapshots in the Josephson regime.* For a junction with 55 sites and 27 particles, a barrier height of 0.2 and weakly-repulsive interactions, $J = 1$ and $U = 0.3$, number fluctuation dynamics convey superfluid Josephson transmission from (**a**) time $t = 1$ in the left well to (**f**) $t = 60$ in the right. At (**b**) time $t = 5$ and (**c**) $t = 10$, interference patterns develop from reflections off the barrier and at (**d**) $t = 20$ the strong on-site or positive fluctuations begin to pull the off-site negative fluctuations away from the edges and toward the barrier. This creates the striped pattern (**e**) at $t = 40$. (**f**) The BEC at $t = 60$ predominantly occupies the right well. The large magnitude of the correlations is due to large superfluid occupation and thus long-range phase coherence.

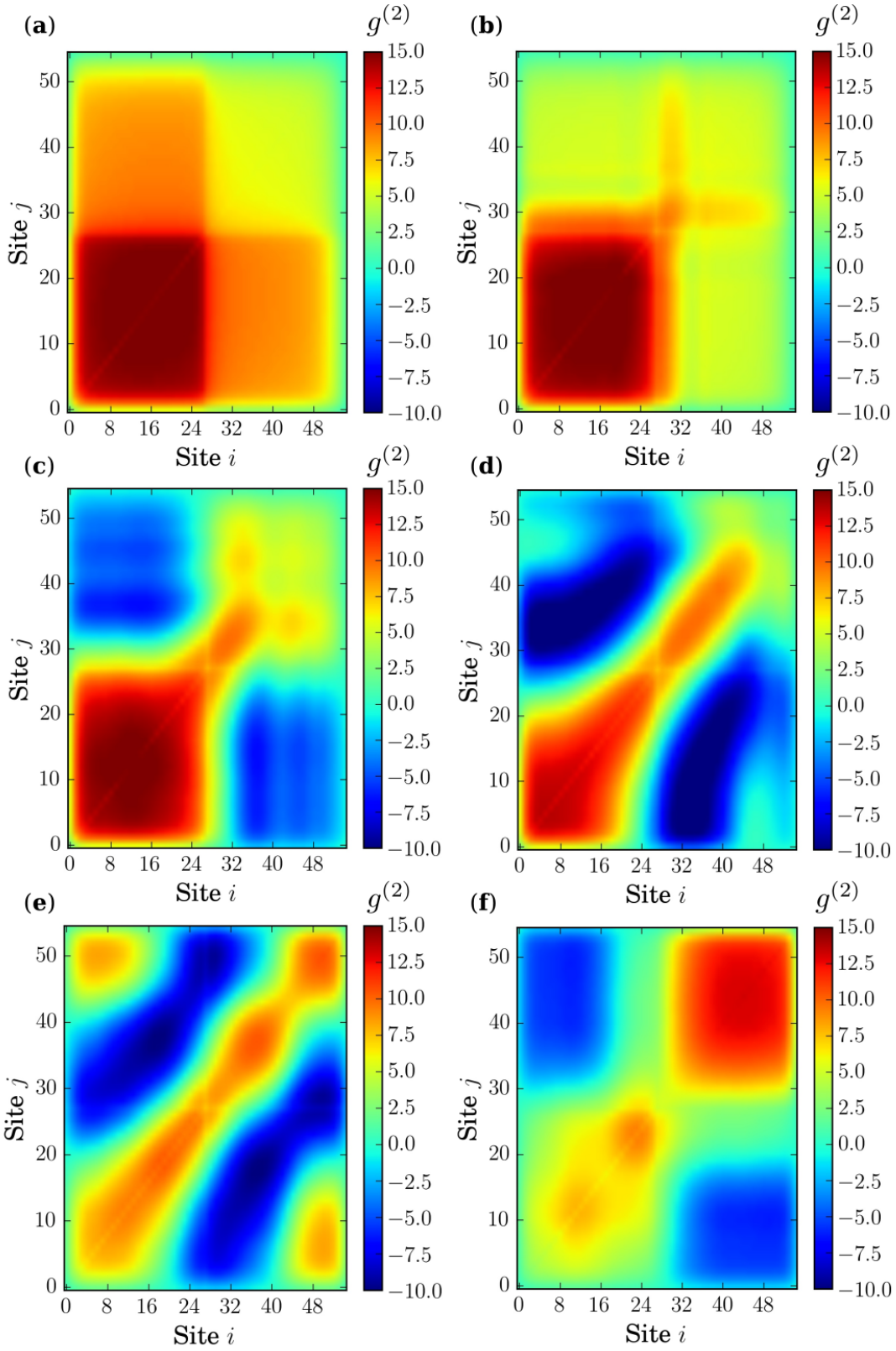

Figure 4.9: *Superfluid number fluctuation snapshots in the Josephson regime.*

The next series of $g^{(2)}$ plots in Figure 4.10 portray the time evolution for a self-trapped BEC as the transmitted fluctuations interact with the barrier, which is at site 26. The system size, particle number, and J and U values are the same as in the previous Figure 4.9, the difference being the barrier has been raised to 1 and the condensate is in the Fock regime. The BEC is initially trapped in the left well (**a**) at $t = 1$; then, transmission of the fluctuations through the barrier region produces diffraction patterns seen (**b**) at $t = 5$ and (**c**) at $t = 10$. The final panel (**d**) $t = 20$ reveals an additional interference and more intense fluctuations from the rebound off the far right wall.

Moving to strongly-interacting systems, Figure 4.11 illustrates a dissemination of the initial concentration of close-neighbor fluctuations in the left well (**a**) at time $t = 1$. The system is the same size of 55 lattice sites and 27 particles, with $J = 1$, $U = 30$, and $V_0 = 1$. By (**b**) $t = 5$, the number fluctuations have congregated in the right well, slightly weaker than the left. Because the junction is near the $\mathbb{Z}_2$ critical point, the fluctuations begin to equilibrate between the two wells without macroscopic oscillations. The magnitude of $g^{(2)}$ in this regime is substantially lower than in the superfluid cases of Figure 4.9 and Figure 4.10, meaning these fluctuations may be more difficult to measure in experiment. For (**c**) $t = 10$ and (**d**) $t = 20$, we compare the fluctuations with Figure 4.5(**b**) at the same time, as it is the same system. The extra fluctuation bands appear at $t = 10$ time because of a collision of the superfluid fragment with the far left boundary, and a smaller superfluid fragment collides with the far right wall. Because the population imbalance still favors the left well and the system is in a Fock regime, the symmetry is broken, which makes the mirror symmetry of the number fluctuations more surprising.

Finally, the *Fock flashlight* develops highly-localized nearest-neighbor correlations in the left well and weaker, delocalized correlations in the right well. For a double well with $J = 1$, $U = 30$, and $V_0 = 5$, the result is (**a**) $t = 1$ the hilt of the flashlight comprises the self-trapped Mott insulator and the bright spot in the right well is immediately present – another possible effect of the diabatic quench. Panel (**b**) at $t = 5$ and (**c**) at $t = 10$ exposes a

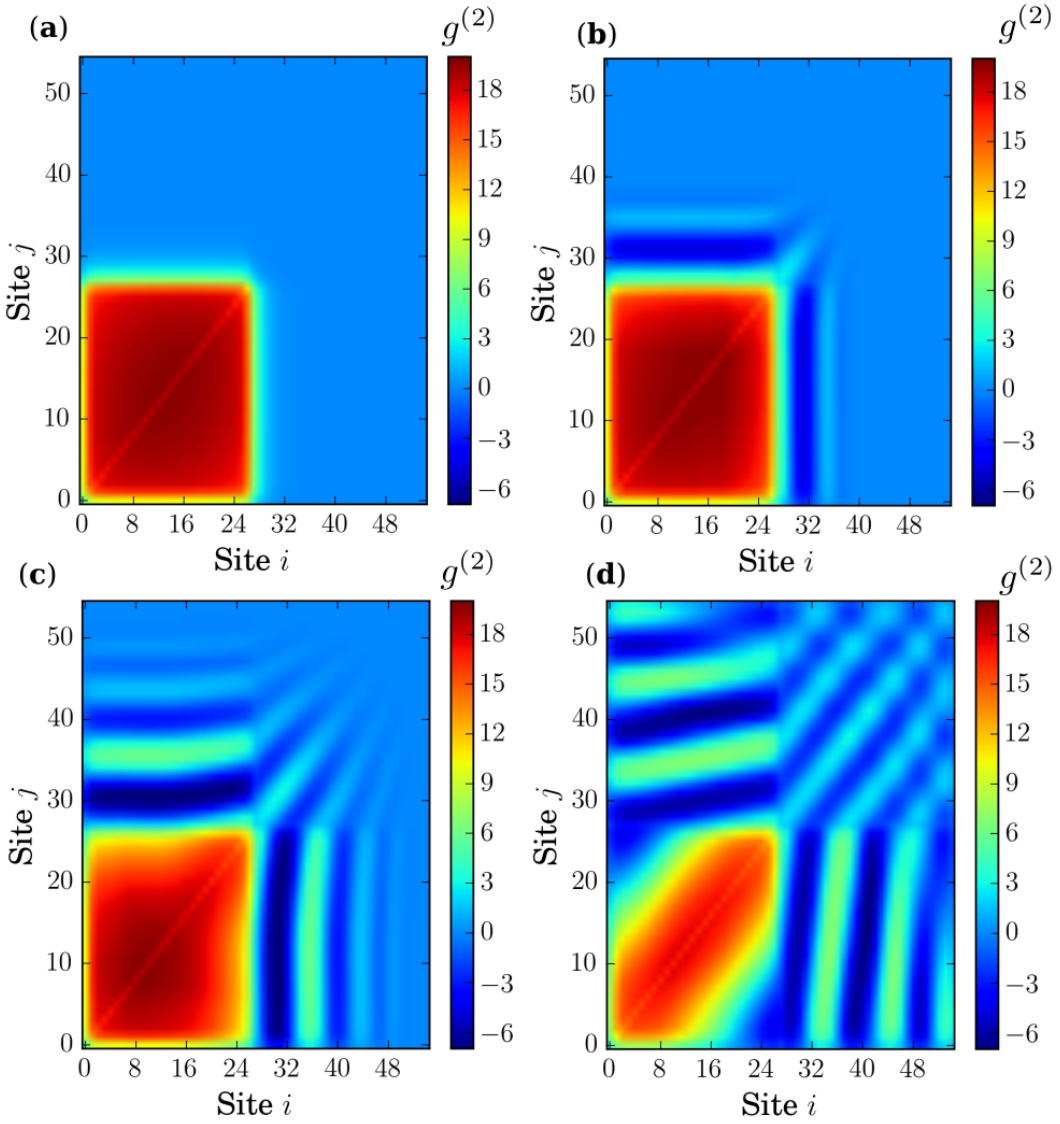

Figure 4.10: *Self-trapping fluctuation diffraction.* Interference patterns arise as the BEC slowly begins to escape the confines of the left well. $J = 1.0$ and $U = 0.3$ for a double well with 55 sites and 27 particles and barrier height $V_0 = 1.0$. As time evolves, (**a**) $t = 1$, (**b**) $t = 5$, (**c**) $t = 10$, (**d**) $t = 20$, the diffraction contrast deepens, but the macrosopic tunneling escape rate is much slower than the time scale of the experiment. Again, as the bosons are weakly-interacting, the long-range coherence leads to an increase in positive correlation magnitude.

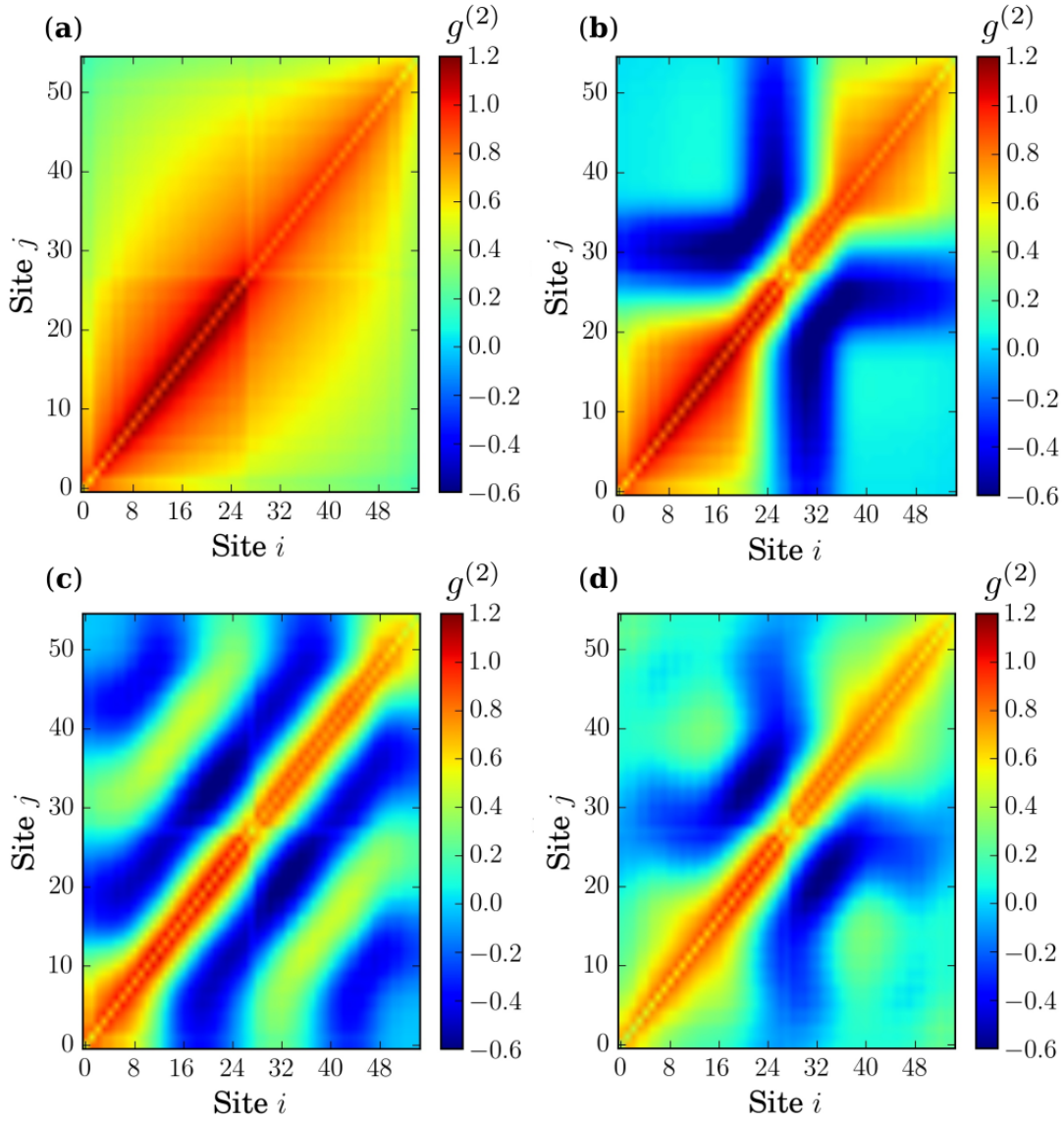

Figure 4.11: *Symmetric fluctuations near the self-trapping critical point.* With strong interactions and barely into the Fock regime, $g^{(2)}$ number fluctuations spread from the left to right well before reaching a meta-stable equilibrium, where the on-site fluctuations are approximately even in both wells. $J = 1$ and $U = 30$ for a junction with 55 sites and 27 particles and barrier height $V_0 = 1$. (**a**) $t = 1$, (**b**) $t = 5$, (**c**) $t = 10$, (**d**) $t = 20$.

familiar diffraction phenomenon, where positive number fluctuations build within the right well and collide with the barrier. Also at $t = 10$, the flashlight begins growing an off-diagonal crossguard of Mott-like bright and dark bands that propagate symmetrically from the barrier toward the walls at (**d**) $t = 20$. For (**e**) $t = 30$, they have reflected off the external potential walls and by (**f**) $t = 60$ they have begun to dissipate except directly along the barrier and the walls, where they have accumulated. The junction is smaller, 27 sites and 14 particles, because the strong interactions and high barrier required to observe this regime required a large bond dimension in TEBD, as we determined from convergence studies, so the larger system size was computationally intractable.

Figure 4.12: *The Fock flashlight effect.* The Fock flashlight forms for strongly-interacting, self-trapped bosonic Josephson junctions. In this case we use a smaller system size of 14 particles on 27 sites due to larger computational demands for convergence. The barrier height is large $V_0 = 5$, with $J = 1$, and $U = 30$. (**a**) At time $t = 1$, the fluctuations are highly localized in the left well and delocalized in the right well, creating the appearance of a flashlight. (**b**) The fluctuations begin to disperse by $t = 5$, and for (**c**) $t = 10$, (**d**) $t = 20$, and (**e**) $t = 30$, fluctuations propagate from the barrier outward as bright and dark bands on the anti-diagonal as fluctuations tunnel out of the right well and create vertical and horizontal diffraction bands. (**f**) Finally, by $t = 60$, these flucutation patterns are dissipating save for the nearest-neighbors in the left well, where the bosons remain self-trapped. Strong interactions suppress long-range coherence, and thus the magnitude of the correlations is much smaller than in the weakly-interacting case.

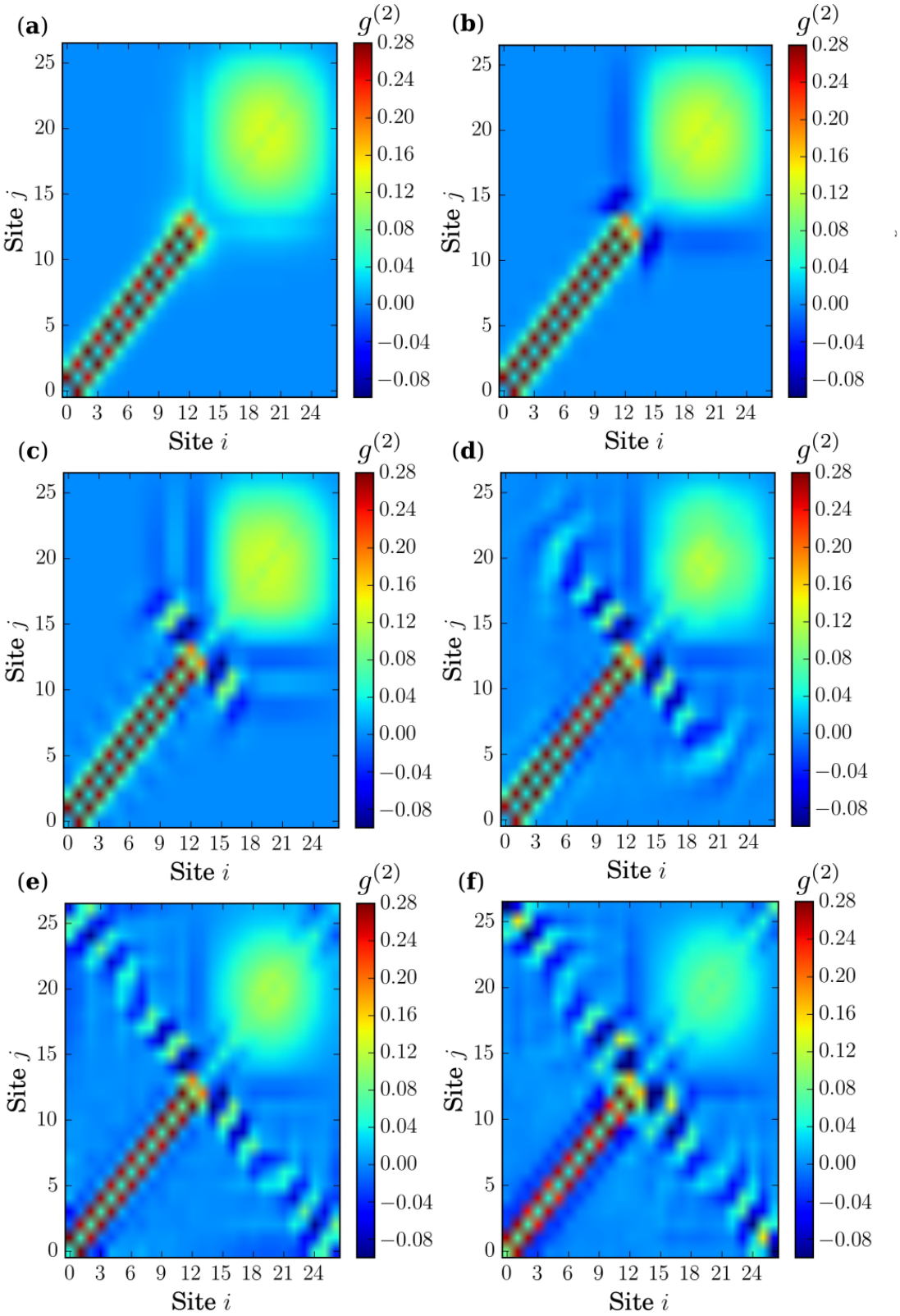

Figure 4.12: *The Fock flashlight effect.*

4.4 Materials and Methods

4.5 Time-evolving block decimation

Figure 4.1 depicts the method we use to simulate a reproducible initial state for double well dynamics. We first run imaginary time propagation using time-evolving block decimation (openTEBD) [4]; the right well of the potential is raised as shown in Figure 4.1(**a**). This provides an exponential decay in imaginary time rotations of the unitary operator that allows the high energy states to decay quickly, leaving us with the ground state of the potential largely occupying the left well. We then lower the right side of the double well at time $t = 0$ as in Figure 4.1(**a**), so we no longer have a stationary state, and propagate forward in real time. We choose this protocol for similarities with experiment [104] and for easier reproducibility.

The total error from the simulations can be written $\epsilon = \epsilon_{\text{method}} + \epsilon_{\chi}$, where ϵ_{method} is due to a combination of errors, the largest of which are the errors due to Trotter decomposition as well as that due to local dimension restrictions. ϵ_{χ} stems from the Schmidt truncation, which is due to truncation of the Hilbert space. From detailed convergence studies, we estimated the local dimension, d = max filling + 1, the bond dimension χ, and the real and imaginary timesteps. We studied convergence of the dynamics as a function of local dimension, bond dimension, and time step. The low-barrier regime with weak interactions required small time steps, on the order of 10^{-4}, and the high-barrier regime with strong interactions required large bond dimension, on the order of $\chi = 100$ for the 27-site system. This slow convergence for the strongly-interacting Fock regime appears to indicate high entanglement that pushes the limits of matrix product state simulations.

The open source openTEBD software can be downloaded from sourceforge.net [4], however, the authors strongly encourage consideration of open source matrix product state methods (OSMPS), also available on sourceforge.net [5] as a more up-to-date simulation tool [143, 193, 194].

4.6 Gross-Pitaevskii equation

The Gross-Pitaevskii equation is a mean-field description of cold and dilute Bose gases. This description assumes a perfectly condensed state, ignoring fluctuations about the mean such that the depletion is always zero. A quasi-1D GPE is given by,

$$i\hbar\frac{\partial}{\partial t}\Psi(x,t) = \left[\frac{-\hbar^2}{2m}\frac{\partial^2}{\partial x^2} + V(x,t) + g_{1\mathrm{D}}|\Psi(x,t)|^2\right]\Psi(x,t). \tag{4.6}$$

where tight harmonic confinement has been assumed in the transverse directions [82]. The order parameter, Ψ, corresponds to the single-particle wave function. The nonlinear interaction parameter, $g_{1\mathrm{D}}$, is proportional to the s-wave scattering length, and results from assuming binary contact between atoms; note, from Table 4.1, $g_{1\mathrm{D}} = g/2\pi\ell_\perp^2$, with transverse harmonic oscillator length $\ell_\perp = \sqrt{\hbar/m\omega_\perp}$, where $\hbar$ is the reduced Plank constant, m is the atomic mass, and $\omega_\perp$ is the transverse confining angular frequency.

Numerics are computed on a discretized version of Equation (4.6), called the Discrete Nonlinear Schrodigner Equation (DNLS),

$$i\hbar\frac{d}{dt}\psi_i = -J(\psi_{i+1} + \psi_{i-1}) + g_{1\mathrm{D}}|\psi_i|^2\psi_i + V_i\psi_i, \tag{4.7}$$

where J, V_i, and $g_{1\mathrm{D}} = U$ correspond to the values given in Table 4.1. In the DNLS, $|\psi_i|^2$ corresponds to the expectation value of $\langle\hat{n}_i\rangle$ on site i, we normalize to the number of particles $\sum_{i=1}^{L}|\psi_i|^2 = N$, and L is the number of lattice sites. The DNLS can also be derived from a mean-field approximation of the BHH, or a direct discretization of the GPE [81].

Similar to many-body dynamics, an initial ground state is calculated using imaginary time propagation on a single potential well, Figure 4.1(**a**), and real time propagation with the barrier well dropped as in Figure 4.1(**b**). Imaginary time propagation is calculated using the fourth-order Runge-Kutta method, and real time propagation is performed with the LSODA implementation in SciPy [195], as originally described in [196]. This algorithm automatically chooses between the Adams-Bashforth method (an explicit numerical method) for non-stiff time evolution and backward differential formula (BDF) method (an implicit numerical method) for stiff evolution. This scheme was used because the dynamics for larger

U, V_0, and, N occasionally require time-steps so small as to be computationally restrictive for explicit methods, in other words the problem behaves as a stiff differential equation. Because it is difficult to know when exactly the equations are stiff, the automatic selection scheme only uses the computationally more intensive BDF method when necessary.

4.7 Sudden Approximation

For strongly-interacting systems in the Josephson regime, particle-hole pairs form immediately as bright and dark bands. They form too quickly for atoms to propagate across the lattice, and they are instead due to the diabatic quench of the potential from a single to a double well. To support this hypothesis, we perform analytical sudden approximation calculations using exact diagonalization together with second-order perturbation theory. The calculations also support an analogous phenomenon that occurs in the Fock regime: the sudden projection of the single well ground state to the double well excites macroscopic modes of the double well.

We perform the calculations on manageably small system sizes for both even and odd numbers of sites, one for 2 particles on 4 sites and the other 3 particles on 5 sites. We implement the sudden quench by projecting the Fock basis of 2 sites onto 4 sites and 3 sites onto 5 sites. The purpose is to demonstrate the immediate response of the initial state to such a quench. For example, for the 4-site case, we do the calculation three ways: (i) we use the ground state of the 2-site system for $J = 0$, or an initial state $|\,1\ 1\ 0\ 0\,\rangle$, (ii) we use a ground state that is a superposition of the possible states for the 2-site system, $\alpha_1|\,2\ 0\,\rangle + \alpha_2|\,1\ 1\,\rangle + \alpha_3|\,2\ 0\,\rangle$ for small, finite J; (iii) we use degenerate perturbation theory for pertubative tunneling, which agrees with the exact diagonalization of method (ii). In all cases, we take $J = 1$ and $U = 30$ so as to focus on the strongly interacting regime.

In the 4-site case for method (ii), we first calculate the eigenvectors for the $L = 4$, $N = 2$ system and the ground state of the $L = 2$, $N = 2$ system using exact diagonalization, which provides a good initial state for the dynamics. Then for unitary time evolution, the only non-zero elements are from $L = 4$ eigenvectors that have any superposition with the initial

state, which in the new basis is a superposition of $|\,2\ 0\ 0\ 0\,\rangle$, $|\,1\ 1\ 0\ 0\,\rangle$, and $|\,0\ 2\ 0\ 0\,\rangle$. We project the eigenvectors of the 10-dimensional $L = 4$ Hilbert space onto the basis vectors to create number density vectors for each of the 4 lattice sites, which provides a common ground for comparison with TEBD simulations. The error in the calculations is due to the approximation itself, which assumes a perfect projection from the $L = 2$ basis to the $L = 4$ basis; this simple projection does provide insight into the diabatic quench in TEBD and its influence on exciting modes in the dynamics. These modes manifest as Fock states $|\,1\ 0\ 1\ 0\,\rangle$ and $|\,0\ 1\ 0\ 1\,\rangle$ and can be seen in Figure 4.13 as the smaller, nonlinear spikes between the larger oscillations. These Fock states, while by definition are not particle-hole pairs due to the limited particle number, support the propensity for the formation of local states of the same symmetries such as those in Figure 4.5(**a**) and (**b**) and Figure 4.7 – i.e. particle-hole pairs. In method (iii), we calculate the eingenvectors instead with perturbation theory in the large U limit and obtain qualitatively the same result. Method (i) was unsuccessful in demonstrating the dynamics because the initial state was purely the Mott ground state of the 2-site system $|\,1\ 1\ 0\ 0\,\rangle$; this approximation is insufficient because the accordion-like excitations will only form for non-zero J.

The same methods were applied to the $L = 5$ case. The odd number of sites case makes an important difference in the dynamical excitations as compared to the $L = 4$ case: even without an explicit barrier, we see mode formation on two distinct sides of the single well. The Fock state $|\,0\ 3\ 0\ 0\ 0\,\rangle$ is clearly an excited mode of the first 3 sites, with an even symmetry among these 3 sites. Although this state is energetically improbable, the overlap of the 3-site basis with the 5-site basis places a weight on the first 3 sites that over-emphasizes this projection compared with TEBD. However, the presence of an excited mode of one side of the potential supports the instanteous excited mode creation in Figure 4.5(**c**). The number density state $|\,0\ 1\ 0\ 1\ 1\,\rangle$ further supports this conclusion, as the boson on the second site demonstrates the same symmetry as a ground mode for these first three sites, and the particles on sites 4 and 5 are Mott ground states of these last two sites; thus, the

dynamics appear to manifest through excited modes of each side of the well. We further note the importance of symmetry when recognizing such manifestations of excited modes, as an even L with the barrier breaks the pairing tendency and injects an extra level of excitation. The same argument holds for excited modes of the overall potential.

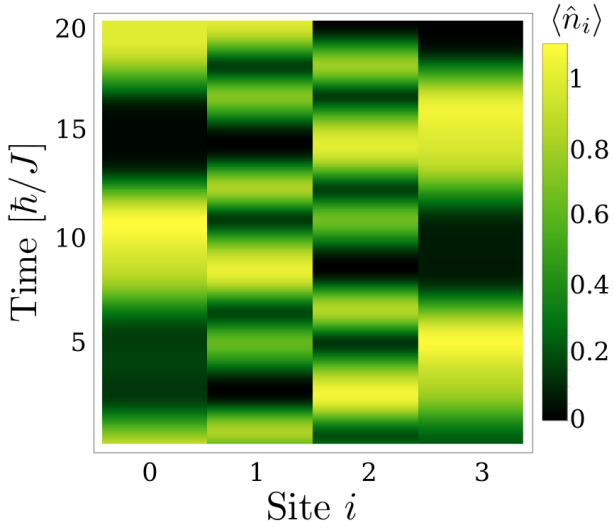

Figure 4.13: *Sudden approximation demonstrates propensity for excited mode formation.* Analytical dynamics calculated with the sudden approximation and exact diagonalization on a system of 2 bosons on 2 sites projected onto 4 sites with $J = 1$ and $U = 30$. Unsurprisingly, the overall dynamics oscillate back and forth within the well. It is the more microscopic behavior, though, that yields insight into the accordion-like effects we see in TEBD simulations. The smaller peaks depict excited modes $|\,1\ 0\ 1\ 0\,\rangle$ and $|\,0\ 1\ 0\ 1\,\rangle$ that demonstrate a preference for mode formation with the same symmetry; this symmetry applies both on the optical lattice scale – as particle-hole pairs – and on the scale of the potential as a whole – as excited modes of the double well.

4.8 Conclusions

In conclusion, we have computationally demonstrated comparisons of mean-field and many-body dynamical regimes based on the interplay of the Mott–superfluid U(1) and the Josephson–self-trapping quantum $\mathbb{Z}_2$ phase transitions (QPTs) in a bosonic Josephson junction. Using initial state information, we design a many-body energy ratio to predict these dynamical regimes; and we find that mean-field theory breaks down as the repulsive interaction strength increases and fails to predict the spontaneous symmetry-breaking transition.

Additionally, we identify a number of strictly many-body phenomena in these dynamical regimes that increase in importance for higher-precision applications: long-lived particle-hole pairs and low-lying double well modes arise due to a sudden quench of the potential and can act as signatures of QPTs - even in mesoscopic systems experimentally accessible on present quantum simulator platforms [197]. Other many-body signatures include soliton formation in the Josephson regime and the $g^{(2)}$ Fock flashlight in the self-trapping regime: these effects manifest in quantities that are measurable experimentally in architectures ranging from cold atoms to nonlinear optics to superconductors. While our present study is discrete by nature of the optical lattice, future work can build on the results in the strongly interacting case by systematically increasing the number of lattice sites toward the continuum limit, for instance in a Tonks-Girardeau gas [149, 198–200]. Further extensions of this research would incorporate fermions for a more encompassing unification with superconductors [201, 202]. With the number of applications relying on two-mode models of the double well, the present study encourages investigation of cold atom double well experiments with optical lattices as highly-controllable quantum simulators of many-body effects in systems previously assumed to be mean-field.

4.9 Acknowledgements

The authors extend appreciation and gratitude toward Verónica Ahufinger and Anna Sanpera for inspiration and collaboration in the conception of these studies. Many heartfelt thanks also to Daniel Jaschke, Gavriil Shchedrin, and Meenakshi Singh for insightful discussions and new perspectives. Computations were performed using high performance computing resources at the Colorado School of Mines in conjunction with the Golden Energy Computing Organization. This material is based in part upon work supported by the US National Science Foundation under grant numbers PHY-1520915, PHY-1207881, PHY-1306638, OAC-1740130, as well as the US Air Force Office of Scientific Research grant number FA9550-14-1-0287. This work was also performed in part at the Aspen Center for Physics, which is supported by National Science Foundation grant PHY-1607611.

CHAPTER 5
MANY-BODY PHASE DIAGRAMS, ENTROPY, ASYMMETRY, AND CONVERGENCE

The goal of this chapter is to highlight results not submitted for publication, but which provide additional insight and/or preliminary results containing substantial open questions. These are original results that, in the case of phase diagrams for the double well and asymmetric well, require further research. Other results, such as entropy, excited mode formation, and convergence studies, are additional to results in chapter 4, for example.

5.1 Ground state phase diagrams

One aim of this dissertation is in part to discern the effects that quantum phase transitions have on the dynamics, particularly, the $\mathbb{Z}_2$ quantum phase transition from Josephson oscillations to a self-trapping phase and the $U(1)$ QPT from a superfluid to a Mott insulator in the BHH. Often the first question that arises when describing quantum phase transitions in quasi-one dimensional potentials revolves around the thermodynamic limit, as the system size and number approach infinite scales. Typically systems are considered to approach the phase transition in this limit, however, the signatures of QPTs are projected onto dimensions below 3D and even in systems with few degrees of freedom. These signatures can actually be so strong as to dominate the dynamics, even in mesoscopic systems experimentally feasible in current quantum simulator architectures [197].

Traditional study of quantum phase transitions often begins with a mapping of the phase diagram calculated from ground states. While the bulk of the work for this dissertation focuses on dynamics, we calculated many-body phase diagrams of the Bose-Hubbard model as an investigation of the influence of the spontaneous symmetry-breaking phase transition in a bosonic Josephson junction of the superfluid to Mott quantum phase transition. The

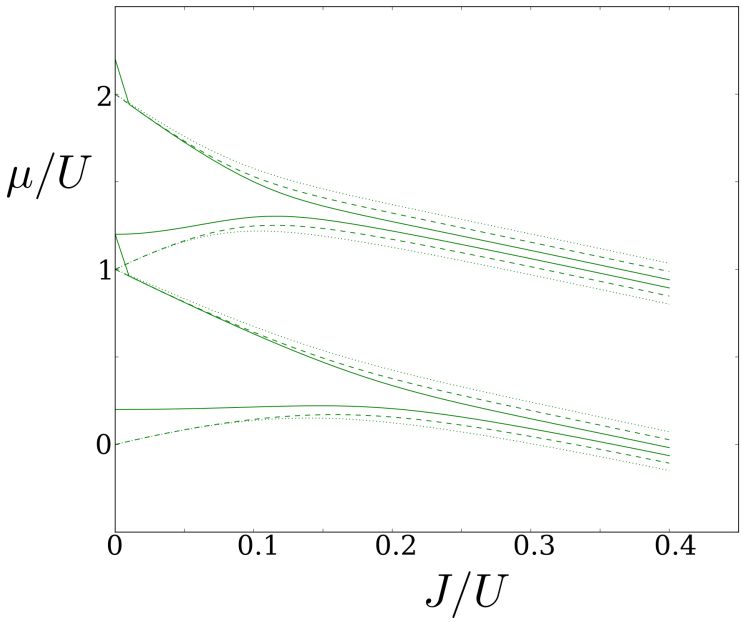

Figure 5.1: *Mott insulator-superfluid phase boundaries for a double well.* Mott lobes with finite barrier demonstrate the issue of determining unit filling. We do not expect crossing phase boundaries for a true Mott insulator. The outer dashed lines represent greater filling factors when determining an estimated chemical potential, with the solid lines depicting unit filling for the lower Mott lobe or twice unit filling for the second Mott lobe.

result is the top half of the Mott lobe exhibits an analyticity for higher barriers of the double well, and the bottom half of the Mott lobe curves upward in the strongly-interacting regime.

Figure 5.1 displays an example of the bizarre cusp in the phase boundaries for the first two Mott lobes for a Josephson junction with 21 lattice sites, 10 in each symmetric well and 1 for the barrier of height $V_0 = 0.2$. The number of particles changes from a filling factor of one, or about 21 particles, for the first Mott lobe to a filling factor of two for the second Mott lobe. The innermost, solid lines, depict an approximate chemical potential $\mu \approx E(N+1)-E(N)$ for the upper boundary and $\mu \approx E(N)-E(N-1)$ for the lower boundary, where N is the average boson occupation per lattice site. The middle, dashed lines represent $\mu \approx E(N+2)-E(N)$ and $\mu \approx E(N)-E(N-2)$, and the outermost dotted lines portray $\mu \approx E(N+3)-E(N)$ and $\mu \approx E(N)-E(N-3)$. The phase diagram of μ/U versus J/U in Figure 5.1 gives an approximation of the chemical potential because the simulations are run as number-

conserving, and thus are in the canonical ensemble. This finite-difference estimation of the chemical potential may be the explanation for the strange cusp-like behavior. Certainly, the influence of the barrier renders a definition of commensurate filling non-exact, and as shown in [190], the "wedding cake" structure from studies of the Bose-Hubbard model allows for Mott behavior for incommensurate fillings.

Next, to determine the influence of the spontaneous symmetry breaking transition on the superfluid-Mott insulator phase diagram, we look at the phase boundaries as a function of barrier height in Figure Figure 5.2. These simulations are run to find ground state energies of the actual double well, as opposed to the initial states used in dynamics simulations. The energies as a function of filling factor, where $N = 1$ is commensurate filling, are used to determine the approximate chemical potential of the phase diagrams as a function of J/U. The system consists of 21 sites, with a local dimension $d = 6$, $U = 1$ and J is swept from 0 to 0.4 with a step size of 0.01; the bond dimension is 25 and the convergence tolerance is 10^{-8}. The previous plot, Figure 5.1, is one particular of these cases, and thus has the same simulation parameters.

5.2 Asymmetric double well

The calculations of the parameters space for both ζ_{MB} and ζ_{MF}, initially shown in section 4.3.1, are for a symmetric double well potential. Prior to running these simulations needed to accurately map the interplay of the barrier height and the interaction strength, we performed the same calculation (not entirely on purpose) of a slightly asymmetric double well, where the barrier was shifted on the lattice by a single site. As symmetry plays a key role in determining both $U(1)$ and $\mathbb{Z}_2$ phase transitions in the double well, adding or subtracting a single site or a single particle drastically changes not only the phase transition, but the dynamics. We see this in the results of Figure 4.7 where shifting the filling by a single particle over 27 lattice sites instigates a soliton. For ζ, the ratio between tunneling and interaction energies, the phase-type diagram shifts considerably from the symmetric case, shown in Figure 5.3. The ratio as a function of interaction strength or lattice depth U/J

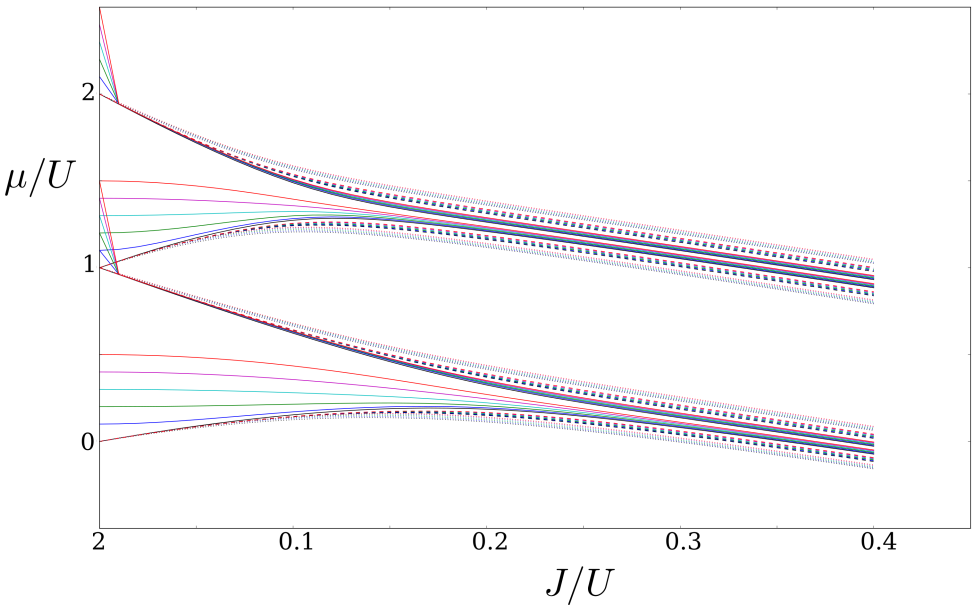

Figure 5.2: *Mott-superfluid phase boundaries for different barrier heights.* The stark cusp on the upper phase boundaries increases with increasing barrier height, especially for the first order chemical potential approximation (solid lines). The higher order estimates show that the Mott regime is not affected by the presence of the barrier. For simulation parameters, see text.

and barrier height V_0 is represented for a double well with 15 total sites and 7 total particles. The resolution in U/J is 1, with $J = 1$ and U from 0 to 15. The resolution in V_0 is 0.5. For small U/J, both ζ_{MB} and ζ_{MF} experience the $\mathbb{Z}_2$ critical region between $V_0 = 0$ and 1, which is a decisive shift from the symmetry case where the critical barrier height is 1. The other major shift occurs in the critical region, which greatly expands in both mean field and many-body cases. The expanded critical region in the many-body case occurs precisely at $\zeta_{\mathrm{MB}} = 1$, whereas the 'critical region' of the mean-field energy ratio is not a critical region at all since the critical point is never reached, indicating a break-down of the mean-field theory. Just as in the symmetric double well case, we find the result that the mean-field measure fails to reach the critical point $\zeta = 1$ for strong interactions and thus does not capture the spontaneous symmetry-breaking transition.

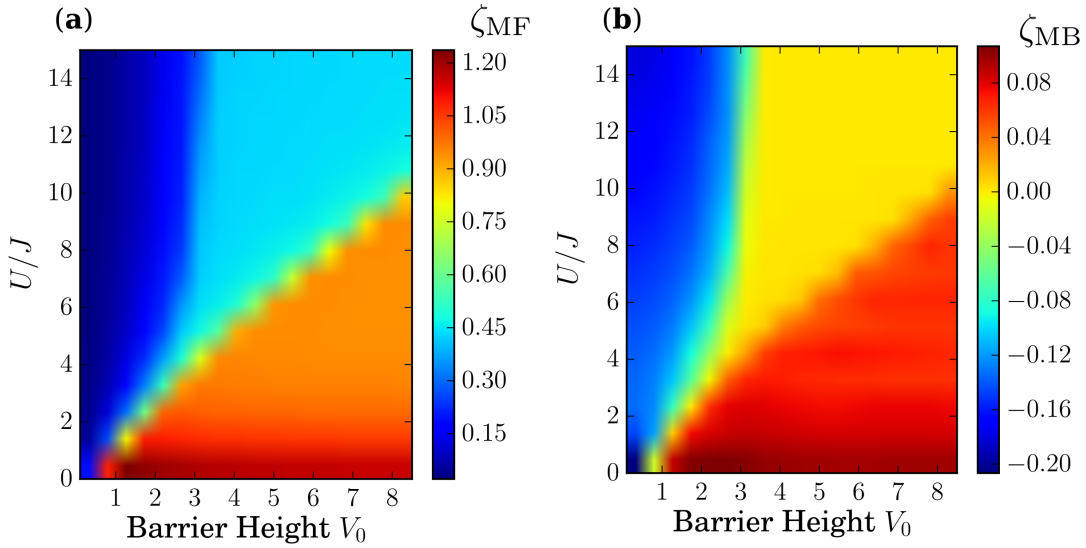

Figure 5.3: *Asymmetric dynamic tunneling regimes.*

5.3 Entropy

For a variety of system sizes and parameters, we investigate the single particle von Neumann entropy, which is calculated from the eigenmodes of the single particle density matrix as $S = -\sum_l (\lambda_l \log \lambda_l)$, where λ_l is the l^{th} eigenvalue of the SPDM. The von Neumann en-

tropy displayed in Figure 5.4 represents the same simulations as the number density plots of Figure 4.5, where the interactions are strong, $J = 1$ and $U = 30$ in a system of 55 lattice sites and 27 particles. For lower barriers, (**a**) $V_0 = 0.5$, we find the same particle-hole pair formation, appearing as lighter and darker vertical bands, that emerges in the number density dynamics. In fact, the magnitude of the von Neumann entropy trends with the number density as well, seen with the darker red in regions of greater boson occupation. These plots that exhibit long-lived regions of higher entropy, specifically for (**b**) $V_0 = 1$ and (**c**) 2, also correspond to the spontaneous symmetry-breaking phase transition critical point, as for larger barrier heights, the system crosses the $\mathbb{Z}_2$ phase boundary. (**d**) For $V_0 = 3$, the system is in the macroscopic self-trapping regime, though the density of the von Neumann entropy decreases as excited macroscopic modes of the double well become more prominent. As mentioned in chapter

The spontaneous symmetry-breaking phase transition for a weakly-interacting bosonic Josephson junction manifests in the von Neumann entropy in Figure 5.5 as a correlation with the number density. For a system with 55 sites and 27 particles, $J = 1$ and $U = 0.3$, we are in the Josephson regime for (**a**) $V_0 = 0.2$ as the superfluid sloshes between wells. There is a backaction of the initial condensate that propels a portion of it against the far left wall, while the other portion begins to tunnel through the barrier immediately. The interference of the condensate with itself begins to give rise to diffraction patterns, especially apparent in regions of lower boson density, such as in the left well around time $60 - 80[\hbar/J]$, where the majority of the bosons have sloshed into the right well. A mild congratulatory remark is also requisite for the reader at this moment for an impressive display of endurance; we encourage you to celebrate with a strong cup of tea. Additionally, the barrier height (**b**) $V_0 = 0.5$ begins to self-trap the atoms as we move into the $\mathbb{Z}_2$ critical region, and the maximum entropy density reaches just above 0.8, where it remains the maximum through the remainder of panels (**c**) for $V_0 = 0.7$ through (**f**) $V_0 = 5$ as the barrier height increases. (**d**) and (**e**) As a larger percentage of the condensate self-traps in the left well for barrier

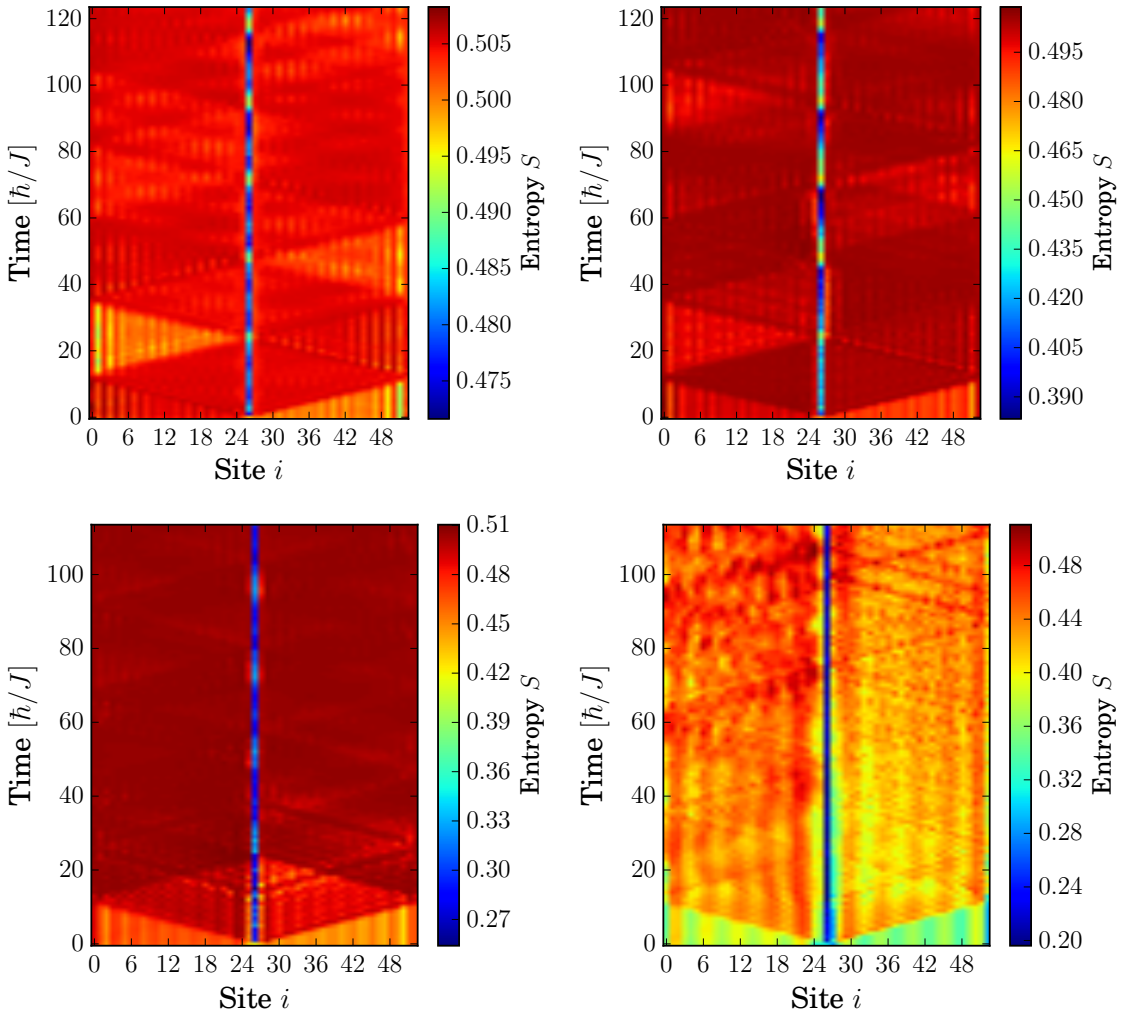

Figure 5.4: *von Neumann entropy for strongly-interacting symmetry breaking transition.* For a double well with 55 sites and 27 particles, $J = 1$ and $U = 30$, the barrier height in each panel is (**a**) $V_0 = 0.5$, (**b**) $V_0 = 1$, (**c**) $V_0 = 2$, (**d**) $V_0 = 3$.

heights $V_0 = 1$ and $V_0 = 2$, respectively, the same diffraction pattern emerges that was seen in Figure 4.4, a reminder of the interferometric nature of the dynamics.

Furthermore, the von Neumann entropy calculation that accompanies Figure 4.7 in Figure 5.6 also provides evidence for the soliton formation in the strongly-interacting Josephson regime, particularly for particle numbers that are ± 1 off commensurate filling. To ensure that this was not a special case, we ran simulations in this regime for a system of $L = 15$ lattice sites and found the same result: the solitons only form when there is one extra boson or one boson removed from unit filling. As mentioned in chapter 4, the solitons form as a superfluid film superposed on the particle-hole insulating background, an exhibition of the well-known "wedding cake" structure of the Bose-Hubbard model for lattices confined with an external trapping potential [190]. The bosonic Josephon junction consists of 27 lattice sites with $J = 1$ and $U = 30$, and particle numbers (**b**) $N = 13$ and (**c**) $N = 14$ are approximately commensurate with a single well and exhibit Josephson oscillations without soliton formation. However, particle numbers (**a**) $N = 12$ and (**d**) $N = 15$ do showcase these long-lived solitons, which propagate through the particle-hole background at about half the speed of sound, surviving multiple collisions with the barrier. This is most extraordinary, though the extreme precision in particle number renders this observation experimentally challenging. There are two of these solitons formed in each figure (**a**) and (**d**), one in each well, and they travel parallel to one another, which surprisingly is in opposite to the mirror symmetry of the double well. While the von Neumann entropy is an additional reference for this many-body feature, it does not necessarily provide additional insight in this case beyond the simulation of the number density dynamics.

5.4 Diabatically-induced excited modes

One result presented in the paper in chapter 4 is the formation of excited modes due to diabatic quenching of the external potential. We attribute the accordion-nature of the strongly-interacting background to the rapid initialization scheme for the dynamics in a bosonic Josephson junction. The sudden approximation, discussed in the analytical methods

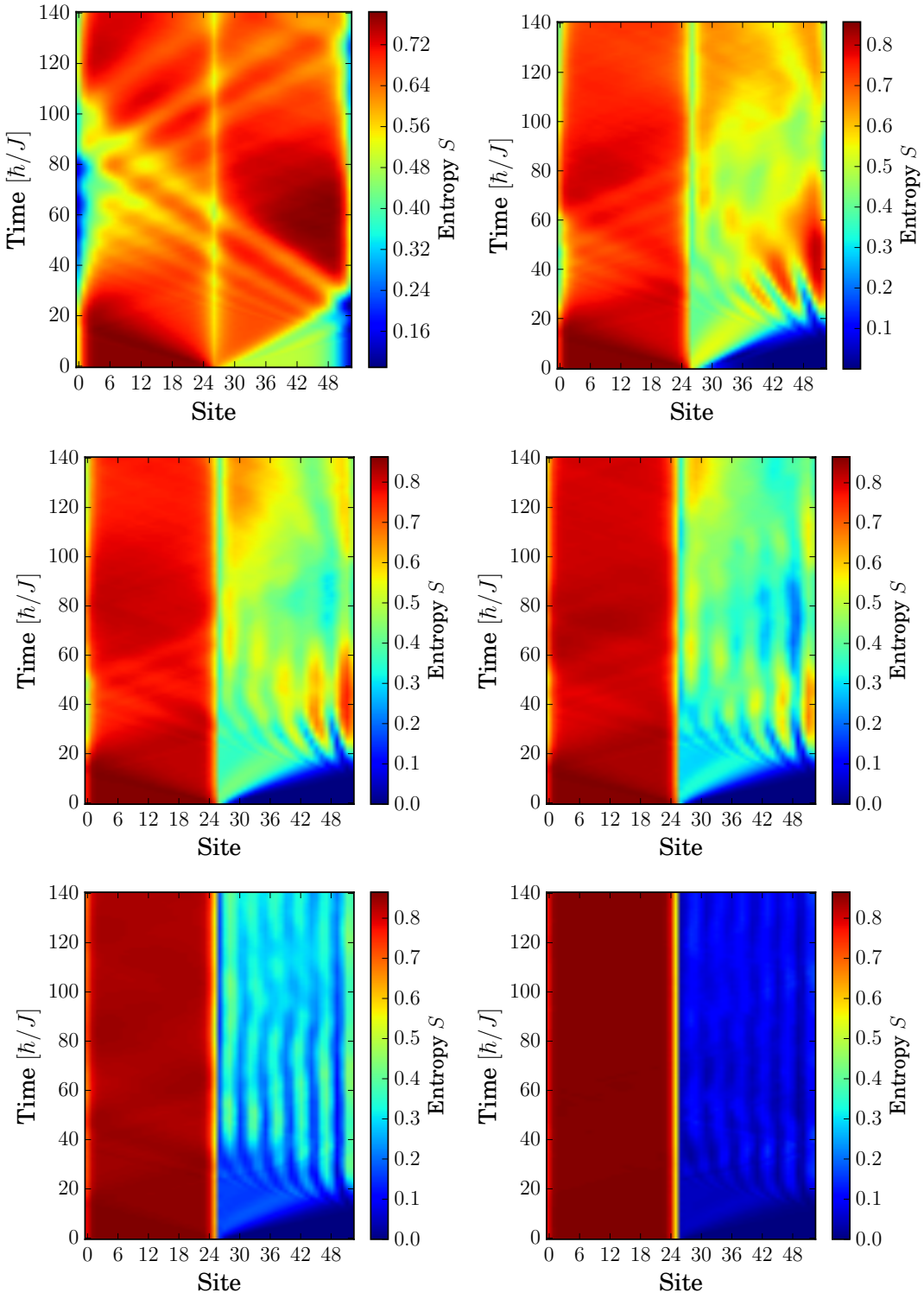

Figure 5.5: *Weakly interacting von Neumann entropy through the Josephson-Fock transition.* For a double well with 55 sites and 27 particles, $J = 1$ and $U = 0.3$, the barrier height in each panel is (**a**) $V_0 = 0.2$, (**b**) $V_0 = 0.5$, (**c**) $V_0 = 0.7$, (**d**) $V_0 = 1$, (**e**) $V_0 = 2$, (**f**) $V_0 = 5$.

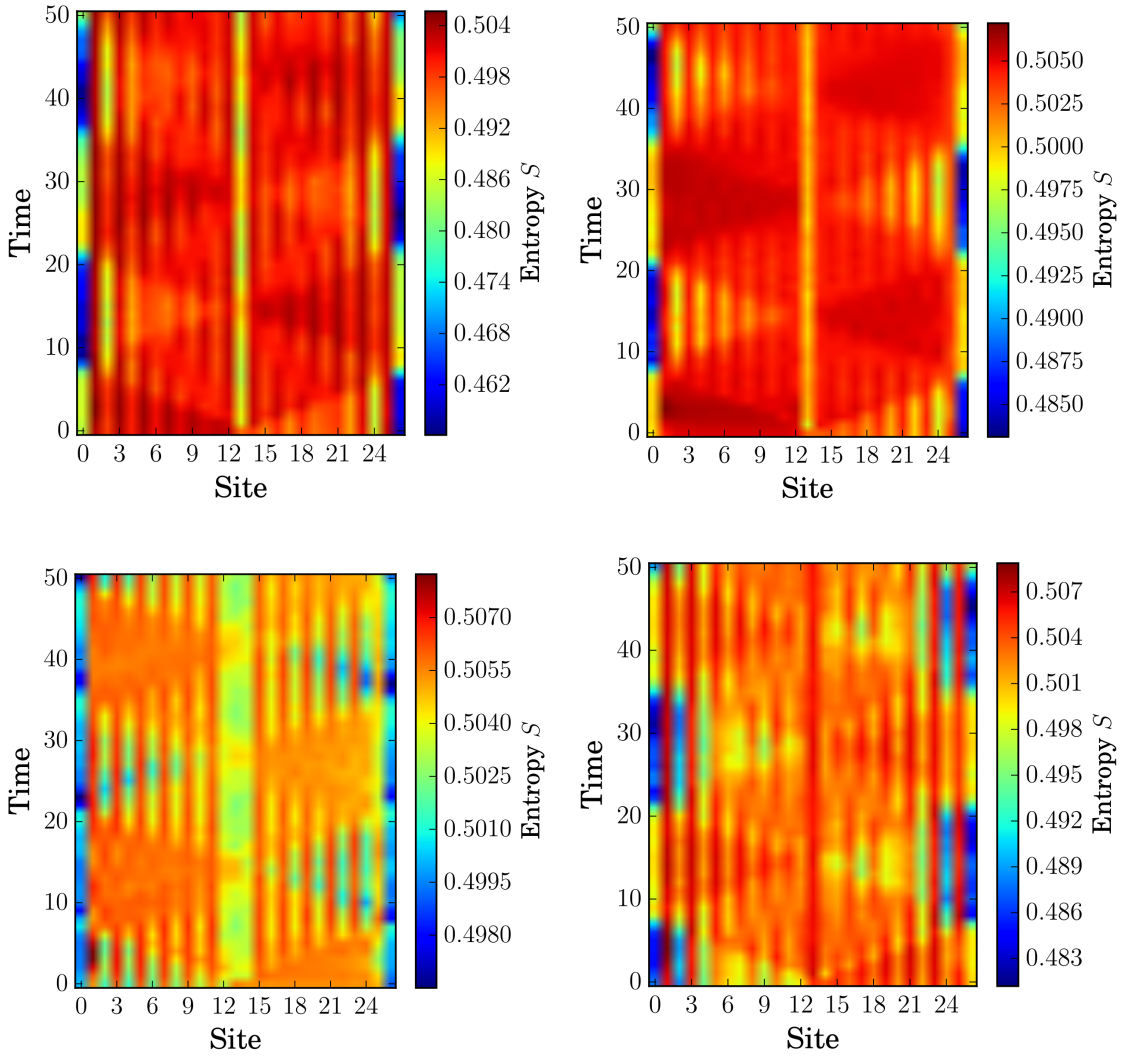

Figure 5.6: *Strongly interacting von Neumann entropy with emergent solitons.* The single-site entropy trends with the particle occupation in divulging the presence of emergent solitons for filling factors sightly above and below unit filling. For a system of 27 lattice sites, the barrier height is $V_0 = 0.2$, $J = 1$, and $U = 30$ in all panels. (**a**) $N = 12$, (**b**) $N = 13$, (**c**) $N = 14$, (**d**) $N = 15$.

of chapter 2, means that the Hamiltonian is changed rapidly, so that the initial state is essentially projected directly into the basis of the new Hamiltonian. In our case, the potential undergoes a rapid change from the imaginary time propagation of TEBD to the real time propagation, and the right well potential is lowered instantaneously. This rapid change incites excited modes in two ways. One way is the emergence of particle-hole pairs across the entire lattice immediately in the real time propagation; this particle-hole pair formation is outlined in chapter 4 as excited modes of the optical lattice. As an addition to the plots presented in that chapter, we include plots exhibiting the second manner in which the sudden approximation induces excited modes – these modes arise due to the shape of the external potential rather than the lattice. The modes arise immediately upon real time propagation, which can be seen in Figure 5.7. Further evidence and detailed calculations are presented in Appendix A.1.

5.5 Convergence and error

Theoretically, the error limit on matrix product state methods is only restricted by numerical machine precision [143]. In practice, the error can be minimized depending on a number of factors, including system size – assuming one or quasi-one dimension, as higher dimensional tensor network computations are beyond the scope of the matrix product state methods in this dissertation – regime of the interaction strength, magnitude and shape of the confining potential, finite size effects, or the intended observables, which also includes natural timescales of the dynamics.

The total error from the simulations can be written $\epsilon = \epsilon_{\text{method}} + \epsilon_{\chi}$, where ϵ_{method} is due to a combination of errors, the largest of which are the error due to Trotter decomposition as well as that due to local dimension restrictions. The local dimension error can be estimated from converging local dimension, d = max filling + 1. ϵ_{χ} stems from the Schmidt truncation, which is due to truncation of the Hilbert space and can be calculated explicitly from Schmidt coefficients. A demonstration of the relative number in a bosonic Josephson junction as the timestep is converged is shown in Figure 5.9, Figure 5.11, and Figure 5.14.

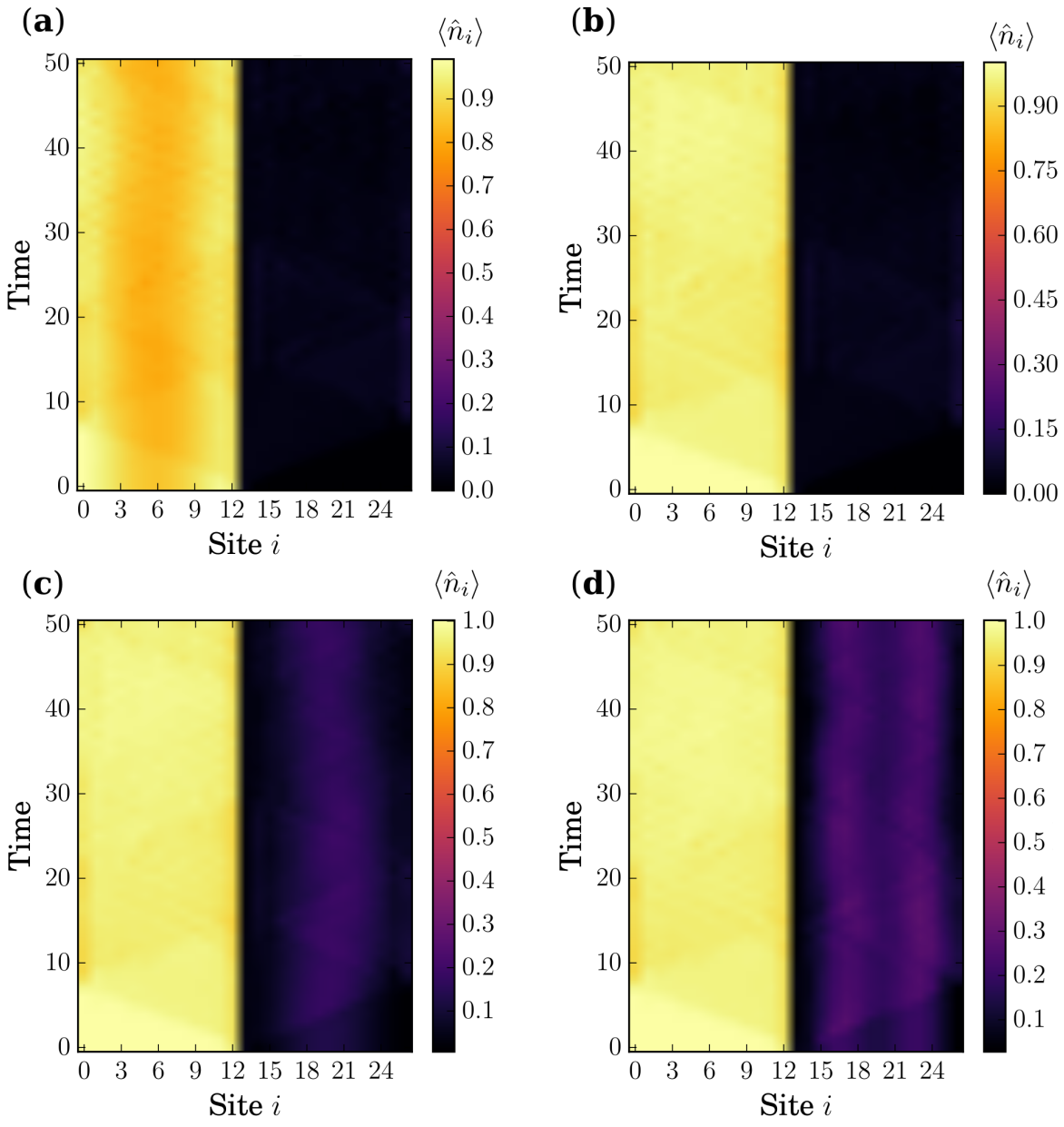

Figure 5.7: *Excited mode formation due to diabatic quenching.* For a system of 27 lattice sites, the barrier height is $V_0 = 5$, $J = 1$, and $U = 30$ in all panels. When the number of bosons (**a**) $N = 12$ is below unit filling, the mode in the left well is lowest-order, even and negative. (**b**) For $N = 13$, there is no mode formation, (**c**) $N = 14$, the mode in the right well is lowest-order, even, and positive, and finally (**d**) when $N = 15$, the mode in the right well is second-order, even, and positive.

Due to normalization in the Schmidt coefficients λ_i, where the index i indicates the bond, such that $\sum_{i=1}^{\chi}(\lambda_i)^2 = 1$, we can write, specifically, the Schmidt truncation error as $\epsilon_\chi = 1 - \sum_i^{\chi}(\lambda_i)^2$. By converging the bond dimension, we can ensure the truncation error is in check for all simulations, which can be seen for the parameters in the bosonic Josephson junction paper in Figure 5.8, Figure 5.10, Figure 5.12, and Figure 5.13.

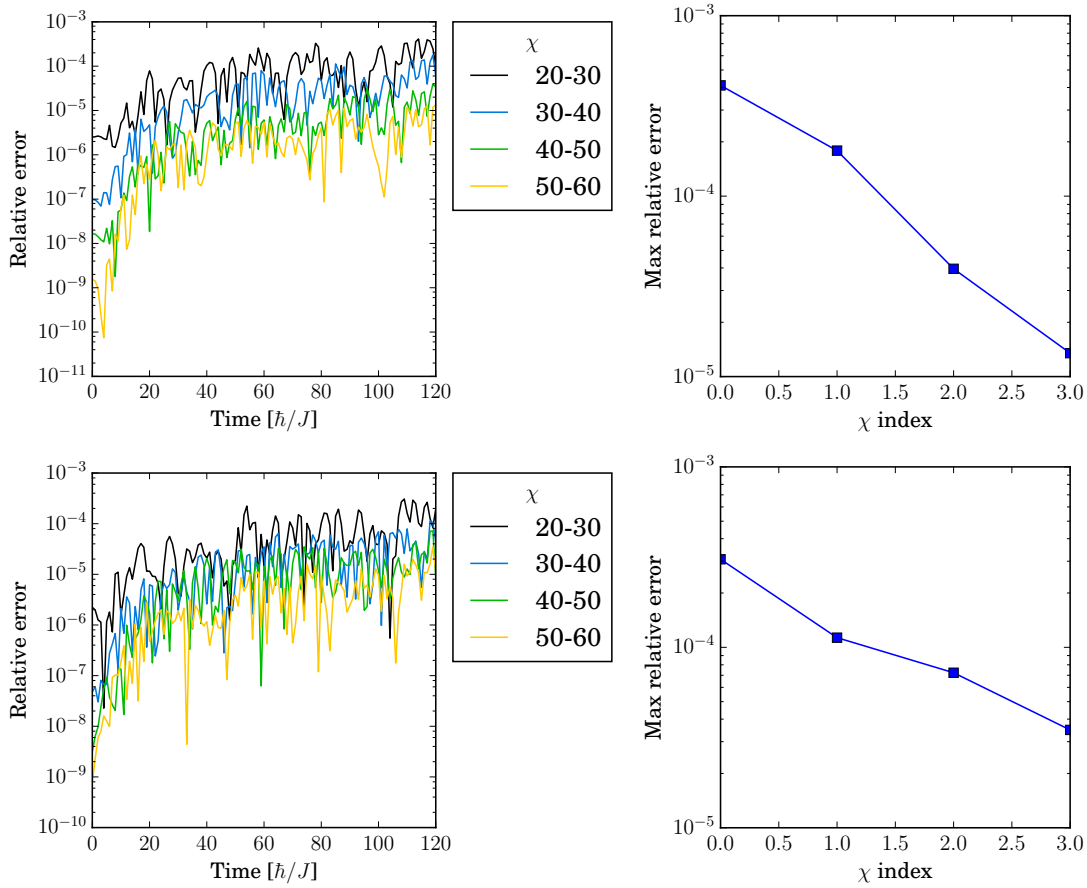

Figure 5.8: *Convergence in bond dimension for* $V_0 = 0.2$ *with strong interactions.*

The figures included in this section provide an example of a typical convergence study. Often, we could estimate the parameters needed for preliminary simulations, and after determining the extrema of parameters needed, would perform convergence only on these maximum or minimum values for each system size. Such parameters include barrier height as well as interaction strength. Once convergence parameters for bond dimension, time step, and local dimension are determined for each of these extrema in parameters, then we can

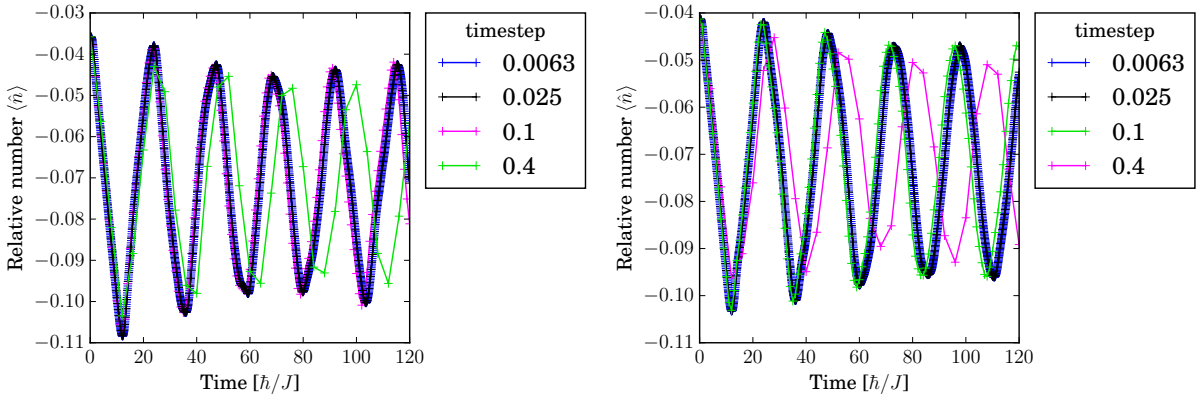

Figure 5.9: *Converging timesteps for* $V_0 = 0.2$ *with strong interactions.*

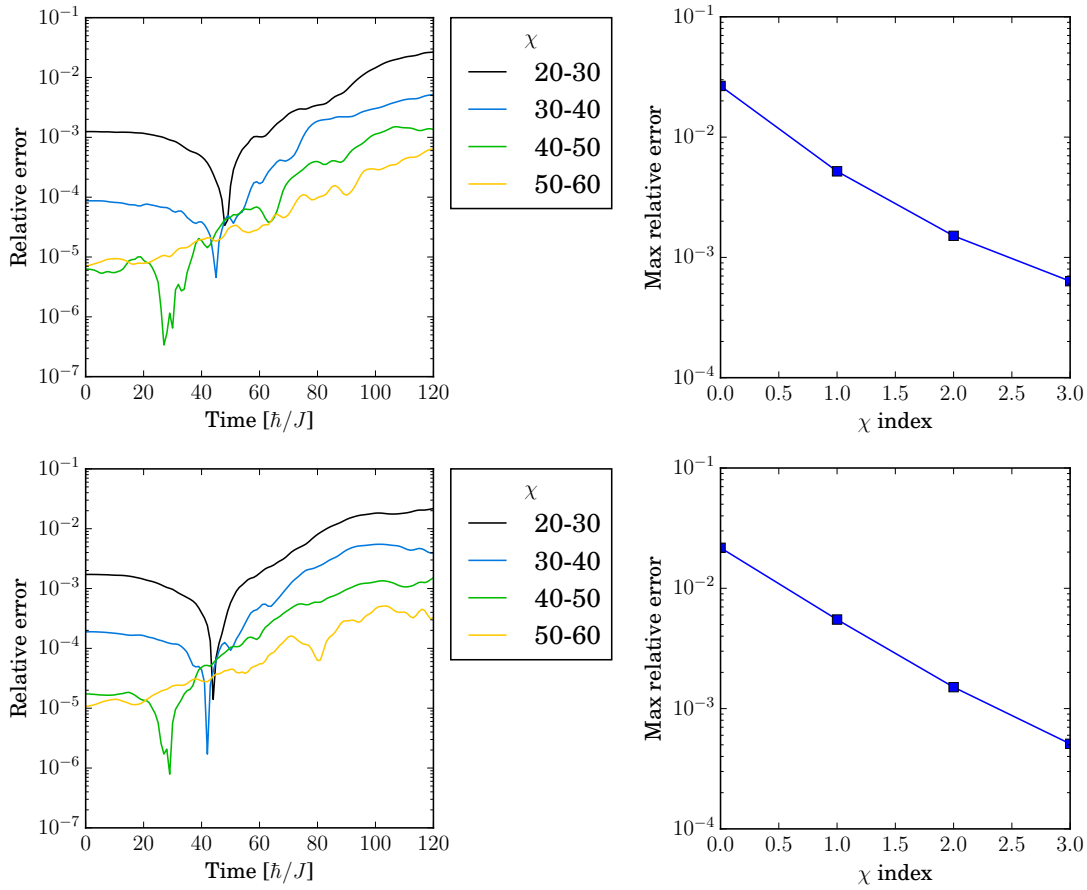

Figure 5.10: *Converging bond dimension for* $V_0 = 0.2$ *with weak interactions.*

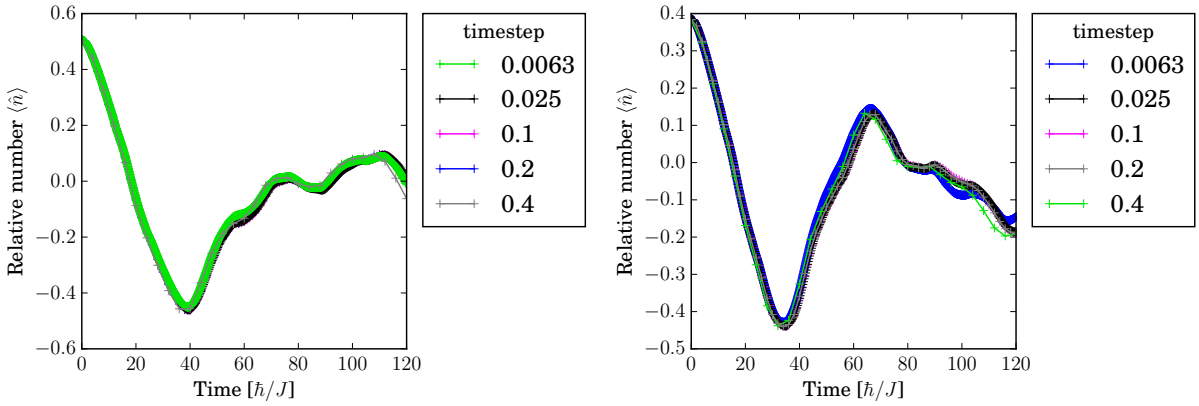

Figure 5.11: *Converging timesteps for* $V_0 = 0.2$ *with weak interactions.*

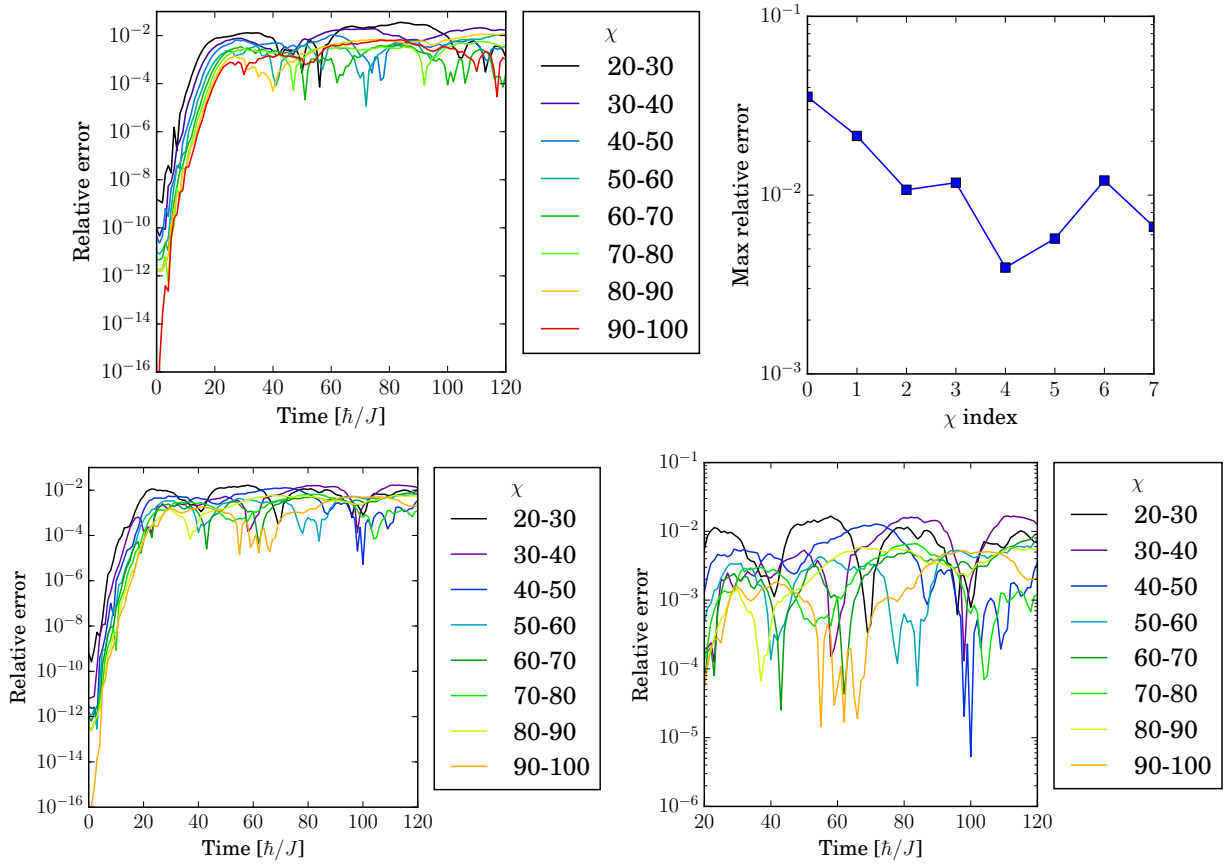

Figure 5.12: *Difficulty with convergence for* $V_0 = 5$ *and strong interactions*

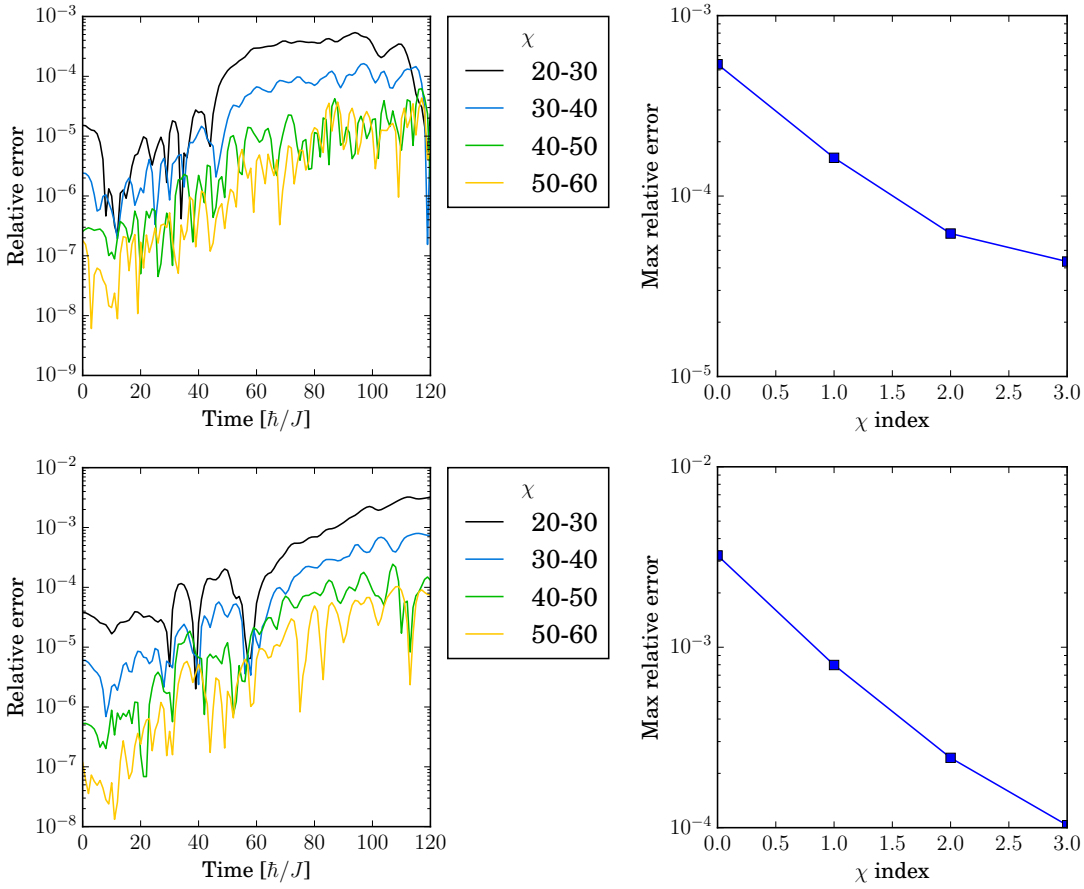

Figure 5.13: *Convergence for $V_0 = 5$ with weak interactions*

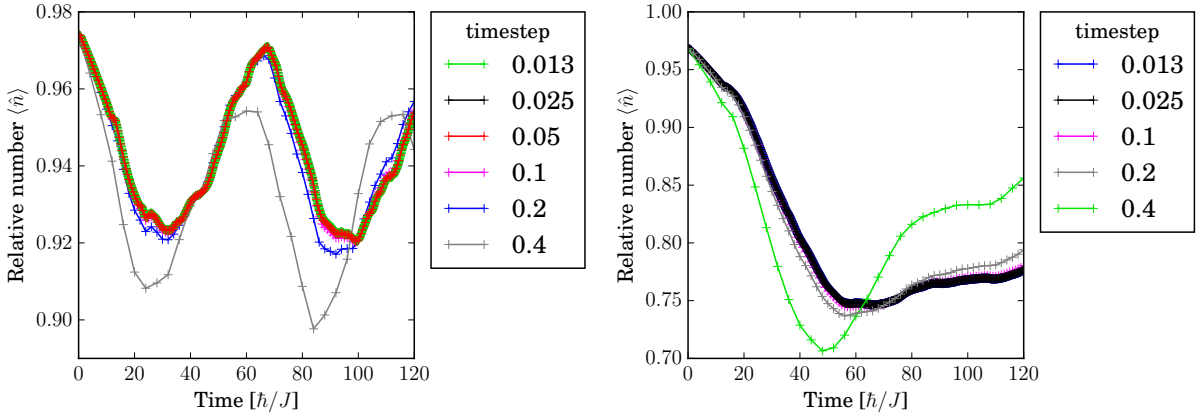

Figure 5.14: *Timestep convergence of relative number for weak interactions and $V_0 = 5$*

say with confidence that all parameters within these extrema are well-converged.

One difficulty in convergence we encountered was converging to a local minimum. For example, when simulating weakly-interacting bosonic Josephson junctions with a low barrier height, TEBD performs poorly in converging the time step. For Figure 4.4 and Figure 4.6, in chapter 4, steps as small as 10^{-4} were needed in these regimes to converge simulations below 10^{-3}. However, before accomplishing this level of convergence, we initially ran dynamics using a second-order Trotter approximation, and was able to converge the dynamics below 10^{-3} with a time step of 0.00625. Upon running the convergence study with a fifth-order Trotter approximation, the dynamics did not converge until the time step was 10^{-4}. So how could the results have appeared converged for a larger time step? My best guess is that the second-order approximation can still allow for convergence, even though the dynamics may not be as precise as the fifth-order solution, and thus the second-order solutions become stuck in a local minimum and are limited by the Trotterization.

Another challenge in the convergence studies was converging the bond dimension χ for large interaction strengths and large barrier heights in the bosonic Josephson junction, particularly as the system sizes became large. In Figure 4.12 for the largest barrier height, the workaround for this problem was simply calculating the $g^{(2)}$ measure on a system half the size of the other barrier heights. This difficulty converging can be seen in Figure 5.12, where a large bond dimension brings down the relative error only by small amounts.

CHAPTER 6

QUANTUM PHASE TRANSITION MODULATION IN AN ATOMTRONIC MOTT SWITCH

A paper submitted to *Quantum Science and Technology*

Marie A. McLain and Lincoln D. Carr

6.1 Abstract

Mott insulators provide stable quantum states and long coherence times due to small number fluctuations, making them good candidates for quantum memory and atomic circuits. We propose a proof-of-principle for a 1D Mott switch using an ultracold Bose gas and optical lattice. With time-evolving block decimation simulations – efficient matrix product state methods – we design a means for transient parameter characterization via a local excitation for ease of engineering into more complex atomtronics. We perform the switch operation by tuning the intensity of the optical lattice, and thus the interaction strength through a conductance transition due to the confined modifications of the "wedding cake" Mott structure. We demonstrate the time-dependence of Fock state transmission and fidelity of the excitation as a means of tuning up the device in a double well and as a measure of noise performance. Two-point correlations via the $g^{(2)}$ measure provide additional information regarding superfluid fragments on the Mott insulating background due to the confinement of the potential.

6.2 Introduction

Ultracold bosons in optical lattices provide highly precise architectures for quantum simulation of systems from solid state materials and superconductors to nonlinear optics. Due to their tunability, parameters governing cold atom dynamics such as interactions, temperature, and defect formations are highly controllable in arbitrary "painted" potentials [6, 108, 203].

Atomtronics – the creation of atomic circuits analogous to their electronic counterparts – is an emerging field in optical lattice platforms because it provides direct translations to descriptions such as solid state circuit elements and batteries [204–208], interferometers [209], transistors [210–212], superconducting or atomtronic quantum interference devices [213–216], and even open quantum circuits [207, 208, 217]. By probing the influence of the Mott phase transition on insulator conductance properties, we aim to demonstrate the opportunity for multi-disciplinary simulations of both semi-classical and quantum systems. The technology readiness level has matured to the point that there is a new need for quantum engineering; this has been achieved through advancements both in computation with numerical methods, in particular matrix product states [5, 143] – well-suited for strongly-interacting 1D lattice chains – and in experiment with Feshbach resonances, trapping techniques, and site-resolved imaging [47, 69, 111, 112, 159, 215]. More fully-quantum descriptions such as those offered by matrix product state methods such as time-evolving block decimation can offer insights beyond semiclassical atomtronic descriptions [218–220].

Additionally, Bose-Einstein condensate interferometry experiments in multiple potential wells admit dephasing is the largest source of error and limits the noise floor on coherence times [221]. Mott insulating atomtronics have the advantage of low number fluctuations and longer coherence times as compared to their weakly-interacting counterparts. We build on initial Mott atomtronic circuits [210] by presenting a proof-of-principle of a single Mott-insulating switch with a modulation tunable via a quantum phase transition, and a transient analysis method distinct from forward or reverse biasing methods [205]. A switch is one of the simplest devices in a circuit; fundamentally, it can only have two states. Switches provide the backbone for Boolean logic and comprise the heart of classical computation through transistors: they are a foundational circuit element that need to be incorporated into larger Mott insulating circuits in order for atomtronics to expand in scope. We test the otherwise passive circuit element through a transient analysis in response to an impulse and compare the junction leakage to the transmission tunneling coefficient. We use time-evolving block

decimation (TEBD) simulations to harness local measures, such as experimentally-observable number density, along with entropy measures to highlight the implications of entanglement in determining atomic conductance in a bosonic Mott insulator. To characterize noise in the system, we observe a microscopic measure – the Fock state fidelity – which offers a clean time domain in the operating regimes, and thus, a discrete Fourier transform of the fidelity offers a robust metric of the noise floor. In addition, the $g^{(2)}$ correlation measure enables many-body characterization that is directly translatable to experiment [192]. We use $g^{(2)}$ to quantify superfluid fragmentation; thus we are able to isolate the more pure Mott insulator that is the switch in its normal operation from these superfluid fragments that manifest on top of the Mott background, signaling the disconnected switch state.

We design the switch as a double well potential with an underlying optical lattice, as shown schematically in Figure 6.1. The 1D potential is well-described by the Bose-Hubbard Hamiltonian,

$$\hat{H}_{\mathrm{BH}} = -J\sum_{\langle i,j\rangle}(\hat{b}_i^\dagger\hat{b}_j + \hat{b}_i\hat{b}_j^\dagger) + \frac{1}{2}U\sum_i \hat{n}_i(\hat{n}_i - 1) + \sum_i V_i\hat{n}_i\,, \tag{6.1}$$

such that J is the bosonic tunneling energy, U is the repulsive interaction energy, $\hat{b}_i^\dagger$ and $\hat{b}_i$ are bosonic creation and annihilation operators, respectively, which satisfy bosonic commutation relations, $\hat{n}_i$ is the number operator for bosons, $\langle i,j\rangle$ indicates a sum over nearest neighbors, and the indices $i,j\epsilon\{0,...,L-1\}$ are over the L-length of the 1D optical lattice. For the purposes of modulating lattice depth in this study, we take $J = 1$ in all cases. V_i is the confining potential of the double well, and we will refer to V_0 as the central barrier height.

To initialize a transient response, we use imaginary time propagation in TEBD to find a modified Mott ground state to the dashed potential in Figure 6.1, where a majority of the lattice is in a unit-filled Mott state, i.e. an average of one atom per site. The first two sites have an initial excitation induced from the potential, which can be created e.g. with lasers as in atom gas microscopes [52, 222, 223]. Due to this local excitation and the commensurate filling of bosons on the lattice, the first site has a hole: it is void of any particles. However,

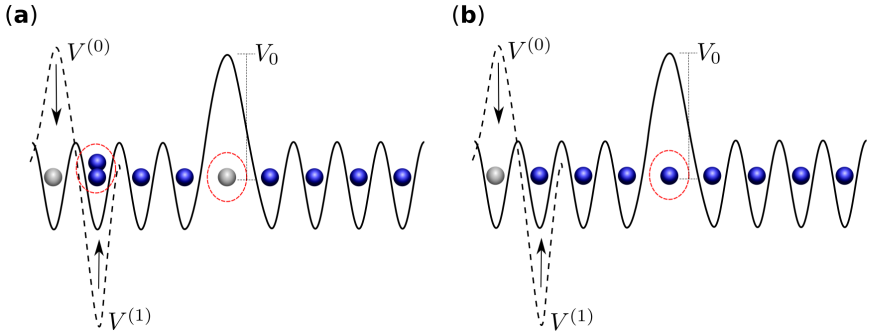

Figure 6.1: *Transient source quench scheme.* We initialize a Mott insulator in a bosonic Mott-insulating junction with a localized excitation, shown as the dashed lines of the potential, by running imaginary time propagation. The local kick in the first two sites of the potential is diabatically quenched, as indicated by the arrows, to the uniform lattice depth indicated with solid curves. The excitation allows for transient characterization of the switch parameters. (**a**) Below an interaction threshold, a particle-hole excitation forms in the initial state that has low conductance. (**b**) Above the interaction threshold, the extra boson from the particle-hole prefers to occupy the barrier region, and the excitation instead instigates a hole in the initial state with high conductance properties.

the strength of the interaction energy U and the potential barrier – which has the width of a single lattice site – compete to determine whether the local excitation is a simple hole in the Mott background (Figure 6.1(**b**)) or whether it is a particle-hole pair (Figure 6.1(**a**)). As we explore further in the results, there is a critical value of interaction strength that dictates whether the excitation is a hole or a particle-hole pair, and this same critical value also governs the conductance of the excitation. Of course, for shallow enough lattice depths, there is an additional threshold where tunneling dominates, so particle-hole creation is no longer energetically favorable. This second threshold is below the Mott limit in one dimension, $U/J \lesssim 3$ [104]. Fundamentally, it is the presence of the barrier that changes the usual Mott ground state enough to let a hole located at the barrier be preferred over a particle-hole. This is similar to changes in a harmonic trap resulting in a wedding-cake structure. Once the initial state has been established, we diabatically quench the first two sites so the underlying optical lattice is uniform, and we measure on-site particle number and fluctuation dynamics. From the local occupation, we calculate reflection and transmission probabilities of the hole

through the double well barrier as a function of time, with oscillations indicating the normal operation of the switch and self-trapping indicating the switch is disconnected.

6.3 Results and Discussion

One method for switch modulation is detailed in [8] that dictates the dynamic regimes of a bosonic Josephson junction in a 1D optical lattice based on height of the central potential barrier. The states of the switch correspond to the two regimes of the spontaneous-symmetry breaking $\mathbb{Z}_2$ quantum phase transition in a 1D double well: Josephson and Fock. In the single-particle limit, the Josephson oscillations in an isolated bosonic Josephson junction approach the Rabi frequency of the double well. As the barrier height is increased beyond some threshold, the junction enters the Fock regime and bosons remain self-trapped on one side of the barrier, an effect also observed as a Coulomb blockade in superconducting Josephson junctions [184]. Signatures of this quantum phase transition persist and dominate the dynamics even for mesoscopic systems with few active degrees of freedom. The results in Figure 6.2(**a**) can be interpreted as analogous, where the Fock regime indicates the switch is disconnected and Figure 6.2(**b**) portrays the Josephson regime, where the switch is connected. The key is that the typical $\mathbb{Z}_2$ shift from macroscopic quantum self-trapping to the Josephson regime as dictated by tunneling through the barrier is smooth and continuous [3, 86] – whereas the phase transition assisted switch in this article exhibits sharp contrast between the switching states. In our case we make use of the strongly-correlated Mott insulating state, leading to a more robust switch and much more localized single-site excitations, allowing for ultimately smaller atomtronic elements.

The switch modulation method we investigate in this article relies on the well-known "wedding cake" model of the Mott insulator to superfluid transition in the presence of a trapping potential [190]. Unconfined optical lattice models of the Mott insulator, for instance, require particle numbers commensurate with the number of lattice sites. The confining potential changes this definition of commensurate fillings, and thus the particle numbers needed to achieve a Mott insulator may be slightly different from traditional unit fillings.

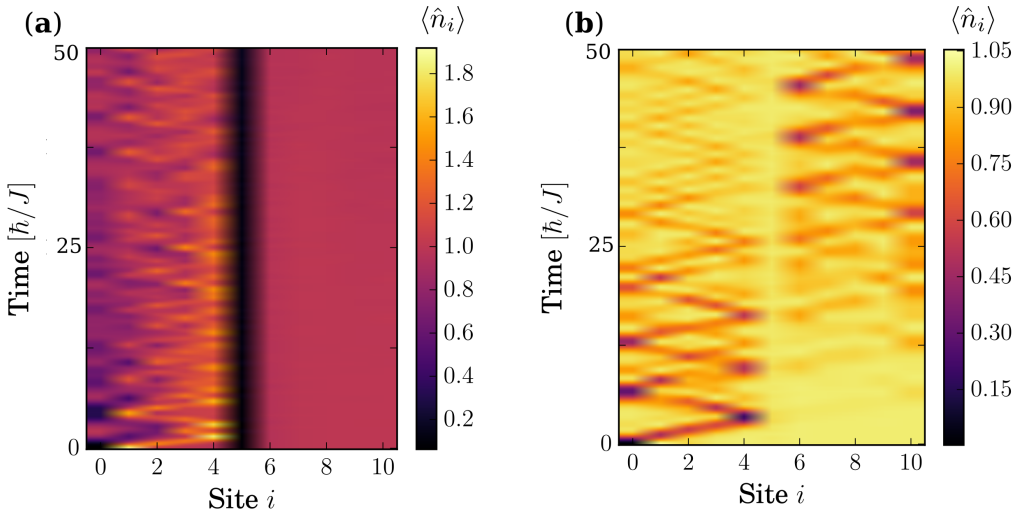

Figure 6.2: *Interaction switch modulation due to "wedding cake" Mott insulator.* The two possible transient response states of the classical Mott switch are (**a**) self-trapping in the left well and (**b**) Josephson oscillations. The barrier height $V_0 = 5$, in both panels, is a sweet spot for switch operation in this system configuration as determined by the number of lattice sites, the interaction strengths, the excitation magnitudes, and the atomic filling factor. The critical switching manifests as a sharp transition between (**a**) $U = 25$ and (**b**) $U = 26$, with all other parameters held constant, indicating the phase transition rather than tunneling is responsible for the division.

This is the case in our present study, where we have 11 lattice sites, 5 in each well, with the barrier occupying a single lattice site. We find a proper filling factor using 10 bosons in this Mott insulator. While we focus on the 1D chain of 11 lattice sites for the data in this article, we find that in order to employ the switch modulation method we propose, for a system of L lattice sites the number of total atoms must be $N = n(L-1)$, where n is an integer dictating the commensurate filling factor. Though, it is no doubt possible for other designer lattice topologies and sizes to exploit similar phase transition induced control, for instance generalizing to larger barriers, in which case the condition would be $N = n(L-w)$, with w the barrier width. To determine experimental feasibility without the requirement for single-site control, we systematically confirmed the effect for barriers up to a width of 3 lattice sites for total lattice sites $L = 9, 11, 13, 15$ from $U = 4$ through 60 where we are in the Mott insulating regime. We consider odd numbers of lattice sites because with a barrier width of 1, this yields an even number of sites on either side to maintain symmetry. For a barrier width of 2,4, etc. it is appropriate to have an even number of lattice sites. Thus, because we find the effect robust for varying barriers, the particle number would scale with the number of lattice sites as would be expected for a unit-filling Mott insulator. While the experimental control of a precise particle number presents a challenge, the minimum experimental implementation would require a Mott insulator with the presence of a double well confining potential, where the number of holes in the Mott background due to the confinement of the potential can indeed vary. Advances in experimental precision may also help to realize the Mott switch, such as controllable two-body collisions for finer Mott manipulation [224]. The critical point occurs between $U = 20$ and 30 for barrier heights $V_0 = 0.1$ to 10 for $L = 11$ sites and $N = 10$ bosons, as will be discussed throughout this article. We intentionally focus on small systems to minimize the size of the atomtronic device, working at the smallest size for which a quantum phase transition is still a relevant concept, about 10 sites plus the barrier accounting for finite size effects [105].

We set the tunneling strength $J = 1$, the central barrier height $V_0 = 5$, and the initial excitation strengths on the zeroth site $V^{(0)} = 10$ and first site $V^{(1)} = -10$, which provide a localized kick that is strong compared with the barrier height. While these excitation strengths were originally designed to favor particle-hole formation on the first two sites, we find that the critical transition to barrier occupation occurs, surprisingly, in spite of the imbalance of the positive and negative excitations. While these excitations can be incited at any site(s) on the lattice, in order to control the direction of propagation we initialize it adjacent to the leftmost wall, which we note has open boundary conditions. In Figure 6.3(**a**), the interaction strength $U = 25$ is below its critical value for turning on the switch, and thus the particle-hole is self-trapped in the left well and the right well remains in an ideal Mott state. The switch is off, or in its disconnected state. The initial state has close to no particle occupation in the barrier, whereas Figure 6.3(**b**) with $U = 26$ illustrates the repulsive interaction is critically strong enough such that the particle prefers to occupy the barrier, thus creating a conductive link to the right well. The switch is therefore on, or in its normally operating state.

An important clue in deciphering the influence of the superfluid-Mott phase transition on the operation of this Mott device is analyzing the initial states. We supply a pure Fock state as an initial guess, $|02111011111\rangle$, into our TEBD imaginary time propagation algorithm, though ultimately the ground state determination of this initial potential has no absolute requirement for initial Fock states. This can be seen in Figure 6.3(**a**) for $V_0 = 2$, as the barrier regions on the 5^{th} lattice site for $U = 20$ and 21 are closer to $\langle \hat{n}_5 \rangle \approx 0.5$ than an integer. These deviations from Fock states are due to superfluid influences on the edge of one layer of the Mott insulating shelf; as a contrast, interaction strengths $U > 21$ are firmly rooted on the Mott side of the transition, with close to unit filling. Additionally, determining the best confinement parameter will optimize the contrast and effectiveness of the switch. In Figure 6.3(**b**) we see that a barrier height of $V_0 = 5$ enables more ideal Fock states and thus, less error in the on-site number as a measure of the switch state. As

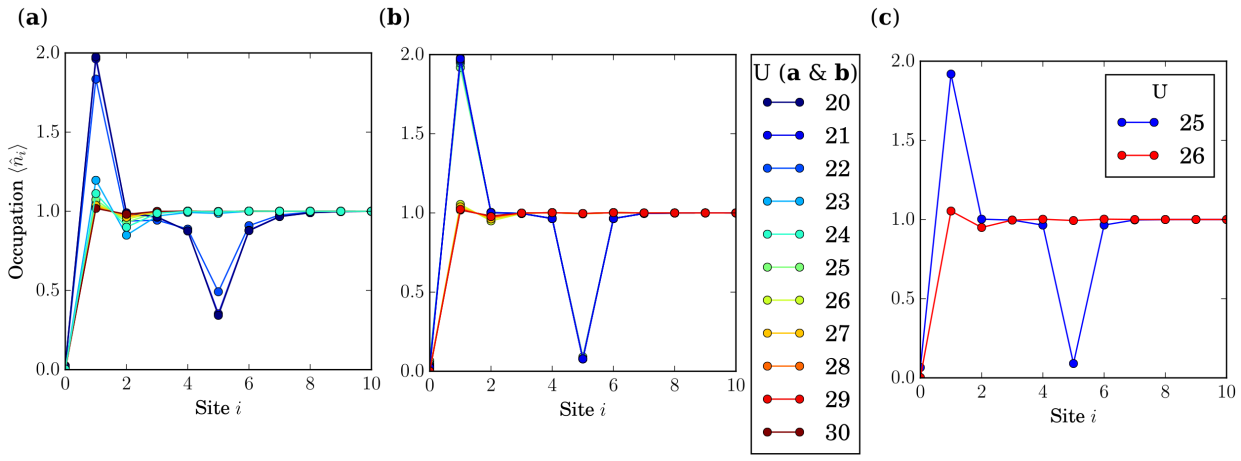

Figure 6.3: *Initial states suggest critical Mott confinement.* (**a**) When the barrier height $V_0 = 2$, a particle-hole pair forms on the first two sites due to the induced excitation of the initial states for $U = 20$ and 21. For larger interaction strengths, the extra boson occupies the central barrier rather than the particle-hole pair. (**b**) At $V_0 = 5$, the initial states approach ideal Mott states as the on-site occupations converge toward integer values. (**c**) The critical transition from particle-hole excitation to barrier occupation occurs between $U = 25$ and 26 for $V_0 = 5$.

shown in Figure 6.3(**c**), the values for $U \geq 26$ at this barrier height are nearly identical $|01111111111\rangle$, at unit filling save for the hole on the first site. For $U \leq 25$ the initial states approach the ansatz $|02111011111\rangle$, and this hole in the barrier region creates a large resistance and inhibits the particle-hole transport. We note that the particle number is conserved in our model, as appropriate for an ultracold Bose gas in an optical lattice.

In investigating the response of the device to the sudden excitation, we consider a Fock transmission of the hole across the barrier region based on inverse number density, as the hole is an absence of a particle within the Mott insulating background. We calculate the time-dependent transmission as the dimensionless ratio

$$T(t) = \frac{\sum_{i=1}^{\lfloor L/2 \rfloor} \hat{n}_i(t) - \sum_{i=1}^{\lfloor L/2 \rfloor} \hat{n}_i(t=0)}{N/2}, \tag{6.2}$$

where L is the total number of lattice sites and N the total number of atoms. The sum is over the left well sites i, where we could have easily calculated the inverse quantity for the right well, as the double well conserves particle number. The transmission provides one means of measuring the signal-to-noise ratio, which we determine by taking the ratio of the maximum double well oscillation amplitude to the amplitude of the junction leakage, or the magnitude of the maximum noise when the switch is off. We calculate the signal-to-noise based on the integer values of U immediately on either side of the switching phase transition, e.g. U_{on} (U_{off}) for the interaction strength when the switch is on (off). The signal is then $(\max(|T|) - \min(|T|))\Big|_{U_{\text{on}}}$ and the noise is $(\max(|T|) - \min(|T|))\Big|_{U_{\text{off}}}$. In Figure 6.4(**a**) at a low barrier height of $V_0 = 0.1$, the shift from off to on occurs from $U = 21$ to $U = 22$ with a small signal-to-noise ratio of ≈ 1.6, where the error on the measurement is machine error and is not represented in the truncation of the decimal. The next barrier height, $V_0 = 2$ displayed in Figure 6.4(**b**), depicts a mildly improved signal-to-noise of ≈ 3.4 between the normally operating tunnel state at $U = 23$ and the disconnected self-trapping at $U = 22$. This operation region of the switch is an improvement over the $V_0 = 0.1$ case, as the phase transition occurs more sharply through the interaction modulation. The switch can be

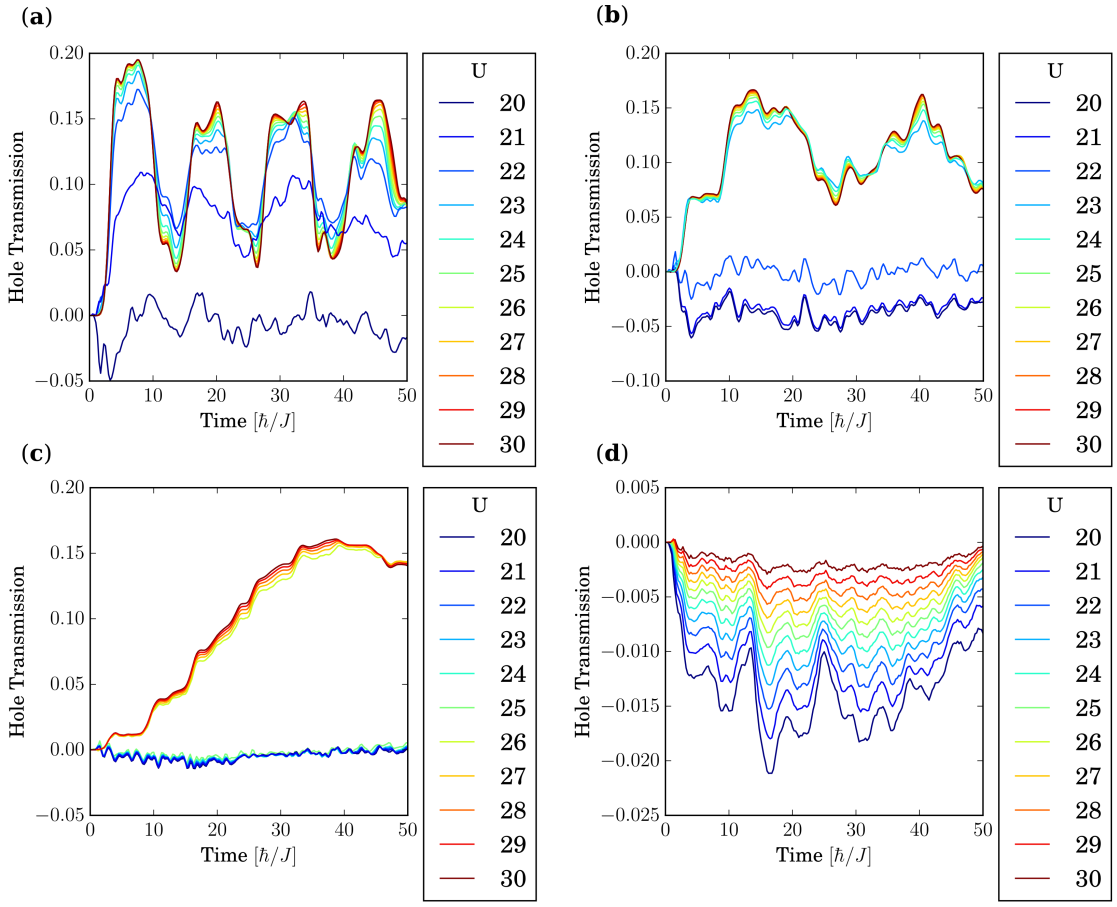

Figure 6.4: *Transmission demonstrates regime with best signal-to-noise ratio.* (**a**) In the low barrier height regime, $V_0 = 0.1$, the hole transmits easily for interaction strengths $U \geq 22$. We begin falling off the shelf of the Mott wedding cake for $U = 21$ and 20 as the superfluid washes out the excitation, and the signal-to-noise is low, ≈ 1.6. (**b**) For $V_0 = 2$, the critical split in transmission behaviors between the two possible types of initial states, occurring between $U = 22$ and 23, becomes exaggerated. However, the the signal-to-noise is still low at ≈ 3.4. (**c**) The divergence in behavior of the two switching states becomes clear for a barrier height $V_0 = 5$, and the signal-to-noise ratio is maximal at ≈ 8.9. (**d**) As the barrier height becomes too large, the transmission of the hole excitation is negligible, and the only transmissions through the barrier are those due to superfluid influences as a result of optical lattice depth.

tuned to a large signal-to-noise ratio of 8.9 between the off state at $U = 25$ and the on state at $U = 26$ for a barrier height of $V_0 = 5$ as shown in Figure 6.4(**c**), providing a robust switching configuration that also offers the most contrast between the two states. The final panel of Figure 6.4(**d**) displays self-trapping for all U and the switch is disconnected. The background loss increases for decreasing interaction strength, as the superfluid fraction grows, thus mediating tunneling through the barrier.

The fidelity provides a microscopic measure of transient response in atomtronic Mott insulators. We calculate the fidelity as a Fock space overlap with the initial state, which is $\langle n(0)|n(t)\rangle/\langle n(0)|n(0)\rangle$, where $|n(t)\rangle$ is the time-dependent Fock state and $|n(0)\rangle$ is the initial Fock state prior to real time propagation. The clean periodic fidelity peaks in Figure 6.5(**a**) are more easily mapped to their Fourier transform, panel (**c**), than transmission, for example. Below the critical point, $U < 22$, the superfluid fragments as portrayed in Figure 6.5(**a**) lower the fidelity below the $\approx 90\%$ Mott threshold and in Figure 6.5(**c**) inject high frequency noise into the discrete Fourier transform, calculated using the one-dimensional fast Fourier transform algorithm in numpy. The superfluid influence also raises the noise floor by about 6 dB. Figure 6.5(**b**) displays a better operating regime for the switch with a barrier height $V_0 = 5$, as the contrast between the two switching states is maximized, such that $U \geq 26$ in blue, the switch is in its normally operating, or on state and $U \leq 25$ in red, the switch is disconnected, or off. The phase transition through U is sharp, yet the operating parameter regions are large, making this switch practical for scalable Mott atomtronics. In addition, Figure 6.5(**d**), the Fourier transform of Figure 6.5(**b**), demonstrates two distinct spectra, the blue for larger U corresponding to Josephson oscillations when the switch is on and the red for smaller U when the switch is off. In this off state, the noise floor is considerably higher by about 3 dB. Also in the off state, the fidelity oscillations are well-resolved for the particle-hole excitation bouncing back and forth within the left well, lending to a more well-defined spectrum for a range of interaction strengths as compared with the $V_0 = 0.1$ case.

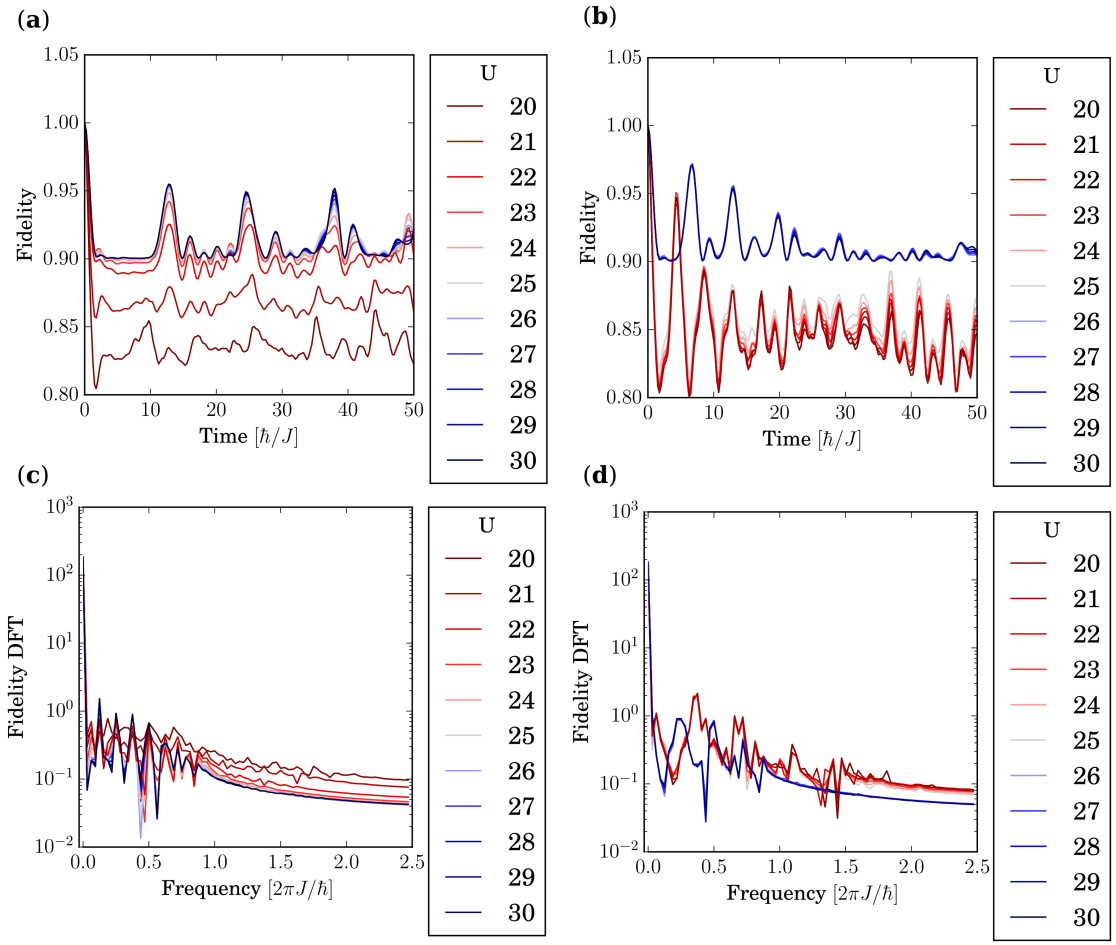

Figure 6.5: *Fidelity and corresponding Fourier transform as robust measurement standards.* (**a**) In the low barrier height regime $V_0 = 0.1$, where $U \geq 22$, the fidelity has a lower limit of $\approx 90\%$ and exhibits metronomic periodicity. This barrier height is too low to observe a critical transition necessary for a switch. (**b**) The two states of the Mott switch converge for $V_0 = 5$, where $U = 20$ to 25 in red means the state of the switch is self-trapped or disconnected, and the initial states were all particle-hole excitations. Interaction strengths $U = 26$ to 30 in blue illustrate the Josephson or normally operating regime, and the initial states all demonstrated particle occupation of the barrier. (**c**) The discrete Fourier transform of the data from (**a**) reveals the continuous raising of the noise floor by approximately 6 dB for an increasing superfluid fraction, as interaction strength decreases from $U = 30$ to 20. (**d**) The Fourier transform of the data from (**b**) reveals a divergence in the spectral behavior between the two switching states and the emergence of higher-frequency superfluid noise when the switch is off for $U \leq 25$.

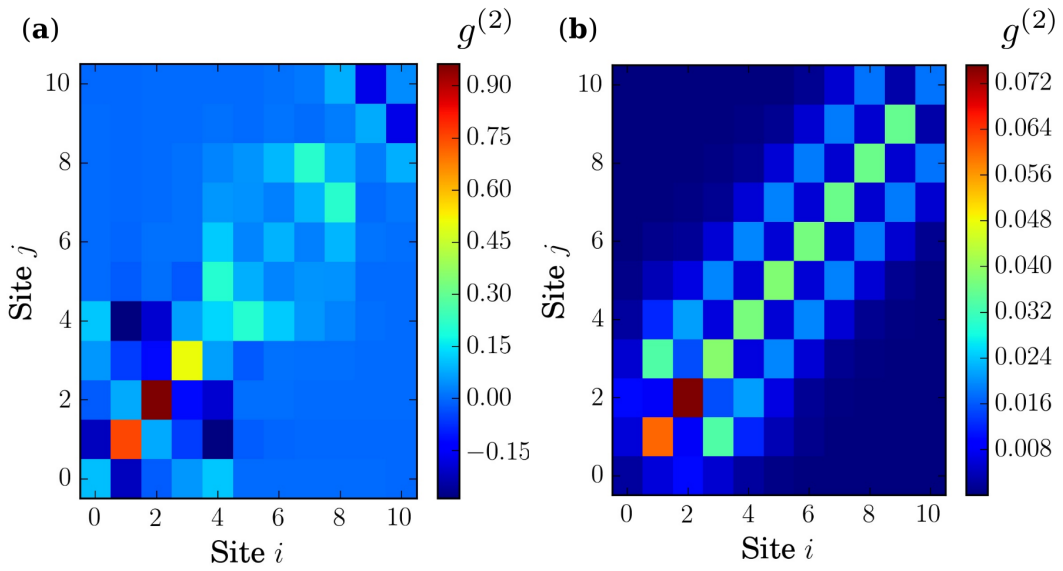

Figure 6.6: *Two-point correlators identify superfluid occupation.* $g^{(2)}$ as a correlation measure distinguishes the presence of superfluid fragments, thus granting an experimentally viable many-body probe of Mott switch states. Both panels illustrate a barrier height tuned to the locality of sharp contrast at $V_0 = 5$. While the switch flips states between $U = 25$ and $U = 26$, this level of precision is not necessary for operation. (**a**) At $U = 20$, and time $t = 0.05$ for example, the large amplitude of $g^{(2)}$ from 0.9 to -0.15 conveys a level of superfluidity in the disconnected switch state, which is more than an order of magnitude larger than (**b**) the connected switch when $U = 30$ also at time $t = 0.05$, which ranges from $g^{(2)} = 0.072$ to 0.008.

Furthermore, the $g^{(2)}$ measure delineates second order correlations that not only provide ease of experimental access and drive local entropy, they act as a guide for entanglement, if not a witness [192]. These $g^{(2)}$ correlators gauge particle fluctuations for optical lattice sites i and j and so $g_{ij}^{(2)} = \langle \hat{n}_i \hat{n}_j \rangle - \langle \hat{n}_i \rangle \langle \hat{n}_j \rangle$. When $g^{(2)}$ is positive, the expectation value of observing two atoms concurrently at sites i and j is greater than that of observing the distinct atoms locally and vice versa. Because the correlations are positive across most of the lattice, this corresponds with a preference for simultaneous two-body measurement over local measurement. Figure 6.6(**a**) portrays the initial (time $t = 0.05$) two-point correlator of the switch in its disconnected state for $U = 20$; the small amount of superfluid on the Mott background resulting from the confinement of the barrier magnifies the $g^{(2)}$ amplitude by an order of magnitude over Figure 6.6(**b**), which illustrates initial ($t = 0.05$) normal switch operation for $U = 30$. This normal switch state is also marked by the extreme localization of the two-point correlations on-site and of nearest neighboring lattice sites.

6.4 Conclusions

We have demonstrated a proof-of-principle of a robust atomtronic switch in a double well Mott insulator by triggering a local excitation in the Mott background and measuring a transient response. The switching mechanism is tuned via the lattice depth and thus the local interaction strength triggers a sharp phase transition. The switching occurs due to the confinement of the double well barrier, which modifies the traditional superfluid-Mott ground states. In the disconnected state, the excitation is a particle-hole pair; in the connected state, the excitation is a hole – an absence of a particle – within the Mott insulating background. The geometry thus changes between the two states, creating a critical transition in the conductance, a point that can be quantified via time-dependent Fock state transmission of the hole through the barrier, which also provides a means of determining signal-to-noise ratio and operating regime. We further demonstrate the fidelity of the Fock states and the corresponding discrete Fourier transform as a tool for optimizing and characterizing the switch noise performance. What is more, $g^{(2)}$ as a measure of the two-point correlations

provides a witness of superfluid fragments on the Mott background, thus demonstrating a many-body probe of Mott switch states that is feasible on current cold atom platforms. The phase transition modulated switch mechanism proposed in this article offers flexibility due to large parameter margins for operation together with sharp contrast of the switch states.

The next steps of many-body quantum simulation of robust Mott atomtronics switches, particularly their applications in strongly-correlated regimes, would address problems of materials science or other disciplines more directly, even in combination with open quantum systems for improved source and drain implementation. We could also look toward ultracold molecules for additional degrees of freedom, where the transport is of a spin rather than a mass [225, 226]. Then we get a "moleculetronics" switch which is in fact spintronics in the ultracold context.

6.5 Acknowledgements

The authors would like to extend gratitude to Diego Alcala for extensive support during the conception of this project – and to Elias Galan and Lewis Graninger for making this paper possible. Many heartfelt thanks to Steven Patton for suggesting the original idea for the project. High performance computing resources at the Colorado School of Mines and the Golden Energy Computing Organization were used to perform simulations. This research is partially based on work supported by the US National Science Foundation under grant numbers PHY-1520915, PHY-1207881, PHY-1306638, OAC-1740130, as well as the US Air Force Office of Scientific Research grant number FA9550-14-1-0287. We acknowledge the support of the U.K. Engineering and Physical Sciences Research Council (EPSRC) under the "Quantum Science with Ultracold Molecules" Programme grant number EP/P01058X/1.

6.6 Appendix

Time-evolving block decimation errors can be split into two categories, $\epsilon = \epsilon_{\text{method}} + \epsilon_{\chi}$, where ϵ_{method} is from a number of sources; the most significant of these are from the fifth-order Suzuki-Trotter approximation that induces a time step error, together with the local

dimension truncation. ϵ_χ dictates the Schmidt truncation error due to truncation of the Hilbert space. We found the time step in the limit of small U and V_0 to require excessively small time steps to converge; whereas in the large U and V_0 limit, the bond dimension χ required for convergence was excessively large. In the parameter space relevant to this paper, $U = 20$ through 30 and $V_0 = 0.1$ through 10, the $V_0 = 0.1$ case is converged below 10^{-4} relative error in the bond dimension, and the $V_0 = 10$ case is also converged below 10^{-4} due to limitations in the bond dimension. All other barrier heights for any interaction strength in this range were converged below 10^{-7}, though we check bond dimension up to $\chi = 140$ in our preferred parameter regime, where the convergence is actually orders of magnitude better, as shown in Figure 6.7. Other interaction ranges were also considered as part of this project, from $U = 4$ to 60, where the regions from $U = 31$ to 60 and $U = 4$ to 19 were converged below 10^{-3} for convenience.

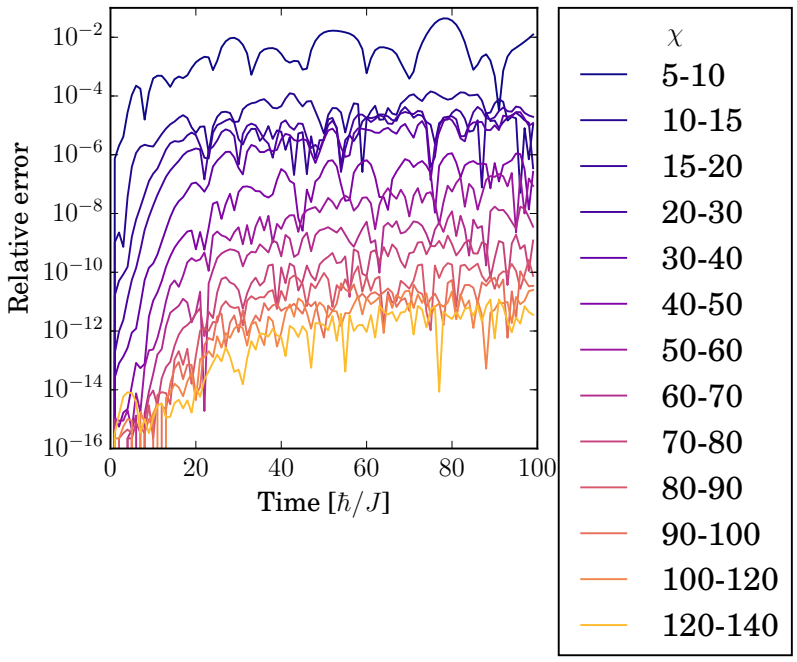

Figure 6.7: *Convergence of the bond dimension.* In the proposed switch operating regime for $L = 11$, $N = 10$, $U = 30$ and a barrier height $V_0 = 5$, we demonstrate convergence below 10^{-11} of the Fock state fidelity for bond dimension up to $\chi = 140$.

CHAPTER 7
CONCLUSIONS AND OUTLOOK

The second quantum revolution is underway, expanding the fundamentals of quantum theory toward far-reaching applications, including atomic clocks, highly precise quantum sensors for microscopy and biomedical devices, secure quantum networks in addition to a quantum internet, and ultimately new computational paradigms. Governments worldwide and industry are both investing substantially in the second quantum revolution, including Google, IBM, Microsoft, and Intel. Bose-Einstein condensates and other manifestations of ultracold gases in optical lattices are one step along this journey as highly-controllable quantum simulators. They confer a mechanism for probing the many-body effects that become crucial in the search for ever-increasing sensitivity, scope, and speed of quantum technologies and devices. In order for these advancements to be possible, the many-body theory must fill the gaps in predicting experimental behavior, particularly in regimes where interactions render many methods, such as mean-field approximations, intractable [6]. The research presented in this dissertation is one rung toward advancing this goal, as a majority of these investigations originate from interactions between atoms and their affect on many-body dynamics. For example, we have found many-body descriptions of initial states that predict the $\mathbb{Z}_2$ quantum phase transition in a bosonic Josephson junction, where its mean-field counterpart failed. In strongly-correlated regimes this became even more crucial, where for instance in an atomtronic Mott insulator, we found a sharp phase transition due to a "wedding cake" type confinement of the optical lattice.

7.1 Summary

An important distinction of this work is its experimental relevance. Whenever possible, the experiments were designed so as to be viable in present quantum simulator platforms: statistical properties of the species, the interatomic interaction parameter values, the shape

of the potentials, the dimension, and the choice of observables were all considered. For example, the first project presented in 3.1 presents evidence from both numerical and analytical theory together with experimental data from our collaborators for non-exponential decay of a BEC [7]. In addition, the advancement of experimental techniques – in tunability of interaction strengths, single-site tailored trapping potentials, and highly precise manipulation and measurements protocols – have propelled ultracold quantum gas experiments to the forefront of true quantum quantum simulation. Therefore, ultracold Bose gases such as those formed by ^{87}Rb provided an ideal backdrop for investigating the dynamics in this research.

One of the major projects on discerning the dynamic regimes of a bosonic Josephson junction based on two competing phase transitions successfully mapped the dynamics regimes qualitatively and quantitatively for both mean-field and many-body dynamics. Other projects included investigations of macroscopic quantum tunneling escape in BECs, partial symmetry breaking in an optical lattice ring trap, and particle-hole tunneling in a bosonic Josephson junction. All projects explored the role of many-body interactions in quantum tunneling of ultracold Bose-gases, providing a map of computational and analytical methods for re-envisioning common assumptions; these results would be attainable in current experimental quantum simulator architectures. The results have demonstrated further broad-reaching applications, as quantum simulators have the highly precise parameter and measurement control to produce true quantum quantum simulations for deciphering critical challenges in analogous architectures geared toward applications, including many-body effects in superconductors and other solid state materials, thin films, and nonlinear optics.

A co-author project on macroscopic quantum tunneling escape of a BEC (section 3.1) brought together experiment and theory to reveal a non-exponential decay in the number of ^{87}Rb atoms trapped in a single well. An important implication of this result was the root cause of the non-exponential behavior: interactions between the atoms, which played a crucial role in understanding differences in many-body tunneling with mean-field approximations [6]. A second co-author project, described in section 3.2, investigated the dynamics

of a quantum quench from a biperiodic lattice to a uniform one, thereby explicitly breaking the symmetry of an optical lattice ring trap. The quench protocol directly countered that used for studying Kibble-Zureck physics and identified a new class of quantum dynamics experiments that required the quantum advantage. The study defined new measures, the symmetry gap and the symmetry memory, that identified critical phenomena outlining when the system remembered its initial symmetry state [7].

The largest project considered in this dissertation in chapter 4 explored the macroscopic tunneling dynamics of an ultracold Bose gas in a square double well using many-body numerical simulations together with mean-field and analytical calculations. We imposed an optical lattice on the double well potential to establish a grid for many-body dynamics. The Bose-Hubbard Hamiltonian described the two length scales of the double well or Josephson junction via two rivaling energy terms: the on-site interaction and the Josephson tunneling strength. Experimentalists would tune the on-site interaction in the optical lattice by Feshbach resonances or by modulating lattice depth. Similarly, Josephson energy would be adjusted by modifying the barrier height or width, which would depend on the specific type of barrier chosen. One length scale was given by the double well. The second length scale was given by the optical lattice underlying the double well.

This lead us to investigate the impact of the $U(1)$ superfluid/Mott insulator quantum phase transition, the first type of phase transition, on this multi-scale tunneling behavior. The second type of phase transition was a discrete $\mathbb{Z}_2$ transition from a Josephson oscillation phase to a macroscopic self-trapping phase. The interplay of the two quantum phase transitions, $\mathbb{Z}_2$ and $U(1)$, reduced to tuning of the barrier height for the spontaneous symmetry breaking transition and tuning of the interaction strength for the superfluid-Mott transition. The ultimate goal then was to characterize the dynamic tunneling regimes that result, from Josephson oscillations to self-trapping. Some of the regimes had previously been identified in literature for weakly-interacting systems, while we explored the dynamics into the strongly-interacting regime.

We computationally demonstrated comparisons of mean-field and many-body dynamic regimes based on the interplay of the two quantum phase transitions in a bosonic Josephson junction. Using initial state information, we designed a many-body energy ratio to predict these dynamic regimes; and we found that mean field theory broke down as the repulsive interaction strength increased and failed to predict the spontaneous symmetry breaking transition. Additionally, we identified a number of strictly many-body phenomena in these dynamic regimes that increased in importance for higher-precision applications: long-lived particle-hole pairs and low-lying double well modes arose due to a sudden quench of the potential and could act as signatures of QPTs - even in systems below the thermodynamic limit previously presumed to be outside the realm of quantum phase transitions. Other many-body signatures included possible antisymmetric soliton formation in the Josephson regime and the $g^{(2)}$ Fock flashlight effect in the self-trapping regime: these effects manifested in quantities that would be measurable experimentally in architectures ranging from cold atoms to nonlinear optics to superconductors. With the number of applications relying on two-mode models of the double well, the result of this investigation of cold atom double well experiments with optical lattices was a recommendation to revisit many-body effects in systems previously assumed to be mean-field.

In the final project in chapter 6, we devised an atomtronic Mott switch device that built on our work on many-body tunneling in bosonic Josephson junctions. We examined the dynamics of a local excitation tunneling in a double well through a Mott insulating background and found that Fock state fidelity and transmission measures indicated noise performance and critical phenomena in the transport properties of these excitations. By tuning the interaction strength through a critical value, the switch state was propelled into a "wedding cake" layer of the Mott insulating structure, marked by a hole – or absence of a particle – on the Mott insulating background. Below the critical point, a particle-hole pair excitation that was self-trapped in one well demonstrated the sharp contrast in conductance modulation. As an experimentally feasible method of identifying switching state, we used

$g^(2)$ two-point correlators to magnify the superfluid occupation present in the particle-hole switching state.

7.2 Future work

A more immediate expansion of this work would include applying the same investigative protocols of bosonic atoms to fermions by simulating the Fermi-Hubbard Hamiltonian (FHH) in place of its Bose-Hubbard counterpart. One of the differences between the BHH and FHH lies in the fermion occupation of only spin up or spin down states, and taking the lowest band approximation, this limits the local dimension to 4. The phase diagram also becomes more complicated, especially for real materials. The FHH allows for the emergence of at least one additional phase in addition to the Mott insulator and band insulator: the superconducting phase. A further consideration is the pairing of fermions and the BEC-BCS crossover, which is distinct from ultracold bosons [201, 202].

Further augmentation of either Hubbard Hamiltonian to long-range Hubbard models would also improve many-body descriptions, particularly in regimes where tunneling is strong. One example would be long-range tunneling [84]. Expansion of the Hamiltonian may also require consideration of higher dimensions [227], especially for quantum simulation of materials such as thin films or bulk materials, such as in the BCS-BEC crossover [228]. For experimentally realistic comparisons, the ramifications of nonzero temperature should also be considered, particularly thermalization and loss of excited modes [229]. Though more specifically, I encourange the expansion of this work to quantum information and quantum atomtronics, the emerging field of atomic circuits. A single Josephson junction can be mapped to the simplest transmon qubit, for example, which would be simulated by adding nearest-neighbor interaction terms in the long-range Hubbard model together with the proper ratio of charging and Josephson energies. Additionally, a tilt or asymmetry would need to be applied to replicate an external driving bias [34, 164, 165]. Another method of exploring quantum simulators would be coupling external quantum devices to ultracold gases in order to measure internal hyperfine states of a flux qubit, for example [230].

With the experimental realization of an atom superconducting quantum interference device (SQUID) [213] and experimental demonstration of the hysteresis necessary for atom rf-SQUIDS [216], a logical extension would be mapping the many-body physics of such devices using matrix product state methods. This would require the superconducting phase of ultracold fermions in two coupled Josephson junctions with periodic boundary conditions. Understanding the influence of charge noise – which is akin to the long-range atomic interaction energy – on SQUIDs is a fundamental problem with superconducting circuits, and one that can likely be solved with many-body characterization in ultracold Fermi gas simulators.

Applying all of these suggestions to open quantum systems is a more challenging undertaking. However, mapping the coupling of atomic systems to a controllable environmental parameter would enable quantum simulator systems to accurately establish the affect of the environment on analogous quantum systems, such as superconductors and nonlinear optics. Determining the effects of thermalization precisely through atomic quantum simulators, for example, would have immediate impact on superconducting devices [231].

REFERENCES CITED

[1] Nobelprize.org. The Nobel Prize in Physics 2001. *Nobel Media AB*, 2014. URL http://www.nobelprize.org/nobel_prizes/physics/laureates/2001/.

[2] C.J. Pethick and H. Smith. *Bose-Einstein Condensation in Dilute Gases*, chapter ISBN 9780511755583. Cambridge University Press, 2001.

[3] L. D. Carr, R. Kanamoto, and M. Ueda. *Understanding Quantum Phase Transitions*, chapter 13. Taylor & Francis, Boca Raton, FL, 2010. URL https://www.crcpress.com/Understanding-Quantum-Phase-Transitions/Carr/p/book/9781439802519.

[4] TEBD. Matrix product state open source code. URL https://sourceforge.net/projects/opentebd/.

[5] OSMPS. Matrix product state open source code. URL https://sourceforge.net/projects/openmps/.

[6] Xinxin Zhao, Diego A. Alcala, Marie A. McLain, Kenji Maeda, Shreyas Potnis, Ramon Ramos, Aephraim M. Steinberg, and Lincoln D. Carr. Macroscopic quantum tunneling escape of Bose-Einstein condensates. *Phys. Rev. A*, 96:063601, 2017. doi: 10.1103/PhysRevA.96.063601. URL https://link.aps.org/doi/10.1103/PhysRevA.96.063601.

[7] X. Zhao, M.A. McLain, J. Vijande, A. Ferrando, L.D. Carr, and M.A. Garcia-March. Nonequilibrium quantum dynamics of partial symmetry breaking for ultracold bosons in an optical lattice ring trap. *Phys. Rev. Lett.*, (under review), 2017.

[8] Marie A. Mclain, Diego A. Alcala, and Lincoln D. Carr. For high precision bosonic Josephson junctions, many-body effects matter. *arXiv:1803.00526v1*, 2018. URL https://arxiv.org/abs/1803.00526.

[9] Marie A. Mclain and Lincoln D. Carr. Quantum phase transition modulation of an atomtronic Mott switch. *arXiv:1804.03804v1*, 2018. URL https://arxiv.org/abs/1804.03804.

[10] R.W. Gurney and E.U. Condon. Quantum Mechanics and Radioactive Disintegration. *Physical Review*, 33:127, 1929.

[11] R.W. Gurney and E.U. Condon. Wave mechanics and radioactive disintegration. *Nature*, 122:439, 1928.

[12] Hans Bethe. Interview with Charles Weiner and Jagdish Mehra. *American Institute of Physics*, Cornell University:Niels Bohr Library & Archives, 27 October 1966.

[13] E. Collini, C.Y. Wong, K.E. Wilk, P.M.G. Curmi, P. Brumer, and G.D. Scholes. Coherently wired light-harvesting in photosynthetic marine algae at ambient temperature. *Nature*, 463:644, 2010.

[14] F. Hund. Fortschritte in der Systematik und Theorie der Molekelspektren. *Z. Physics*, 40:742, 1927.

[15] P.W. Anderson. More Is Different. *Science*, 177:393–396, 1972.

[16] Michael Meo. *Houtermans, Friederich Georg*, pages 1013–1014. Springer New York, New York, NY, 2014.

[17] S. Coleman. Fate of the false vacuum: Semiclassical theory. *Phys. Rev. D*, 15:2929, 1977.

[18] D.M. Ostovsky, G.W. Carter, and E.V. Shuryak. Forced tunneling and turning state explosion in pure Yang-Mills theory. *Phys. Rev. D*, 66:036004, 2002.

[19] J. B. Rommel, Y. Liu, H.-J. Werner, and J. Kaestner. Role of tunneling in the enzyme glutamate mutase. *J. Phys. Chem. B*, 116:13682, 2012.

[20] K. Choi, G. Ryu, F. Yesilkoy, A. Chrissis, N. Goldsman, M. Daganais, and M. Peckerar. A focused asymmetric metal-insulator-metal tunneling diode: fabrication, D.C. characteristics and R.F. rectification analysis. *IEEE Trans. El. Dev.*, 28:C6050, 2010.

[21] Jun-Yi Ge, Vladimiar N. Gladilin, Jacques Tempere, Cun Xue, Jozef T. Devreese, Joris Van d Vondel, Youhe Zhou, and Victor V. Moshchalkov. Nanoscale assembly of superconducting vortices with scanning tunneling microscope tip. *Nature Communications*, 7:13880, 2016.

[22] R. Wieser. Manipulation of magnetic skyrmions with a scanning tunneling microscope. *Phys. Rev. B.*, 95:064417, 2017. doi: 10.1103/PhysRevB.95.064417. URL `https://journals.aps.org/prb/abstract/10.1103/PhysRevB.95.064417`.

[23] A.I. Kolesnikov, G.F. Reiter, n. Choudhury, T.R. Prisk, E. Mamantov, A. Podlesnyak, G. Ehlers, A.G. Seel, D.J. Wesolowski, and L.M. Anovitz. Quantum tunneling of water in Beryl: A new state of the water molecule. *Phys. Rev. Lett.*, 116:167802, 2016.

[24] Friedrich Hund. linienspektren und periodisches System der Elemente. *Habil.Schrift, Universität Göttingen, Springer*, 1927.

[25] R. Mohsen. *Quantum Theory of Tunneling*. World Scientific, New York, NY, 2003.

[26] M.H. Anderson, J.R. Ensher, M.R. Matthewes, C.E. Wieman, and E.A. Cornell. Observation of Bose-Einstein Condensation in a Dilute Atomic Vapor. *Science*, 269:198, 1995.

[27] K.B. Davis, M.O. Mewes, M.R. Andrews, N.J. van Druten, D.S. Durfee, D.M. Kurn, and W. Ketterle. Bose-Einstein Condensation in a Gas of Sodium Atoms. *Phys. Rev. Lett.*, 75:3969, 1995.

[28] Dallin D. Durfee and Wolfgang Ketterle. Experimental studies of Bose-Einstein condensation. *Optics Express*, 2:299–313, 1998.

[29] B.D. Josephson. Possible new effects in superconducting tunneling. *Phys. Lett.*, 1: 167802, 1962.

[30] B.D. Josephson. The discovery of tunneling supercurrents. *Rev. Mod. Phys.*, 46(2): 251–254, 1974.

[31] P.W. Anderson and J.M. Rowell. Probable observation of the Josephson tunnel effect. *Phys. Rev. Lett.*, 10:230, 1963.

[32] Paul D Dresselhaus, Michael M Elsbury, David Olaya, Charles J Burroughs, and Samuel P Benz. 10 volt programmable Josephson voltage standard circuits using NbSi-barrier junctions. *IEEE Transactions on Applied Superconductivity*, 21:693–696, 2011.

[33] M. Albeiz, R. Gati, J. Flling, S. Hunsmann, M. Cristiani, and M.K. Oberthaler. Direct Observation of Tunneling and Nonlinear Self-Trapping in a Single Bosonic Josephson Junction. *Phys. Rev. Lett.*, 95:010402, 2005. doi: 10.1103/PhysRevLett.95.010402. URL `https://journals.aps.org/prl/abstract/10.1103/PhysRevLett.95.010402`.

[34] S. Levy, E. Lahoud, I. Shomroni, and J. Steinhauer. The a.c. and d.c. Josephson effects in a Bose-Einstein condensate. *Nature*, 449:579–583, 2007. doi: doi:10.1038/nature06186. URL `https://www.nature.com/articles/nature06186?free=2`.

[35] Shreyas Potnis, Ramon Ramos, Kenji Maeda, Lincoln D. Carr, and Aephraim M. Steinberg. Interaction-assisted quantum tunneling of a Bose-Einstein condensate out of a single trapping well. *Phys. Rev. Lett.*, 118:060402, 2017.

[36] D.A. Alcala, J.A. Glick, and L.D. Carr. Entangled dynamics in macroscopic quantum tunneling of Bose-Einstein condensates. *Phys. Rev. Lett.*, 118:210403, 2017.

[37] D.J. Griffiths. *Iintroduction to Quantum Mechanics, 2nd Ed.*, pages 315–322. Pearson Education, Inc., New York, New York, 2014.

[38] E. Schrödinger. Quantization as an eigenvalue-problem. *Annalen der Physik*, 79,81, 1926.

[39] A. Einstein. *Sitzungsbericht der Preussischen Akademie der Wissenshaften*, page 3, 1925.

[40] S.N. Bose. Plancks Gesetz und Lichtquantenhypothese. *Z. Phys.*, 26:178, 1924.

[41] I. Bloch. Ultracold quantum gases in optical lattices. *Nature Physics*, 1:23, 2005.

[42] F. London. The Rare Isotope of Helium, ^{3}He; A Key to the Strange Properties of Ordinary Liquid Helium. *Nature*, 141:643, 1938.

[43] C.J. Foot. Laser Cooling and Trapping of Atoms. *Contemp. Phys.*, 32:369, 1991.

[44] C.C. Bradley, C.A. Sackett, J.J. Tollet, and R. Hulet. Evidence of Bose-Einstein Condensation in an Atomic Gas with Attractive Interactions. *Phys. Rev. Lett.*, 78:985, 1997.

[45] K. Bongs and K. Sengstock. Physics with coherent matter waves. *Reports on Progress in Physics*, 67:907, 2004.

[46] S. Inouye, M. R. Andrews, J. Stenger, H.-J. Miesner, D. M. Stamper-Kurn, and W. Ketterle. Observation of Feshbach resonances in a Bose-Einstein condensate. *Nature*, 392: 151, 1998. doi: 10.1038/32354. URL `https://www.nature.com/articles/32354`.

[47] S.E. Pollack, D. Dries, M. Junker, Y.P. Chen, T.A. Corcovilos, and R.G. Hulet. Extreme tunability of interactions in a ^{7}Li Bose-Einstein condensate. *Phys. Rev. Lett.*, 102:090402, 2009. doi: 10.1103/PhysRevLett.102.090402. URL `https://journals.aps.org/prl/abstract/10.1103/PhysRevLett.102.090402`.

[48] T. Fernholz, R. Gerritsma, P. Krueger, and R.J.C. Spreeuw. Dynamically Controlled Toroidal and Ring-Shaped Magnetic Traps. *Phys. Rev. A.*, page 75:063406, 2007. doi: 10.1103/PhysRevA.75.063406. URL `https://journals.aps.org/pra/abstract/10.1103/PhysRevA.75.063406`.

[49] K.C. Wright, R.B. Blakestad, C.J. Lobb, W.D. Phillips, and G.K. Campbell. Driving Phase Slips in a Superfluid Atom Circuit with a Rotating Weak Link. *Phys. Rev. Lett.*, 110:025302, 2013. doi: 10.1103/PhysRevLett.110.025302. URL `https://journals.aps.org/prl/abstract/10.1103/PhysRevLett.110.025302`.

[50] W.S. Bakr, A. Peng, M.E. Tai, R. Ma, J. Simon, J.I. Gillen, S. Foelling, L. Pollet, and M. Greiner. Probing the Superfluid-to-Mott Insulator Transition at the Single-Atom Level. *Science*, pages 329:547–550, 2010. doi: 10.1126/science.1192368. URL `http://science.sciencemag.org/content/329/5991/547`.

[51] W. S. Bakr, J. I. Gillen, A. Peng, S. Fölling, and M. Greiner. A quantum gas microscope for detecting single atoms in a hubbard-regime optical lattice. *Nature*, 462:74, 2009. doi: 10.1038/nature08482. URL `https://www.nature.com/articles/nature08482`.

[52] Jacob F. Sherson, Christof Weitenberg, Manuel Endres, Marc Cheneau, Immanuel Bloch, and Stefan Kuhr. Single-atom-resolved fluorescence imaging of an atomic Mott insulator. *Nature*, 467:68, 2010. doi: 10.1038/nature09378. URL `http://dx.doi.org/10.1038/nature09378`.

[53] M. Greiner, O. Mandel, T. Esslinger, T. W. Hnsch, and I. Bloch. Quantum phase transition from a superfluid to a Mott insulator in a gas of ultracold atoms. *Nature*, 415:39, 2002.

[54] D. Jaksch, C. Bruder, J.I. Cirac, C.W. Gardiner, and P. Zoller. Cold bosonic atoms in optical lattices. *Phys. Rev. Lett.*, 81:3108, 1998. doi: 10.1103/PhysRevLett.81.3108. URL `https://journals.aps.org/prl/abstract/10.1103/PhysRevLett.81.3108`.

[55] R. Jördens, N. Strohmaier, K. Günter, H. Moritz, and T. Esslinger. A Mott insulator of fermionic atoms in an optical lattice. *Nature*, 455:204, 2008.

[56] U. Schneider, L. Hackermller, S. Will, T. Best, I. Bloch, T. A. Costi, R. W. Helmes, D. Rasch, and A. Rosch. Metallic and insulating phases of repulsively interacting fermions in a 3D optical lattice. *Science*, 322:1520, 2008.

[57] M. Köhl, H. Moritz, T. Stöferle, K. Günter, and T. Esslinger. Fermionic atoms in a three dimensional optical lattice: Observing Fermi surfaces, dynamics, and interactions. *Phys. Rev. Lett.*, 94:080403, 2005.

[58] C. Cohen-Tannoudji, J. Dupont-Roc, and G. Grynberg. *Atom-photon interactions: Basic processes and applications*, chapter ISBN 0471625566. Wiley-VCH, 1992.

[59] A. Lewenstein, M. Sanpera, V. Ahufinger, B. Damski, A. Sen De, and U. Sen. Ultracold atomic gases in optical lattices: Mimicking condensed matter physics and beyond. *Adv. Phys.*, 56:243–379, 2007.

[60] A. Kolovsky and D.N. Maksimov. Mott-insulator state of cold atoms in tilted optical lattices: doublon dynamics and multi-level Landau-Zener tunneling. *Phys. Rev. A*, 94: 043630, 2016.

[61] I. Bloch, J. Dalibard, and W. Zwerger. Many-body physics with ultracold gases. *Rev. Mod. Phys.*, 80:885, 2008.

[62] Wolfgang Ketterle and Han-Joachim Miesner. Coherence properties of Bose-Einstein condensates and atom lasers. *Phys. Rev. A*, 56:3291, 1997. doi: 10.1103/PhysRevA.56.3291. URL `https://doi.org/10.1103/PhysRevA.56.3291`.

[63] W. Ketterle, D. S. Durfee, and D. M. Stamper-Kurn. Making, probing and understanding Bose-Einstein condensates. *Phys. Part. Nuclei*, Proc. Intl. Sch. Phys. "Enrico Fermi":67–176, 1999. URL `https://arxiv.org/abs/cond-mat/9904034`.

[64] W.D. Phillips. Laser cooling and trapping of neutral atoms. *Mol. Opt. Phys.*, 70: 721–741, 1998.

[65] Ana Maria Rey. *Ultracold Bosonic Atoms in Optical Lattices*. PhD thesis, University of Maryland, 2004.

[66] C.N. Cohen-Tannoudji. Manipulating atoms with photons. *Mol. Opt. Phys.*, 70:707–719, 1998.

[67] Thomas Anker. *Ultracold quantum gases in one-dimensional optical lattice potentials - nonlinear matter wave dynamics*. PhD thesis, University of Heidelberg, Germany, 2005.

[68] R. Grimm, M. Weidemüller, and Y.B. Ovchinnikov. Optical dipole traps for neutral atoms. *Mol. Opt. Phys.*, 42:95–170, 2000.

[69] E.S. Shuman, J.F. Barry, and D. DeMille. Laser cooling of a diatomic molecule. *Nature*, 467:820, 2010. doi: 10.1038/nature09443. URL `http://dx.doi.org/10.1038/nature09443`.

[70] S. Chu, L. Hollberg, J.E. Bjorkholm, A. Cable, and A. Ashkin. Three-dimensional viscous confinement and cooling of atoms by resonance radiation pressure. *Phys. Rev. Lett.*, 55:48, 1985.

[71] S. Chu. The manipulation of neutral particles. *Rev. Mod. Phys.*, 70:685–706, 1998.

[72] N. Masuhara, J.M Doyle, J.C. Sandberg, D. Kleppner, T.J. Greytak, H.F. Hess, and G.P. Kochanski. Evaporative Cooling of Spin-Polarized Atomic Hydrogen. *Phys. Rev. Lett.*, 61:935, 1988.

[73] F. Dalfovo, S. Giorgini, and S. Stringari. Theory of Bose-Einstein condensation in trapped gases. *Reviews of Modern Physics*, 71:463, 1999.

[74] E.P. Gross. Structure of a Quantized Vortex in Boson Systems. *Nuovo Cimiento*, 20: 454, 1961.

[75] L.P. Pitaevskii. Vortex Lines in an Imperfect Bose Gas. *Sov. Phys. JETP*, 13:451, 1961.

[76] N.N. Bogoliubov. On the Theory of Superfluidity. *J. Phys. (USSR)*, 11:23, 1947.

[77] Lincoln D. Carr Diego A. Alcala, Joseph A. Glick. Entangled dynamics in macroscopic quantum tunneling of Bose-Einstein condensates. *Phys. Rev. Lett.*, 118:210403, 2017.

[78] T. Kühner, S. White, and H. Monien. One-dimensional Bose-Hubbard model with nearest-neighbor interaction. *Phys. Rev. B.*, 61:12474, 2000.

[79] U. Bissbort, F. Deuretzbacher, and W. Hofstetter. Effective multibody-induced tunneling and interactions in the Bose-Hubbard model of the lowest dressed band of an optical lattice. *Phys. Rev. A*, 86:023617, 2012.

[80] Dirk-Sören Lühmann, Ole Jürgensen, and Klaus Sengstock. Multi-orbital and density-induced tunneling of bosons in optical lattices. *New Journ. of Phys.*, 14:033021, 2012.

[81] R. V. Mishmash and L. D. Carr. Ultracold atoms in 1D optical lattices: Mean field, quantum field, computation, and soliton formation. *Mathematics and Computers in Simulation*, 80:732–740, 2009. doi: 10.1016/j.matcom.2009.08.025. URL `https://www.sciencedirect.com/science/article/pii/S0378475409002754`.

[82] R. Carretero-Gonzlez, D. J. Frantzeskakis, and P. G. Kevrekidis. Nonlinear waves in Bose-Einstein condensates: Physical relevance and mathematical techniques. *Nonlinearity*, 21:R139, 2008. doi: 10.1088/0951-7715/21/7/R01. URL `http://stacks.iop.org/0951-7715/21/i=7/a=R01`.

[83] M.L. Chiofalo, M. Polini, and M.P. Tosi. Collective excitations of a periodic Bose condensate in the Wannier representation. *The European Physical Journal D - Atomic, Molecular, Optical and Plasma Physics*, 11:371–378, 2000. doi: 10.1007/s100530070065. URL `https://doi.org/10.1007/s100530070065`.

[84] Philipp Moritz Preiss. *Atomic Bose-Hubbard Systems with Single-Particle Control*. PhD thesis, Harvard University, 2015.

[85] M. Abbarchi, A. Amo, V. G. Sala, D. D. Solnyshkov, H. Flayac, L. Ferrier, I. Sagnes, E. Galopin, A. Lemaître, G. Malpuech, and J. Bloch. Macroscopic quantum self-trapping and Josephson oscillations of exciton polaritons. *Nature Physics*, 9:275, 2013. doi: 10.1038/nphys2609. URL `https://www.nature.com/articles/nphys2609`.

[86] Subir Sachdev. *Quantum Phase Transitions (2nd Ed.)*, chapter ISBN 9780521514682. Cambridge University Press, 2011. URL https://www.amazon.com/Quantum-Phase-Transitions-Subir-Sachdev/dp/0521514681.

[87] H. Eugene Stanley. *Introduction to Phase Transitions and Critical Phenomena*, chapter ISBN 9780195053166. Oxford University Press, 1989.

[88] T. Kühner and H. Monien. Phases of the one-dimensional Bose-Hubbard model. *Phys. Rev. B.*, 58:R14741, 1998. doi: 10.1103/PhysRevB.58.R14741. URL https://journals.aps.org/prb/abstract/10.1103/PhysRevB.58.R14741.

[89] M. Lacki, B. Damski, and J. Zakrewski. Locating the quantum critical point of the Bose-Hubbard model through singularities of simple observables. *Sci Rep.*, 6:38340, 2016. doi: 10.1038/srep38340. URL https://www.nature.com/articles/srep38340.

[90] R.K. Pathria and Paul D. Beale. *Statistical Mechanics (3rd Ed)*. Elsevier Ltd., Oxford, UK, 2011.

[91] R.P. Feynman. *Statistical Mechanics: A Set of Lectures*, chapter ISBN 081334610X. Westview Press, 1972.

[92] Ole Jürgensen. *Extended Hubbard Models for Ultracold Atoms in Optical Lattices*. PhD thesis, Universität Hamburg, 2015.

[93] D. Jaksch and P. Zoller. The cold atom Hubbard toolbox. *Annals of Physics*, 315:52, 2005.

[94] Ph. W. Courteille, V.S> Bagnato, and V.I. Yuakolov. Bose-Einstein condensation of trapped gases. *Laser Phys.*, 11:659–800, 2001.

[95] L.P. Pitaevskii and S. Stringari. *Bose-Einstein Condensation*. Oxford University Press, Oxford, UK, 2003.

[96] M. Ueda. *Fundamentals and New Frontiers of Bose-Einstein Condensation*. World Scientific, Toh Tuck, Singapore, 2010.

[97] I. Danshita, J. Williams, C. Sá de Melo, and C. Clark. Quantum phases of bosons in double-well optical lattices. *Phys. Rev. A*, 76:043606, 2007.

[98] R.P. Feynman. Quantum mechanical computers. *Foundations of Physics*, 16:507, 1986.

[99] P. Perez-Fernandez, P. Cejnar, J.M. Arias, J Dukelsky, J.E. Garcia-Ramos, and A. Relano. Quantum quench influenced by an excited-state phase transition. *Phys. Rev. A*, 83:033802, 2011.

[100] P. Cejnar, S. Heinze, and M. Macek. Coulomb analogy for nonhermitian degeneracies near quantum phase transitions. *Phys. Rev. Lett.*, 99:100601, 2007.

[101] W.D. Heiss and W.H. Steeb. *Level Repulsion and Exceptional Points*, chapter ISBN 9789401101691, pages 91–98. Springer Netherlands, 1995.

[102] P. Cejnar and P. Stransky. Impact of quantum phase transitions on excited-level dynamics. *Phys. Rev. E*, 78:031130, 2008.

[103] P. Ribeiro, J. Vidal, and R. Mosseri. Exact spectrum of the Lipkin-Meshkov-Glick model in the thermodynamic limit and finite-size corrections. *Phys. Rev. E*, 78:021106, 2008.

[104] M. Cristiani, O. Morsch, J.H. Muller, D. Ciampini, and E. Arimondo. Experimental properties of Bose-Einstein condensates in one-dimensional optical lattices: Bloch oscillations, Landau-Zener tunneling, and mean-field effects. *Phys. Rev. A.*, 65:063612, 2002. doi: 10.1103/PhysRevA.65.063612. URL `https://journals.aps.org/pra/abstract/10.1103/PhysRevA.65.063612`.

[105] L. D. Carr, M. L. Wall, D. G. Schirmer, R. C. Brown, J. E. Williams, and Charles W. Clark. Mesoscopic effects in quantum phases of ultracold quantum gases in optical lattices. *Phys. Rev. A*, 81:013613, 2010. doi: 10.1103/PhysRevA.81.013613. URL `https://link.aps.org/doi/10.1103/PhysRevA.81.013613`.

[106] Rudolf Gati, Michael Albiez, Jonas Foelling, Beorge Hemmerling, and Markus K. Oberthaler. Realization of a single Josephson junction for Bose-Einstein condensates. *Appl. Phys. B*, 82:207, 2006. doi: 10.1007/s00340-005-2059-z. URL `https://doi.org/10.1007/s00340-005-2059-z`.

[107] Maxwell Frederick Parsons. *Probing the Hubbard model with single-site resolution*. PhD thesis, Harvard University, 2016.

[108] R. Islam, R. Ma, P.M. Preiss, M.E. Tai, A. Lukin, M. Rispoli, and M. Greiner. Measuring entanglement entropy in a quantum many-body system. *Nature*, 528:77–83, 2015. doi: 10.1038/nature15750. URL `http://dx.doi.org/10.1038/nature15750`.

[109] Amir Itah, Hagar veksler, Oren Lahav, Alex Blumkin, Coral Moreno, Carmit Gordon, and Jeff Steinhauer. Direct observation of a sub-Poissonian number distribution of atoms in an optical lattice. *Phys. Rev. Lett.*, 104:113001, 2010.

[110] M.F. Parsons, A. Mazurenko, C.S. Chiu, G. Ji, D. Greif, and M. Greiner. Site-resolved measurement of the spin-correlation function in the fermi-hubbard model. *Science*, 353: 1253–1256, 2016. doi: 10.1126/science.aag1430. URL `http://science.sciencemag.org/content/353/6305/1253`.

[111] M.F. Parsons, F. Huber, A. Mazurenko, C.S. Chiu, W. Setiawan, K. Wooley-Brown, S. Blatt, and M. Greiner. Site-resolved imaging of fermion ^{6}Li in an optical lattice. *Phys. Rev. Lett.*, 114:213002, 2015. doi: 10.1103/PhysRevLett.114.213002. URL https://journals.aps.org/prl/abstract/10.1103/PhysRevLett.114.213002.

[112] D. Greif, M.F. Parsons, A. Mazurenko, C.S. Chiu, s. Blatt, F. Huber, G. Ji, and M. Greiner. Site-resolved imaging of a fermionic Mott insulator. *Science*, 351: 953, 2016. doi: 10.1126/science.aad9041. URL http://science.sciencemag.org/content/351/6276/953.

[113] M.P. Feynman. *Lectures on physics*. Addison-Wesley, New York, NY, 1965.

[114] M. A. García-March, D. R. Dounas-Frazer, and L. D. Carr. Macroscopic superposition of ultracold atoms with orbital degrees of freedom. *Phys. Rev. A*, 83:043612, 2011. doi: 10.1103/PhysRevA.83.043612. URL https://link.aps.org/doi/10.1103/PhysRevA.83.043612.

[115] J. Esteve, C. Gross, A. Weller S. Giovanazzi, and M.K. Oberthaler. Squeezing and entanglement in a Bose-Einstein condensate. *Nature*, 455:7217:1216–1219, 2008.

[116] T. Gericke, P. Wuertz, D. Reitz, T. Langen, and H. Ott. High-resolution scanning electron microscopy of an ultracold quantum gas. *Nature Phys.*, 4:949–953, 2008.

[117] R. Gerritsma, S. Whitlock, T. Fernholz, H. Schlatter, J.A. Luigjes, J.U. Thiele, J.B. Goedkoop, and R.J.C. Spreeuw. Lattice of microtraps for ultracold atoms based on patterned magnetic films. *Phys. Rev. A*, 76:033408, 2007.

[118] J. Joger, A. Negretti, and R. Gerritsma. Quantum dynamics of an atomic double-well system interacting with a trapped ion. *Phys. Rev. A*, 89:063621, 2014.

[119] J.M. Schurer, R. Gerritsma, P. Schmelcher, and A. Negretti. Impact of many-body correlations on the dynamics of an ion-controlled bosonic Josephson junction. *Phys. Rev. A*, 93:063602, 2016.

[120] M. Galbiati et al. Polariton condensation in photonic molecules. *Phys. Rev. Lett.*, 108: 126403, 2012. doi: 10.1103/PhysRevLett.108.126403. URL https://journals.aps.org/prl/abstract/10.1103/PhysRevLett.108.126403.

[121] Y. Yu, S. Han, X. Chu, S-I Chu, and Z Wang. Coherent temporal oscillations of macroscopic quantum states in a Josephson junction. *Science*, 296:889, 2002. doi: 10.1126/science.1069452. URL http://science.sciencemag.org/content/296/5569/889.

[122] B. Gaury, J. Weston, and X. Waintel. The a.c. Josephson effect without superconductivity. *Nature Comm.*, 6:6524, 2015. doi: 10.1038/ncomms7524. URL `https://www.nature.com/articles/ncomms7524`.

[123] S. Raghavan, A. Smerzi, S. Fantoni, and S.R. Shenoy. Coherent oscillations between two weakly coupled Bose-Einstein condensates: Josephson effects, π oscillations, and macroscopic quantum self-trapping. *Phys. Rev. A.*, 59:620, 1999. doi: 10.1103/PhysRevA.59.620. URL `https://journals.aps.org/pra/abstract/10.1103/PhysRevA.59.620`.

[124] A. Smerzi, S. Fantoni, S. Giovanazzi, and S. R. Shenoy. Quantum coherent atomic tunnelling between two trapped Bose-Einstein condensates. *Phys. Rev. Lett.*, 79:4950, 1997. doi: 10.1103/PhysRevLett.79.4950. URL `https://journals.aps.org/prl/abstract/10.1103/PhysRevLett.79.4950`.

[125] Rudolf Gati. *Bose-Einstein Condensates in a Single Double Well Potential*. PhD thesis, University of Heidelberg, Germany, 2004.

[126] M. Albiez. *Observation of nonlinear tunneling of a Bose-Einstein condensate in a single Josephson junction*. PhD thesis, University of Heidelberg, Germany, 2005.

[127] M. Tinkham. *Introduction to Superconductivity (2nd Ed.)*. McGraw-Hill, New York, NY, 2004.

[128] Markus Ansmann. *Benchmarking the Superconducting Josephson Phase Qubit - The Violation of Bell's Inequality*. PhD thesis, University of California - Santa Barbara, 2009.

[129] Daniel Sank. *Fast, Accurate State Measurement in Superconducting Qubits*. PhD thesis, University of California - Santa Barbara, 2014.

[130] T. van Duzer. *Principles of Superconducting Devices and Circuits (2nd Ed.)*. Prentice Hall, Upper Saddle River, NJ, 1999.

[131] M.A. Nielsen and I.L. Chuang. *Quantum Computation and Quantum Information*. Cambridge University Press, 2000.

[132] A.J. Berkley, H. Xu, R.C. Ramos, M.A. Gubrud, F.W. Strauch, P.R. Johnson, J.R. Anderson, A.J. Dragt, C.J. Lobb, and F.C. Wellstood. Entangled Macroscopic Quantum States in Two Superconducting Qubits. *Science*, 300:1548, 2003.

[133] M.D. Kim and J. Kim. Scalable quantum computing model in the circuit-QED lattice with circulator function. *J. Quantum Inf Process*, 16:192, 2017.

[134] A.N. Omelyanchouk, S. Savel'ev, A.M. Zagoskin, E. Il'iche, and Franco Nori. Noise-induced quantum coherence and persistent Rabi oscillations in a Josephson flux qubit. *Phys. Rev. B*, 80:212503, 2009.

[135] R. Augusiak, F.M. Cucchietti, and M. Lewenstein. *Modern Theories of Many-Particle Systems in Condensed Matter Physics*, chapter 843, pages 245–294. Springer, Berlin, Heidelberg, 2012.

[136] F. Verstrate, V. Murg, and J.I. Cirac. Matrix product states, projected entangled pair states, and variational renormalization group methods for quantum spin systems. *Adv. Phys.*, 57:143–224, 2008.

[137] J.I. Cirac and F. Verstrate. Renormalization and tensory product states in spin chains and lattices. *J. Phys. A:Math. Theor.*, 42:504004, 2009.

[138] V. Vedral. Mean-field approximations and multipartite thermal correlations. *New J. Pys.*, 6:22, 2004.

[139] M. Troyer and U.-J. Wiese. Computational complexity and fundamental limitations to fermionic quantum Monte Carlo simulations. *Phys. Rev. Lett.*, 94:170201, 2005.

[140] J. Oitmaa, C. Hamer, and W. Zheng. *Series Expansion Methods for Strongly Interacting Lattice Models*. Cambridge University Press, New York, 2006.

[141] K.Sakmann, A.I. Streltsov, O.E. Alon, and L.S. Cederbaum. Exact Quantum Dynamics of a Bosonic Josephson Junction. *Phys. Rev. Lett.*, 103:220601, 2009.

[142] J. Eisert, M. Cramer, and M.B. Plenio. Area laws for the entanglement entropy. *Rev. Mod. Phys.*, 82:277, 2010.

[143] U. Schollwöck. The density-matrix renormalization group in the age of matrix product states. *Annals of Phys.*, 326:96, 2011. doi: 10.1016/j.aop.2010.09.012. URL `https://doi.org/10.1016/j.aop.2010.09.012`.

[144] N. Ogawa, T. Takayanagi, and T. Ugajin. Holographic Fermi surfaces and entangelement entropy. *J. High Energy Phys.*, 1201:125, 2012.

[145] S.A. Hartnoll. Lectures on holographic methods for condensed matter physics. *Classical Quantum Gravity*, 26:224002, 2009.

[146] I. Danshita and A. Polkovnikov. Accurate numerical verification of the instanton method for macroscopic quantum tunneling: Dynamics of phase slips. *Phys. Rev. B*, 82:094304, 2010.

[147] I. Danshita and A. Polkovnikov. Quantum phase slips in one-dimensional superfluids in a periodic potential. *Phys. Rev. A.*, 85:023638, 2012.

[148] R. Beinke, S. Klaiman, L.S. Cederbaum, A.I. Streltsov, and O.E. Alon. Many-body tunneling dynamics of Bose-Einstein condensates and vortex states in two spatial dimensions. *Phys. Rev. A.*, 92:043627, 2015.

[149] Lode, Axel U.J. and Streltsov, Alexej I. and Sakmann, Kaspar and Alon, Ofir E. and Cederbaum, Lorenz S. How an interacting many-body system tunnels through a potential barrier to open space. *Proceedings of the National Academy of Sciences*, 109:13521–13525, 2012. doi: 10.1073/pnas.1201345109. URL `http://www.pnas.org/content/109/34/13521`.

[150] MPS. Matrix product state open source code. https://sourceforge.net/projects/openmps/.

[151] Steven Wayne Patton. *Attenuation Estimation from Acoustic Well Logs.* PhD thesis, Oklahoma State University, 1986.

[152] R.V. Mishmash. Quantum many-body dynamics of ultracold bosons in one-dimensional lattices: Theoretical aspects, simulation methods, and soliton formation and stability. Master's thesis, Colorado School of Mines, 2008.

[153] A.J. Daley. *Manipulation and Simulation of Cold Atoms in Optical Lattices.* PhD thesis, Leopold-Franzens-Universitat Innsbruck, 2005.

[154] G. Shchedrin. The degenerate case: perturbation theory. *Lecture notes*, pages 7–10, 2017.

[155] Khan W. Mahmud, Heidi Perry, and William P. Reinhardt. Quantum phase-space picture of Bose-Einstein condensates in a double well. *Phys. Rev. A*, 71:023615, 2005. doi: 10.1103/PhysRevA.71.023615. URL `http://link.aps.org/doi/10.1103/PhysRevA.71.023615`.

[156] David L. Vargas and Lincoln D. Carr. Detecting Quantum Phase Transitions via Mutual Information Complex Networks. 2015. URL `https://www.scienceopen.com/document?vid=db7328ca-7dba-4029-ada9-326211bbee03`.

[157] S.T. Tserkis, Ch.C. Moustakidis, S.E. Massen, and C.P. Panos. Quantum tunneling and information entropy in a double square well potential: The ammonia molecule. *Physics Letters A*, 378:497 – 504, 2014. doi: http://dx.doi.org/10.1016/j.physleta.2013.12.004. URL `http://www.sciencedirect.com/science/article/pii/S037596011301102X`.

[158] Giovanni Jona-Lasinio, Carlo Presilla, and Cristina Toninelli. Interaction induced localization in a gas of pyramidal molecules. *Phys. Rev. Lett.*, 88:123001, 2002. doi: 10.1103/PhysRevLett.88.123001. URL http://link.aps.org/doi/10.1103/PhysRevLett.88.123001.

[159] A. del Campo, F. Delgado, G. García-Calderón, J. G. Muga, and M. G. Raizen. Decay by tunneling of bosonic and fermionic Tonks-Girardeau gases. *Phys. Rev. A*, 74:013605, 2006. doi: 10.1103/PhysRevA.74.013605. URL http://link.aps.org/doi/10.1103/PhysRevA.74.013605.

[160] G. Zürn, A. N. Wenz, S. Murmann, A. Bergschneider, T. Lompe, and S. Jochim. Pairing in few-fermion systems with attractive interactions. *Phys. Rev. Lett.*, 111: 175302, 2013. doi: 10.1103/PhysRevLett.111.175302. URL http://link.aps.org/doi/10.1103/PhysRevLett.111.175302.

[161] L. Salasnich, N. Manini, and F. Toigo. Macroscopic periodic tunneling of fermi atoms in the bcs-bec crossover. *Phys. Rev. A*, 77:043609, 2008. doi: 10.1103/PhysRevA.77.043609. URL http://link.aps.org/doi/10.1103/PhysRevA.77.043609.

[162] John M. Martinis, M. Ansmann, and J. Aumentado. Energy decay in superconducting josephson-junction qubits from nonequilibrium quasiparticle excitations. *Phys. Rev. Lett.*, 103:097002, 2009. doi: 10.1103/PhysRevLett.103.097002. URL http://link.aps.org/doi/10.1103/PhysRevLett.103.097002.

[163] G. Catelani, S. E. Nigg, S. M. Girvin, R. J. Schoelkopf, and L. I. Glazman. Decoherence of superconducting qubits caused by quasiparticle tunneling. *Phys. Rev. B*, 86:184514, 2012. doi: 10.1103/PhysRevB.86.184514. URL http://link.aps.org/doi/10.1103/PhysRevB.86.184514.

[164] D. R. Dounas-Frazer, A. M. Hermundstad, and L. D. Carr. Ultracold bosons in a tilted multilevel double-well potential. *Phys. Rev. Lett.*, 99:200402, 2007. doi: 10.1103/PhysRevLett.99.200402. URL https://link.aps.org/doi/10.1103/PhysRevLett.99.200402.

[165] L. D. Carr, D. R. Dounas-Frazer, and M. A. Garcia-March. Dynamical realization of macroscopic superposition states of cold bosons in a tilted double well. *EPL (Europhysics Letters)*, 90:10005, 2010. URL http://stacks.iop.org/0295-5075/90/i=1/a=10005.

[166] Seyed Ebrahim Gharashi and D. Blume. Tunneling dynamics of two interacting one-dimensional particles. *Phys. Rev. A*, 92:033629, 2015. doi: 10.1103/PhysRevA.92.033629. URL https://link.aps.org/doi/10.1103/PhysRevA.92.033629.

[167] R. Lundmark, C. Forssén, and J. Rotureau. Tunneling theory for tunable open quantum systems of ultracold atoms in one-dimensional traps. *Phys. Rev. A*, 91:041601, 2015. doi: 10.1103/PhysRevA.91.041601. URL https://link.aps.org/doi/10.1103/PhysRevA.91.041601.

[168] Masahito Ueda and Anthony J. Leggett. Macroscopic quantum tunneling of a Bose-Einstein condensate with attractive interaction. *Phys. Rev. Lett.*, 80:1576–1579, 1998. doi: 10.1103/PhysRevLett.80.1576. URL http://link.aps.org/doi/10.1103/PhysRevLett.80.1576.

[169] L.D. Carr, M.J. Holland, and B.A. Malomed. Macroscopic quantum tunnelling of Bose-Einstein condensates in a finite potential well. *J. Phys. B: At. Mol. Opt. Phys.*, 38:3217, 2005.

[170] Hidehiro Asai, Yukihiro Ota, Shiro Kawabata, Masahiko Machida, and Franco Nori. Theory of macroscopic quantum tunneling with josephson-leggett collective excitations in multiband superconducting josephson junctions. *Phys. Rev. B*, 89:224507, 2014. doi: 10.1103/PhysRevB.89.224507. URL http://link.aps.org/doi/10.1103/PhysRevB.89.224507.

[171] Sudip Kumar Haldar, Pankaj Kumar Debnath, and Barnali Chakrabarti. Macroscopic quantum many-body tunneling of attractive Bose-Einstein condensates in an anharmonic trap. *The European Physical Journal D*, 67:188, 2013. doi: 10.1140/epjd/e2013-40008-7. URL http://dx.doi.org/10.1140/epjd/e2013-40008-7.

[172] Daniel A. Steck, Windell H. Oskay, and Mark G. Raizen. Fluctuations and decoherence in chaos-assisted tunneling. *Phys. Rev. Lett.*, 88:120406, 2002. doi: 10.1103/PhysRevLett.88.120406. URL http://link.aps.org/doi/10.1103/PhysRevLett.88.120406.

[173] A. Mouchet, C. Miniatura, R. Kaiser, B. Grémaud, and D. Delande. Chaos-assisted tunneling with cold atoms. *Phys. Rev. E*, 64:016221, 2001. doi: 10.1103/PhysRevE.64.016221. URL http://link.aps.org/doi/10.1103/PhysRevE.64.016221.

[174] Michael Schreiber, Sean S. Hodgman, Pranjal Bordia, Henrik P. Lüschen, Mark H. Fischer, Ronen Vosk, Ehud Altman, Ulrich Schneider, and Immanuel Bloch. Observation of many-body localization of interacting fermions in a quasirandom optical lattice. *Science*, 349:842–845, 2015. doi: 10.1126/science.aaa7432. URL http://science.sciencemag.org/content/349/6250/842.

[175] Rahul Nandkishore and David A. Huse. Many-body localization and thermalization in quantum statistical mechanics. *Annual Review of Condensed Matter Physics*, 6:15–38, 2015. doi: 10.1146/annurev-conmatphys-031214-014726. URL https://doi.org/10.1146/annurev-conmatphys-031214-014726.

[176] Boris A. Malomed. *Spontaneous Symmetry Breaking, Self-Trapping, and Josephson Oscillations*, chapter ISBN 9783642212062. Springer, 2014.

[177] Han Du, Xingwang Zhang, Guiqiang Chen, Jie Deng, Fook Siong Chau, and Guangya Zhou. Precise control of coupling strength in photonic molecules over a wide range using nanoelectromechanical systems. *Sci. Rep.*, 6:24766, 2016. doi: 10.1038/srep24766. URL https://www.nature.com/articles/srep24766.

[178] B.A. Malomed. Nonlinear optics: Symmetry breaking in laser cavities. *Nature Photonics*, 9(5):287–289, 2015. doi: 10.1038/nphoton.2015.66. URL https://www.nature.com/articles/nphoton.2015.66.

[179] K. Baumann, C. Guerlin, F. Brennecke, and T.D. Esslinger. The Dicke quantum phase transition with a superfluid gas in an optical cavity. *Nature*, 464:1301–1306, 2010. doi: 10.1038/nature09009. URL https://www.nature.com/articles/nature09009.

[180] A. Alberucci, A. Piccardi, N. Kravets, O. Buchnev, and G. Assanto. Soliton enhancement of spontaneous symmetry breaking. *Optica*, 2(9):783, 2015. doi: https://doi.org/10.1364/OPTICA.2.000783. URL https://www.osapublishing.org/optica/abstract.cfm?uri=optica-2-9-783.

[181] A. Trenkwalder, G. Spagnolli, G. Semeghini, S. Coop, M. Landini, P. Castilho, L. Pezze, G. Modugno, M. inguscio, A. Smerzi, and M. Fattori. Quantum phase transitions with parity-symmetry breaking and hysteresis. *Nature Physics*, 12:826–829, 2016. doi: doi:10.1038/nphys3743. URL https://www.nature.com/articles/nphys3743?WT.feed_name=subjects_physics.

[182] Philippe Hamel, Samir Haddadi, Fabrice Raineri, Paul Monnier, Gregoire Beaudoin, Isabelle Sagnes, Ariel Levenson, and Alejandro M. Yacomotti. Spontaneous mirror-symmetry breaking in two coupled nanolasers. *Nature Photonics*, 9:311–315, 2015. doi: https://doi.org/10.1364/CLEO_QELS.2015.FW1D.7. URL https://www.osapublishing.org/abstract.cfm?uri=CLEO_QELS-2015-FW1D.7.

[183] E.B. Sonin. Effect of shot noise on a Coulomb blockaded single Josephson junction. *Phys. Rev. B*, 70:140506, 2004. doi: 10.1103/PhysRevB.70.140506. URL https://journals.aps.org/prb/abstract/10.1103/PhysRevB.70.140506.

[184] D. B. Haviland, L. S. Kuzmin, P. Delsing, and T. Claeson. Observation of the Coulomb Blockade of Cooper Pair Tunnelling in Single Josephson Junctions. *EPL (Europhysics Letters)*, 16:103, 1991. doi: https://doi.org/10.1209/0295-5075/16/1/018. URL http://iopscience.iop.org/article/10.1209/0295-5075/16/1/018/meta.

[185] L. J. Geerligs, V. F. Anderegg, C. A. van der Jeugd, J. Romijn, and J. E. Mooij. Influence of dissipation on the Coulomb blockade in small tunnel junctions. *EPL (Europhysics Letters)*, 10:79, 1989. doi: https://doi.org/10.1209/0295-5075/10/1/014. URL http://stacks.iop.org/0295-5075/10/i=1/a=014.

[186] David B. Haviland, Karin Andersson, and Peter øAgren. Superconducting and insulating behavior in one-dimensional Josephson junction arrays. *J. Low Temp. Phys.*, 118:5-6:733–749, 2000. doi: 10.1023/A:1004603814529. URL https://doi.org/10.1023/A:1004603814529.

[187] R. Khomeriki, S. Ruffo, and S. Wimberger. Driven collective quantum tunneling of ultracold atoms in engineered optical lattices. *EPL (Europhysics Letters)*, 77:40005, 2007. URL http://stacks.iop.org/0295-5075/77/i=4/a=40005.

[188] M. Olshanii. Atomic Scattering in the Presence of an External Confinement and a Gas of Impenetrable Bosons. *Phys. Rev. Lett.*, 81:938–941, 1998. doi: 10.1103/PhysRevLett.81.938. URL https://link.aps.org/doi/10.1103/PhysRevLett.81.938.

[189] Matthew P.A. Fisher, Peter B. Weichman, G. Grinstein, and Daniel S. Fisher. Boson localization and the superfluid-insulator transition. *Phys. Rev. B.*, 40:546, 1989. doi: 10.1103/PhysRevB.40.546. URL https://journals.aps.org/prb/abstract/10.1103/PhysRevB.40.546.

[190] G.G. Batrouni, V. Rousseau, R.T. Scalettar, M. Rigol, A. Muramatsu, P.J.H. Denteneer, and M. Troyer. Mott domains of bosons confined on optical lattices. *Phys. Rev. Lett.*, 89:117203, 2002. doi: https://doi.org/10.1103/PhysRevLett.89.117203. URL https://journals.aps.org/prl/abstract/10.1103/PhysRevLett.89.117203.

[191] W.P. Reinhardt, I.I. Satija, B. Robbins, and C.W. Clark. Bright and dark solitons and breathers in strongly repulsive Bose-Einstein condensates. *arXiv:1102.4042v1*, 2011. URL https://arxiv.org/abs/1102.4042.

[192] H. Francis Song, S. Rachel, and K.L. Hur. General relation between entanglement and fluctuations in one dimension. *Phys. Rev. B.*, 82:012405, 2010. doi: 10.1103/PhysRevB.82.012405. URL https://journals.aps.org/prb/abstract/10.1103/PhysRevB.82.012405.

[193] M.L. Wall and L.D. Carr. Out of equilibrium dynamics with Matrix Product States. *New J. Phys.*, 14:125015, 2012. doi: https://doi.org/10.1088/1367-2630/14/12/125015. URL http://stacks.iop.org/1367-2630/14/i=12/a=125015.

[194] U. Schollwöck. The density-matrix renormalization group. *Rev. Mod. Phys.*, 77:259, 2005. doi: https://doi.org/10.1103/RevModPhys.77.259. URL https://journals.aps.org/rmp/abstract/10.1103/RevModPhys.77.259.

[195] Eric Jones, Travis Oliphant, Pearu Peterson, et al. SciPy: Open source scientific tools for Python, 2001–. URL http://www.scipy.org/.

[196] L. Petzold. Automatic Selection of Methods for Solving Stiff and Nonstiff Systems of Ordinary Differential Equations. *SIAM Journal on Scientific and Statistical Computing*, 4:136–148, 1983. doi: 10.1137/0904010. URL http://epubs.siam.org/doi/abs/10.1137/0904010.

[197] S. van Frank, M. Bonneau, J. Schmiedmayer, S. Hild, C. Gross, M. Cheneau, I. Bloch, T. Pichler, A. Negretti, T. Calarco, and S. Montangero. Optimal control of complex atomic quantum systems. *Scientific Reports*, 6:34187, 2016. doi: 10.1038/srep34187. URL https://www.nature.com/articles/srep34187.

[198] Sascha Zöllner, Hans-Dieter Meyer, and Peter Schmelcher. Tunneling dynamics of a few bosons in a double well. *Phys. Rev. A*, 78:013621, 2008. doi: 10.1103/PhysRevA.78.013621. URL https://link.aps.org/doi/10.1103/PhysRevA.78.013621.

[199] Axel U. J. Lode, Alexej I. Streltsov, Ofir E. Alon, Hans-Dieter Meyer, and Lorenz S. Cederbaum. Exact decay and tunnelling dynamics of interacting few-boson systems. *Journal of Physics B: Atomic, Molecular and Optical Physics*, 42:044018, 2009. URL http://stacks.iop.org/0953-4075/42/i=4/a=044018.

[200] Immanuel Bloch, Jean Dalibard, and Sylvain Nascimbene. Quantum simulations with ultracold quantum gases. *Nature Physics*, 8:267–276, 2012. doi: 10.1038/nphys2259. URL https://www.nature.com/articles/nphys2259.

[201] Giacomo Valtolina, Alessia Burchianti, Andrea Amico, Elettra Neri, Klejdja Xhani, Jorge Amin Seman, Andrea Trombettoni, Augusto Smerzi, Matteo Zaccanti, Massimo Inguscio, and Giacomo Roati. Josephson effect in fermionic superfluids across the bec-bcs crossover. *Science*, 350:1505–1508, 2015. doi: 10.1126/science.aac9725. URL http://science.sciencemag.org/content/350/6267/1505.

[202] A. Burchianti, F. Scazza, A. Amico, G. Valtolina, J. A. Seman, C. Fort, M. Zaccanti, M. Inguscio, and G. Roati. Connecting dissipation and phase slips in a josephson junction between fermionic superfluids. *Phys. Rev. Lett.*, 120:025302, 2018. doi: 10.1103/PhysRevLett.120.025302. URL https://link.aps.org/doi/10.1103/PhysRevLett.120.025302.

[203] K Henderson, C Ryu, C MacCormick, and M G Boshier. Experimental demonstration of painting arbitrary and dynamic potentials for Bose-Einstein condensates. *New Journal of Physics*, 11:043030, 2009. URL http://stacks.iop.org/1367-2630/11/i=4/a=043030.

[204] V. Balachandran, G. Beneti, E. Pereira, G. Casati, and D. Poletti. Perfect diode in quantum spin chains. *arXiv*, 2017. URL https://arxiv.org/abs/1707.08823.

[205] B. T. Seaman, M. Krämer, D. Z. Anderson, and M. J. Holland. Atomtronics: Ultracold-atom analogs of electronic devices. *Phys. Rev. A*, 75:023615, 2007. doi: 10.1103/PhysRevA.75.023615. URL https://link.aps.org/doi/10.1103/PhysRevA.75.023615.

[206] Aijun Li, Stephen Eckel, Benjamin Eller, Kayla E. Warren, Charles W. Clark, and Mark Edwards. Superfluid transport dynamics in a capacitive atomtronic circuit. *Phys. Rev. A*, 94:023626, 2016. doi: 10.1103/PhysRevA.94.023626. URL https://link.aps.org/doi/10.1103/PhysRevA.94.023626.

[207] Chen-Yen Lai and Chih-Chun Chien. Challenges and constraints of dynamically emerged source and sink in atomtronic circuits: From closed-system to open-system approaches. *Scientific Reports*, 6:37256, 2016. doi: 10.1038/srep37256. URL https://www.nature.com/articles/srep37256.

[208] Seth C Caliga, Cameron J E Straatsma, and Dana Z Anderson. Experimental demonstration of an atomtronic battery. *New Journal of Physics*, 19:013036, 2017. URL http://stacks.iop.org/1367-2630/19/i=1/a=013036.

[209] T. Haug, H. Heimonen, R. Dumke, L.-C. Kwek, and L. Amico. The Aharonov-Bohm effect in mesoscopic Bose-Einstein condensates. *arXiv*, 2017. URL https://arxiv.org/abs/1706.05180v2.

[210] R. A. Pepino, J. Cooper, D. Z. Anderson, and M. J. Holland. Atomtronic circuits of diodes and transistors. *Phys. Rev. Lett.*, 103:140405, 2009. doi: 10.1103/PhysRevLett.103.140405. URL https://link.aps.org/doi/10.1103/PhysRevLett.103.140405.

[211] Seth C Caliga, Cameron J E Straatsma, Alex A Zozulya, and Dana Z Anderson. Principles of an atomtronic transistor. *New Journal of Physics*, 18:015012, 2016. URL http://stacks.iop.org/1367-2630/18/i=1/a=015012.

[212] J. Y. Vaishnav, Julius Ruseckas, Charles W. Clark, and Gediminas Juzeliūnas. Spin Field Effect Transistors with Ultracold Atoms. *Phys. Rev. Lett.*, 101:265302, 2008. doi: 10.1103/PhysRevLett.101.265302. URL https://link.aps.org/doi/10.1103/PhysRevLett.101.265302.

[213] C. Ryu, P. W. Blackburn, A. A. Blinova, and M. G. Boshier. Experimental realization of Josephson junctions for an atom SQUID. *Phys. Rev. Lett.*, 111:205301, 2013. doi: 10.1103/PhysRevLett.111.205301. URL https://link.aps.org/doi/10.1103/PhysRevLett.111.205301.

[214] Amy C Mathey and L Mathey. Realizing and optimizing an atomtronic SQUID. *New Journal of Physics*, 18:055016, 2016. URL http://stacks.iop.org/1367-2630/18/i=5/a=055016.

[215] Tobias Haug, Joel Tan, Mark Theng, Rainer Dumke, Leong-Chuan Kwek, and Luigi Amico. Readout of the atomtronic quantum interference device. *Phys. Rev. A*, 97: 013633, 2018. doi: 10.1103/PhysRevA.97.013633. URL https://link.aps.org/doi/10.1103/PhysRevA.97.013633.

[216] S. Eckel, J.G. Lee, F. Jendrzejewski, N. Murray, C.W. Clark, C.J. Lobb, W.D. Phillips, M. Edwards, and G.K. Campbell. Hysteresis in a quantized superfluid atomtronic circuit. *Nature*, 506:200–203, 2014. doi: 10.1038/nature12958. URL https://www.nature.com/articles/nature12958.

[217] Luigi Amico, Gerhard Birkl, Malcolm Boshier, and Leong-Chuan Kwek. Focus on atomtronics-enabled quantum technologies. *New Journal of Physics*, 19:020201, 2017. URL http://stacks.iop.org/1367-2630/19/i=2/a=020201.

[218] M. K. Olsen and A. S. Bradley. Quantum ultracold atomtronics. *Phys. Rev. A*, 91: 043635, 2015. doi: 10.1103/PhysRevA.91.043635. URL https://link.aps.org/doi/10.1103/PhysRevA.91.043635.

[219] Damian Draxler, Jutho Haegeman, Frank Verstraete, and Matteo Rizzi. Continuous matrix product states with periodic boundary conditions and an application to atomtronics. *Phys. Rev. B*, 95:045145, 2017. doi: 10.1103/PhysRevB.95.045145. URL https://link.aps.org/doi/10.1103/PhysRevB.95.045145.

[220] Daniel Jaschke, Michael L. Wall, and Lincoln D. Carr. Open source Matrix Product States: Opening ways to simulate entangled many-body quantum systems in one dimension. *Computer Physics Communications*, 225:59 – 91, 2018. doi: https://doi.org/10.1016/j.cpc.2017.12.015. URL http://www.sciencedirect.com/science/article/pii/S0010465517304204.

[221] William Cody Burton, Colin J. Kennedy, Woo Chang Chung, Samarth Vadia, Wenlan Chen, and Wolfgang Ketterle. Coherence times of Bose-Einstein condensates beyond the shot-noise limit via superfluid shielding. *Phys. Rev. Lett.*, 117:275301, 2016. doi: 10.1103/PhysRevLett.117.275301. URL https://link.aps.org/doi/10.1103/PhysRevLett.117.275301.

[222] Ryuta Yamamoto, Jun Kobayashi, Takuma Kuno, Kohei Kato, and Yoshiro Takahashi. An ytterbium quantum gas microscope with narrow-line laser cooling. *New Journal of Physics*, 18:023016, 2016. URL http://stacks.iop.org/1367-2630/18/i=2/a=023016.

[223] W. S. Bakr, A. Peng, M. E. Tai, R. Ma, J. Simon, J. I. Gillen, S. Fölling, L. Pollet, and M. Greiner. Probing the superfluid–to–Mott insulator transition at the single-atom level. *Science*, 329:547–550, 2010. doi: 10.1126/science.1192368. URL http://science.sciencemag.org/content/329/5991/547.

[224] Takafumi Tomita, Shuta Nakajima, Ippei Danshita, Yosuke Takasu, and Yoshiro Takahashi. Observation of the Mott insulator to superfluid crossover of a driven-dissipative Bose-Hubbard system. *Science Advances*, 3(12), 2017. doi: 10.1126/sciadv.1701513. URL http://advances.sciencemag.org/content/3/12/e1701513.

[225] Mark T. Lusk, Charles A. Stafford, Jeramy D. Zimmerman, and Lincoln D. Carr. Control of exciton transport using quantum interference. *Phys. Rev. B*, 92:241112, 2015. doi: 10.1103/PhysRevB.92.241112. URL https://link.aps.org/doi/10.1103/PhysRevB.92.241112.

[226] Xiaoning Zang, Simone Montangero, Lincoln D. Carr, and Mark T. Lusk. Engineering and manipulating exciton wave packets. *Phys. Rev. B*, 95:195423, 2017. doi: 10.1103/PhysRevB.95.195423. URL https://link.aps.org/doi/10.1103/PhysRevB.95.195423.

[227] Soeren Lammers, Igor Boettcher, and Christof Wetterich. Dimensional crossover of nonrelativistic bosons. *Phys. Rev. A*, 93:063631, 2016. doi: 10.1103/PhysRevA.93.063631. URL https://link.aps.org/doi/10.1103/PhysRevA.93.063631.

[228] Soeren Lammers, Igor Boettcher, and Christof Wetterich. Reliable equation of state for composite bosons in the 2D BCS-BEC crossover. *Journal of Superconductivity and Novel Magnetism*, 29:697, 2016. URL https://arxiv.org/abs/1512.04067.

[229] Jayson G. Cosme and Oleksandr Fialko. Relaxation dynamics of ultracold bosons in a double-well potential: Thermalization and prethermalization in a nearly integrable model. *Phys. Rev. A*, 92:033607, 2015. doi: 10.1103/PhysRevA.92.033607. URL https://link.aps.org/doi/10.1103/PhysRevA.92.033607.

[230] Kelly R. Patton. Fully controllable kondo system: Coupling a flux qubit and an ultracold fermi gas. *Phys. Rev. A*, 93:023643, 2016. doi: 10.1103/PhysRevA.93.023643. URL https://link.aps.org/doi/10.1103/PhysRevA.93.023643.

[231] Antonio Lara, Farkhad G. Aliev, Victor V. Moshchalkov, and Yuri M. Galperin. Thermally driven inhibition of superconducting vortex avalanches. *Phys. Rev. Applied*, 8: 034027, 2017. doi: 10.1103/PhysRevApplied.8.034027. URL `https://link.aps.org/doi/10.1103/PhysRevApplied.8.034027`.

APPENDIX

CALCULATIONS AND USEFUL SCRIPTS

The following appendices are a selection of calculations that may be useful and are not meant as an exhaustive list of calculations performed as part of this PhD.

A.1 Sudden Approximation

The following is a Mathematica notebook wherein a single well is suddenly quenched from 2 sites to 4 sites. The Hamiltonian is diagonalized exactly and propagated in real time. The purpose is to demonstrate the immediate response of the initial state to such a quench. In the low barrier limit with strong interactions, the projected state exhibits particle-hole pairing, which are low-lying excited states of a Mott insulating ground state. In the high barrier limit for strong interactions, the projected sates exhibits low-lying excited states of the two wells themselves. We performed the calculation three ways: one way we used the ground state of the 2-site system for $J = 0$, or an initial state $|1100\rangle$, the next way we used a ground state that is a superposition of the possible states for the 2-site system, $\alpha_1|20\rangle + \alpha_2|11\rangle + \alpha_3|20\rangle$ for small, finite J. The third way we used perturbation theory for small finite J, which agrees with the exact diagonalization case.

Sudden Approximation Dynamics for the BHH

Marie McLain

This notebook demonstrates the projection of the ground state of N = 2 particles on L = 2 lattice sites onto a system of L = 4 lattice sites, number conserving, for strong interactions. Clearly, local dimension is 2 for all cases.
The Fock basis dimension is 3 for L = 2:
| 0 2 >
| 1 1 >
| 2 0 >
While the basis dimension is 10 for L = 4:
| 0 0 0 2 >
| 0 0 1 1 >
| 0 0 2 0 >
| 0 1 0 1 >
| 0 1 1 0 >
| 0 2 0 0 >
| 1 0 0 1 >
| 1 0 1 0 >
| 1 1 0 0 >
| 2 0 0 0 >

---

1. Initial state is | 1 1 0 0 > (i.e. ground state of L=2 for J=0). But, projected states have small J. (If the projected states had J=0, then we would have a stationary state)

In[1]:=
```
Clear["Global`*"]
```

In[2]:=
```
(*define parameters and numerical resolution*)
params = {ħ → 1, U → 30.0, J → 1.};
resolution = 1.0 * 10^-13;
```

In[4]:=
```
(*Find Eigenvalues and eigenvectors of 10x10 Hamiltonian for L=4, for projection*)
H2 = {{U, -Sqrt[2.] J, 0, 0, 0, 0, 0, 0, 0, 0},
   {-Sqrt[2.] J, 0, -Sqrt[2.] J, -J, 0, 0, 0, 0, 0, 0},
   {0, -Sqrt[2.] J, U, 0, -Sqrt[2.] J, 0, 0, 0, 0, 0}, {0, -J, 0, 0, -J, 0, -J, 0, 0, 0},
   {0, 0, -Sqrt[2.] J, -J, 0, -Sqrt[2.] J, 0, -J, 0, 0},
   {0, 0, 0, 0, -Sqrt[2.] J, U, 0, 0, -Sqrt[2.] J, 0}, {0, 0, 0, -J, 0, 0, 0, -J, 0, 0},
   {0, 0, 0, 0, -J, 0, -J, 0, -J, 0}, {0, 0, 0, 0, 0, -Sqrt[2.] J, 0, -J, 0, -Sqrt[2.] J},
   {0, 0, 0, 0, 0, 0, 0, 0, -Sqrt[2.] J, U}};
{eVals2, eVects2} = Eigensystem[H2 /. params];
For[ii = 1, ii < Length[eVals2] + 1, ii++,
 For[jj = 1, jj < Length[eVals2] + 1, jj++,
  (*Limit numerical resolution*)
  If[Abs[eVects2[[ii]][[jj]]] ≤ resolution, eVects2[[ii]][[jj]] = 0.0]
 ]]
(* Wait to normalize until after projection onto superposition of 4-
 site basis states
  For[kk=1,kk<Length[eVals2],kk++,
   eVects2[[kk]]=2eVects2[[kk]]/Total[Abs[eVects2[[kk]]]]
  ]*)
eVects2
```

Out[7]=
```
{{-0.269404, 0.0431729, -0.650904, -0.00345848, 0.0611366,
  -0.650904, 0.000228837, -0.00345848, 0.0431729, -0.269404},
 {-0.498899, 0.0468808, -0.498899, -0.0015558, 0., 0.498899, 0., 0.0015558,
  -0.0468808, 0.498899}, {-0.652933, 0.0180085, 0.270241, 0.000248679,
  -0.0254621, 0.270241, -0.0000165571, 0.000248679, 0.0180085, -0.652933},
 {-0.5, 0., 0.5, 0., 0., -0.5, 0., 0., 0., 0.5}, {-0.010471, -0.239162, -0.0308495,
  -0.491956, -0.465455, -0.0308495, -0.42754, -0.491956, -0.239162, -0.010471},
 {-0.0104634, -0.205919, -0.0320837, 0.506694, -0.425486, -0.0320837,
  -0.467334, 0.506694, -0.205919, -0.0104634}, {-0.023455, -0.515243,
  -0.023455, -0.48314, 0., 0.023455, 0., 0.48314, 0.515243, 0.023455},
 {-0.0234516, -0.482002, -0.0234516, 0.516308, 0., 0.0234516, 0., -0.516308,
  0.482002, 0.0234516}, {0.0209367, 0.445556, 0.0338064, -0.0346713,
  0.273879, 0.0338064, -0.722761, -0.0346713, 0.445556, 0.0209367},
 {0.0210397, 0.446868, -0.0130072, 0.00508743, -0.723131,
  -0.0130072, 0.27645, 0.00508743, 0.446868, 0.0210397}}
```

In[8]:=
```
(*Eigenvalues of the 4-site system*)
ListPlot[Sort[eVals2], PlotMarkers → {Automatic, Medium}, ImageSize → Large,
 Frame → True, FrameLabel → {"Eigen index", "Energy"}, PlotLabel → "Eigenenergies, L=4"]
```

Out[8]=

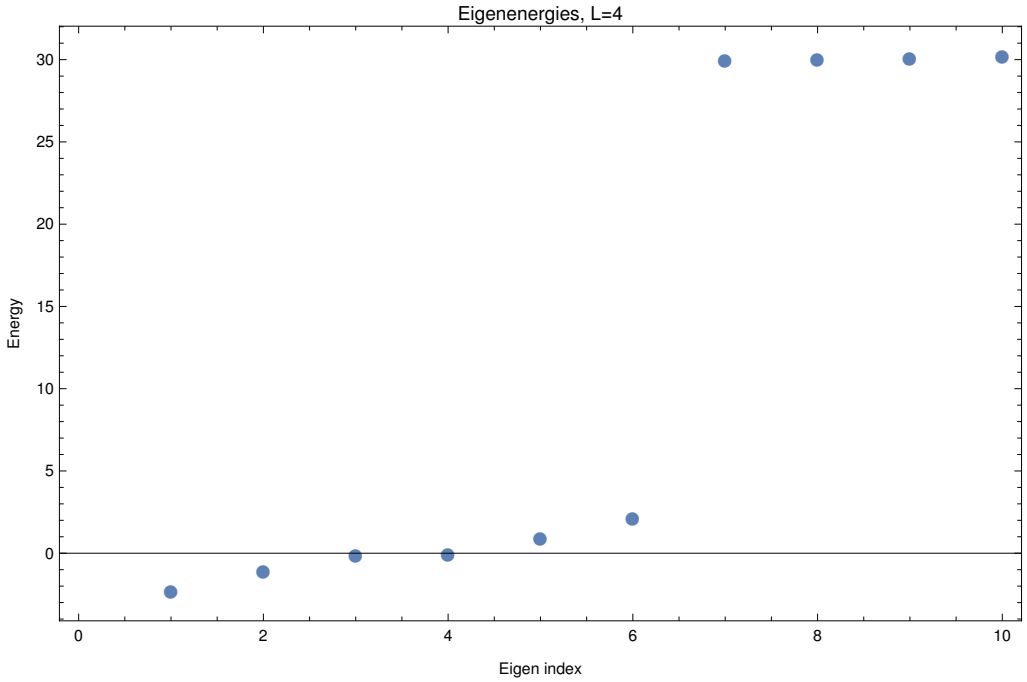

In[9]:=
```
(*Map eigenvectors from the 10-dimensional Hamiltonian onto 4-site superpositions*)
eVectsM = Array[Null &, Length[eVals2]];
For[iii = 1, iii <= Length[eVals2], iii++,
 eVectsM[[iii]] = eVects2[[iii]][[1]] * {0, 0, 0, 2} + eVects2[[iii]][[2]] * {0, 0, 1, 1} +
   eVects2[[iii]][[3]] * {0, 0, 2, 0} + eVects2[[iii]][[4]] * {0, 1, 0, 1} +
   eVects2[[iii]][[5]] * {0, 1, 1, 0} + eVects2[[iii]][[6]] * {0, 2, 0, 0} +
   eVects2[[iii]][[7]] * {1, 0, 0, 1} + eVects2[[iii]][[8]] * {1, 0, 1, 0} +
   eVects2[[iii]][[9]] * {1, 1, 0, 0} + eVects2[[iii]][[10]] * {2, 0, 0, 0}
]
eVectsM;
```

In[12]:=
```
(*Non-normalized Eigenvectors for L=4, after projection onto 4-sites*)
Table[ListLinePlot[eVectsM[[i]], PlotRange → {{1, 4}, {-2, 2}}], {i, 1, 10}]
```

Out[12]=

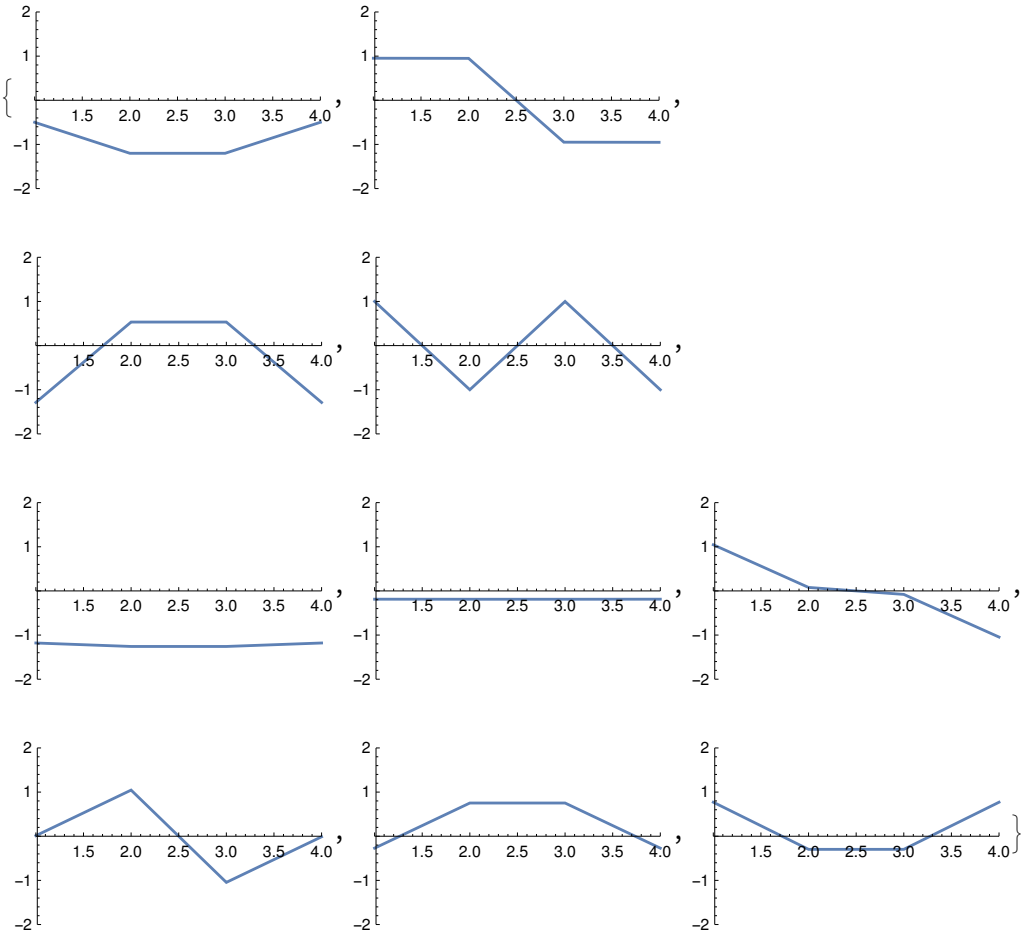

In[13]:=
```
(*The non-zero elements in the sum of the time-evolving state are
  from eigenvectors that have any superposition with the initial state,
though a couple states are more dominant due to large overlaps. The
  initial state is |1 1 0 0 >, the ground state of the L=2 case for J=0.*)
(*timeEvolveState[tt_]:=Exp[-i eVals2[[1]] tt]eVects2[[1]][[9]]*eVectsM[[1]]+
  Exp[-i eVals2[[3]] tt]eVects2[[3]][[9]]*eVectsM[[3]]+
  Exp[-i eVals2[[7]] tt]eVects2[[7]][[9]]*eVectsM[[7]]+
  Exp[-i eVals2[[8]] tt]eVects2[[8]][[9]]*eVectsM[[8]]+
  Exp[-i eVals2[[9]] tt]eVects2[[9]][[9]]*eVectsM[[9]]+
  Exp[-i eVals2[[10]] tt]eVects2[[10]][[9]]*eVectsM[[10]]*)
```

In[14]:=
```
timeEvolveState[tt_] :=
 Sum[Exp[-i eVals2[[zz]] tt] eVects2[[zz]][[9]] * eVectsM[[zz]], {zz, Length[eVals2]}]
```

In[15]:=
```
(*Normalize and propagate in real time, plotting the probability amplitude*)
Animate[ListLinePlot[2 Abs[timeEvolveState[tt]]^2 / (Total[Abs[timeEvolveState[tt]]^2]),
  PlotRange → {{0.9, 4.1}, {0, 1.5}}, ImageSize → Large,
  PlotMarkers → {"◆", Large}], {tt, 0, 80, 0.2}, AnimationRate → 1.5]
```

Out[15]=

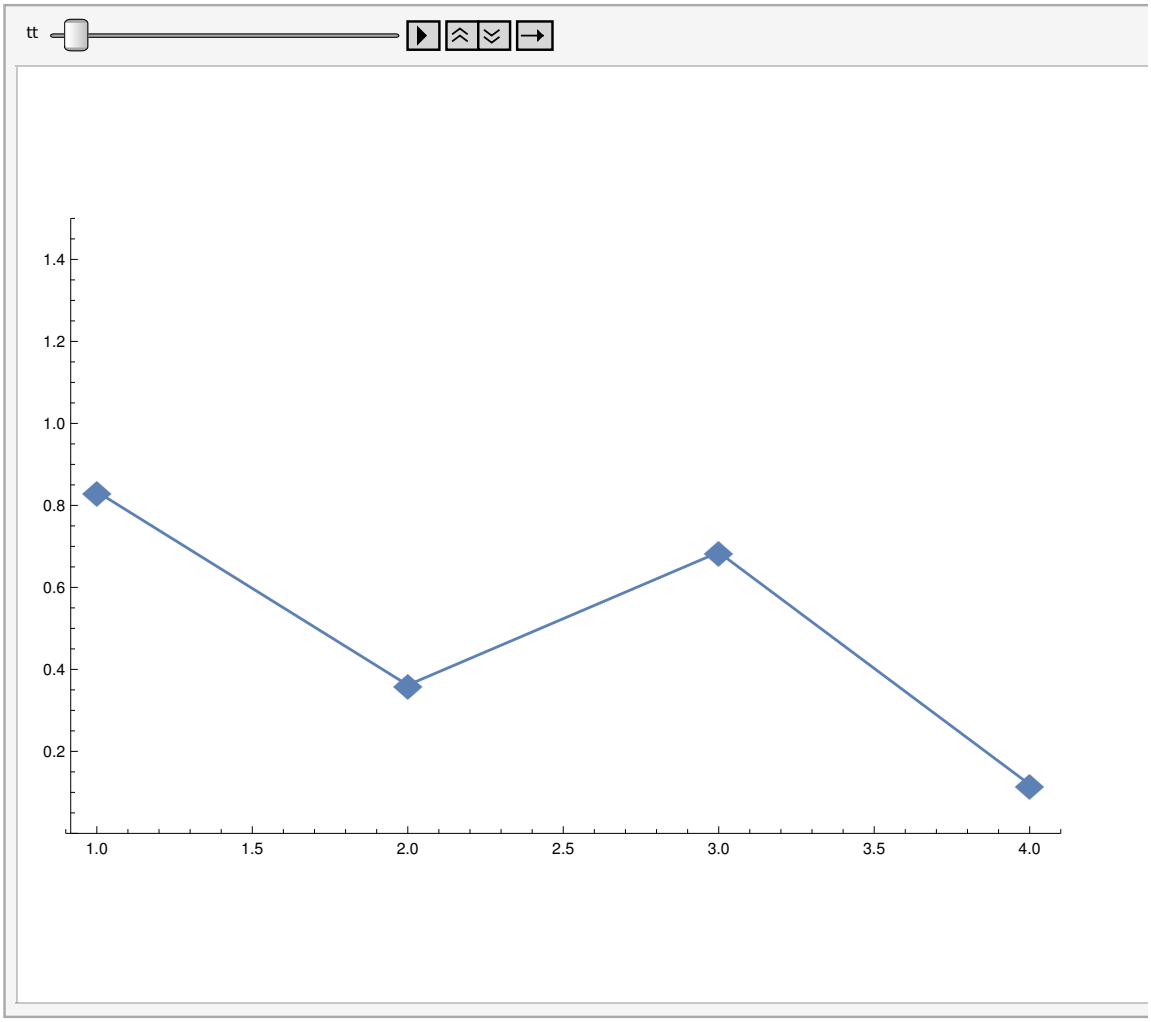

In[16]:=
```
(*Double check normalization -- Take 2|ψ|^2→ <n_i> for 2 particles*)
Table[Total[2 Abs[timeEvolveState[tt]]^2 / (Total[Abs[timeEvolveState[tt]]^2])],
 {tt, 0, 5, 0.2}]
```

Out[16]=
```
{2., 2., 2., 2., 2., 2., 2., 2., 2., 2., 2.,
 2., 2., 2., 2., 2., 2., 2., 2., 2., 2., 2., 2., 2.}
```

In[17]:=
```
timesteps1 = 40 * 20;
stepsize1 = 0.01;
filter1 = 1; (*Moving average filter of discrete data,
requires integer, minimum is 1*)
(*Create time-discretized data from continuous time-
 evolution (for application of filters)*)
discreteTimeStates = Array[{Null &, Null &, Null &, Null &}, timesteps1];
For[ss = 1, ss ≤ timesteps1, ss++,
 discreteTimeStates[[ss]] = 2 Abs[timeEvolveState[ss * stepsize1]]^2 /
     (Total[Abs[timeEvolveState[ss * stepsize1]]^2])
]
discreteTimeStates;
(*Density plot representation of time evolution*)
ListDensityPlot[discreteTimeStates, ColorFunction → "AvocadoColors",
 PlotLegends → Placed[BarLegend[Automatic, LegendMargins → {{0, 0}, {10, 5}},
    LegendLabel → "<n_i>", LabelStyle → {Italic, FontFamily → "Helvetica"}], Right],
 InterpolationOrder → 5,
 Frame → True, FrameLabel → {"Site i", "Timesteps"},
 PlotLabel → "On-site occupation dynamics"]
```

Out[23]=

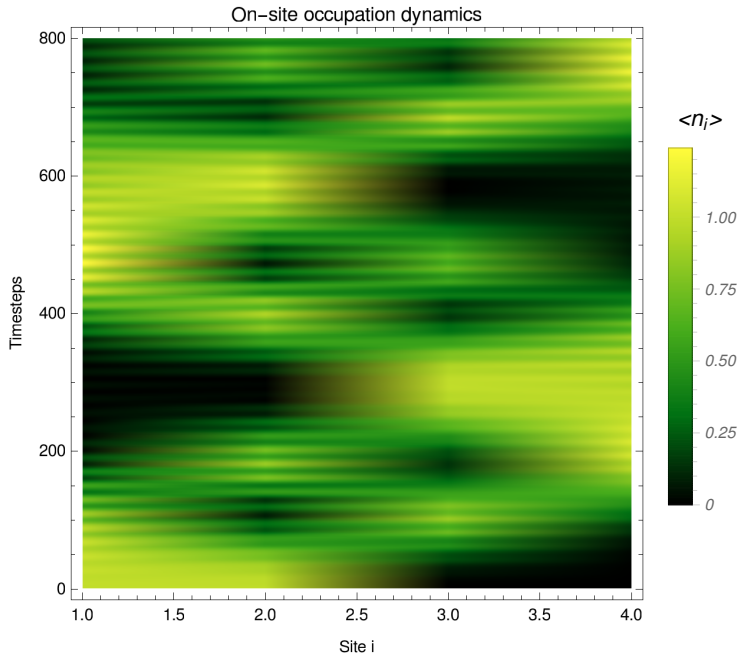

In[24]:=

```
Plot[{2 Abs[timeEvolveState[t][[2]]]^2 / (Total[Abs[timeEvolveState[t]]^2]),
  2 Abs[timeEvolveState[t][[3]]]^2 / (Total[Abs[timeEvolveState[t]]^2])},
 {t, 0, 50}, ImageSize → Large, Frame → True, FrameLabel → {"Time", "<n_i>"},
 PlotLabel → "Occupation of sites 2 and 3", PlotLegends → {"<n_2>", "<n_3>"}]
(*Plot[2Abs[timeEvolveState[t][[3]]]^2/(Total[Abs[timeEvolveState[t]]^2]),
 {t,0,120},PlotStyle→RGBColor[1,0,1]]*)
(*Plot[Sum[(2Abs[timeEvolveState[t][[qq]]]^2),{qq,1,2}]/
   (Total[Abs[timeEvolveState[t]]^2]),{t,0,120},PlotStyle→RGBColor[0.25,0,0.75]]*)
DiscretePlot[2 Abs[timeEvolveState[t][[2]]]^2 / (Total[Abs[timeEvolveState[t]]^2]),
 {t, 0, 20, stepsize1}, ImageSize → Large, Frame → True, FrameLabel → {"Time", "<n_2>"},
 PlotLabel → "Occupation of site 2 for discretized data"]
DiscretePlot[2 Abs[timeEvolveState[t][[3]]]^2 / (Total[Abs[timeEvolveState[t]]^2]),
 {t, 0, 20, stepsize1}, PlotStyle → RGBColor[1, 0, 1],
 ImageSize → Large, Frame → True, FrameLabel → {"Time", "<n_3>"},
 PlotLabel → "Occupation of site 3 for discretized data"]
(*DiscretePlot[Sum[(2Abs[timeEvolveState[t][[qq]]]^2),{qq,1,2}]/
   (Total[Abs[timeEvolveState[t]]^2]),{t,0,120,0.2},PlotStyle→RGBColor[0.25,0,0.75]]*)
```

Out[24]=

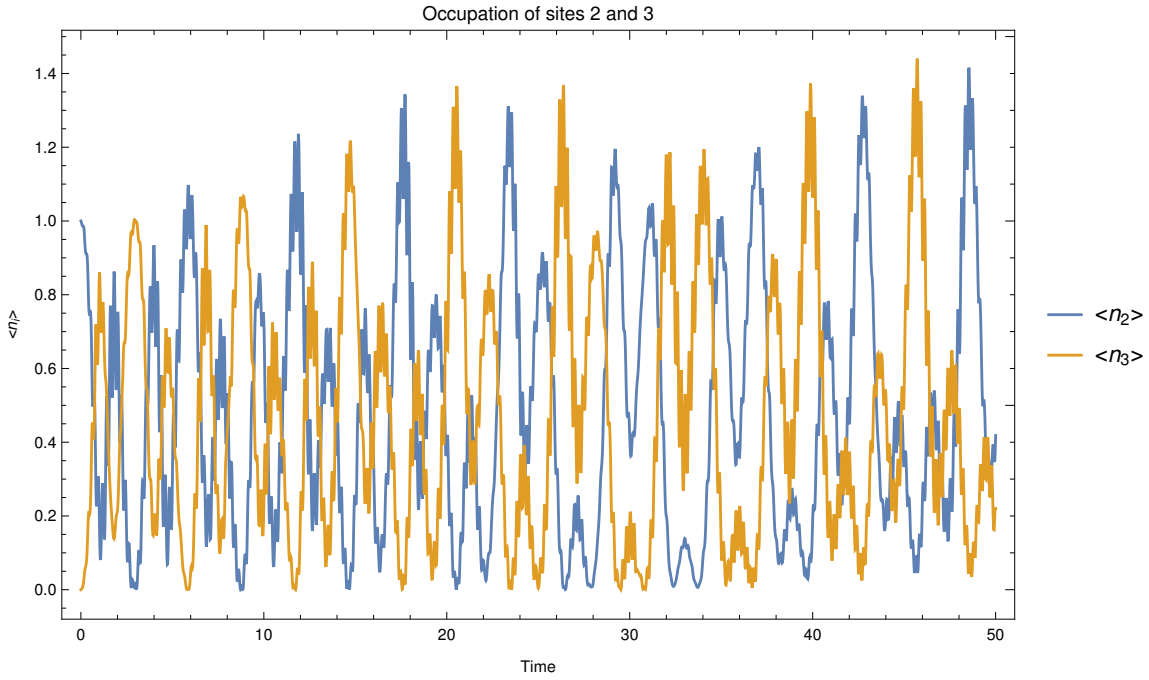

Out[25]=

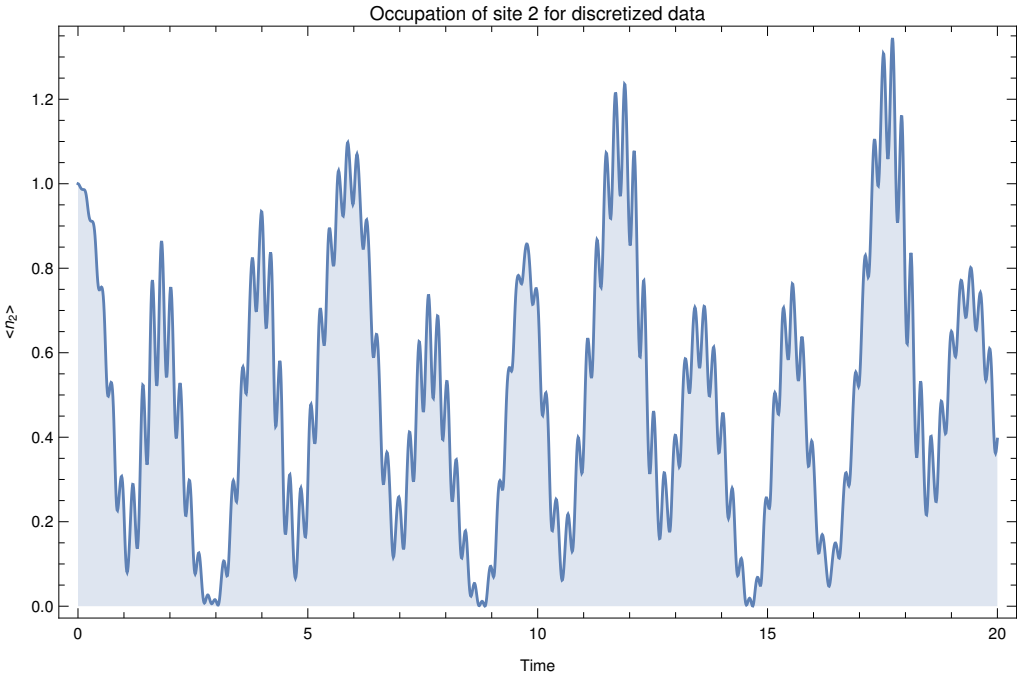

Out[26]=

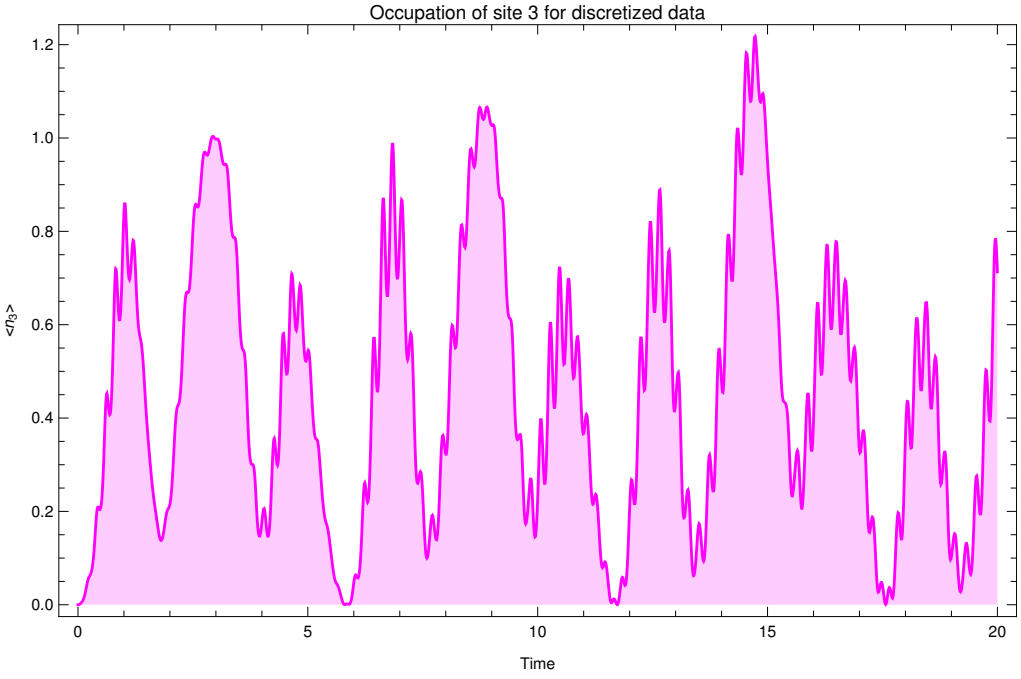

In[27]:=
```
nrel = ((2 Abs[timeEvolveState[t][[1]]]^2 + 2 Abs[timeEvolveState[t][[2]]]^2) -
    (2 Abs[timeEvolveState[t][[3]]]^2 + 2 Abs[timeEvolveState[t][[4]]]^2)) /
  (Total[Abs[timeEvolveState[t]]^2]);
DiscretePlot[nrel, {t, 0, 20, stepsize1}, PlotStyle → RGBColor[1, 0, 1],
 ImageSize → Large, Frame → True, FrameLabel → {"Time", "<n_rel>"},
 PlotLabel → "Population imbalance for discretized data"]
SetDirectory[NotebookDirectory[]]
dataa = Table[{t, nrel}, {t, 0, 20, stepsize1}] // N;
Export["test.txt", dataa, "Table", "FieldSeparators" → " "]
```

Out[28]=

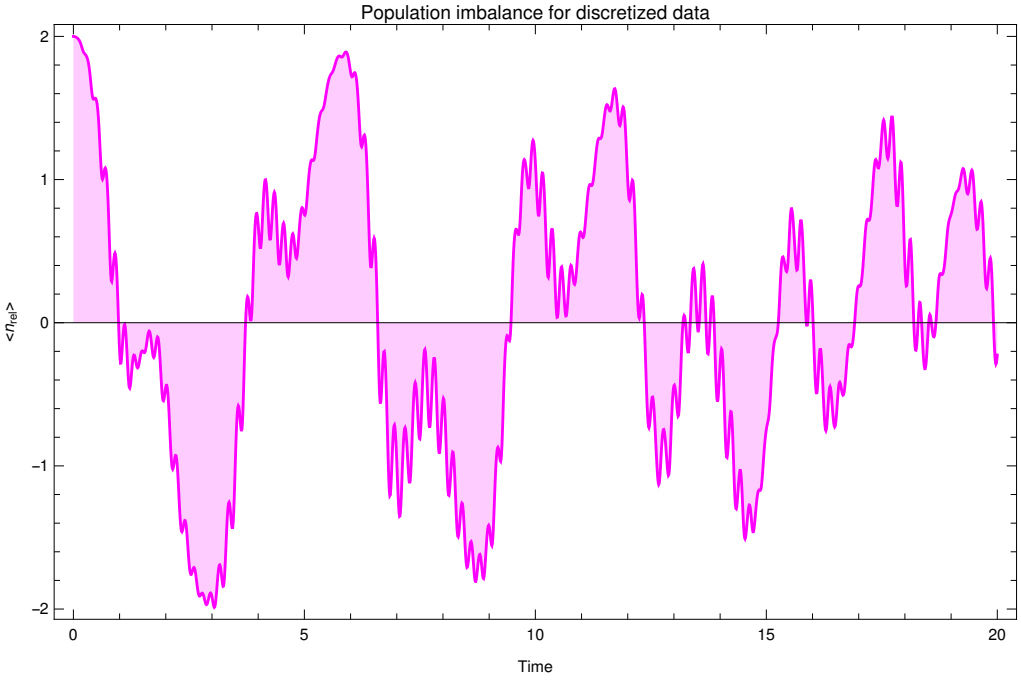

Out[29]= /home/marie/Documents/PhD/QPTclass

Out[31]= test.txt

In[32]:=

In[33]:=

In[34]:=

In[35]:=

In[36]:=

Note: I am unsure why there are high-frequency modes with this initial condition (J=0), but not with an initial condition with J ≠ 0...

In[37]:=
```
ListLinePlot[
 {MovingAverage[Flatten[Take[Take[discreteTimeStates, timesteps1, 2], timesteps1, -1]],
   filter1], MovingAverage[
   Flatten[Take[Take[discreteTimeStates, timesteps1, 3], timesteps1, -1]], filter1]},
 ImageSize → Large, Frame → True, FrameLabel → {"Time", "<nᵢ>"},
 PlotLabel → "Occupation of sites 2 and 3 for discretized data with filter",
 PlotLegends → {"<n₂>", "<n₃>"}]
ListLinePlot[{MovingAverage[Flatten[
    Take[Take[discreteTimeStates, timesteps1, 2], timesteps1, -1]], 1], MovingAverage[
   Flatten[Take[Take[discreteTimeStates, timesteps1, 3], timesteps1, -1]], 1]},
 ImageSize → Large, Frame → True, FrameLabel → {"Time", "<nᵢ>"},
 PlotLabel → "Occupation of sites 2 and 3 for discretized data without filter",
 PlotLegends → {"<n₂>", "<n₃>"}]
(*ListLinePlot[MovingAverage[Flatten[Take[discreteTimeStates,timesteps1,1]]+
   Flatten[Take[Take[discreteTimeStates,timesteps1,3],timesteps1,-1]],
  filter1],PlotStyle→RGBColor[0.25,0,0.75]]*)
```

Out[37]=

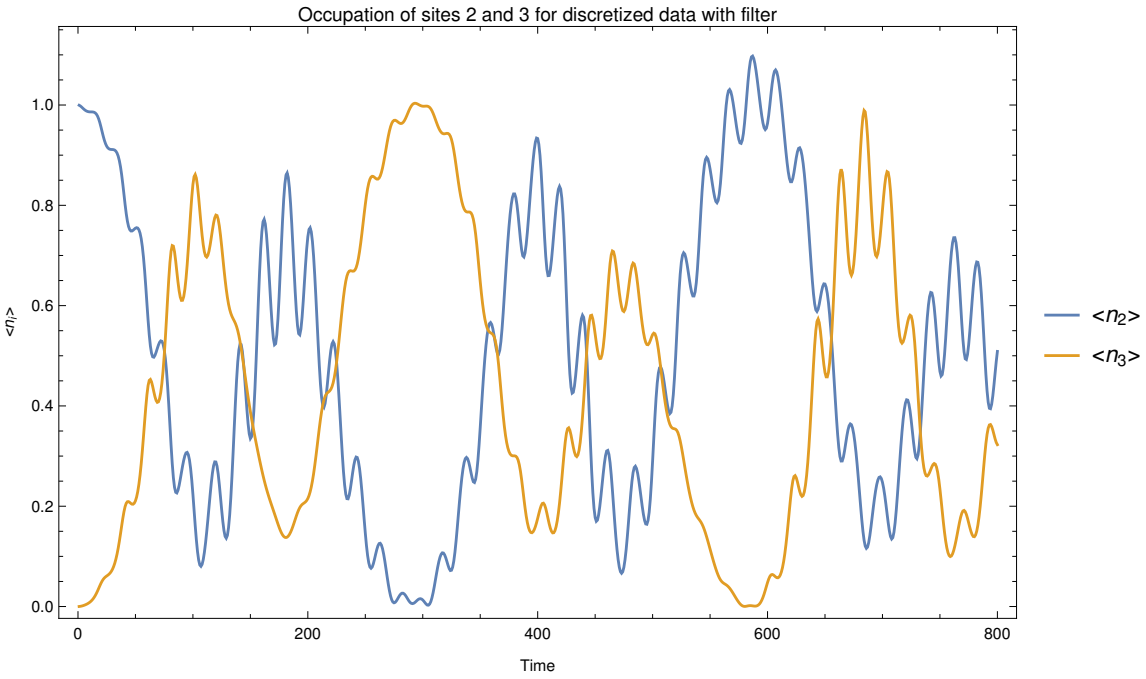

Out[38]=

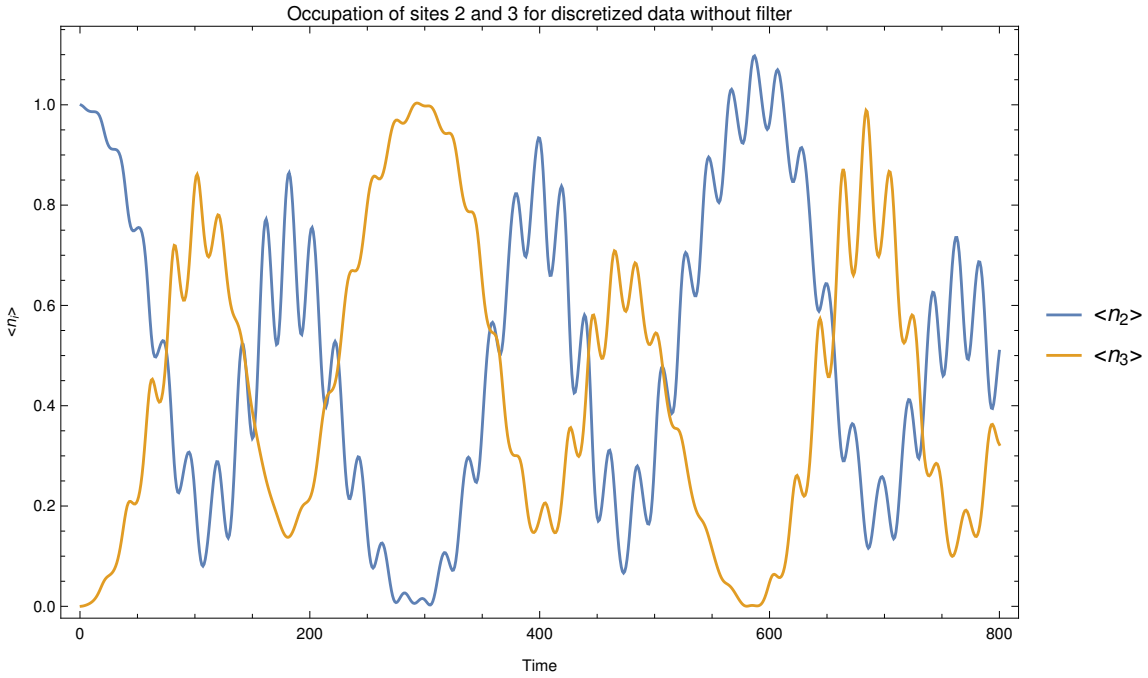

In[39]:=
```
FourierDataN2 =
  Take[Abs[Fourier[MovingAverage[Flatten[Take[Take[discreteTimeStates, timesteps1, 2],
        timesteps1, -1]], 1]]]^2, Length[Abs[Fourier[MovingAverage[Flatten[
       Take[Take[discreteTimeStates, timesteps1, 2], timesteps1, -1]], 1]]]^2]/2];
FourierDataN3 = Take[Abs[Fourier[MovingAverage[Flatten[Take[Take[discreteTimeStates,
       timesteps1, 3], timesteps1, -1]], 1]]]^2, Length[FourierDataN2]];
```

In[41]:=
```
(*Two frequency peaks in the Fourier spectrum (non-normalized)*)
ListLinePlot[{FourierDataN2, FourierDataN3}, ImageSize → Large,
 Frame → True, FrameLabel → {"Frequency", "Amplitude"},
 PlotLabel → "FT of sites 2 and 3 for discretized data without filter"]
```

Out[41]=

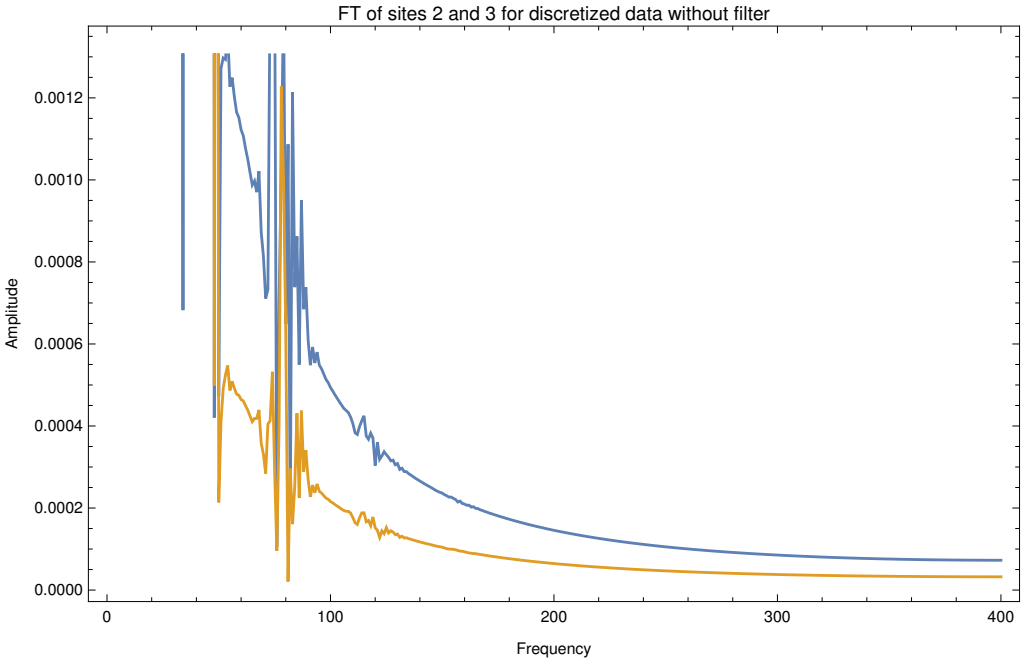

2. Initial state is α_1| 1 1 0 0 > + α_2| 2 0 0 0 > + α_3| 0 2 0 0 > (i.e. ground state of L=2 for small J, so $\alpha_1 > \alpha_2$ and $\alpha_1 > \alpha_3$)

In[42]:=
```
(*Determine non-trivial ground state of L=2 for the initial state*)
H1 = {{U, -Sqrt[2] J, 0}, {-Sqrt[2] J, 0, -Sqrt[2] J}, {0, -Sqrt[2] J, U}};
{eVals1, eVects1} = Eigensystem[H1]
```

Out[43]=

$$\left\{\left\{U, \frac{1}{2}\left(U-\sqrt{16\,J^2+U^2}\right), \frac{1}{2}\left(U+\sqrt{16\,J^2+U^2}\right)\right\},\right.$$
$$\left.\left\{\{-1, 0, 1\}, \left\{1, -\frac{-\sqrt{2}\,U-\sqrt{2}\,\sqrt{16\,J^2+U^2}}{4\,J}, 1\right\}, \left\{1, -\frac{-\sqrt{2}\,U+\sqrt{2}\,\sqrt{16\,J^2+U^2}}{4\,J}, 1\right\}\right\}\right\}$$

In[44]:=
```
For[mm = 1, mm < Length[eVals1], mm++,
 eVects1[[mm]] = 2 eVects1[[mm]] / Total[Abs[eVects1[[mm]]]]
]
{eVals1, eVects1} /. params
```

Out[45]=
```
{{30., -0.132746, 30.1327},
 {{-1, 0, 1}, {0.0858109, 1.82838, 0.0858109}, {1, -0.0938656, 1}}}
```

In[46]:=
```
For[iii = 1, iii <= Length[eVals1], iii++,
 eVectsM[[iii]] = eVects2[[iii]][[1]] * {0, 0, 0, 2} + eVects2[[iii]][[2]] * {0, 0, 1, 1} +
   eVects2[[iii]][[3]] * {0, 0, 2, 0} + eVects2[[iii]][[4]] * {0, 1, 0, 1} +
   eVects2[[iii]][[5]] * {0, 1, 1, 0} + eVects2[[iii]][[6]] * {0, 2, 0, 0} +
   eVects2[[iii]][[7]] * {1, 0, 0, 1} + eVects2[[iii]][[8]] * {1, 0, 1, 0} +
   eVects2[[iii]][[9]] * {1, 1, 0, 0} + eVects2[[iii]][[10]] * {2, 0, 0, 0}
]
```

In[47]:=
```
(*The non-zero elements in the sum of the time-evolving state are from
  eigenvectors that have any superposition with the initial state. This time,
the initial state is a ground state from the L=
 2 case with a small tunneling term. Therefore, there are more projection overlaps,
since the initial state is a superposition of the |
 2 0 0 0 >, | 1 1 0 0 >, | 0 2 0 0 > L=2 basis,
rather than | 1 1 0 0 >, as was the case for J=0. *)
timeEvolveState2[ttt_] := Sum[
  Exp[-i eVals2[[nn]] ttt] (eVects2[[nn]][[6]] * eVects1[[2]][[1]] + eVects2[[nn]][[9]] * eVects1[[2]][[2]] +
      eVects2[[nn]][[10]] * eVects1[[2]][[3]]) * eVectsM[[nn]] /. params, {nn, 1, Length[eVals2]}]
```

In[48]:=
```
(*Normalize and propogate in real time, plotting the probability amplitude*)
Animate[
 ListLinePlot[2 Abs[timeEvolveState2[ttt]]^2 / (Total[Abs[timeEvolveState2[ttt]]^2]),
  PlotRange → {{0.9, 4.1}, {0, 1.5}}, ImageSize → Large, PlotMarkers -> {"◆", Large}],
 {ttt, 0, 120, 0.2}, AnimationRate → 1.5]
```

Out[48]=

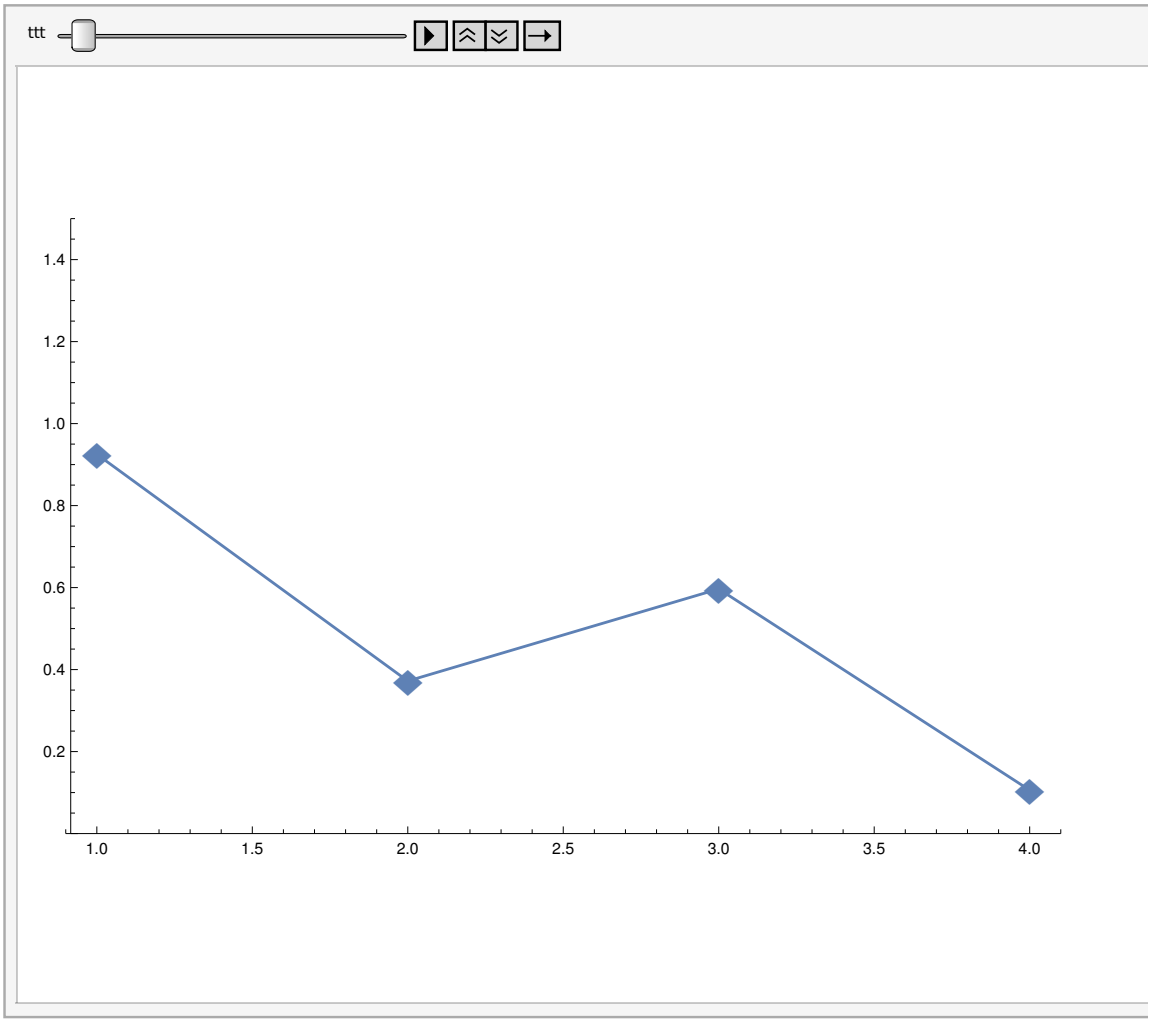

In[49]:=
```
(*Double check normalization -- Take 2|ψ|^2→ <n_i> for 2 particles*)
Table[Total[2 Abs[timeEvolveState2[tt]]^2 / (Total[Abs[timeEvolveState2[tt]]^2])],
 {tt, 0, 5, 0.2}]
```

Out[49]=
```
{2., 2., 2., 2., 2., 2., 2., 2., 2., 2., 2.,
 2., 2., 2., 2., 2., 2., 2., 2., 2., 2., 2., 2., 2., 2.}
```

In[50]:=
```
timesteps = 10 * 20;
stepsize = 0.05;
filter = 1 (*Moving average filter of discrete data,
requires integer, minimum is 1*)
(*Create time-discretized data from continuous time-
 evolution (for application of filters)*)
discreteTimeStates2 = Array[{Null &, Null &, Null &, Null &}, timesteps];
For[rr = 1, rr ≤ timesteps, rr++,
 discreteTimeStates2[[rr]] = 2 Abs[timeEvolveState2[rr * stepsize]]^2 /
     (Total[Abs[timeEvolveState2[rr * stepsize]]^2])
]
discreteTimeStates2;
(*Density plot representation of time evolution*)
ListDensityPlot[discreteTimeStates2, ColorFunction → "AvocadoColors",
 PlotLegends → Placed[BarLegend[Automatic, LegendMargins → {{0, 0}, {10, 5}},
    LegendLabel → "<n_i>", LabelStyle → {Italic, FontFamily → "Helvetica"}], Right],
 InterpolationOrder → 5,
 Frame → True, FrameLabel → {"Site i", "Timesteps"},
 PlotLabel → "On-site occupation dynamics"]
```

Out[52]= 1

Out[56]=

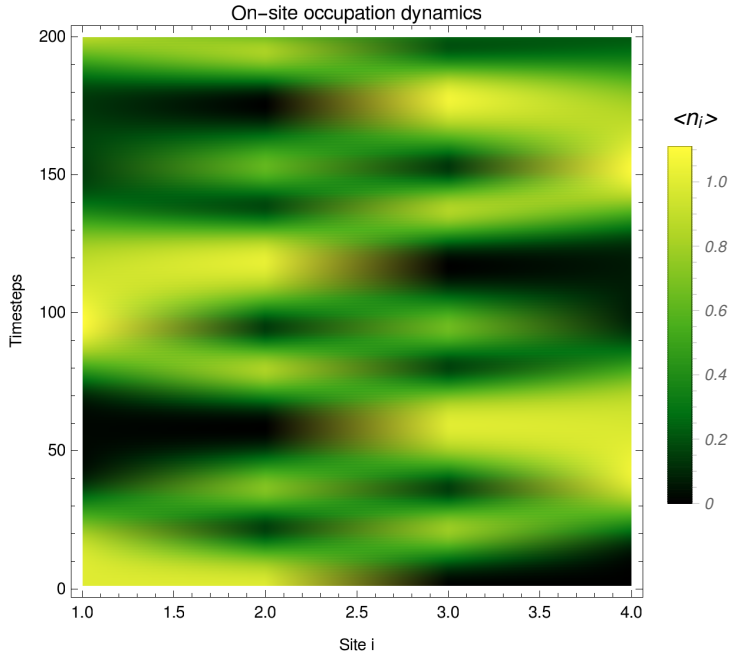

In[57]:=
```
Plot[{2 Abs[timeEvolveState2[t][[2]]]^2 / (Total[Abs[timeEvolveState2[t]]^2]),
  2 Abs[timeEvolveState2[t][[3]]]^2 / (Total[Abs[timeEvolveState2[t]]^2])},
 {t, 0, 50}, ImageSize → Large, Frame → True, FrameLabel → {"Time", "<n_i>"},
 PlotLabel → "Occupation of sites 2 and 3", PlotLegends → {"<n_2>", "<n_3>"}]
(*Plot[Sum[(2Abs[timeEvolveState2[t][[qq]]]^2),{qq,1,2}]/
  (Total[Abs[timeEvolveState2[t]]^2]),{t,0,120},PlotStyle→RGBColor[0.25,0,0.75]]*)
DiscretePlot[2 Abs[timeEvolveState2[t][[2]]]^2 / (Total[Abs[timeEvolveState2[t]]^2]),
 {t, 0, 20, stepsize}, ImageSize → Large, Frame → True, FrameLabel → {"Time", "<n_2>"},
 PlotLabel → "Occupation of site 2 for discretized data"]
DiscretePlot[2 Abs[timeEvolveState2[t][[3]]]^2 / (Total[Abs[timeEvolveState2[t]]^2]),
 {t, 0, 20, stepsize}, PlotStyle → RGBColor[1, 0, 1],
 ImageSize → Large, Frame → True, FrameLabel → {"Time", "<n_3>"},
 PlotLabel → "Occupation of site 3 for discretized data"]
(*DiscretePlot[Sum[(2Abs[timeEvolveState2[t][[qq]]]^2),{qq,1,2}]/
  (Total[Abs[timeEvolveState2[t]]^2]),{t,0,120,0.2},PlotStyle→RGBColor[0.25,0,0.75]]*)
```

Out[57]=

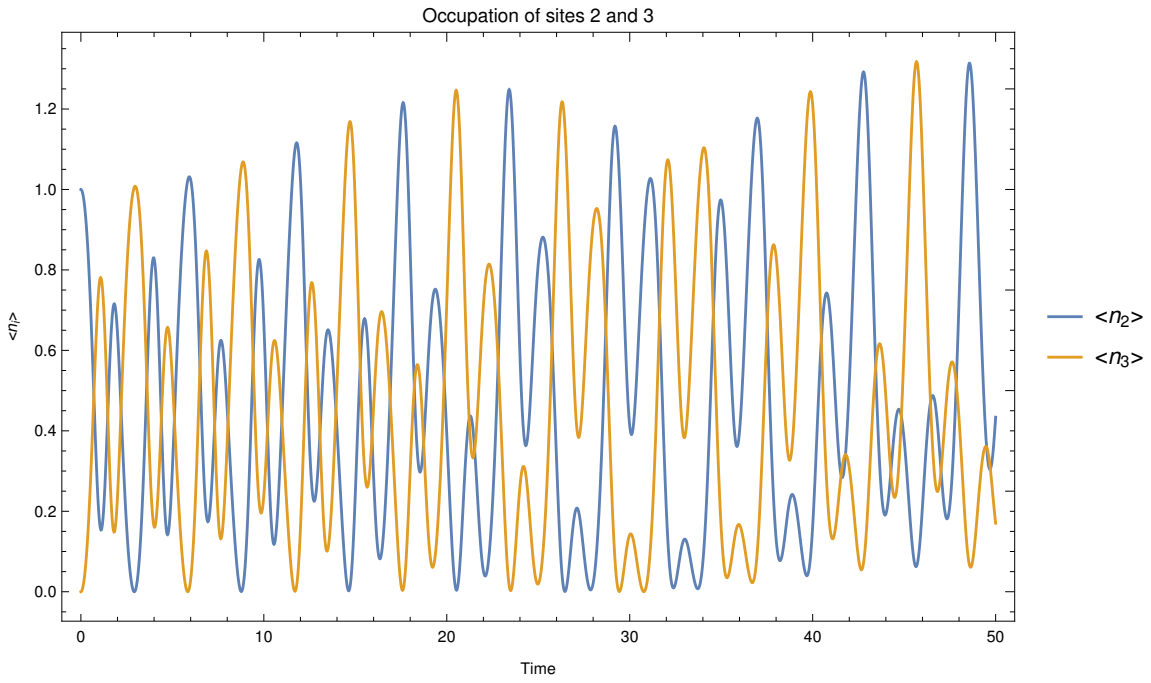

Out[58]=

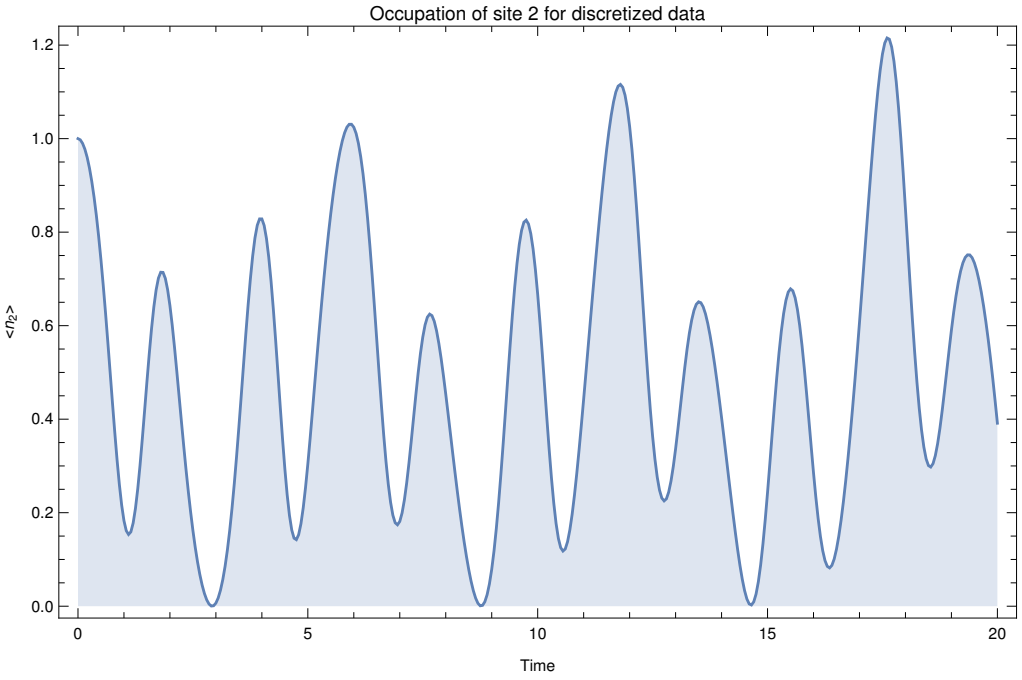
Occupation of site 2 for discretized data
<n2>
Time
0.0
0.2
0.4
0.6
0.8
1.0
1.2
0
5
10
15
20

Out[59]=

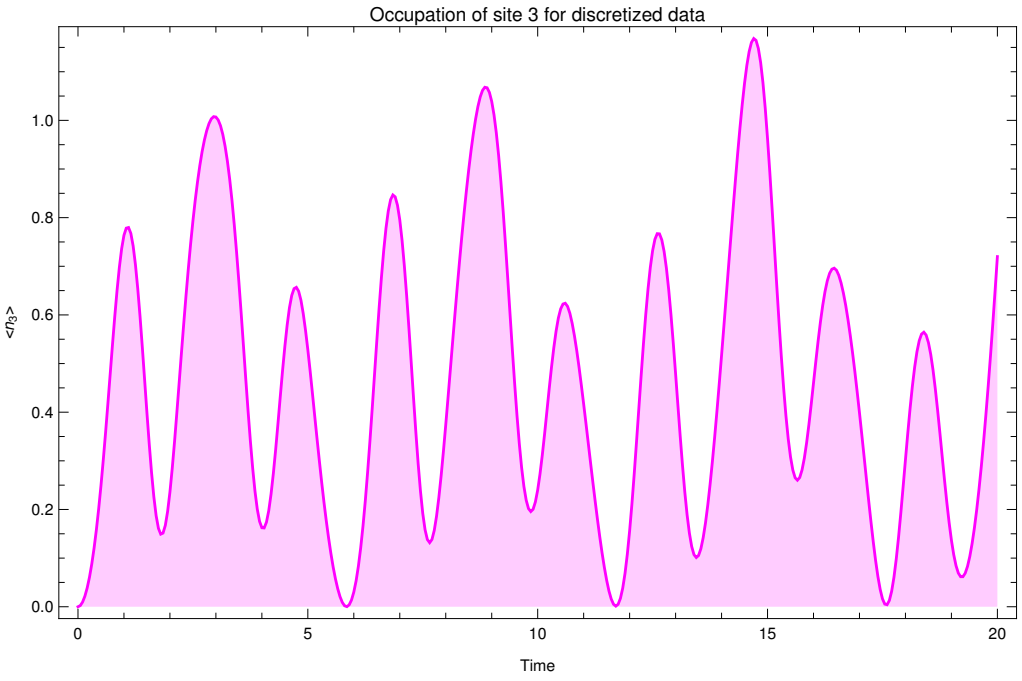
Occupation of site 3 for discretized data
<n3>
Time
0.0
0.2
0.4
0.6
0.8
1.0
0
5
10
15
20

In[60]:=
```
(*No high-frequency modes here, so no filter necessary*)
ListLinePlot[
 {MovingAverage[Flatten[Take[Take[discreteTimeStates2, timesteps, 2], timesteps, -1]],
   filter], MovingAverage[
   Flatten[Take[Take[discreteTimeStates2, timesteps, 3], timesteps, -1]], filter]},
 ImageSize → Large, Frame → True, FrameLabel → {"Time", "<n_i>"},
 PlotLabel → "Occupation of sites 2 and 3 for discretized data",
 PlotLegends → {"<n_2>", "<n_3>"}]
(*ListLinePlot[MovingAverage[Flatten[Take[discreteTimeStates2,timesteps,1]]+
   Flatten[Take[Take[discreteTimeStates2,timesteps,2],timesteps,-1]],
  filter],PlotStyle→RGBColor[0.25,0,0.75]]*)
```

Out[60]=

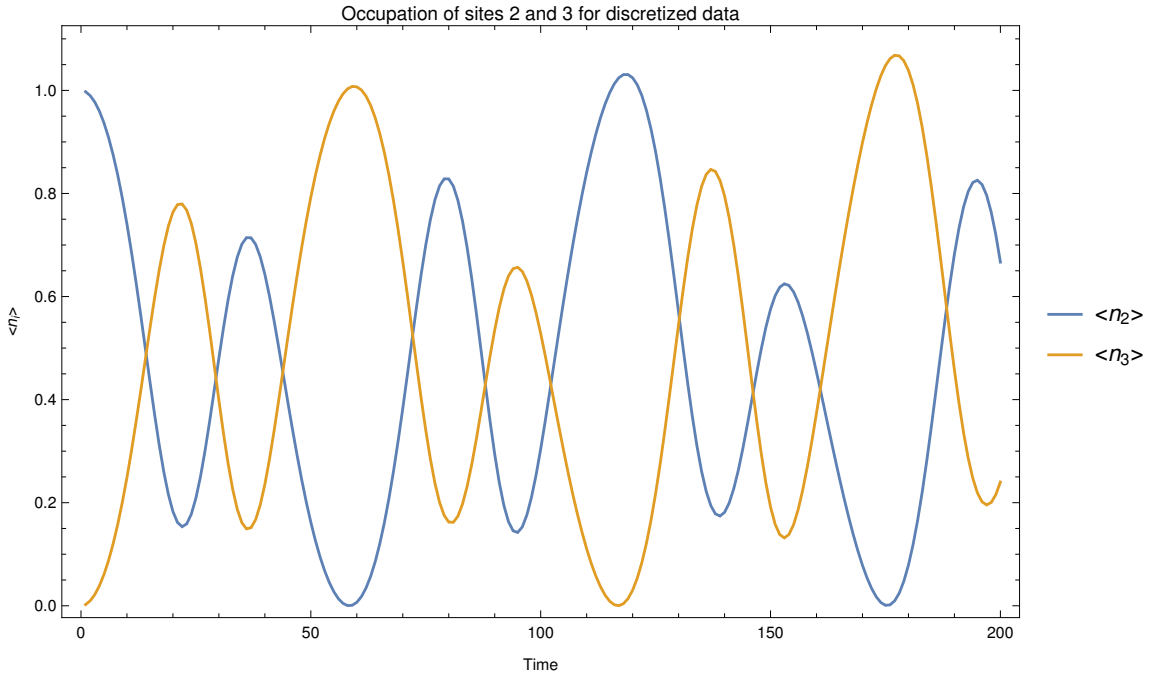

In[61]:=
```
SetDirectory[NotebookDirectory[]]
```

Out[61]= /home/marie/Documents/PhD/QPTclass

In[62]:=
```
stepss = 0.25;
nrel = ((2 Abs[timeEvolveState2[t][[1]]]^2 + 2 Abs[timeEvolveState2[t][[2]]]^2) -
      (2 Abs[timeEvolveState2[t][[3]]]^2 + 2 Abs[timeEvolveState2[t][[4]]]^2))/
   (4 * Total[Abs[timeEvolveState2[t]]^2]);
DiscretePlot[nrel, {t, 0, 60, stepss}, PlotStyle → RGBColor[1, 0, 1],
 ImageSize → Large, Frame → True, FrameLabel → {"Time", "<n_rel>"},
 PlotLabel → "Population imbalance for discretized data"]
dataa = Table[{t, nrel}, {t, 0, 60, stepss}] // N;
Export["test.txt", dataa, "Table", "FieldSeparators" → " "]
```

Out[64]=

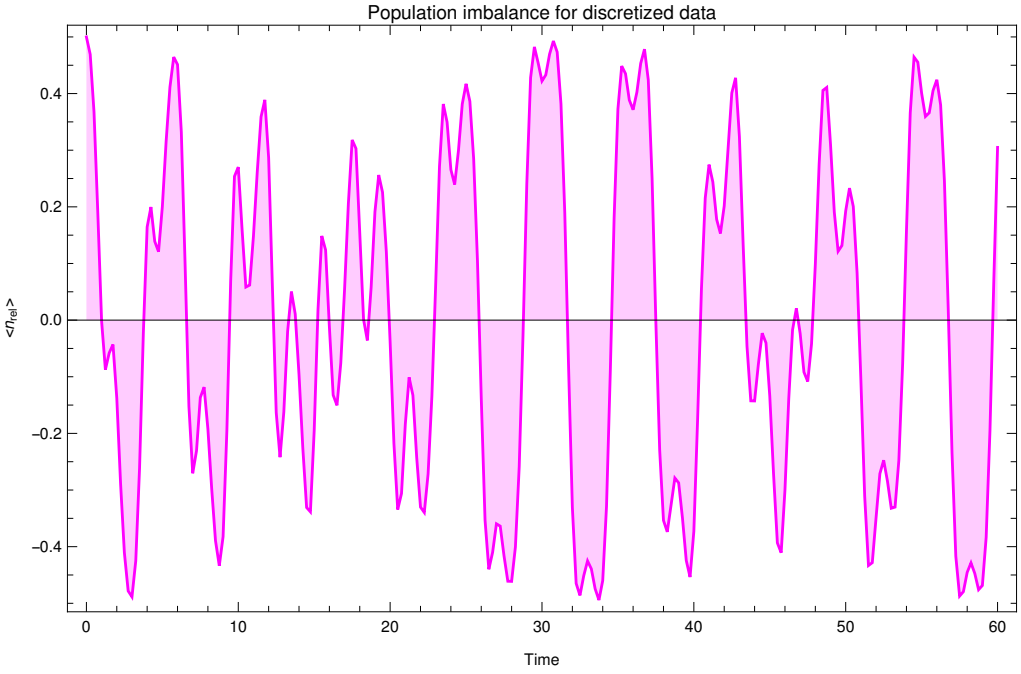

Out[66]= test.txt

In[67]:=
```
Abs[timeEvolveState2[1][[1]]]^2
Abs[timeEvolveState2[1][[2]]]^2
Abs[timeEvolveState2[1][[3]]]^2
Abs[timeEvolveState2[1][[4]]]^2
```

Out[67]= 1.66592

Out[68]= 0.374412

Out[69]= 1.56383

Out[70]= 0.490787

In[71]:=
```
FourierDataN22 =
  Take[Abs[Fourier[MovingAverage[Flatten[Take[Take[discreteTimeStates2, timesteps, 2],
        timesteps, -1]], 1]]]^2, Length[Abs[Fourier[MovingAverage[Flatten[
         Take[Take[discreteTimeStates2, timesteps, 2], timesteps, -1]], 1]]]^2]/2];
FourierDataN33 = Take[Abs[Fourier[MovingAverage[Flatten[Take[Take[discreteTimeStates2,
        timesteps, 3], timesteps, -1]], 1]]]^2, Length[FourierDataN22]];
(*One frequency peak in the Fourier spectrum (non-normalized)*)
ListLinePlot[{FourierDataN22, FourierDataN33}]
```

Out[73]=

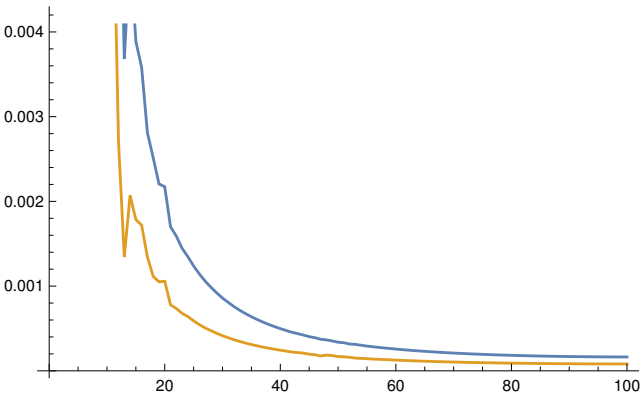

3.) Degenerate perturbation theory of the same result as (2.)

In[74]:=
```
w1 = {{0, 1, 0, 0, 0, 0}, {1, 0, 1, 1, 0, 0}, {0, 1, 0, 0, 1, 0},
    {0, 1, 0, 0, 1, 0}, {0, 0, 1, 1, 0, 1}, {0, 0, 0, 0, 1, 0}};
```

In[75]:=
```
engySplitting1 = -J Eigenvalues[w1]
```

Out[75]= $\left\{\sqrt{5}\ J, -\sqrt{5}\ J, J, -J, 0, 0\right\}$

In[76]:=
```
engySplitting2 = {Sqrt[5] J, -Sqrt[5] J, J, -J, 0, 0, U, U, U, U}
```

Out[76]= $\left\{\sqrt{5}\ J, -\sqrt{5}\ J, J, -J, 0, 0, U, U, U, U\right\}$

In[77]:=
```
(*First order energy perturbations split the six-fold ground state degeneracy,
but not the second cluster degeneracy, due to the Mott gap*)
ListPlot[Sort[engySplitting2 /. params], PlotMarkers → {Automatic, Medium},
 ImageSize → Large, Frame → True, FrameLabel → {"Eigen index", "Energy"},
 PlotLabel → "First order perturbation degeneracy splitting"]
```

Out[77]=

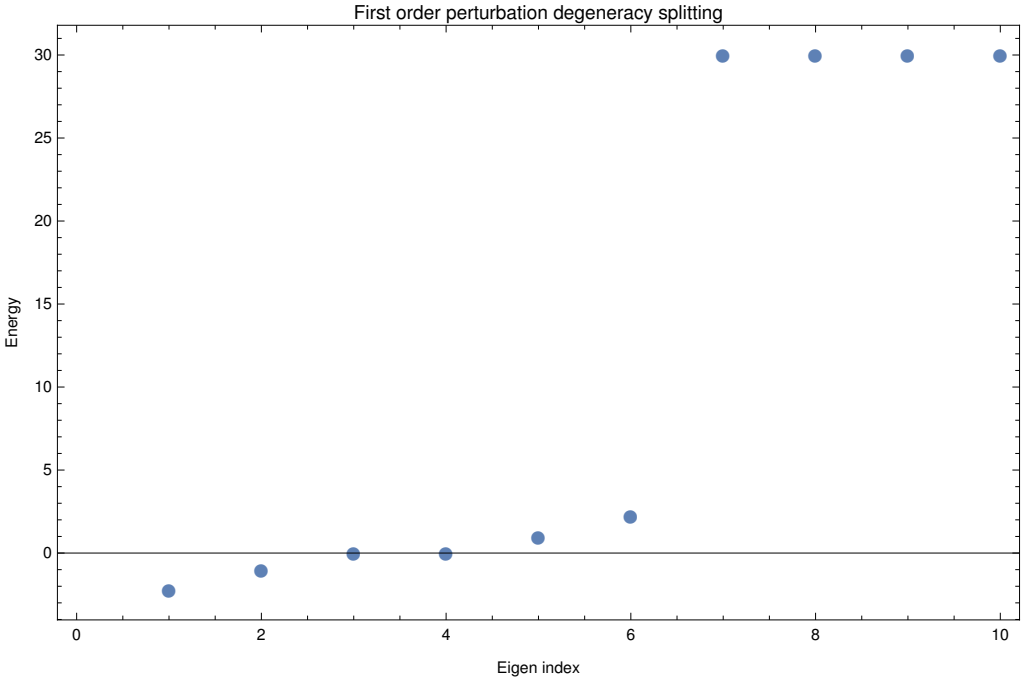

In[78]:=
```
w1vects = -J Eigenvectors[w1]
```

Out[78]=
$$\left\{\left\{-J, \sqrt{5}\ J, -2\ J, -2\ J, \sqrt{5}\ J, -J\right\}, \left\{-J, -\sqrt{5}\ J, -2\ J, -2\ J, -\sqrt{5}\ J, -J\right\},\right.$$
$$\left.\{J, -J, 0, 0, J, -J\}, \{J, J, 0, 0, -J, -J\}, \{-J, 0, J, 0, 0, -J\}, \{0, 0, J, -J, 0, 0\}\right\}$$

In[79]:=
```
m1 = {{1, 0, 0, 0, 0, 0}, {0, 1, 0, 0, 0, 0}, {0, 0, 1, 0, 0, 0},
   {0, 0, 0, 1, 0, 0}, {0, 0, 0, 0, 1, 0}, {0, 0, 0, 0, 0, 1}};
Engy1m2 = {{0, 0, 0, 0, 0, 0}, {0, 0, 0, 0, 0, 0}, {0, 0, 0, 0, 0, 0},
   {0, 0, 0, 0, 0, 0}, {0, 0, 0, 0, 0, 0}, {0, 0, 0, 0, 0, 0}};
```

In[81]:=
```
For[uu = 1, uu ≤ Length[m1], uu++,
 For[vv = 1, vv ≤ Length[m1], vv++,
  Engy1m2[[uu]][[vv]] = m1[[uu]].(w1.w1vects[[vv]])
 ]]
Engy1m2
```

Out[82]=
$$\left\{\left\{\sqrt{5}\ J, -\sqrt{5}\ J, -J, J, 0, 0\right\}, \{-5\ J, -5\ J, J, J, 0, 0\}, \left\{2\sqrt{5}\ J, -2\sqrt{5}\ J, 0, 0, 0, 0\right\},\right.$$
$$\left.\left\{2\sqrt{5}\ J, -2\sqrt{5}\ J, 0, 0, 0, 0\right\}, \{-5\ J, -5\ J, -J, -J, 0, 0\}, \left\{\sqrt{5}\ J, -\sqrt{5}\ J, J, -J, 0, 0\right\}\right\}$$

In[83]:=
```
Table[ListLinePlot[w1vects[[ww]] /. params], {ww, 1, 6}];
```

In[84]:=
```
(*Map eigenvectors from the 10-dimensional Hamiltonian onto 4-site superpositions*)
eVectsW = Array[Null &, 10];
For[xx = 1, xx ≤ 6, xx++,
 eVectsW[[xx]] = (w1vects[[xx]][[1]] * {0, 0, 1, 1} + w1vects[[xx]][[2]] * {0, 1, 0, 1} +
    w1vects[[xx]][[3]] * {0, 1, 1, 0} + w1vects[[xx]][[4]] * {1, 0, 0, 1} +
    w1vects[[xx]][[5]] * {1, 0, 1, 0} + w1vects[[xx]][[6]] * {1, 1, 0, 0})
]
eVectsW[[7]] = {0, 0, 0, 2};
eVectsW[[8]] = {0, 0, 2, 0};
eVectsW[[9]] = {0, 2, 0, 0};
eVectsW[[10]] = {2, 0, 0, 0};
(*non-normalized 1st order perturbing eigenfunctions on Mott side*)
Table[ListLinePlot[eVectsW[[yy]] /. params], {yy, 1, 10}]
```

Out[87]=

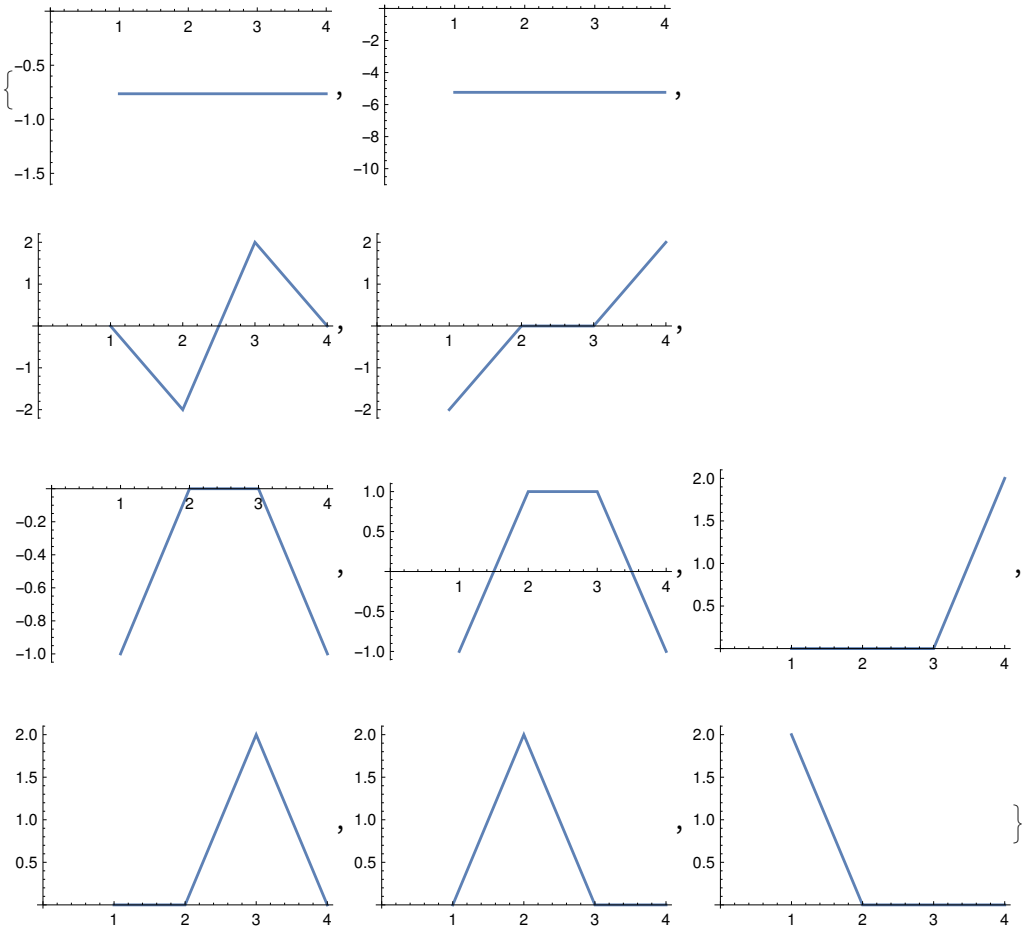

In[88]:=
```
Abs[Total[(w1vects[[1]][[1]] * {0, 0, 1, 1} + w1vects[[1]][[2]] * {0, 1, 0, 1} +
    w1vects[[1]][[3]] * {0, 1, 1, 0} + w1vects[[1]][[4]] * {1, 0, 0, 1} +
    w1vects[[1]][[5]] * {1, 0, 1, 0} + w1vects[[1]][[6]] * {1, 1, 0, 0})]]
```

Out[88]=
$$\text{Abs}\left[-12\,J+4\sqrt{5}\,J\right]$$

In[89]:=
```
eVals3 = engySplitting2 /. params;
eVects3 =
  {{-J, √5 J, -2 J, -2 J, √5 J, -J, 0, 0, 0, 0}, {-J, -√5 J, -2 J, -2 J, -√5 J, -J,
    0, 0, 0, 0}, {J, -J, 0, 0, J, -J, 0, 0, 0, 0}, {J, J, 0, 0, -J, -J, 0, 0, 0, 0},
   {-J, 0, J, 0, 0, -J, 0, 0, 0, 0}, {0, 0, J, -J, 0, 0, 0, 0, 0, 0},
   {0, 0, 0, 0, 0, 0, 1, 0, 0, 0}, {0, 0, 0, 0, 0, 0, 0, 1, 0, 0},
   {0, 0, 0, 0, 0, 0, 0, 0, 1, 0}, {0, 0, 0, 0, 0, 0, 0, 0, 0, 1}} /. params;
```

In[91]:=

In[92]:=
```
timeEvolveState3[t5_] :=
 Sum[Exp[-i eVals3[[nnn]] t5] (eVects3[[nnn]][[9]] * eVects1[[2]][[1]] + eVects3[[nnn]][[6]] *
     eVects1[[2]][[2]] + eVects3[[nnn]][[10]] * eVects1[[2]][[3]]) *
   eVectsW[[nnn]] /. params, {nnn, 1, Length[eVals3]}]
```

In[93]:=
```
(*Normalize and propogate in real time, plotting the probability amplitude*)
Animate[
 ListLinePlot[2 Abs[timeEvolveState3[t5]]^2 / (Total[Abs[timeEvolveState3[t5]]^2]),
  PlotRange → {{0.9, 4.1}, {0, 1.5}}, ImageSize → Large,
  PlotMarkers -> {"◆", Large}], {t5, 0, 40, 0.2}, AnimationRate → 1.5]
```

Out[93]=

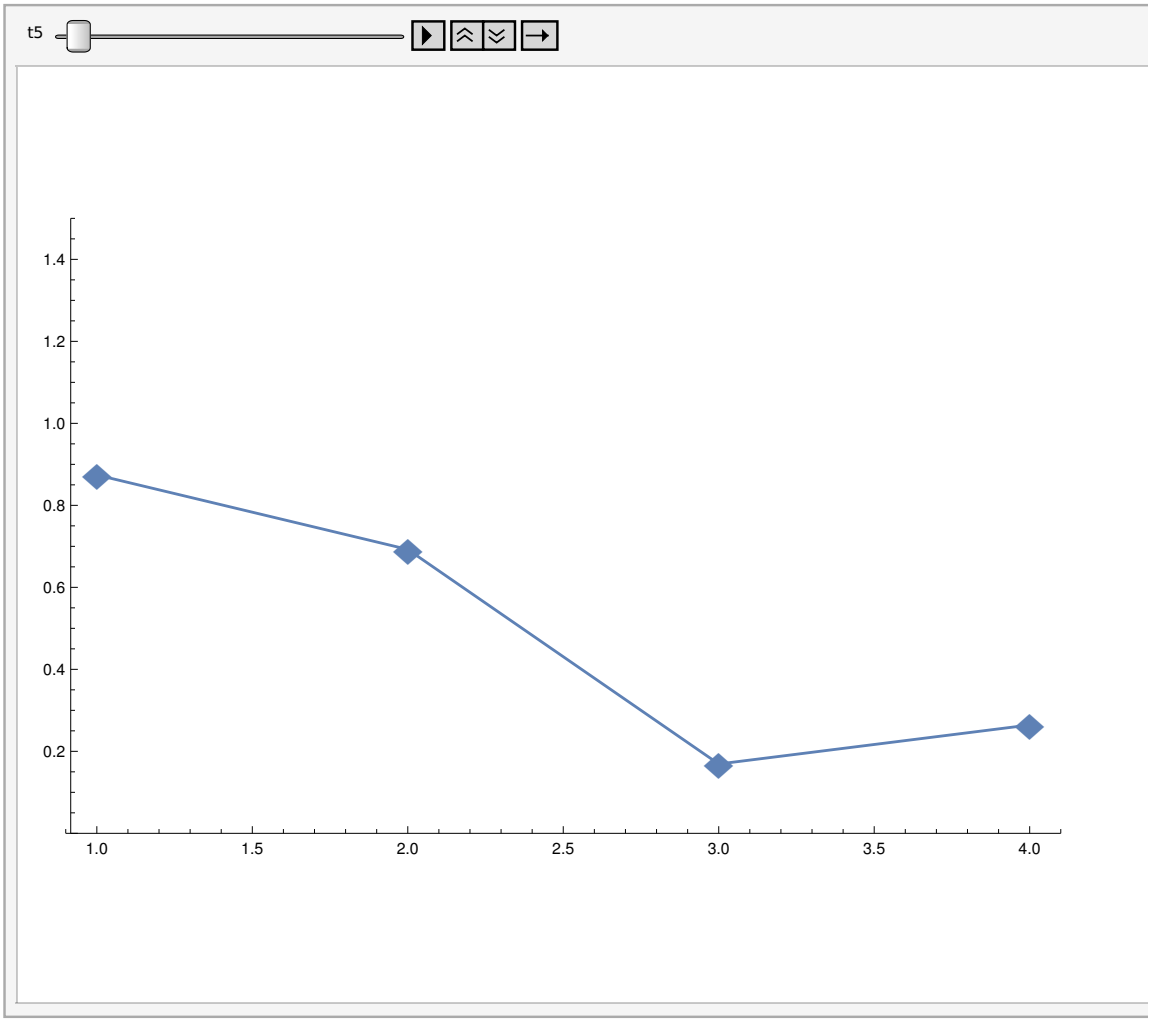

In[94]:=
```
(*Double check normalization -- Take 2|ψ|^2→ <n_i> for 2 particles*)
Table[Total[2 Abs[timeEvolveState3[t2]]^2 / (Total[Abs[timeEvolveState3[t2]]^2])],
 {t2, 0, 5, 0.2}]
```

Out[94]=
```
{2., 2., 2., 2., 2., 2., 2., 2., 2., 2., 2.,
 2., 2., 2., 2., 2., 2., 2., 2., 2., 2., 2., 2., 2.}
```

In[95]:=
```
timesteps3 = 10 * 100;
stepsize3 = 0.01;
filter3 = 1 (*Moving average filter of discrete data,
requires integer, minimum is 1*)
(*Create time-discretized data from continuous time-
 evolution (for application of filters)*)
discreteTimeStates3 = Array[{Null &, Null &, Null &, Null &}, timesteps3];
For[rr = 1, rr ≤ timesteps3, rr++,
 discreteTimeStates3[[rr]] = 2 Abs[timeEvolveState3[rr * stepsize3]]^2 /
     (Total[Abs[timeEvolveState3[rr * stepsize3]]^2])
]
discreteTimeStates3;
(*Density plot representation of time evolution*)
ListDensityPlot[discreteTimeStates3, ColorFunction → "AvocadoColors",
 PlotLegends → Placed[BarLegend[Automatic, LegendMargins → {{0, 0}, {10, 5}},
    LegendLabel → "<n_i>", LabelStyle → {Italic, FontFamily → "Helvetica"}], Right],
 InterpolationOrder → 5,
 Frame → True, FrameLabel → {"Site i", "Timesteps"},
 PlotLabel → "On-site occupation dynamics from 1st order perturbation"]
```

Out[97]= 1

Out[101]=

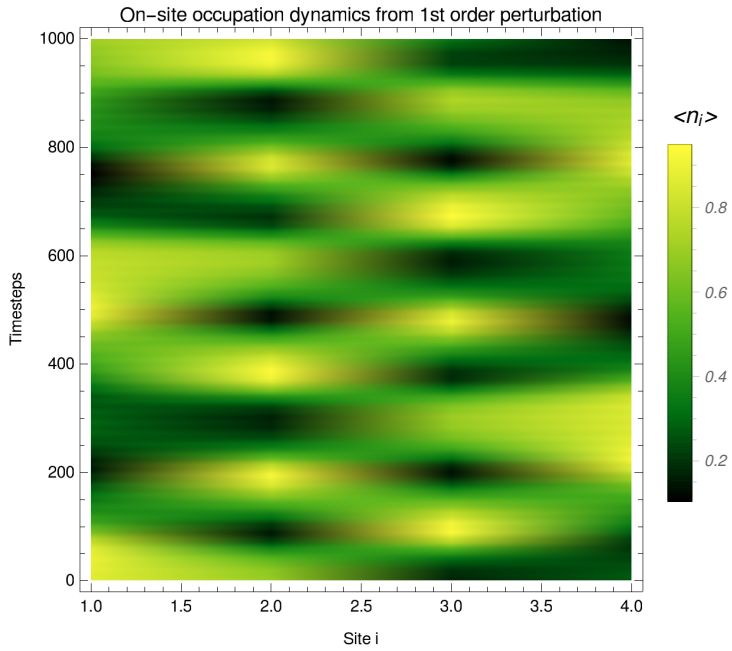

In[102]:=
```
Plot[{2 Abs[timeEvolveState3[t][[2]]]^2 / (Total[Abs[timeEvolveState3[t]]^2]),
  2 Abs[timeEvolveState3[t][[3]]]^2 / (Total[Abs[timeEvolveState3[t]]^2])},
 {t, 0, 20}, ImageSize → Large, Frame → True, FrameLabel → {"Time", "<n_i>"},
 PlotLabel → "Occupation of sites 2 and 3", PlotLegends → {"<n_2>", "<n_3>"}]
(*Plot[Sum[(2Abs[timeEvolveState2[t][[qq]]]^2),{qq,1,2}]/
  (Total[Abs[timeEvolveState2[t]]^2]),{t,0,120},PlotStyle→RGBColor[0.25,0,0.75]]*)
DiscretePlot[2 Abs[timeEvolveState3[t][[2]]]^2 / (Total[Abs[timeEvolveState3[t]]^2]),
 {t, 0, 20, stepsize3}, ImageSize → Large, Frame → True, FrameLabel → {"Time", "<n_2>"},
 PlotLabel → "Occupation of site 2 for discretized data"]
DiscretePlot[2 Abs[timeEvolveState3[t][[3]]]^2 / (Total[Abs[timeEvolveState3[t]]^2]),
 {t, 0, 20, stepsize3}, PlotStyle → RGBColor[1, 0, 1],
 ImageSize → Large, Frame → True, FrameLabel → {"Time", "<n_3>"},
 PlotLabel → "Occupation of site 3 for discretized data"]
(*DiscretePlot[Sum[(2Abs[timeEvolveState2[t][[qq]]]^2),{qq,1,2}]/
  (Total[Abs[timeEvolveState2[t]]^2]),
 {t,0,120,0.2},PlotStyle→RGBColor[0.25,0,0.75]]*)
(*Note: I am unsure why the dynamics show clipped behavior at the
  peaks -- the time evolution is continuous for the first plot here*)
```

Out[102]=

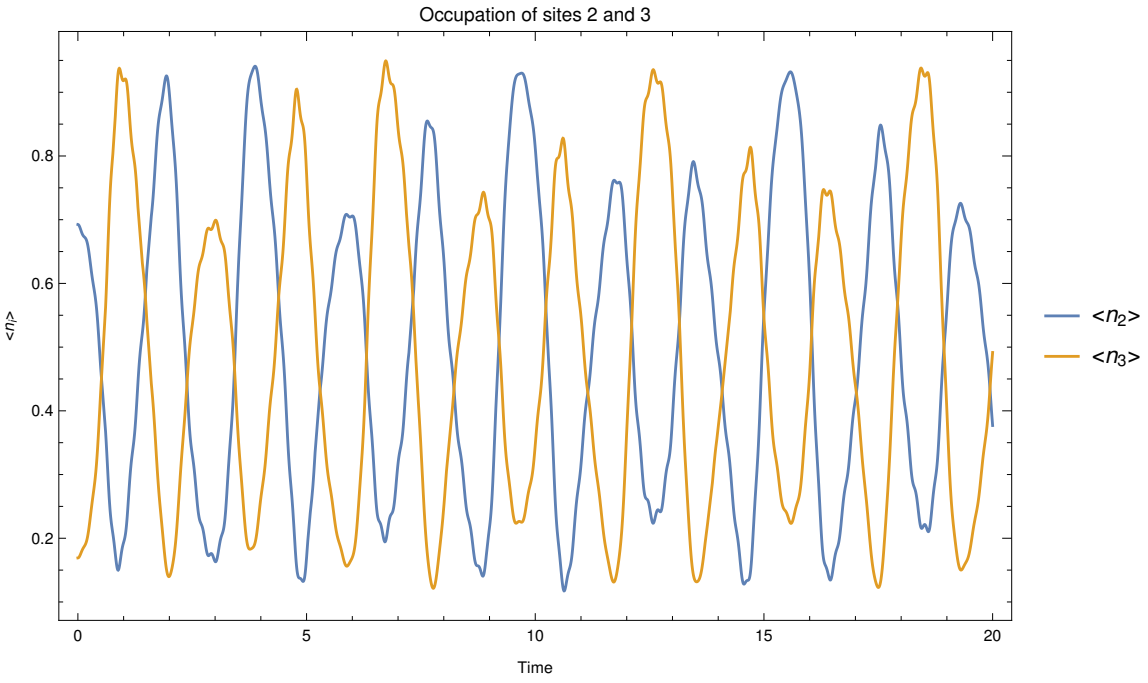

Out[103]=

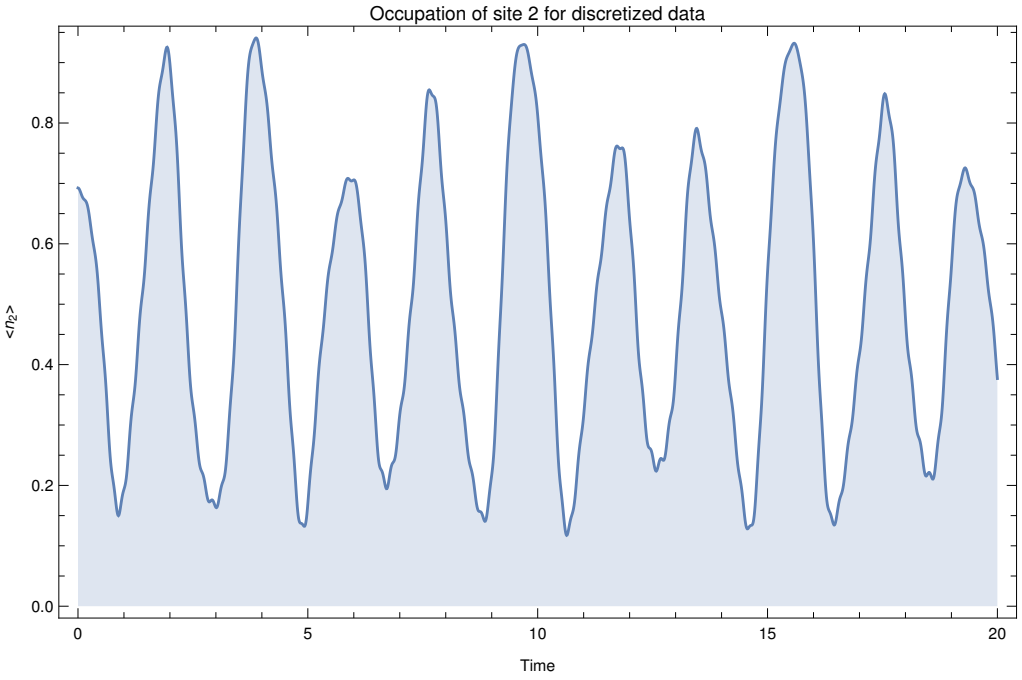

Out[104]=

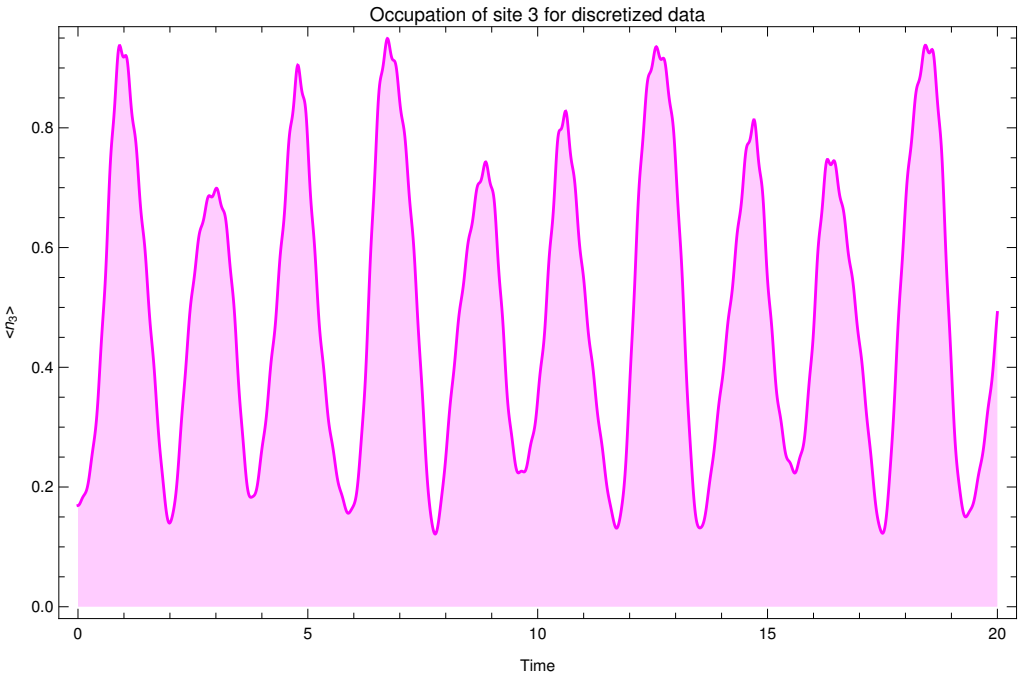

In[105]:=
```
(*No high-frequency modes here, so no filter necessary*)
ListLinePlot[{MovingAverage[
   Flatten[Take[Take[discreteTimeStates3, timesteps3, 2], timesteps3, -1]],
   filter3], MovingAverage[
   Flatten[Take[Take[discreteTimeStates3, timesteps3, 3], timesteps3, -1]], filter3]},
 ImageSize → Large, Frame → True, FrameLabel → {"Time", "<n_i>"},
 PlotLabel → "Occupation of sites 2 and 3 for discretized data",
 PlotLegends → {"<n_2>", "<n_3>"}]
(*ListLinePlot[MovingAverage[Flatten[Take[discreteTimeStates2,timesteps,1]]+
   Flatten[Take[Take[discreteTimeStates2,timesteps,2],timesteps,-1]],
  filter],PlotStyle→RGBColor[0.25,0,0.75]]*)
```

Out[105]=

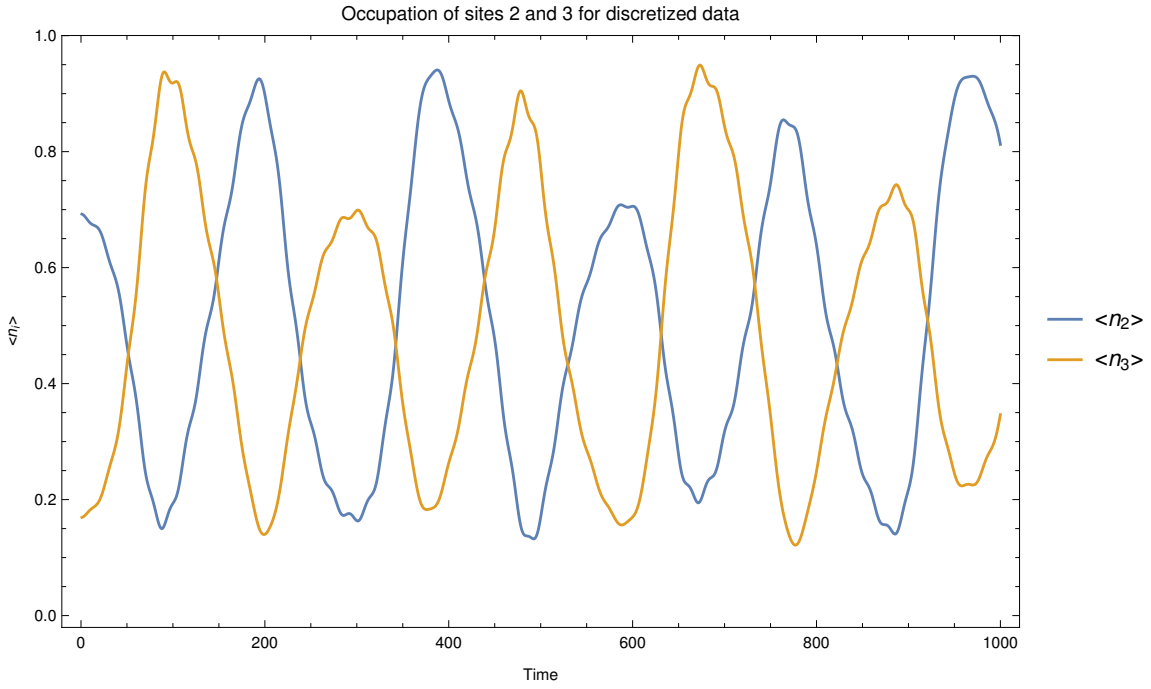

In[106]:=
```
FourierDataN2a = Take[Abs[Fourier[MovingAverage[
      Flatten[Take[Take[discreteTimeStates3, timesteps3, 2], timesteps3, -1]], 1]]]^2,
   Length[Abs[Fourier[MovingAverage[Flatten[Take[Take[discreteTimeStates3,
         timesteps3, 2], timesteps3, -1]], 1]]]^2] / 2];
FourierDataN3a = Take[Abs[Fourier[MovingAverage[Flatten[Take[Take[discreteTimeStates3,
      timesteps3, 3], timesteps3, -1]], 1]]]^2, Length[FourierDataN2a]];
(*One large frequency peak in the Fourier spectrum (non-normalized) --
 if the step size is too small, the side band peaks increase*)
ListLinePlot[{FourierDataN2a, FourierDataN3a}]
```

Out[108]=

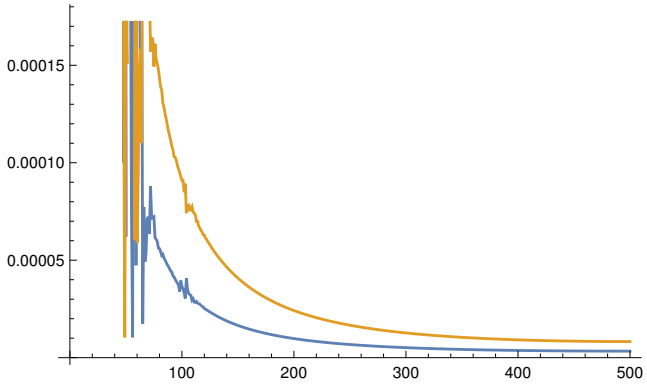

A.2 Exact Diagonalization

Included is a Python script for determining eigenvalues and eigenvectors of Fock states in the Bose-Hubbard model for any value of J, U, optional external potential V, particle number N, or number of lattice sites L. The first script is for open boundary conditions. The second script is for periodic boundary conditions and contains an added feature of optional even-site J_{even} and odd-site J_{odd} tunneling terms that can be set to different values.

```
#! /user/bin/python2
#
# ED_OBC.py
#
# Description:
# ------------
# Exact diagonalization code of the BHH for N particles and L sites with open
boundary conditions
#
# Usage:
# ------
# Execute
#                       python2 ED_OBC.py
# from the command line to execute this for the file's default behavior.
# main exactly diagonalizes a Hamiltonian using the matrix method for the Bose-
Hubbard model of N0 # of particles, L0 sites
# open boundary conditions are employed, but periodic BC's can be added with little
effort
# Different even and odd tunneling terms possible (be careful with signs if you
combine them)

# N0 is number of particles
# L0 is number of sites
# t_e is "even site" hopping
# t_o is "odd site" hopping, for uniform hopping, set t_e = t_o = J
# U0 is same-site interaction energy

# By Marie McLain
# Last updated 1 September 2017
#================================================================================

# Import Libraries
# ================
import itertools as it
import numpy as np
import scipy.sparse as sps
from scipy.sparse.linalg import eigsh
import matplotlib.pyplot as plt
from scipy.linalg import expm
import matplotlib.legend as lgnd
import matplotlib.cm as cm
from matplotlib.colors import LogNorm

from mpl_toolkits.mplot3d import Axes3D                          #3d plotting
from matplotlib.ticker import LinearLocator, FormatStrFormatter, MaxNLocator
#Format tick points

import time
import sys
start_time = time.time()



def main(N0,L0,t_e,t_o,U0):

      #the basis states depend on number of sites and number of particles
      #these are made in the Fock or number basis
      def make_basis_kets(N0,L0):
```

```
            L = np.arange(L0+1)
            Ls = [L]*L0
            basis_gen = it.product(*Ls)
            for basis_el in basis_gen:
                  if sum(basis_el) == N0:
                        yield tuple(basis_el)

      #order the basis into a list
      #determine how big the system is
      count = 0
      New_Basis = []
      for i in make_basis_kets(N0,L0):
            count = count + 1
            New_Basis.append(i)
      dim = len(New_Basis)
      kindex = np.arange(count)


      print 'matrix size = ', count, 'x', count


      #define 1-dimensional quantum operators
      def araise(g,gp):
            return (g+1)**(0.5)*int((g+1)==gp)
      def alower(g,gp):
            return g**(0.5)*int((g-1)==gp)
      def numop(g,gp):
            return g*int(g==gp)

      epsilon = (t_e-t_o)/(t_e+t_o)
      numberops = np.zeros((dim,dim),dtype=float)
      tunnelops = np.zeros((dim,dim),dtype=float)

      #define tunneling function
      #open boundary conditions
      def tunnel(j,m):
            tunneltemp = np.zeros((dim,dim),dtype=float)
            for i in range(dim):
                  for k in range(dim):
                        l1 = np.zeros(L0, dtype=float)
                        l2 = np.zeros(L0, dtype=float)
                        l1[m] = New_Basis[k][m]
                        l1[j] = New_Basis[k][j]
                        l2[m] = New_Basis[i][m]
                        l2[j] = New_Basis[i][j]

                        if np.array_equal(np.add(New_Basis[k],-1.0*l1) ,
np.add(New_Basis[i],-1.0*l2)):
                              alower_el = alower(New_Basis[k][j],New_Basis[i][j])
                              araise_neighbor = araise(New_Basis[k]
[(m)],New_Basis[i][(m)])
                              araise_el = araise(New_Basis[k][j],New_Basis[i][j])
                              alower_neighbor = alower(New_Basis[k]
[(m)],New_Basis[i][(m)])
                              tunneltemp[k][i] = alower_el*araise_neighbor +
araise_el*alower_neighbor
            return tunneltemp
```

```
      #define number function
      def numberop(j):
            numbertemp = np.zeros((dim,dim),dtype=float)
            for i in range(dim):
                  for k in range(dim):
                        if New_Basis[k]==New_Basis[i]:
                              numbertemp[k][i] = (New_Basis[k][j])**2-New_Basis[k]
[j]
            return numbertemp

      #build tunneling and number operators
      for i in range(L0-1):
            if i %2 ==0:
                  tunnelops = np.add(tunnelops,(1+epsilon)*tunnel(i,i+1))
            else:
                  tunnelops = np.add(tunnelops,(1-epsilon)*tunnel(i,i+1))
      for i in range(L0):
            numberops = np.add(numberops,numberop(i))

      tunnelops=np.add(tunnelops,(1-epsilon)*tunnel(L0-1,0))

      #define coefficients and assemble Hamiltonian
      tbar = (t_e+t_o)/2.0
      Ucoeff = (U0/(2.0*tbar))
      Uterm = Ucoeff*numberops

      H = np.add(Uterm, -1.0*tunnelops)
      evals, evects = np.linalg.eigh(H)
      #sys.stdout=open("HprimeN3.txt","w")

      #print 'eigenenergies are ' , evals
      #print 'eigenvectors are ' , evects



      plt.figure(0)
      plt.scatter(kindex,evals, facecolor = '0.0')
      plt.ylabel("Energy/Interaction (E/U)")
      plt.xlabel("Excitation Index k")
      #plt.ylim((-1,4))
      #plt.xlim((-1,count+1))
      #plt.savefig('20150920_strong_N=6__')

      #plt.figure(1)
      #plt.scatter(kindex,evals/(tbar), facecolor = '0.0')
      #plt.ylabel("Energy/Hopping (E/t)")
      #plt.xlabel("Excitation Index k")
      ##plt.ylim((-15,15))
      #plt.xlim((0,count))
      ##plt.savefig('20150920_weak_N=6')

      #plt.figure(2)
      #m03plot = plt.scatter(m03index, m03, c=u'r',marker=u's',linewidths=None)
      #m1plot = plt.scatter(m1index,m1, c=u'g', marker=u'o',linewidths=None)
      #m2plot = plt.scatter(m2index,m2, c=u'b', marker=u'^',linewidths=None)
      #plt.title('First cluster of excitations')
      #plt.xlim((-.5,30))
      #plt.ylim((1.15,1.8))
      #leg = plt.legend([m03plot, m1plot, m2plot],['$m_6 = 0, \pm 3$','$m_6 = \pm
```

```
1$','$m_6 = \pm 2$'], loc=4)
      filling = 0.0
      for i in range(dim):
            for j in range(dim):
                  if H[i][j] != 0.0:
                        filling = filling+1
      percentfilling = filling/dim

      print 'percent filling is: ', percentfilling

      for i in range(dim):
            for j in range(dim):
                  if H[i][j] > 0:
                        H[i][j] = np.log(H[i][j])

      plot2 = plt.figure(2)
      ax = plot2.add_subplot(111)
      im = ax.imshow(H, interpolation='none',cmap=cm.afmhot) #extent=[0, N, 0,
maxsteps])
      xaxis=ax.get_xaxis()
      xaxis.set_major_locator(MaxNLocator(integer=True))
      ax.set_title('Hamiltonian')
      #ax.set_xlabel("Fourier coefficient", fontsize=16)
      #ax.set_ylabel("J/U (scaled)", fontsize=16)
      plot2.colorbar(im)
      plt.savefig('symm_Hamiltonian')


      #how long did that take?
      print("--- %s seconds ---" % (time.time() - start_time))


      plt.show()
      plt.close()

main(6,6,1.0,1.0,30.)
```

```
import itertools as it
import numpy as np
import scipy.sparse as sps
from scipy.sparse.linalg import eigsh
import matplotlib.pyplot as plt
from scipy.linalg import expm
import matplotlib.legend as lgnd
import matplotlib.cm as cm
from matplotlib.colors import LogNorm

from mpl_toolkits.mplot3d import Axes3D                              #3d plotting
from matplotlib.ticker import LinearLocator, FormatStrFormatter, MaxNLocator
#Format tick points

import time
import sys
start_time = time.time()


#main exactly diagonalizes a Hamiltonian using the matrix method for the Bose-
Hubbard model of N0 # of particles, L0 sites
#periodic boundary conditions are employed, but can be removed with little effort
#Different even and odd tunneling terms possible (be careful with signs if you
combine them)

#N0 is number of particles
#L0 is number of sites
#t_e is "even site" hopping
#t_o is "odd site" hopping
#U0 is same-site interaction energy

def main(N0,L0,t_e,t_o,U0):

      #the basis states depend on number of sites and number of particles
      #these are made in the Fock or number basis
      def make_basis_kets(N0,L0):

            L = np.arange(L0+1)
            Ls = [L]*L0
            basis_gen = it.product(*Ls)
            for basis_el in basis_gen:
                  if sum(basis_el) == N0:
                        yield tuple(basis_el)

      #order the basis into a list
      #determine how big the system is
      count = 0
      New_Basis = []
      for i in make_basis_kets(N0,L0):
            count = count + 1
            New_Basis.append(i)
      dim = len(New_Basis)
      kindex = np.arange(count)


      print 'matrix size = ', count, 'x', count


      #define 1-dimensional quantum operators
```

```
      def araise(g,gp):
            return (g+1)**(0.5)*int((g+1)==gp)
      def alower(g,gp):
            return g**(0.5)*int((g-1)==gp)
      def numop(g,gp):
            return g*int(g==gp)

      epsilon = (t_e-t_o)/(t_e+t_o)
      numberops = np.zeros((dim,dim),dtype=float)
      tunnelops = np.zeros((dim,dim),dtype=float)

      #define tunneling function
      #periodic boundary conditions
      def tunnel(j,m):
            tunneltemp = np.zeros((dim,dim),dtype=float)
            for i in range(dim):
                  for k in range(dim):
                        l1 = np.zeros(L0, dtype=float)
                        l2 = np.zeros(L0, dtype=float)
                        l1[m] = New_Basis[k][m]
                        l1[j] = New_Basis[k][j]
                        l2[m] = New_Basis[i][m]
                        l2[j] = New_Basis[i][j]

                        if np.array_equal(np.add(New_Basis[k],-1.0*l1) ,
np.add(New_Basis[i],-1.0*l2)):
                              alower_el = alower(New_Basis[k][j%L0],New_Basis[i][j
%L0])
                              araise_neighbor = araise(New_Basis[k][(m)
%L0],New_Basis[i][(m)%L0])
                              araise_el = araise(New_Basis[k][j%L0],New_Basis[i][j
%L0])
                              alower_neighbor = alower(New_Basis[k][(m)
%L0],New_Basis[i][(m)%L0])
                              tunneltemp[k][i] = alower_el*araise_neighbor +
araise_el*alower_neighbor
            return tunneltemp

      #define number function
      def numberop(j):
            numbertemp = np.zeros((dim,dim),dtype=float)
            for i in range(dim):
                  for k in range(dim):
                        if New_Basis[k]==New_Basis[i]:
                              numbertemp[k][i] = (New_Basis[k][j])**2-New_Basis[k]
[j]
            return numbertemp

      #build tunneling and number operators
      for i in range(L0-1):
            if i %2 ==0:
                  tunnelops = np.add(tunnelops,(1+epsilon)*tunnel(i,i+1))
            else:
                  tunnelops = np.add(tunnelops,(1-epsilon)*tunnel(i,i+1))
      for i in range(L0):
            numberops = np.add(numberops,numberop(i))

      tunnelops=np.add(tunnelops,(1-epsilon)*tunnel(L0-1,0))
```

```
      #define coefficients and assemble Hamiltonian
      tbar = (t_e+t_o)/2.0
      Ucoeff = (U0/(2.0*tbar))
      Uterm = Ucoeff*numberops

      H = np.add(Uterm, -1.0*tunnelops)
      #Define unitary rotation operator
      #Cln = expm(1j*(2/3)*np.pi*
      #H = Uterm
      #evals, evects = eigsh(H, k = count-2)
      evals, evects = np.linalg.eigh(H)
      #sys.stdout=open("HprimeN3.txt","w")
      #print H[46], H[47], H[48], H[49], H[50], H[51], H[52], H[53], H[54], H[55]

      #print evals[0],evals[1],evals[2],evals[3],evals[4],evals[5],evals[6]
      print evals
      #print abs(evals[4]) - abs(evals[3])
      #m03 =
(1/U0)*np.array([evals[1],evals[6],evals[9],evals[12],evals[17],evals[18],evals[19]
,evals[20],evals[27],evals[30]])
      #m03index = np.array([0,5,8,11,16,17,18,19,26,29])
      #m1 =
(1/U0)*np.array([evals[2],evals[3],evals[7],evals[8],evals[15],evals[16],evals[23],
evals[24],evals[28],evals[29]])
      #m1index = np.array([1,2,6,7,14,15,22,23,27,28])
      #m2 =
(1/U0)*np.array([evals[4],evals[5],evals[10],evals[11],evals[13],evals[14],evals[21
],evals[22],evals[25],evals[26]])
      #m2index = np.array([3,4,9,10,12,13,20,21,24,25])

      #print m03

      #print 'eigenenergies are ' , evals
      #print 'eigenvectors are ' , evects



      plt.figure(0)
      plt.scatter(kindex,evals, facecolor = '0.0')
      plt.ylabel("Energy/Interaction (E/U)")
      plt.xlabel("Excitation Index k")
      #plt.ylim((-1,4))
      #plt.xlim((-1,count+1))
      #plt.savefig('20150920_strong_N=6__')

      #plt.figure(1)
      #plt.scatter(kindex,evals/(tbar), facecolor = '0.0')
      #plt.ylabel("Energy/Hopping (E/t)")
      #plt.xlabel("Excitation Index k")
      ##plt.ylim((-15,15))
      #plt.xlim((0,count))
      ##plt.savefig('20150920_weak_N=6')

      #plt.figure(2)
      #m03plot = plt.scatter(m03index, m03, c=u'r',marker=u's',linewidths=None)
      #m1plot = plt.scatter(m1index,m1, c=u'g', marker=u'o',linewidths=None)
      #m2plot = plt.scatter(m2index,m2, c=u'b', marker=u'^',linewidths=None)
      #plt.title('First cluster of excitations')
      #plt.xlim((-.5,30))
```

```
      #plt.ylim((1.15,1.8))
      #leg = plt.legend([m03plot, m1plot, m2plot],['$m_6 = 0, \pm 3$','$m_6 = \pm
1$','$m_6 = \pm 2$'], loc=4)
      filling = 0.0
      for i in range(dim):
            for j in range(dim):
                  if H[i][j] != 0.0:
                        filling = filling+1
      percentfilling = filling/dim

      print 'percent filling is: ', percentfilling

      for i in range(dim):
            for j in range(dim):
                  if H[i][j] > 0:
                        H[i][j] = np.log(H[i][j])

      plot2 = plt.figure(2)
      ax = plot2.add_subplot(111)
      im = ax.imshow(H, interpolation='none',cmap=cm.afmhot) #extent=[0, N, 0,
maxsteps])
      xaxis=ax.get_xaxis()
      xaxis.set_major_locator(MaxNLocator(integer=True))
      ax.set_title('Hamiltonian')
      #ax.set_xlabel("Fourier coefficient", fontsize=16)
      #ax.set_ylabel("J/U (scaled)", fontsize=16)
      plot2.colorbar(im)
      plt.savefig('symm_Hamiltonianweak')


      #how long did that take?
      print("--- %s seconds ---" % (time.time() - start_time))


      plt.show()
      plt.close()

main(4,4,1.0,1.0,0.3)
```

A.3 Single particle density matrix plotting

The following is an example of a Python script for plotting the SPDM in density map format and generating plots for each time step.

```
#! /user/bin/python3
#
# SPDM_density.py
#
# Description:
# ------------
# Enables plotting of of depletion dynamics for varying barrier height and other
# parameters from TEBD *extPotcorrelationfunctions.txt files
#
# Usage:
# ------
# Execute
#                       python3 SPDM_density.py
# from the command line to execute this files dfault behavior. The default
# behavior is set at the end of this file and it is there that you can set a
# directory containing the data files to be processed. All the files in that
# directory are filtered using the fnames_and_params function. The filtering
# allows specific parameter value selection or all values of a parameter found
# in the directory using a wildcard string '*'.
#
# By Logan Hillberry
# and Marie McLain
# Last updated 12 August 2017
#================================================================================

# Import Libraries
# ================

# Built in libraries
# ------------------
import re
import os.path

# External libraries
# ------------------
import numpy as np
import matplotlib as mpl
import matplotlib.cm as cm
import matplotlib.pyplot as plt
import matplotlib.colors as colorss
from matplotlib.ticker import LinearLocator, FormatStrFormatter, MaxNLocator    #Format tick p
oints
import operator
# The following two lines ensure type 1 fonts are used
mpl.rcParams['pdf.fonttype'] = 42
mpl.rcParams['ps.fonttype'] = 42
# plotting defaults
plt_params = {
          'font.size' : 14,
          'font.family' : 'serif',
          'text.usetex' : True,
          }
plt.rcParams.update(plt_params)


# File I/O
# ========

# Metadata name
# -------------
# Generic names of data files containing parameter values
# NOTE: dec=1 for the H parameter because when i renamed files, I didn't do it
# in a way consistent with the TEBD style. This is of course easily fixed but
```

```
# this shows the utility of the helper function.
def name(H, L, N, Chi, jTunn, U0):
    blank_name = r'H{:<0' + width(H, ndec=1) + '}L{}N{}Chi{}jTunn{:<0' +\
        width(jTunn) + r'}U0{:<0' + width(U0) +r'}OBC'
    return blank_name.format(H, L, N, Chi, jTunn, U0)

# Zero padding helper function
# ----------------------------
# Helper function returns the required width of a parameters value. Eg, U0=0.3
# must be padded to 0.30 which has a width of 4, but U0=30.0 must be padded
# to 30.00 which has a width of 5. The ndec keyword argument specifies the
# number of places to the right of the decimal that must be made 0 if not
# specified. ndec defaults to 2 for use with TEBD-style names
def width(param, ndec=3):
    # Edge case if user specifies a wild card. For this return an empty string
    if type(param) is str:
        return ''
    #  Edge case if requested param is zero
    if  param == 0.0:
        decade = 1
    # Typical behavior, get decade of param to add to the width
    else:
        decade = int(np.log10(param))
   # the number of places to the left of the decimal plus one for the decimal
   # point plus the number of places used after the decimal point.
    return str(decade + 1 + ndec)

# List of filenames and their associated simulation params
# --------------------------------------------------------
# dir is an argument pointing to the folder containing data files.
# Parameters H, L, N, Chi, jTunn, and U0 are the associated TEBD parameters
# stored in the file's name. Passing the string '*' will 'wildcard' that
# parameter, so all values of that parameter will be found. Suffix is appended
# to the name making this function reusable for various TEBD-style file names.
# Returns a tuple of two lists. The first is a list of file names matching the
# requested parameters. The second is a list of dictionaries storing the
# numeric parameter values with keys of strings corresponding to the TEBD
# parameter names.
def fnames_and_params(H, L, N, Chi, jTunn, U0, suffix, dir):
    # list of parameter selections
    selections = [H, L, N, Chi, jTunn, U0]
    # list of parameter types
    types = [float, int, int, int, float, float]
    # list of named keys for parameters
    keys = ['H', 'L', 'N', 'Chi', 'jTunn', 'U0']
    # regex for an integer of float
    anynumber = r'[-/+]?\d*\.?\d+'
    # replace any '*' paramters with the regex for an integer or float
    selections = [anynumber if s is '*' else s for s in selections]
    # walk the dir for filenames matching name with parameter selections
    fnames = [os.path.join(dir, f) for f in os.listdir(dir)
        if re.match(name(*selections) + suffix + r'.txt', f)]
    # parse the name for the numeric parameters and store in a dictionary
    params = [dict(zip(keys, [types[i](param) for i, param in
        enumerate(re.findall(anynumber, f))])) for f in fnames]
    #params.sort(key=operator.itemgetter('N'))
    print('names dict', fnames)
    print('params dict', params)
    return fnames, params


# Analysis and plotting
# =====================
```

```
# Process and the list of file names and parameters as given by the
# fnames_params function to get the depletion metric.
def process(fnames, params, plot_name):
    if len(fnames) == 0:
        raise ValueError('No files to load!')
    print('\nFrom ', os.path.dirname(fnames[0]), '\n')
    numPlt = len(fnames)
    cmap = plt.get_cmap('viridis')
    colors = [cmap(i) for i in np.linspace(0,1,numPlt)]

    # loop through filtered files
    for f, p, c in zip(fnames, params, colors):
        print ('processing ' + os.path.basename(f) + '...')

        # Gather important constants
        L      = p['L']
        N      = p['N']
        H      = p['H']
        jTunn  = p['jTunn']
        Lhalf  = int(L/2)
        #TT     = int(241)

        # import data
        Xa = np.genfromtxt(f)
        # Get size of correlation matrix
        rows = np.shape(Xa)[0]
        cols = np.shape(Xa)[1]

        # Get size of lattice -- if needed
        LL=int(cols/2)

        #Get number of timesteps
        TT=int(rows/LL)

        # arrange data into complex matrix form
        Xb = np.array(Xa[:, :L] + 1.0j * Xa[:, L:])
        print 'Xb min', np.real(Xb).min()
        comparekey = np.real(Xb).min()
        Xb = abs(Xb)

        #if np.real(Xb).min() < 0:
        #    Xb = Xb - np.real(Xb).min() + abs(np.real(Xb).min())/10.
        print 'new Xb min' , np.real(Xb).min()
            # initialize and form non-normalized spdm (off by one timestep due to ITP)
        Xc = np.zeros((TT, L, L), dtype=complex)
        diags = np.zeros((TT,L))
        diagMat = np.zeros((TT,L,L))
        Xd = np.zeros((TT,L,L))
        Xc[0, ::, ::] = Xb[:L, :L]
        for t in range(1, TT):
            Xc[t, ::, ::] = Xb[(t - 1) * L:(t - 1) * L + L, :L]
            diags[t] = np.diagonal(Xc[t])
            np.fill_diagonal(diagMat[t],diags[t])
            Xd[t] = Xc[t]-diagMat[t]

        print 'diag mat', len(Xd[1])


        numPlt2 = 20 #TT/4
        cmap2 = plt.get_cmap('viridis')
        colors2 = [cmap2(i) for i in np.linspace(0,1,numPlt2)]
        timedict = np.linspace(int(0),int(numPlt2),int(numPlt2+1))
        timedict2 = np.linspace(int(0),int(TT),int(TT+1))
```

```
        for ttime, col in zip(timedict, colors2):
            # plot SPDM
            fig = plt.figure(int(ttime),(4,4)) # fignum, (sizex, sizey), inches
            ax = fig.add_subplot(1,1,1)
            im = ax.imshow(abs(Xd[ttime+130]), interpolation='bilinear',cmap=cm.inferno, norm=
colorss.SymLogNorm(0.1,vmin=0.,vmax=1.))
            xaxis=ax.get_xaxis()
            xaxis.set_major_locator(MaxNLocator(integer=True))
            fig.gca().invert_yaxis()
            #ax.set_title('SPDM')
            ax.set_xlabel("Site $i$", fontsize=16)
            ax.set_ylabel("Site $j$", fontsize=16)
            ax.set_aspect('auto')
            fig.colorbar(im, label=r'$\mid \langle b^{\dagger}_i b_j \rangle \mid$')
            #ax.legend(bbox_to_anchor=(1.05, 1), loc=2, title='$\langle n_{L} \rangle$')
            new_name =  plot_name  + 'time00' + str(int(ttime+130)) + '.jpg'
            plt.savefig(new_name, format='jpg', dpi=300, bbox_inches='tight')
            print('\nSaved plot to ', plot_name)
            plt.close()



# Run default behavior
if __name__ == "__main__":

    # Directory of this file
    #data_dir = os.path.dirname(os.path.realpath(__file__))
    #
    # Directory where I stored data on my machine
    data_dir = "/home/marie/Documents/PhD/test_data"

    # Description of files to import
    H     = 1.0
    L     = 55
    N     = 27
    Chi   = 80
    jTunn = 1.0
    U0    = 30.0

    # gather list of file names and parse them for the associated parameters
    fnames, params = fnames_and_params(
        H, L, N, Chi, jTunn, U0, 'extPotcorrelationfunctions', data_dir)

    # Examples testing width command, multi wildcard use, and no file error.

    #fnames, params = fnames_and_params(
    #    '*', 27, 14, 40, 1.0, 30.0, 'extPotcorrelationfunctions', data_dir)
    #fnames, params = fnames_and_params(
    #    '*', 27, 14, 40, 1.0, '*', 'extPotcorrelationfunctions', data_dir)
    #fnames, params = fnames_and_params(
    #    0.0, 0, 0, 0, 0.0, 0.0, 'extPotcorrelationfunctions', data_dir)

    # name of plot to be saved
    plot_name = 'SPDM-nodiag_' + name(H, L, N, Chi, jTunn, U0)

    # import, process, and plot the data
    process(fnames, params, plot_name)
```